











Appendix H

WTC 2 EAST FACE COMBINED FIRE AND WINDOW CONDITION AND WINDOW SMOKE CONDITION

This appendix provides visual representations of the data contained in data sheets describing observations of fire, smoke, and window condition on a window-by-window basis as a function of time for the east face of WTC 2. The data for window condition and fire observations are combined into single representations, with the data for fire taking precedence. Observations are represented using the key provided in Figure 5-1 as follows:  - window glass in place,  - window open,  - spot fire,  - fire visible inside,  - external flaming, and  - not visible. The data for smoke are shown in separate figures using the key from Figure 5-1 as follows:  - no smoke visible,  - light smoke,  - heavy smoke, and  - not visible. For a given time, the window condition and fire data are shown first.

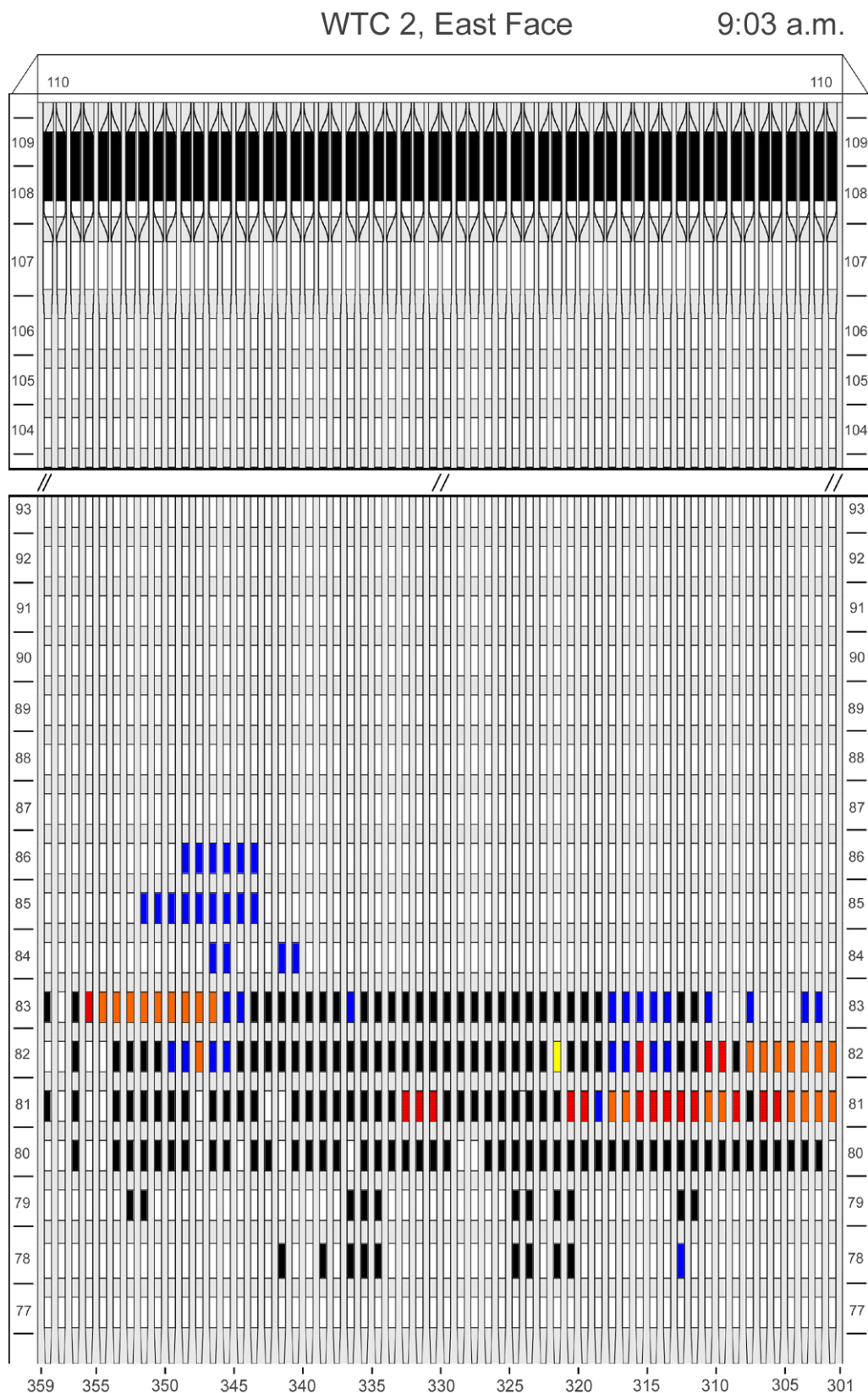


Figure H-1. Diagram of the east face of WTC 2 for floors 77 to 93 and floors 104 to 110 at 9:03 a.m. showing the condition of windows and locations of fires.

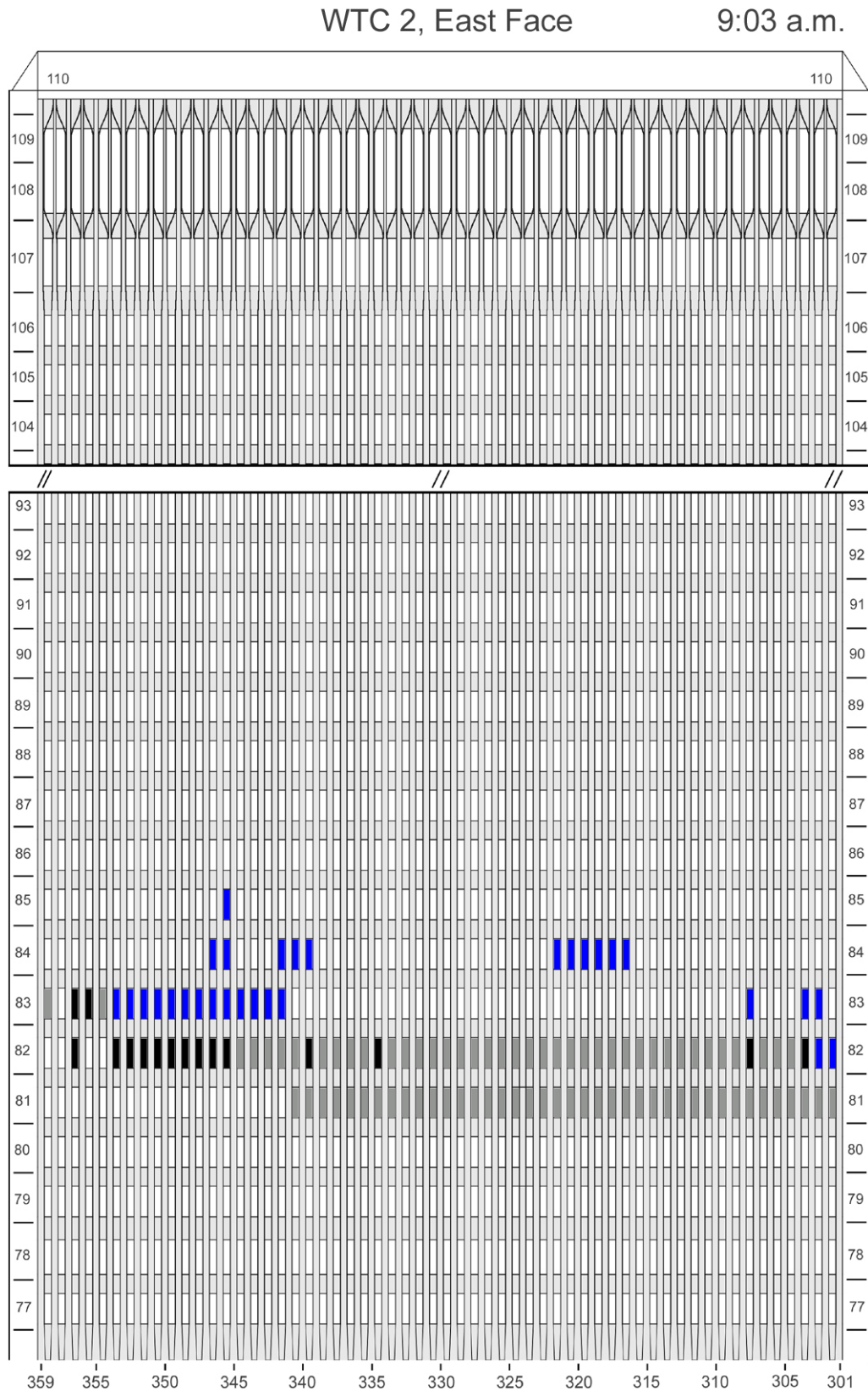


Figure H-2. Diagram of the east face of WTC 2 for floors 77 to 93 and floors 104 to 110 at 9:03 a.m. showing windows where smoke was observed and those hidden from view.

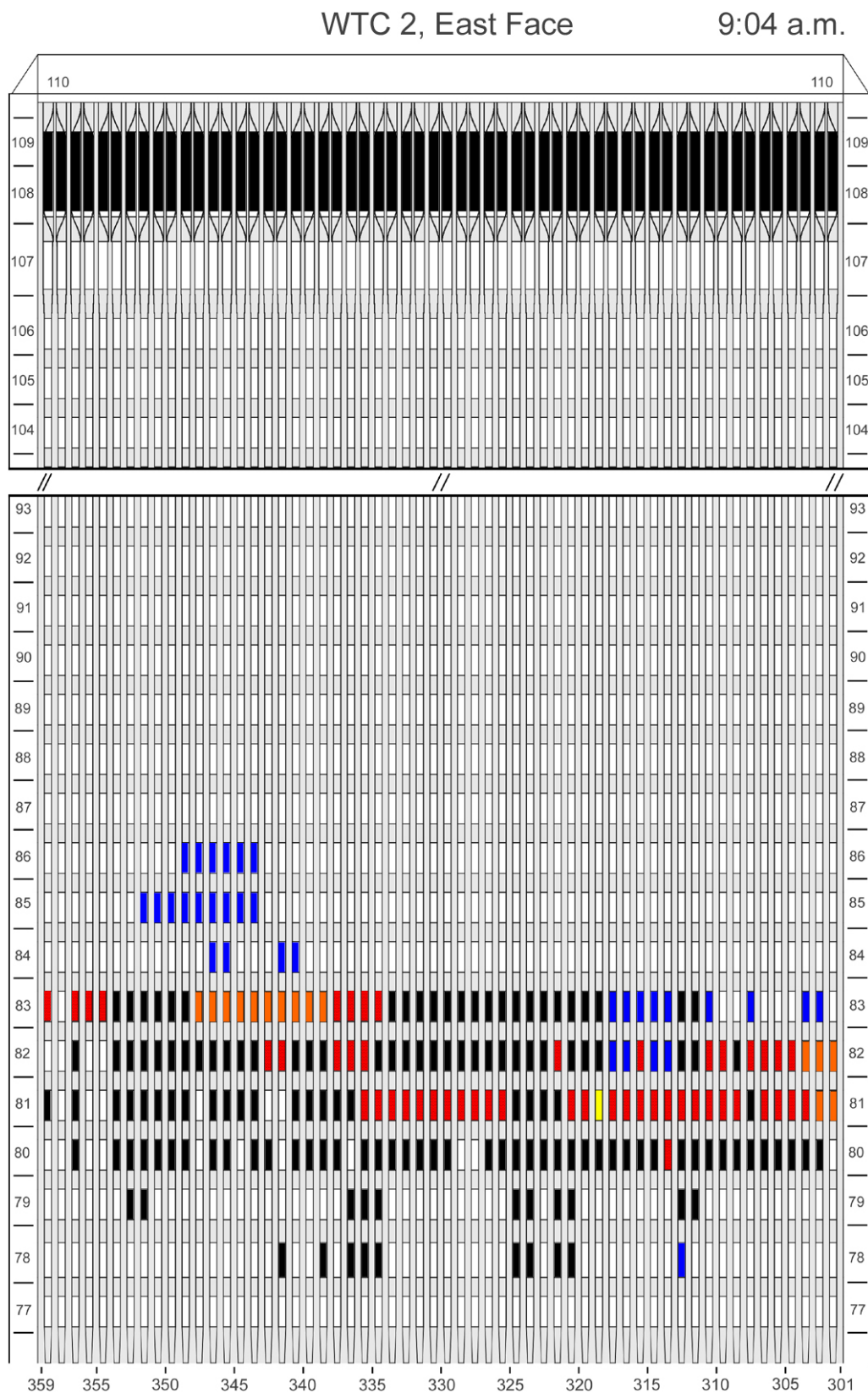


Figure H-3. Diagram of the east face of WTC 2 for floors 77 to 93 and floors 104 to 110 at 9:04 a.m. showing the condition of windows and locations of fires.

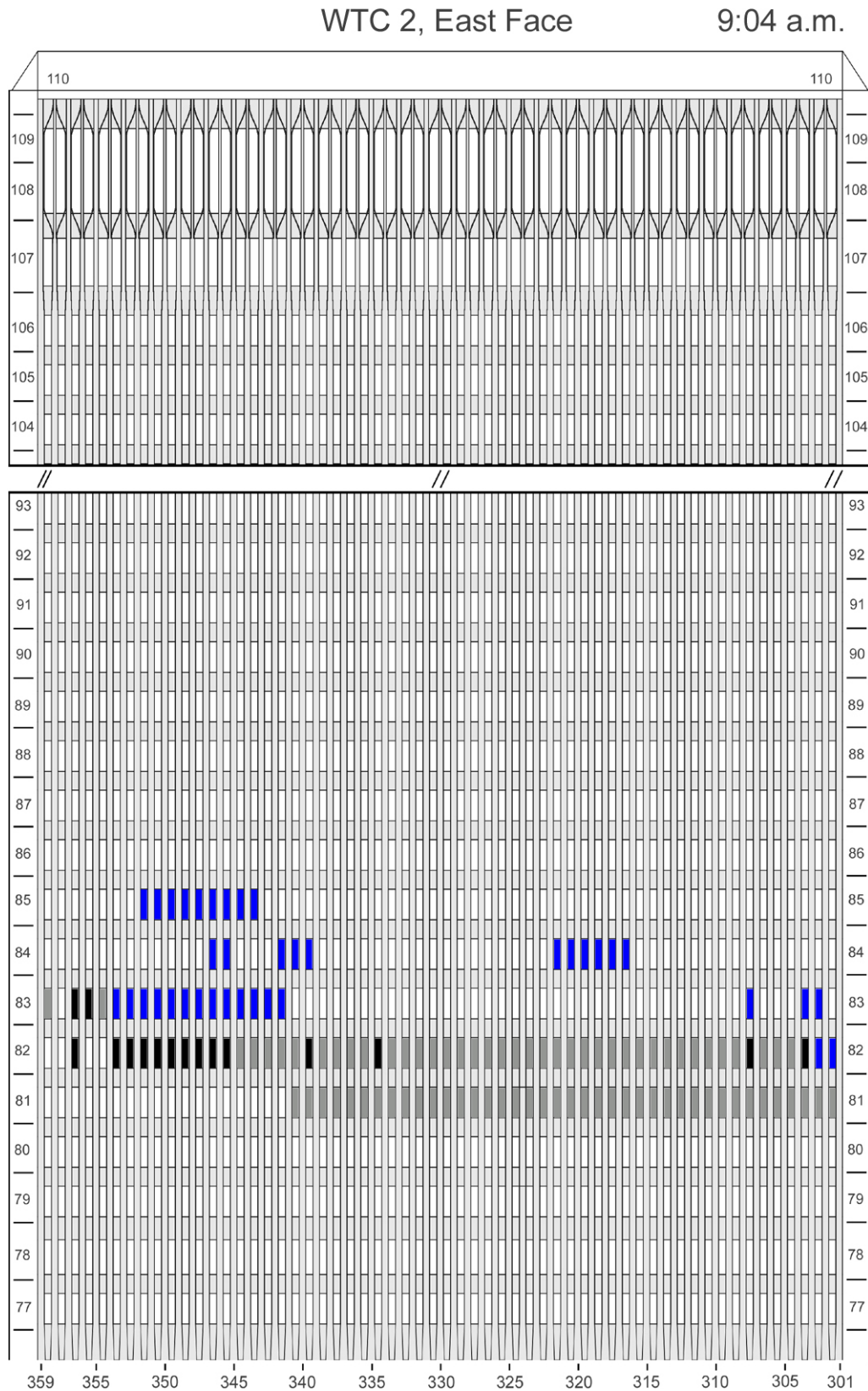


Figure H-4. Diagram of the east face of WTC 2 for floors 77 to 93 and floors 104 to 110 at 9:04 a.m. showing windows where smoke was observed and those hidden from view.

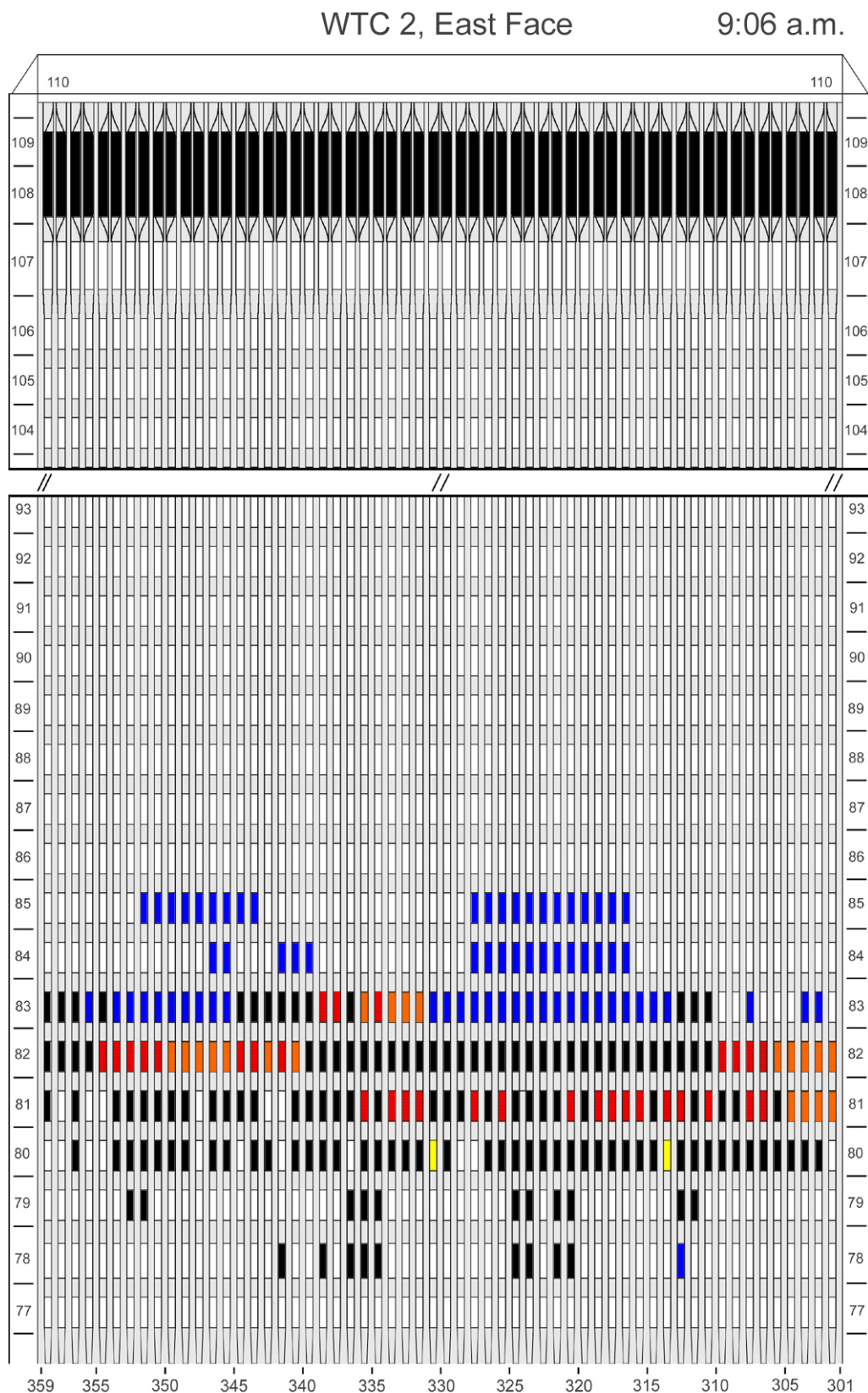


Figure H-5. Diagram of the east face of WTC 2 for floors 77 to 93 and floors 104 to 110 at 9:06 a.m. showing the condition of windows and locations of fires.

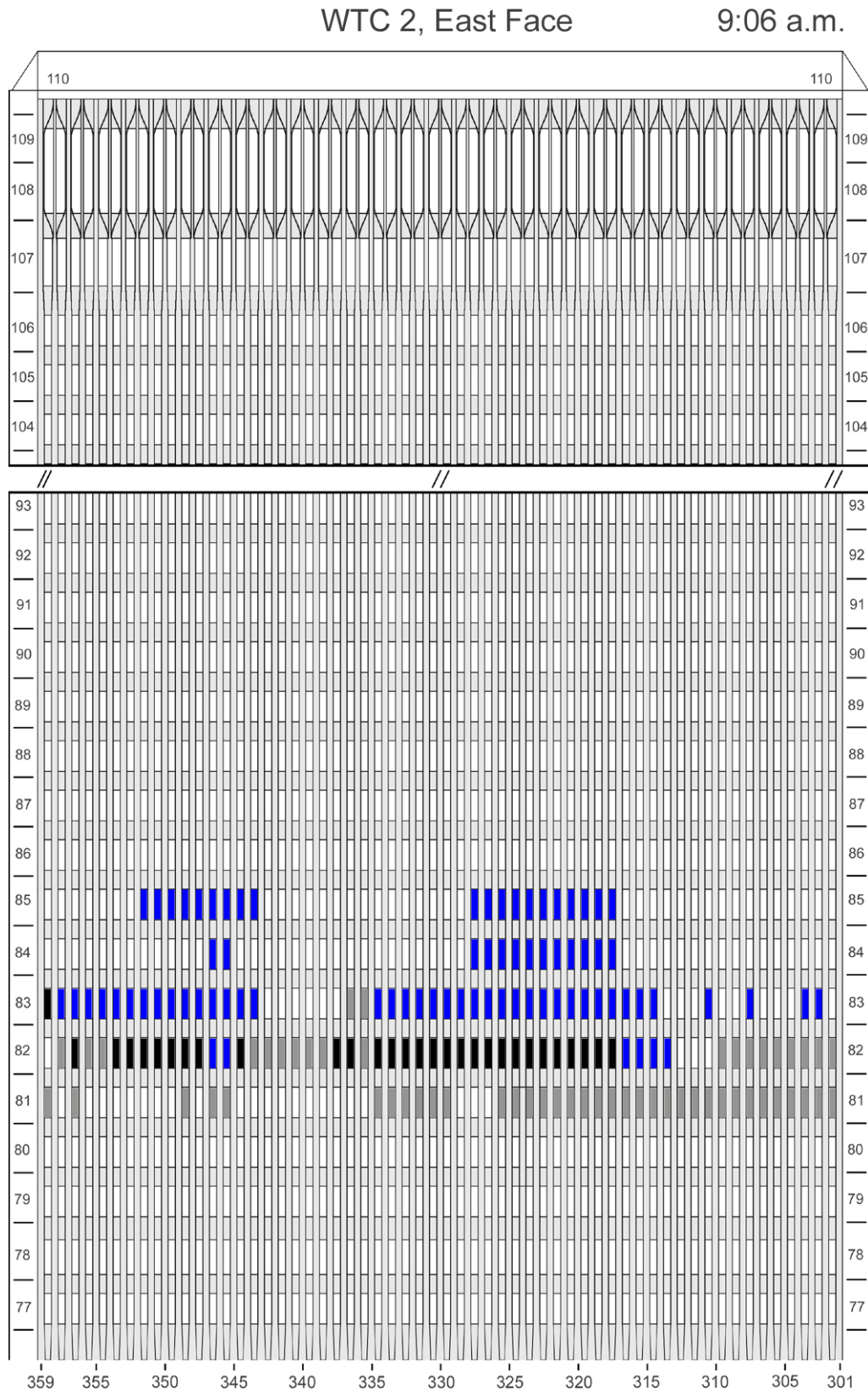


Figure H-6. Diagram of the east face of WTC 2 for floors 77 to 93 and floors 104 to 110 at 9:06 a.m. showing windows where smoke was observed and those hidden from view.

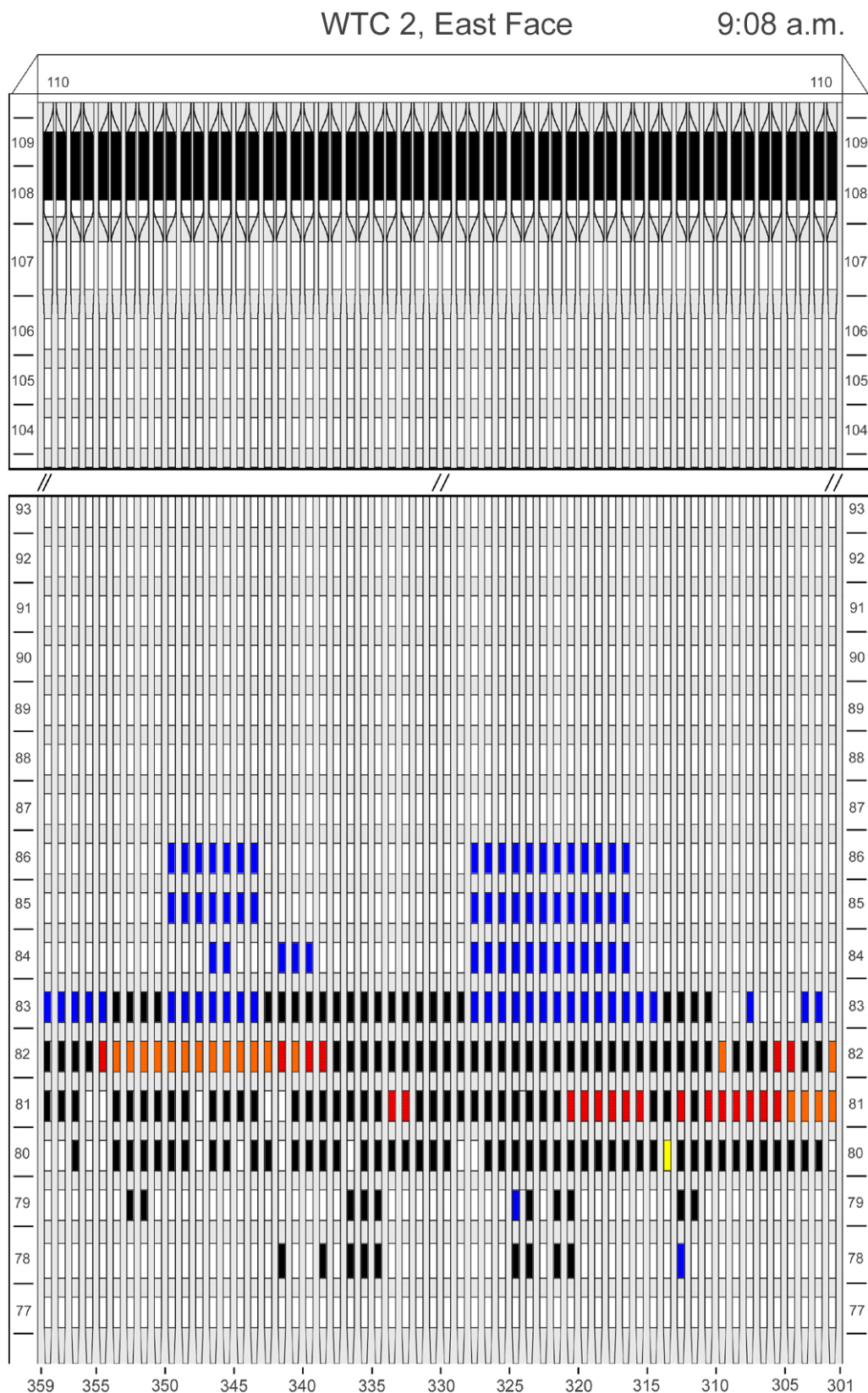


Figure H-7. Diagram of the east face of WTC 2 for floors 77 to 93 and floors 104 to 110 at 9:08 a.m. showing the condition of windows and locations of fires.

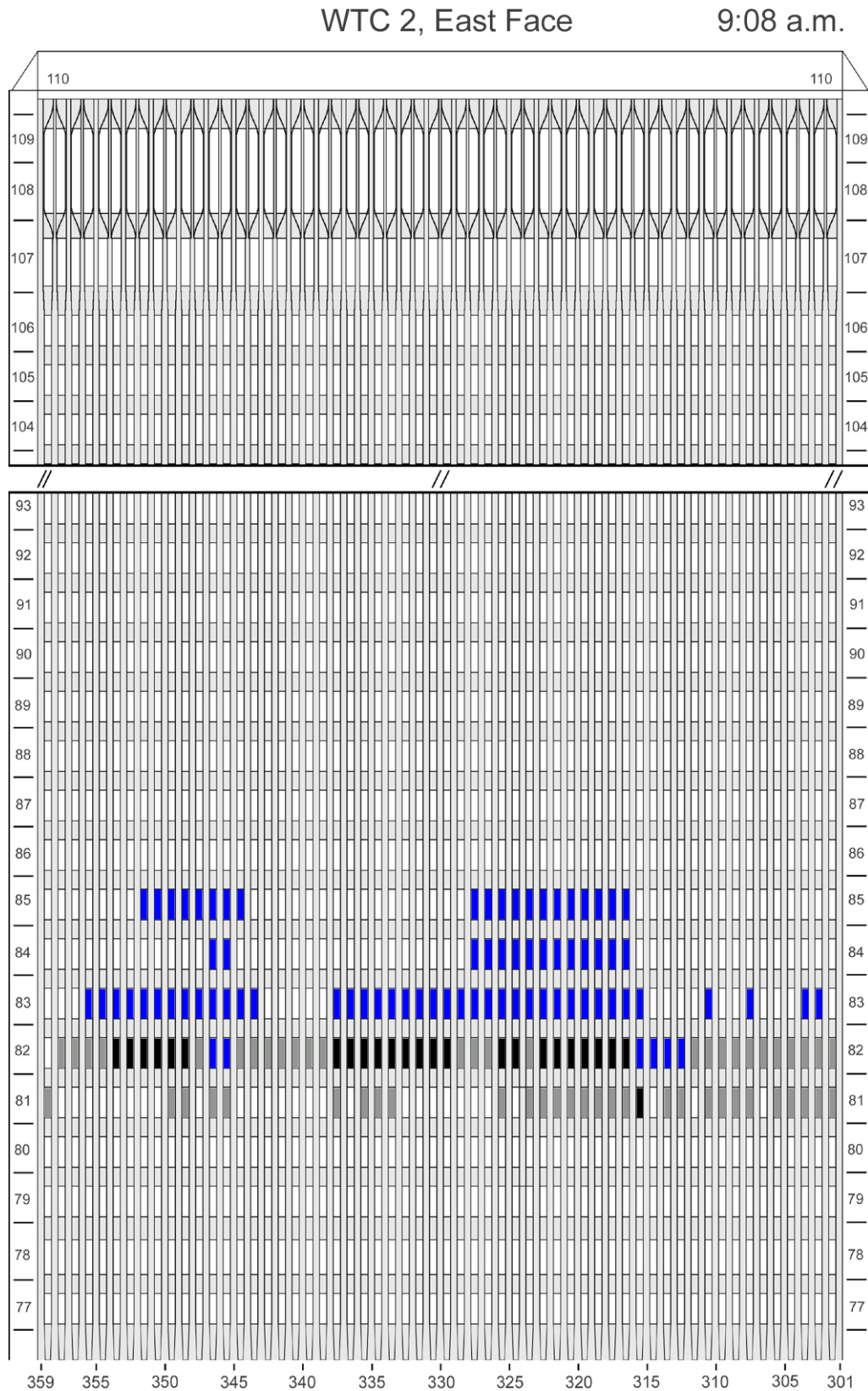


Figure H-8. Diagram of the east face of WTC 2 for floors 77 to 93 and floors 104 to 110 at 9:08 a.m. showing windows where smoke was observed and those hidden from view.

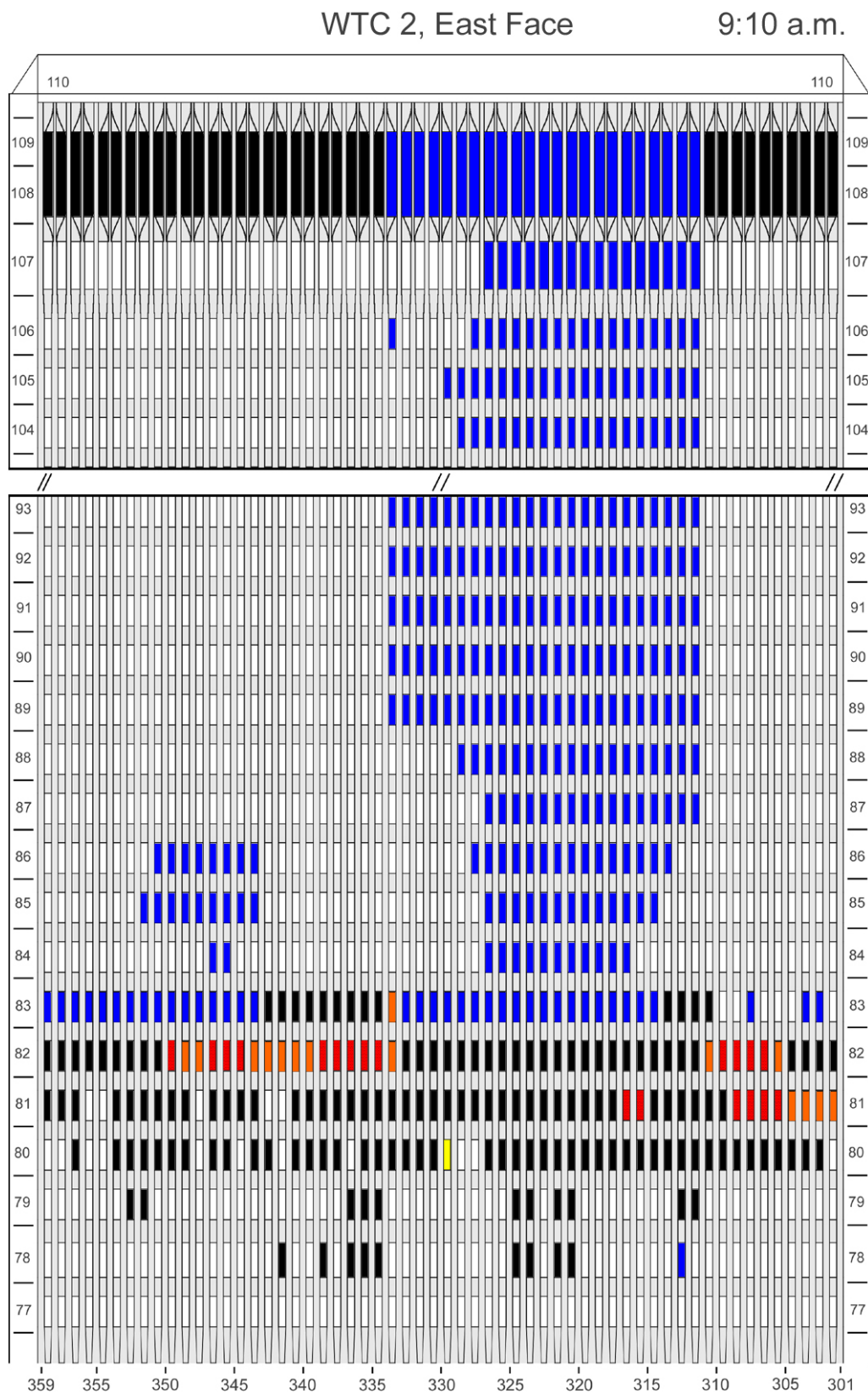


Figure H-9. Diagram of the east face of WTC 2 for floors 77 to 93 and floors 104 to 110 at 9:10 a.m. showing the condition of windows and locations of fires.

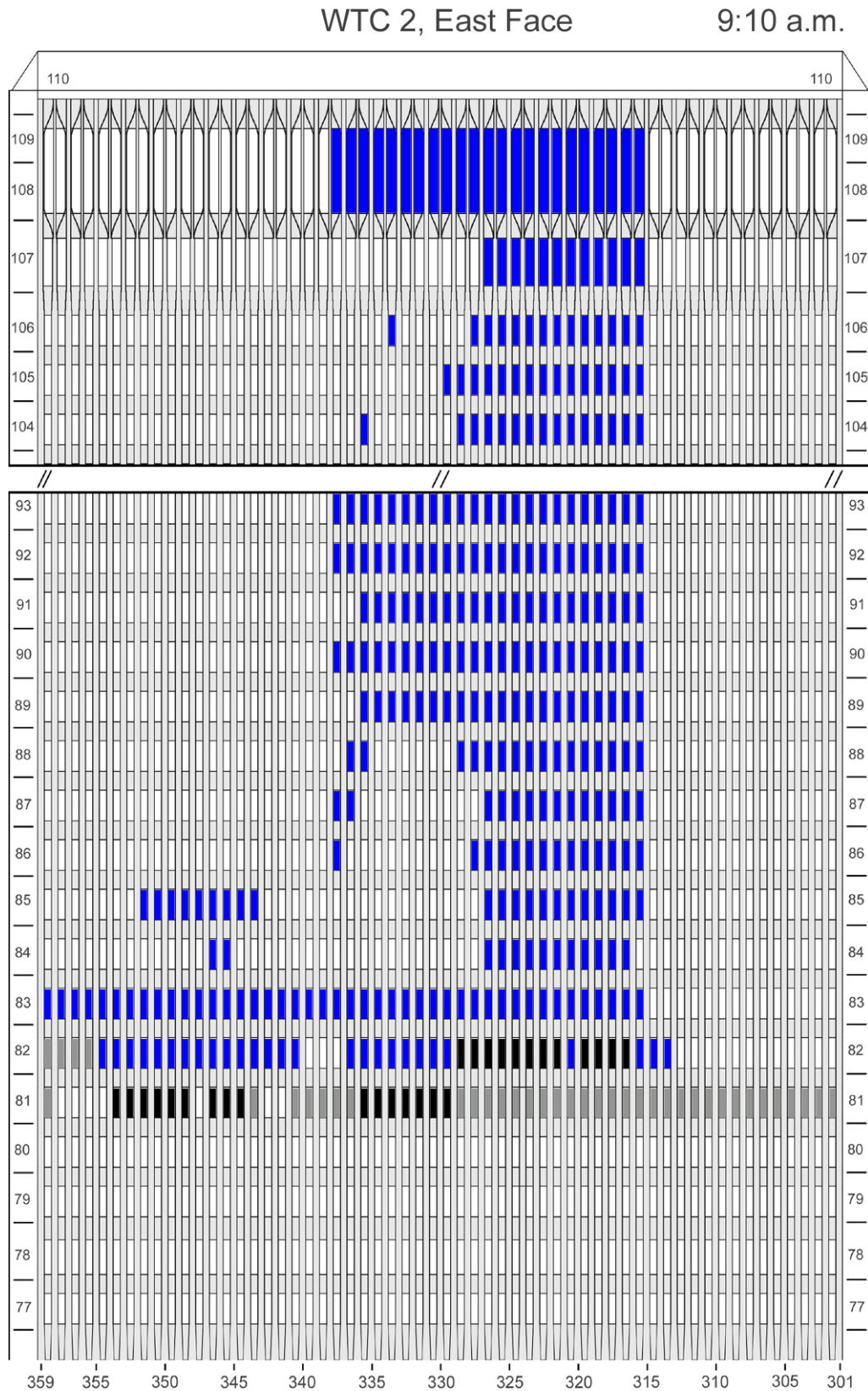


Figure H-10. Diagram of the east face of WTC 2 for floors 77 to 93 and floors 104 to 110 at 9:10 a.m. showing windows where smoke was observed and those hidden from view.

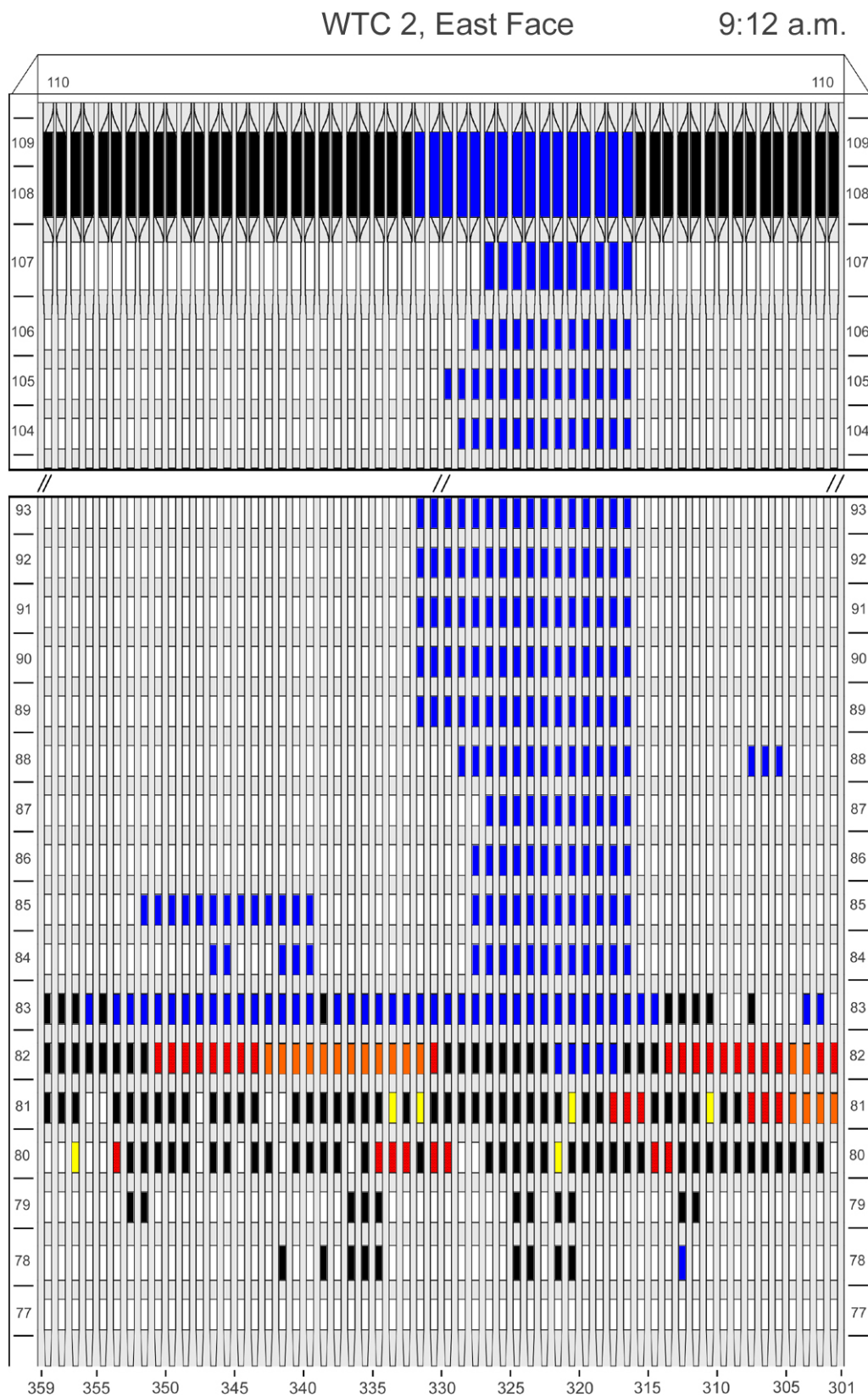


Figure H-11. Diagram of the east face of WTC 2 for floors 77 to 93 and floors 104 to 110 at 9:12 a.m. showing the condition of windows and locations of fires.

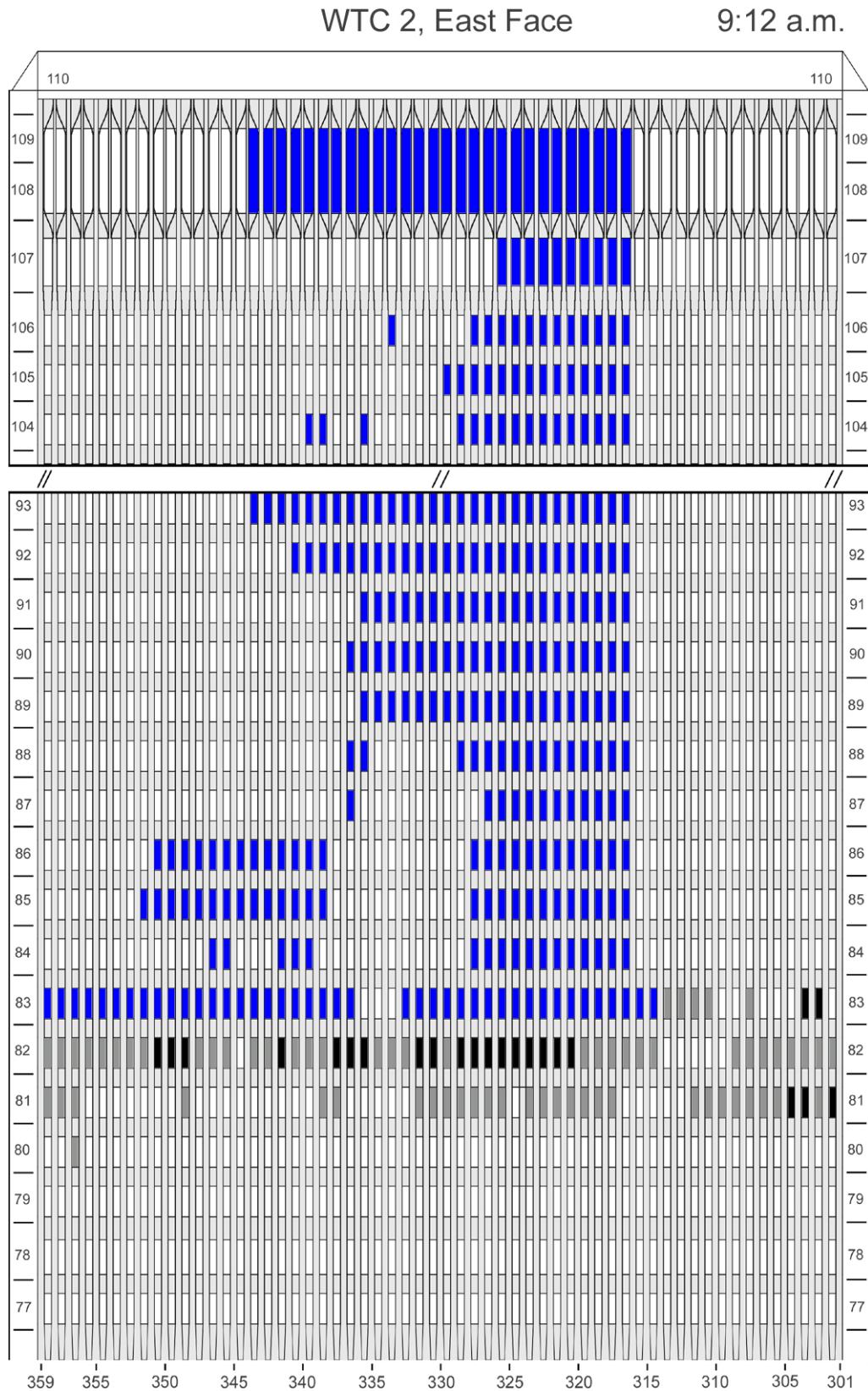


Figure H-12. Diagram of the east face of WTC 2 for floors 77 to 93 and floors 104 to 110 at 9:12 a.m. showing windows where smoke was observed and those hidden from view.

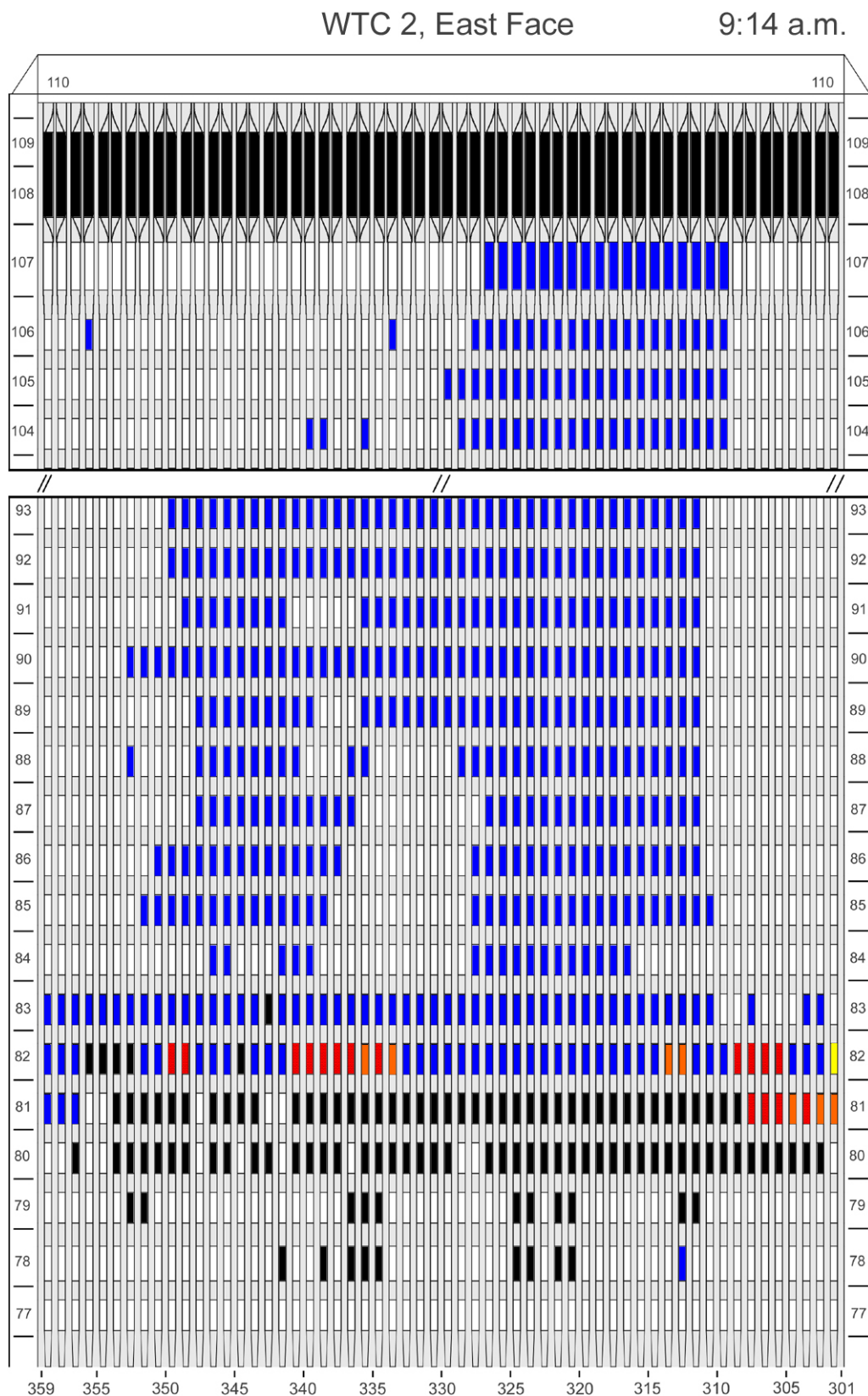


Figure H-13. Diagram of the east face of WTC 2 for floors 77 to 93 and floors 104 to 110 at 9:14 a.m. showing the condition of windows and locations of fires

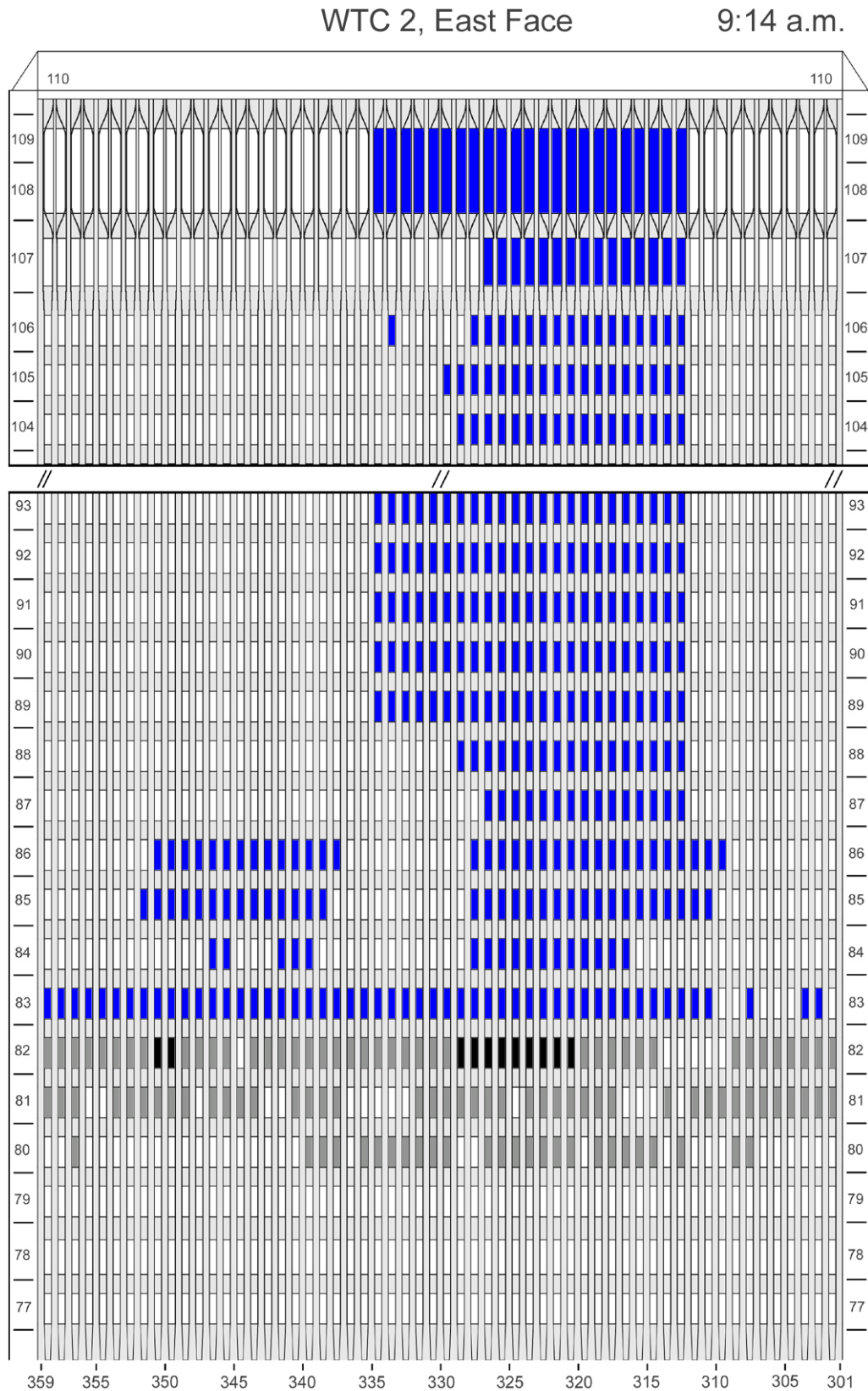


Figure H-14. Diagram of the east face of WTC 2 for floors 77 to 93 and floors 104 to 110 at 9:14 a.m. showing windows where smoke was observed and those hidden from view.

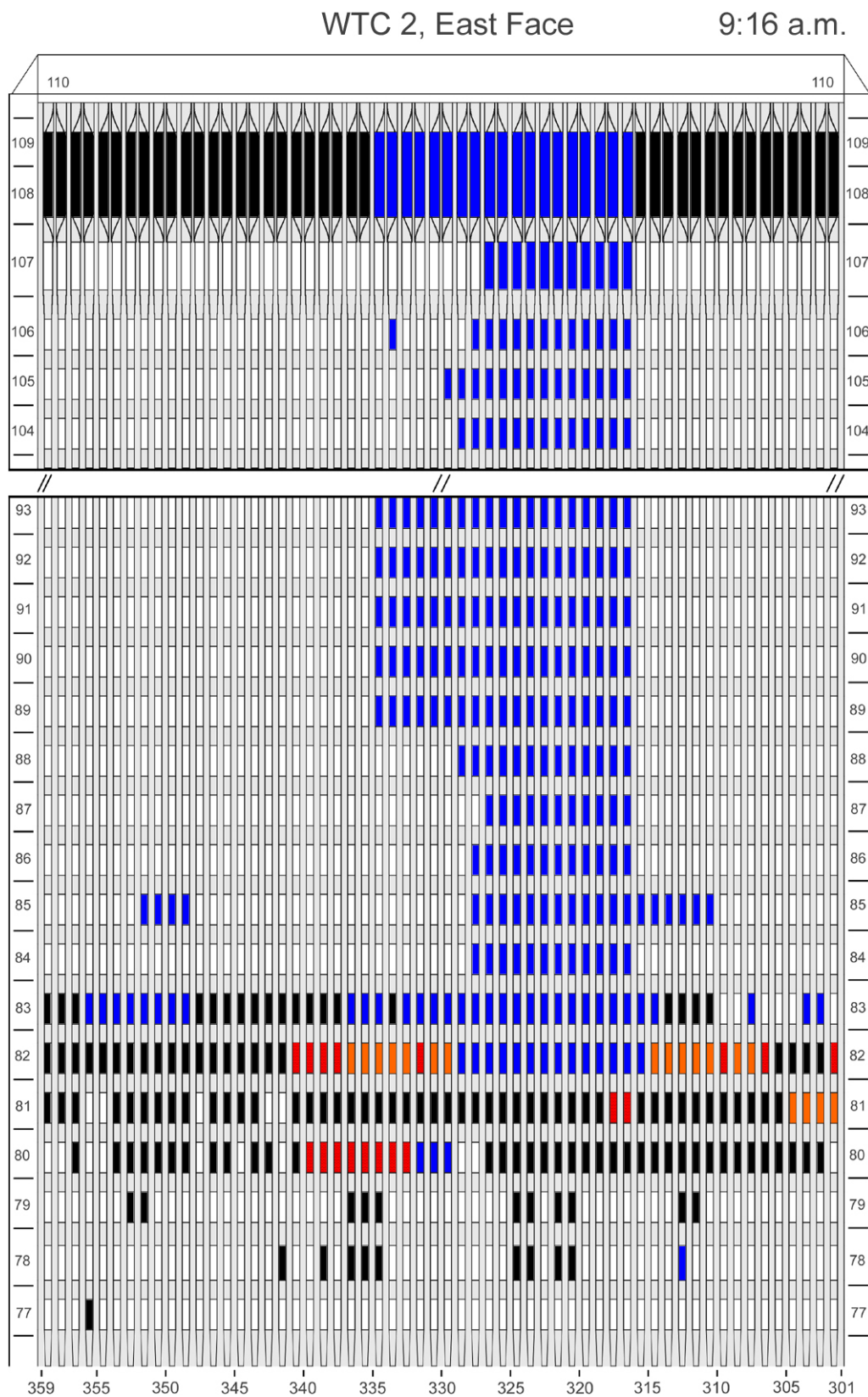


Figure H-15. Diagram of the east face of WTC 2 for floors 77 to 93 and floors 104 to 110 at 9:16 a.m. showing the condition of windows and locations of fires.

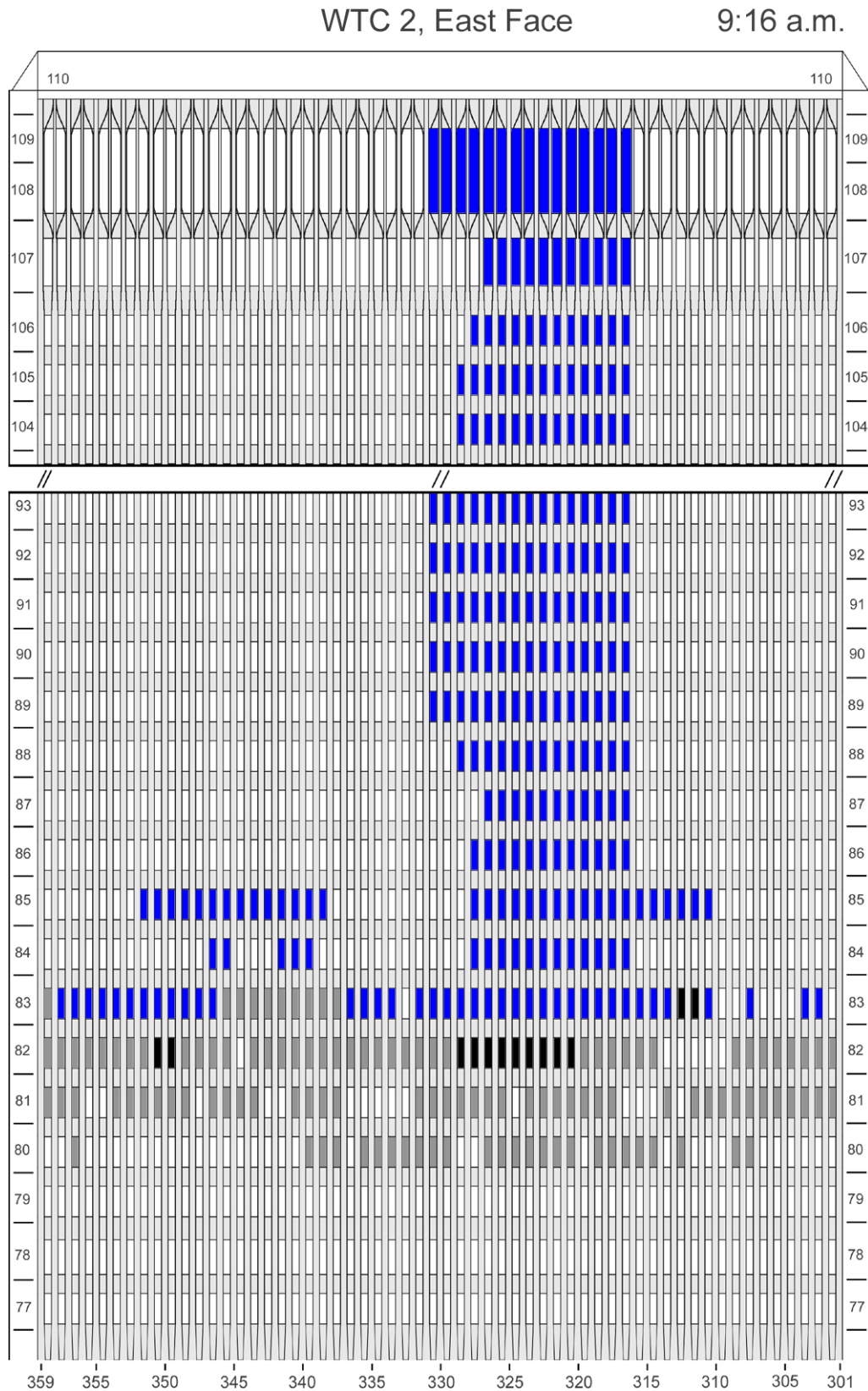


Figure H-16. Diagram of the east face of WTC 2 for floors 77 to 93 and floors 104 to 110 at 9:16 a.m. showing windows where smoke was observed and those hidden from view.

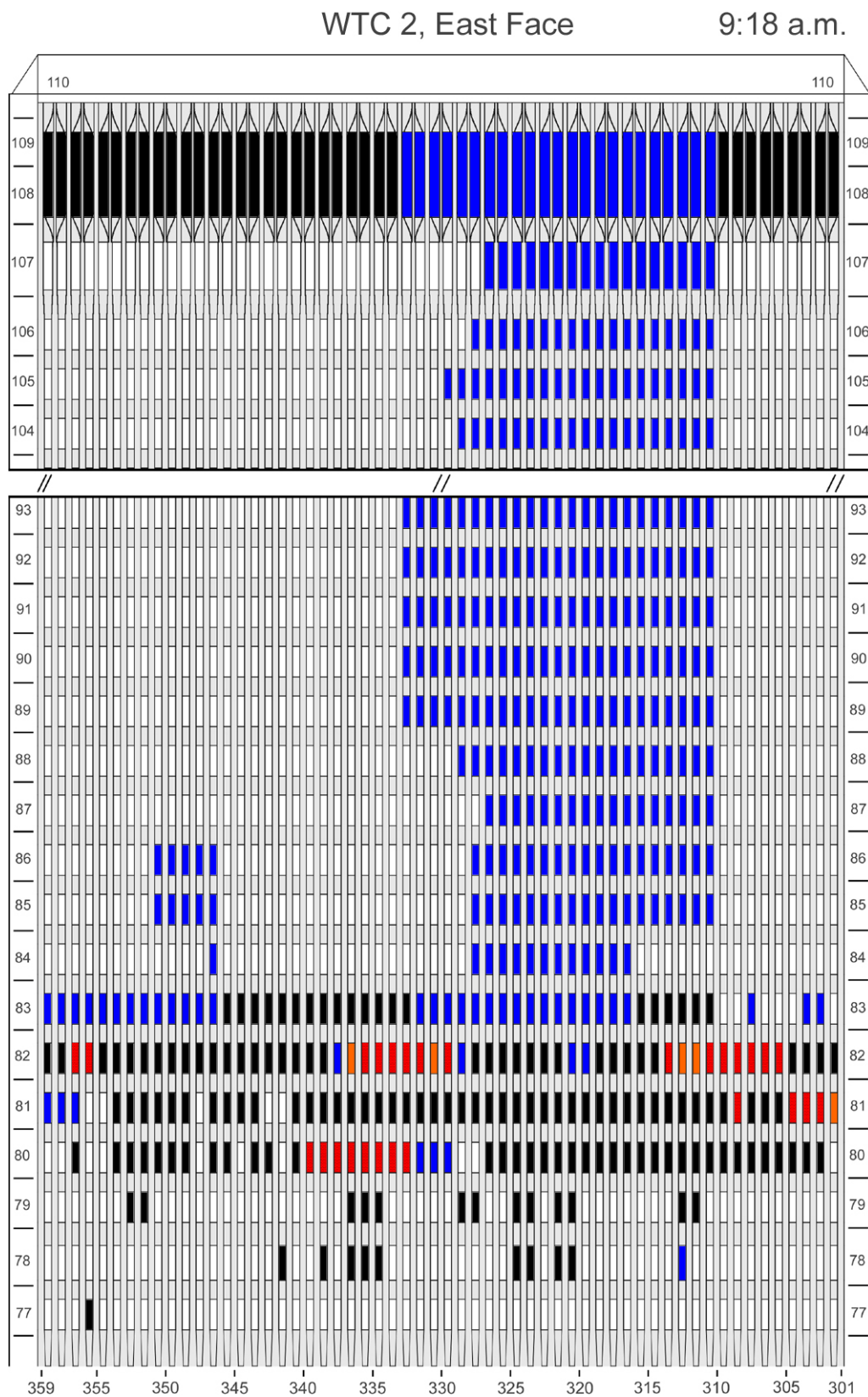


Figure H-17. Diagram of the east face of WTC 2 for floors 77 to 93 and floors 104 to 110 at 9:18 a.m. showing the condition of windows and locations of fires.

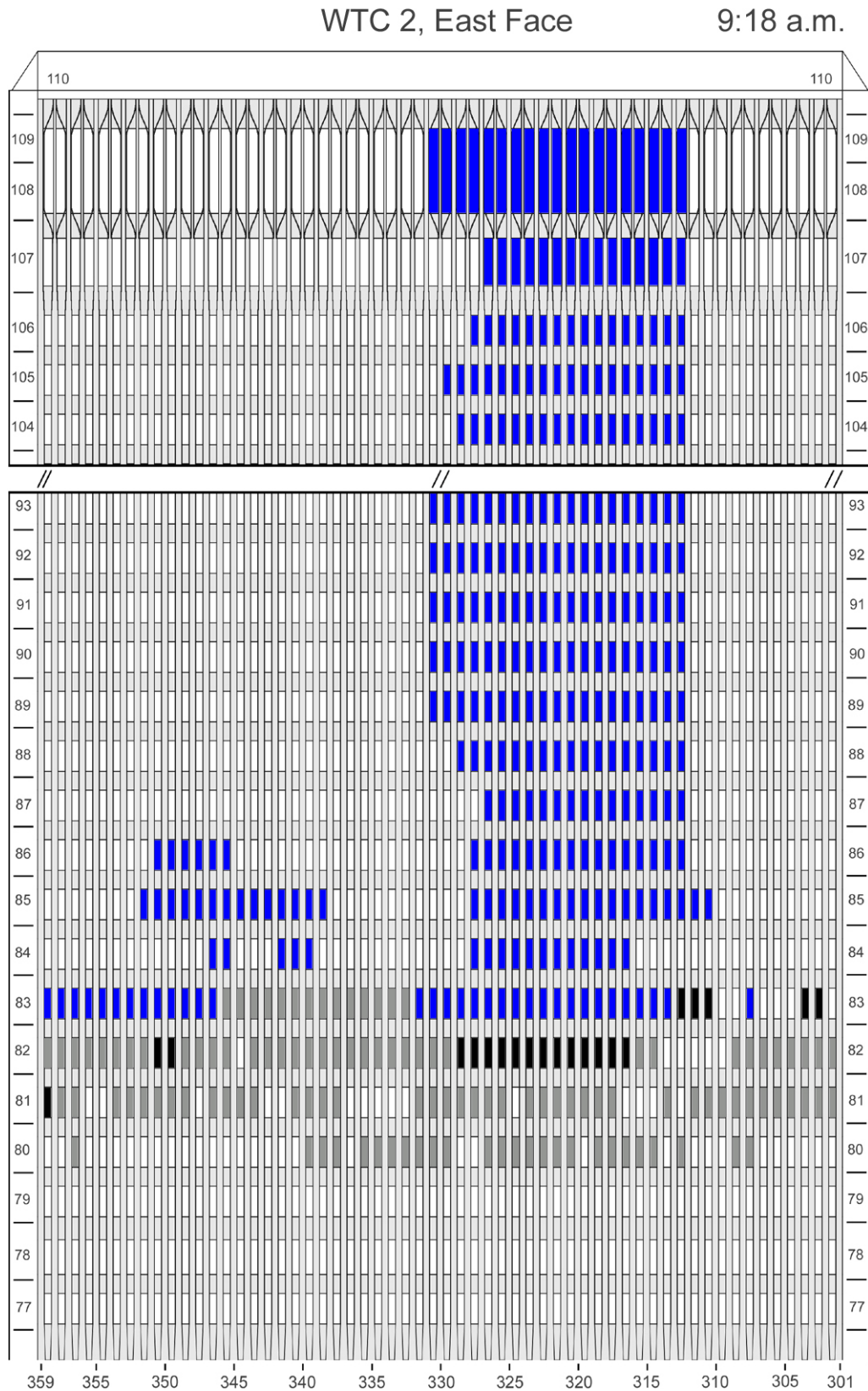


Figure H-18. Diagram of the east face of WTC 2 for floors 77 to 93 and floors 104 to 110 at 9:18 a.m. showing windows where smoke was observed and those hidden from view.

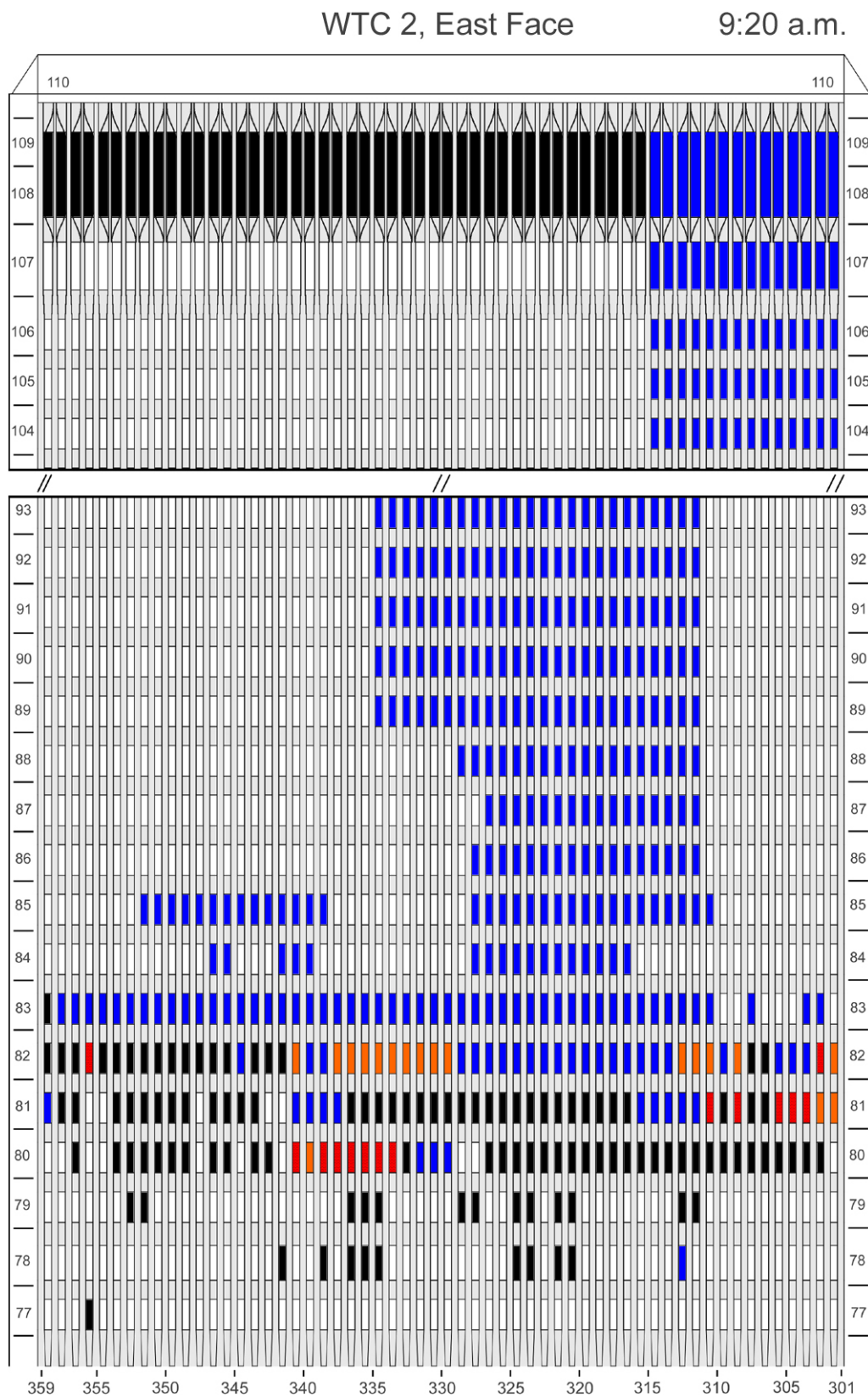


Figure H-19. Diagram of the east face of WTC 2 for floors 77 to 93 and floors 104 to 110 at 9:20 a.m. showing the condition of windows and locations of fires.

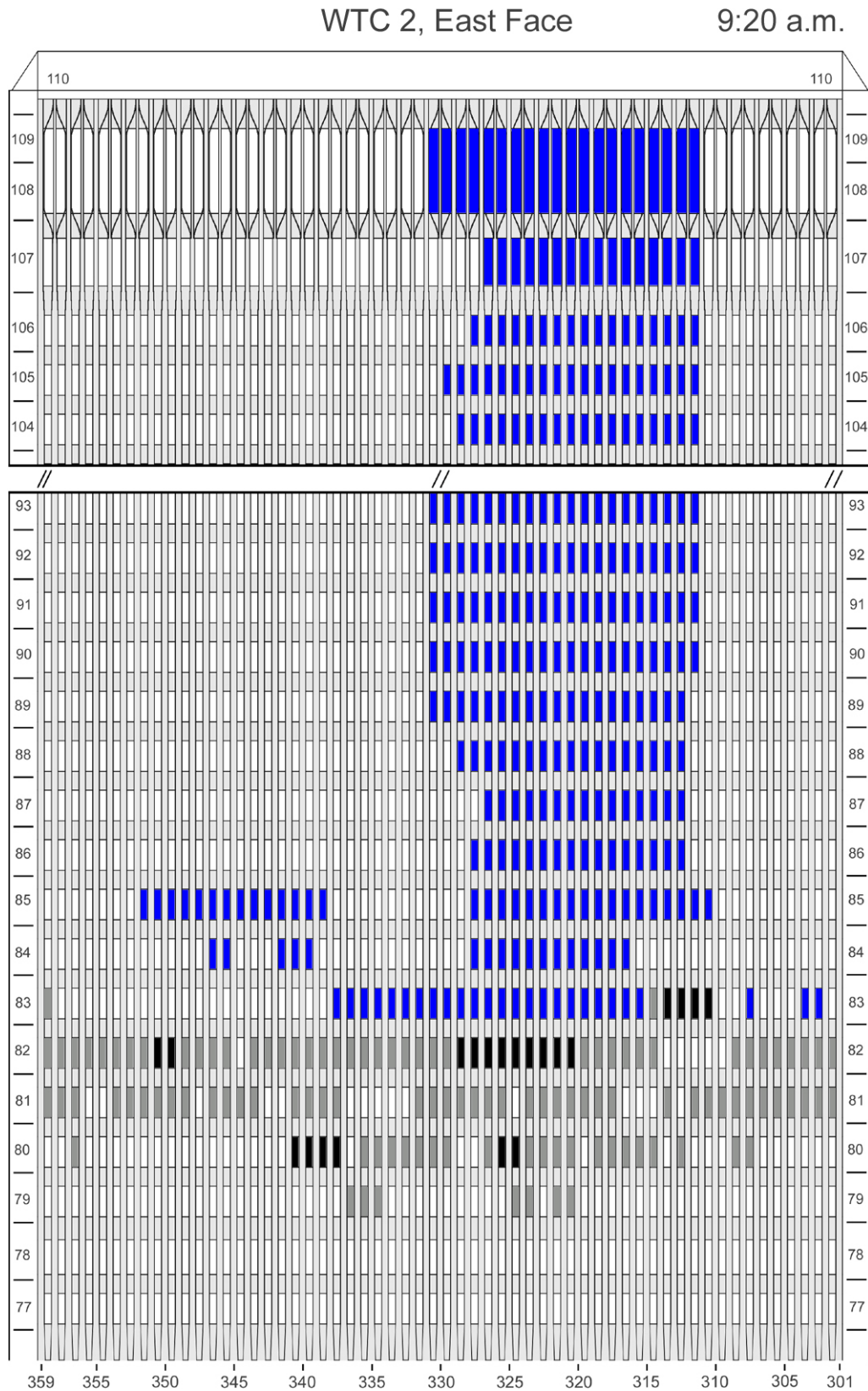


Figure H-20. Diagram of the east face of WTC 2 for floors 77 to 93 and floors 104 to 110 at 9:20 a.m. showing windows where smoke was observed and those hidden from view.

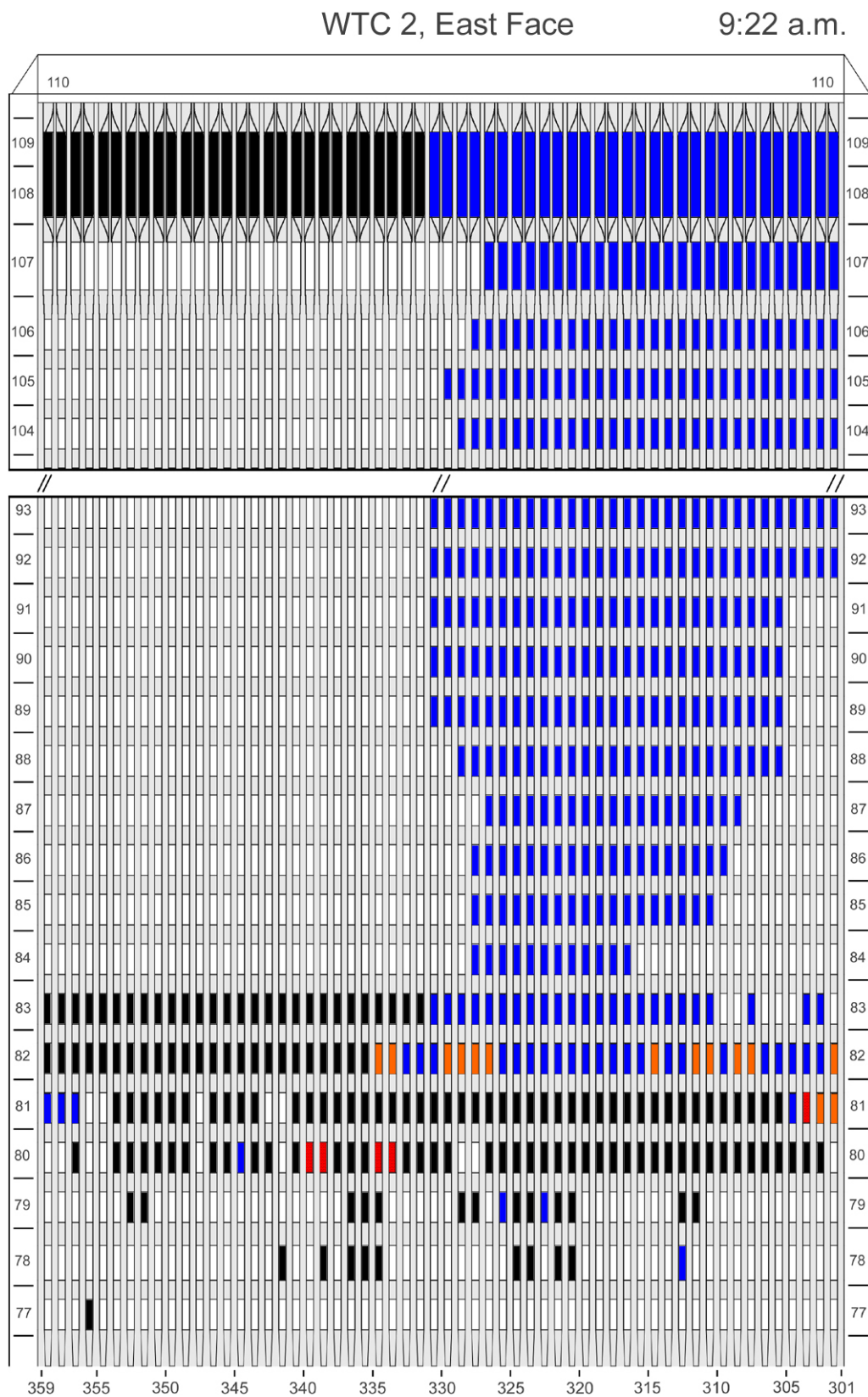


Figure H-21. Diagram of the east face of WTC 2 for floors 77 to 93 and floors 104 to 110 at 9:22 a.m. showing the condition of windows and locations of fires.

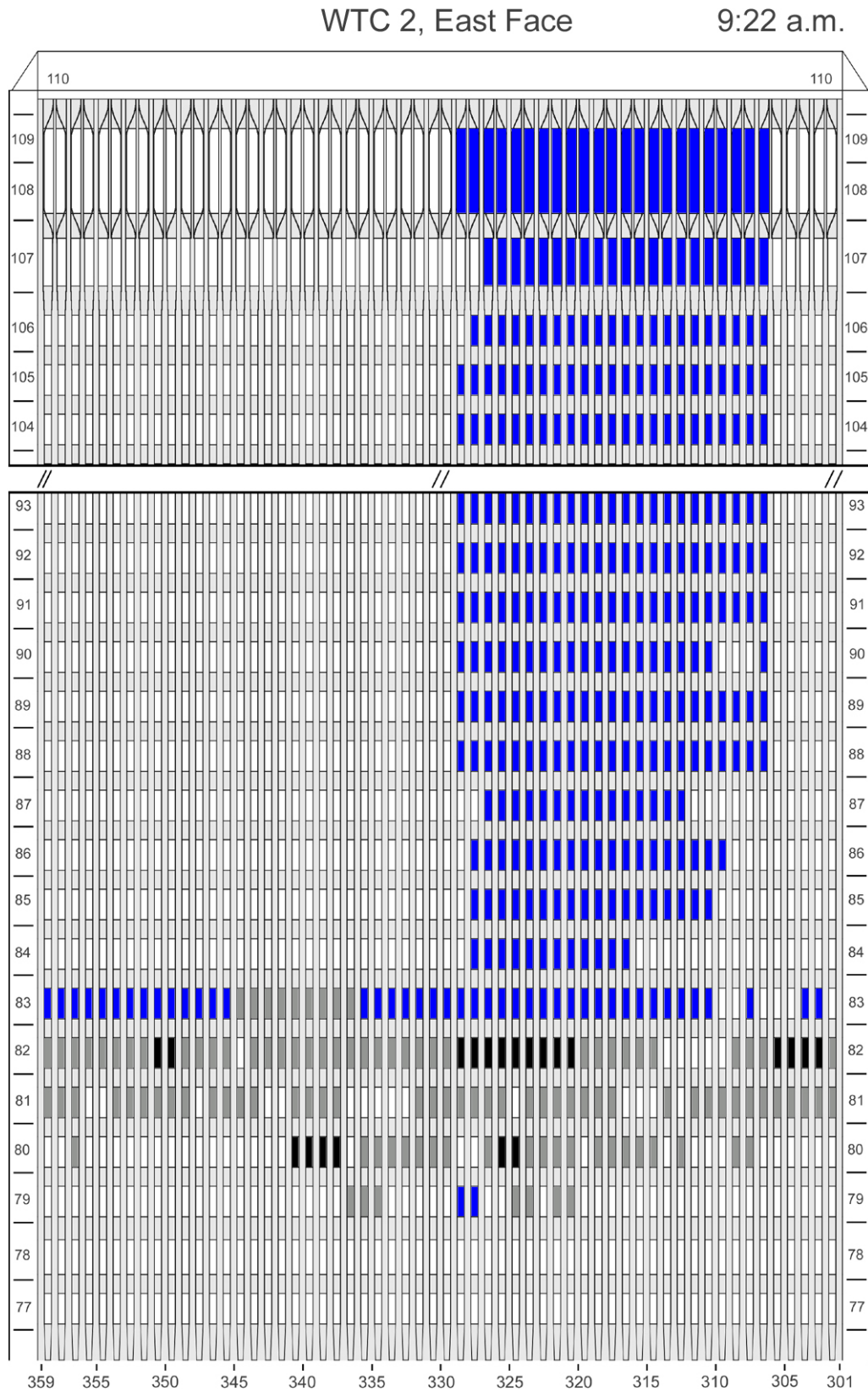


Figure H-22. Diagram of the east face of WTC 2 for floors 77 to 93 and floors 104 to 110 at 9:22 a.m. showing windows where smoke was observed and those hidden from view.

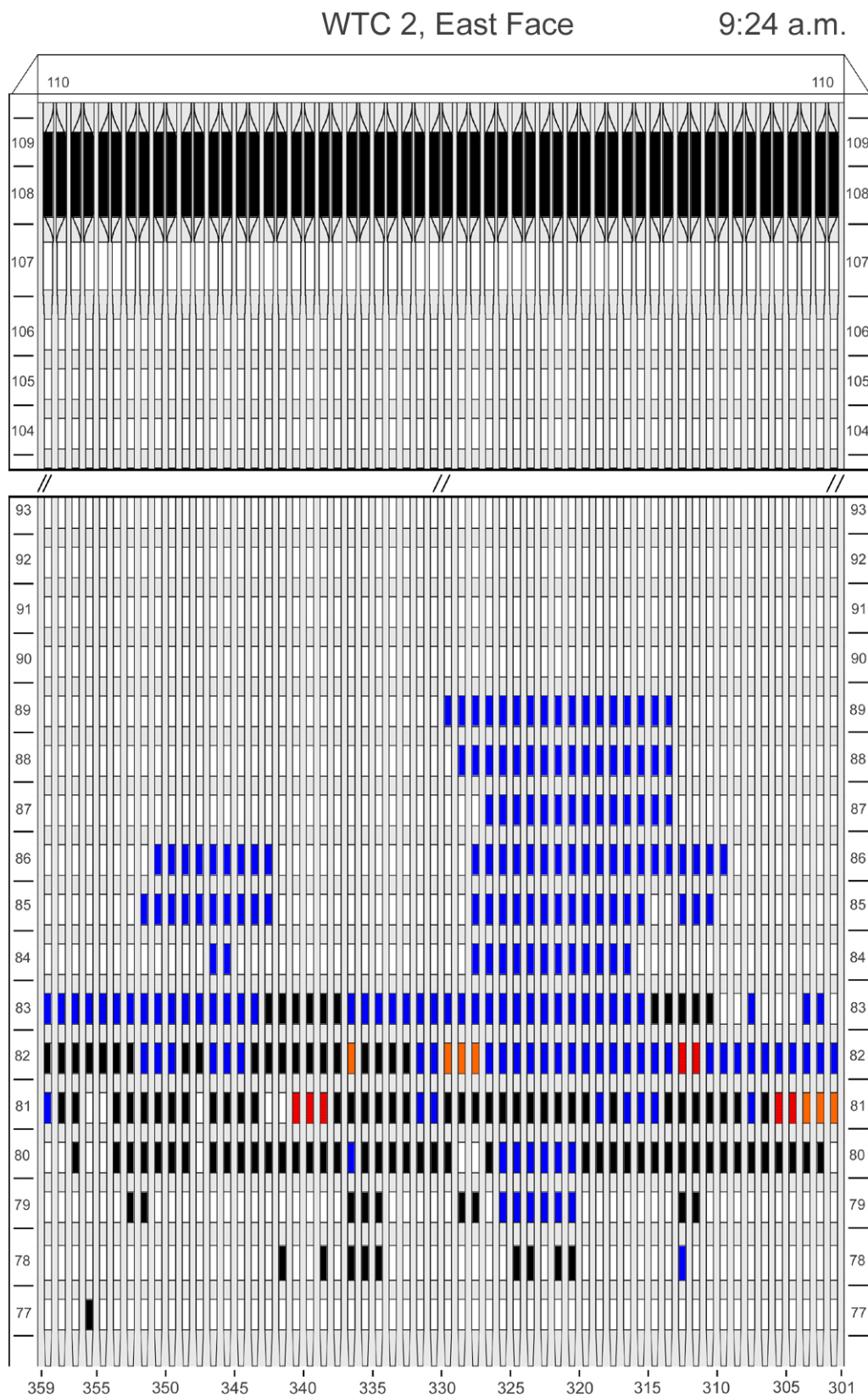


Figure H-23. Diagram of the east face of WTC 2 for floors 77 to 93 and floors 104 to 110 at 9:24 a.m. showing the condition of windows and locations of fires.

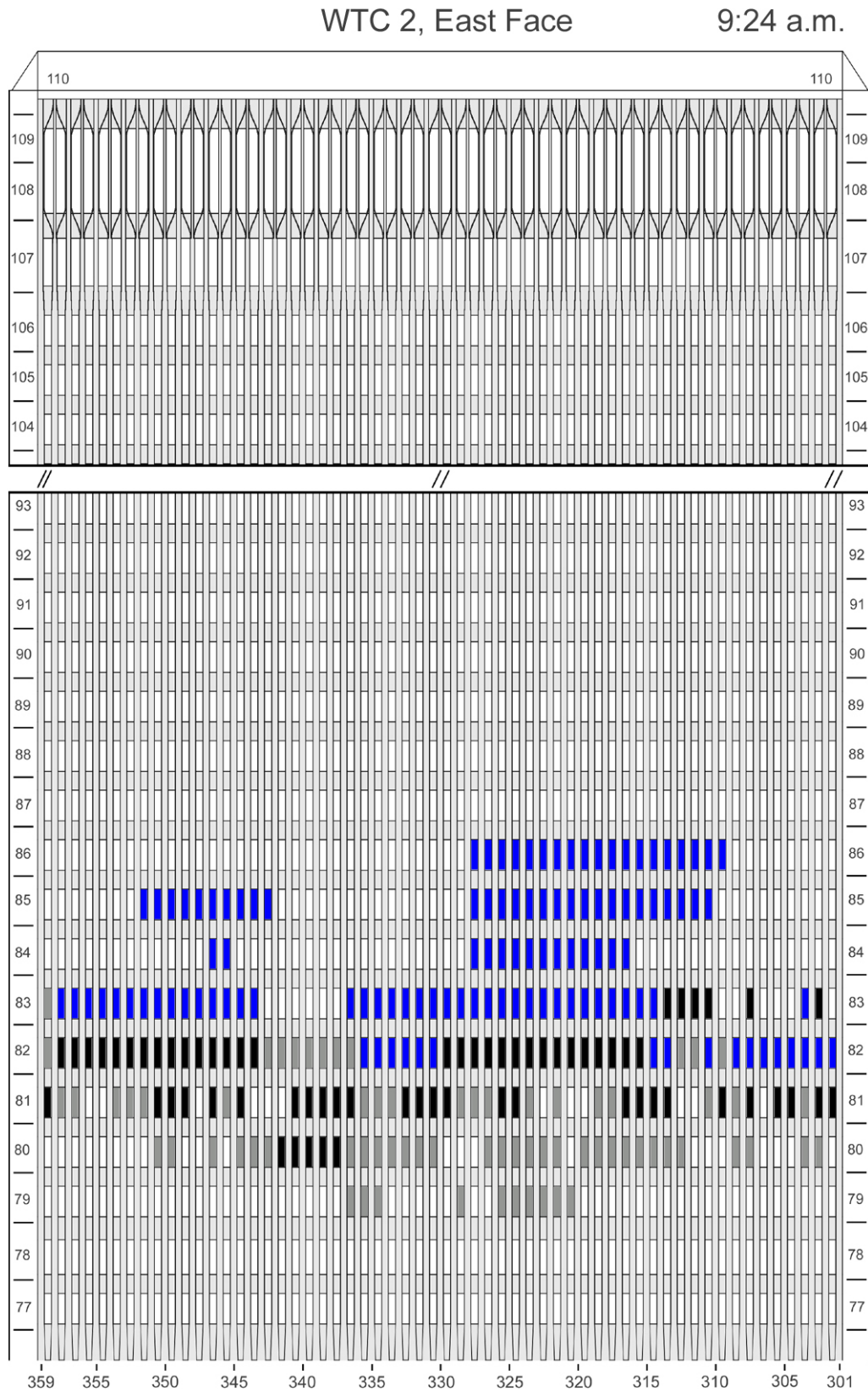


Figure H-24. Diagram of the east face of WTC 2 for floors 77 to 93 and floors 104 to 110 at 9:24 a.m. showing windows where smoke was observed and those hidden from view.

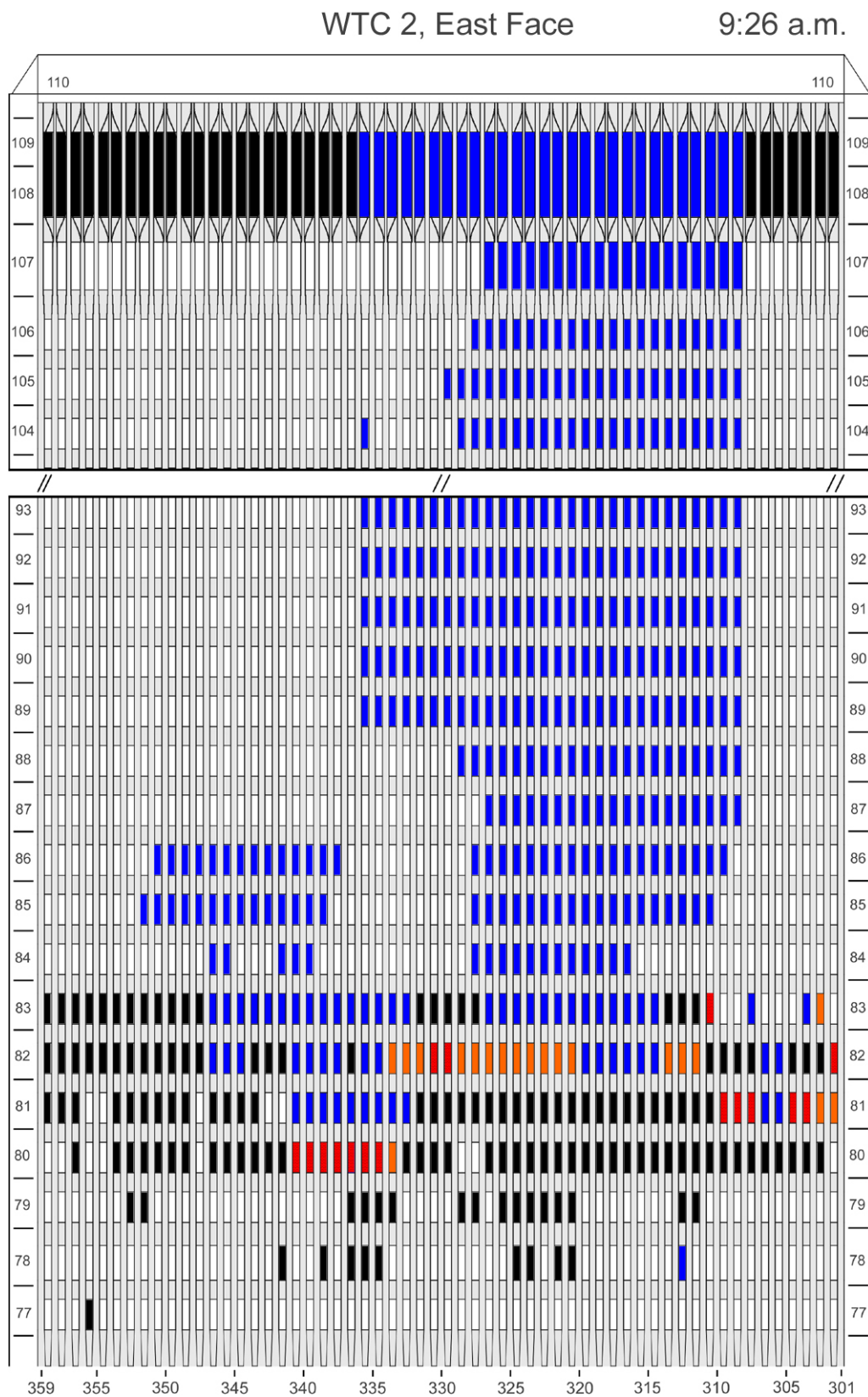


Figure H-25. Diagram of the east face of WTC 2 for floors 77 to 93 and floors 104 to 110 at 9:26 a.m. showing the condition of windows and locations of fires.

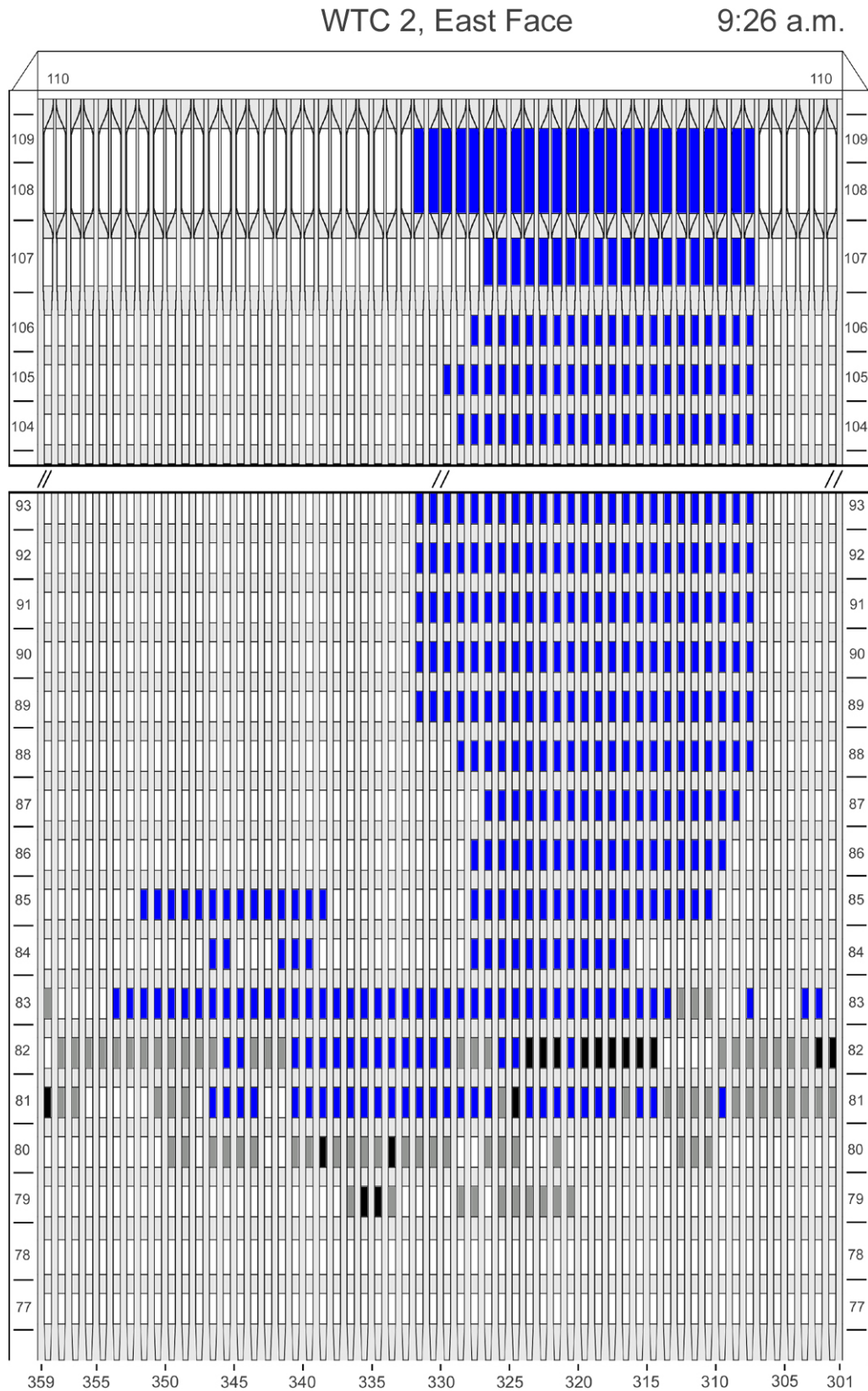


Figure H-26. Diagram of the east face of WTC 2 for floors 77 to 93 and floors 104 to 110 at 9:26 a.m. showing windows where smoke was observed and those hidden from view.

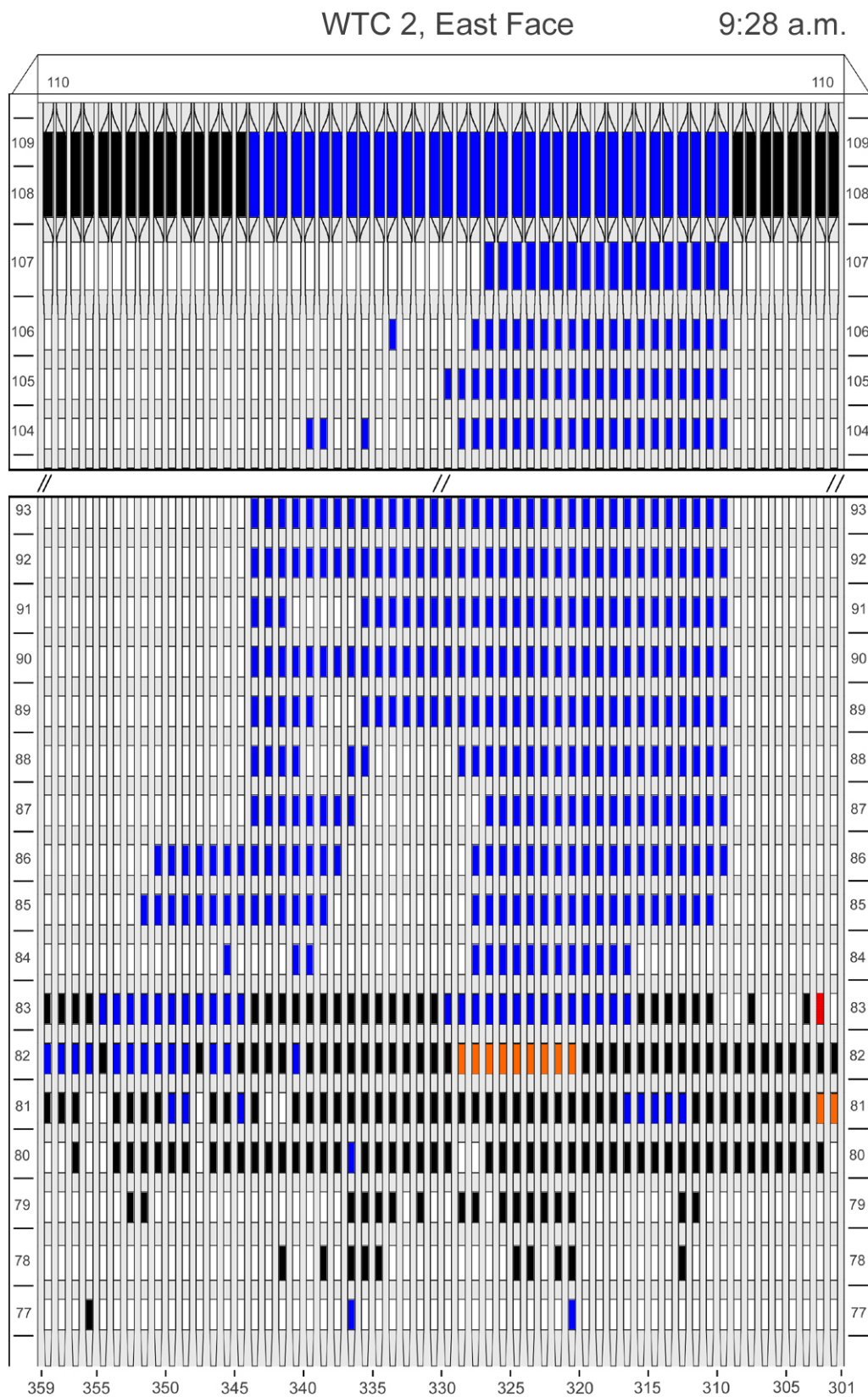


Figure H-27. Diagram of the east face of WTC 2 for floors 77 to 93 and floors 104 to 110 at 9:28 a.m. showing the condition of windows and locations of fires.

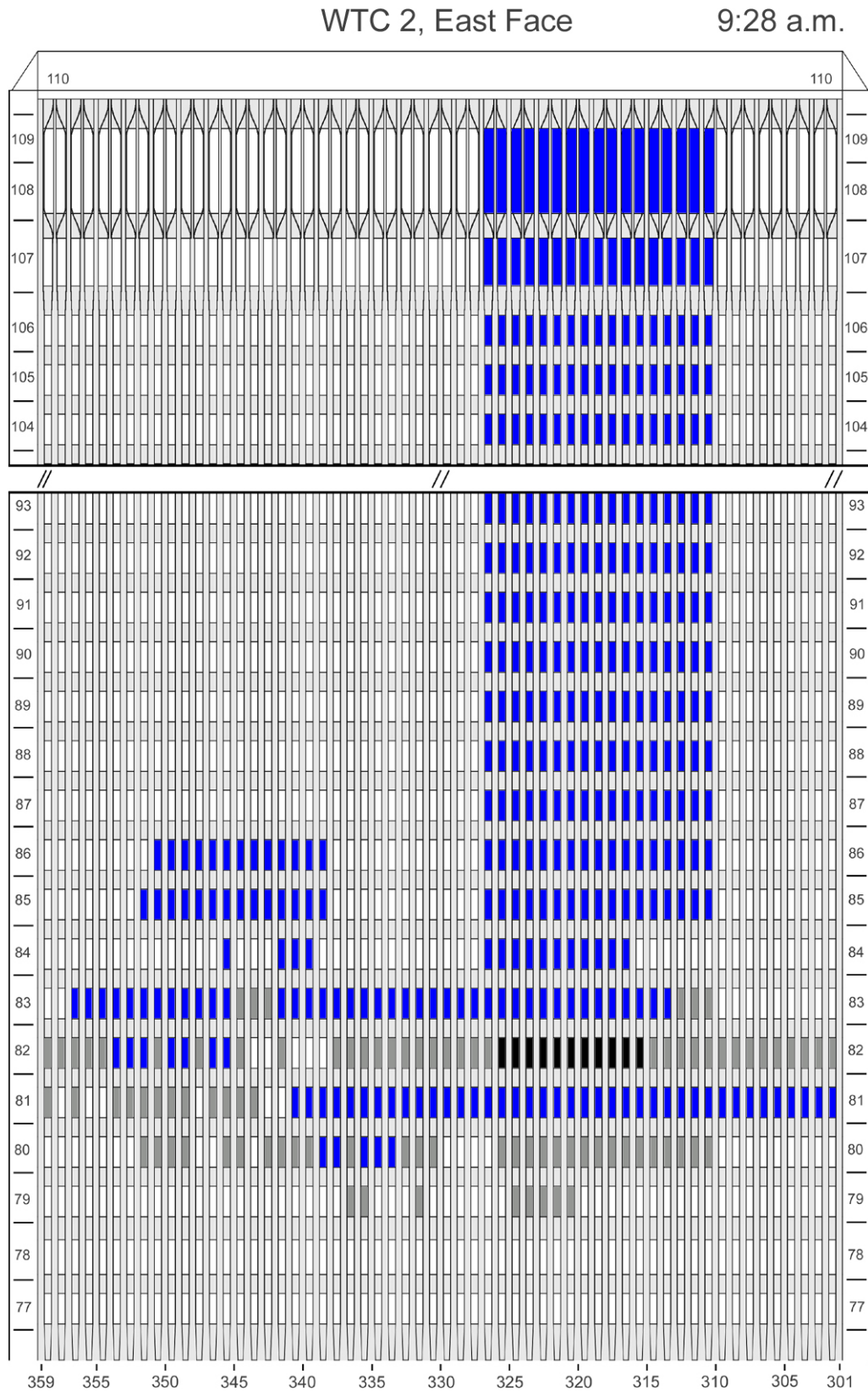


Figure H-28. Diagram of the east face of WTC 2 for floors 77 to 93 and floors 104 to 110 at 9:28 a.m. showing windows where smoke was observed and those hidden from view.

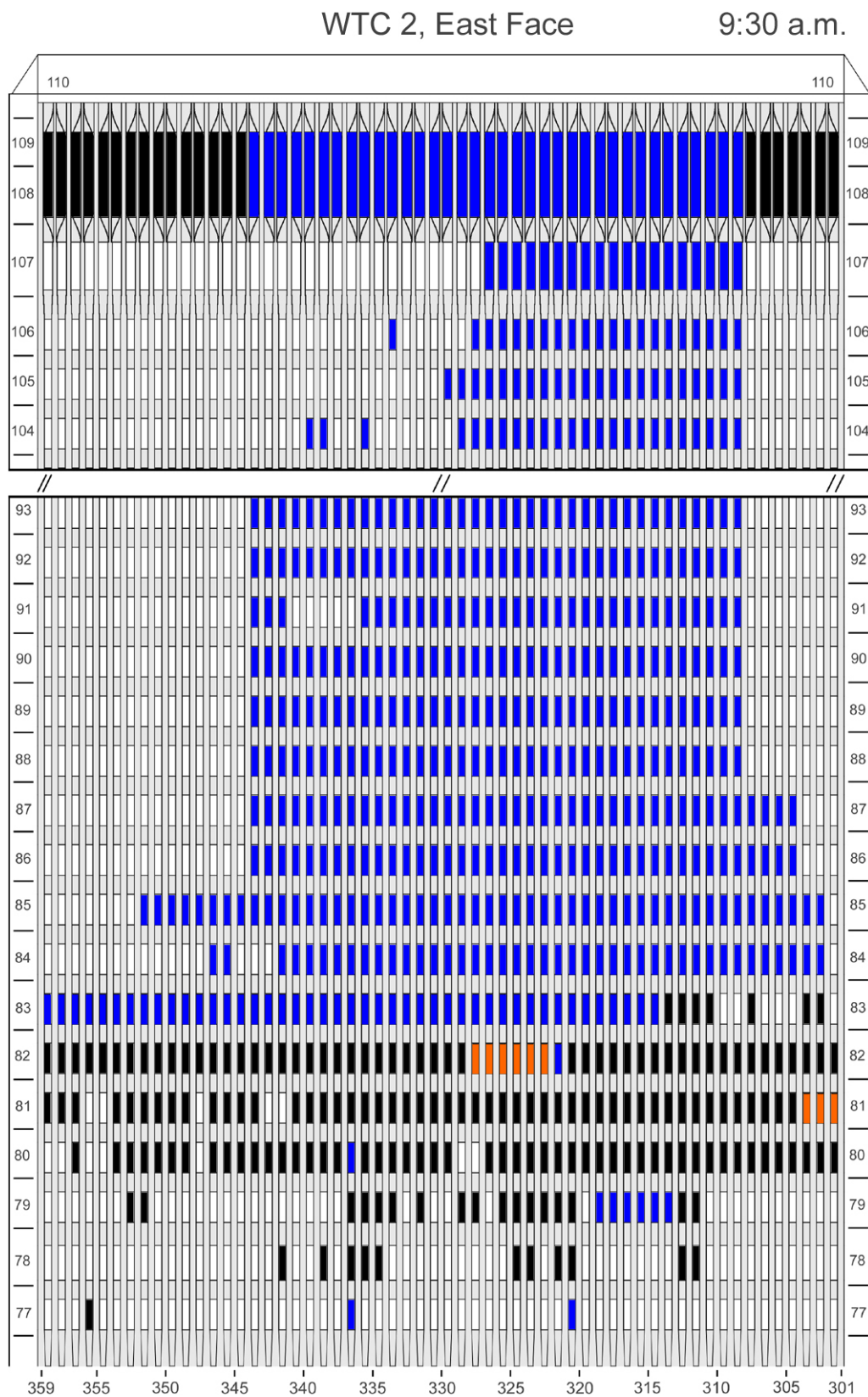


Figure H-29. Diagram of the east face of WTC 2 for floors 77 to 93 and floors 104 to 110 at 9:30 a.m. showing the condition of windows and locations of fires.

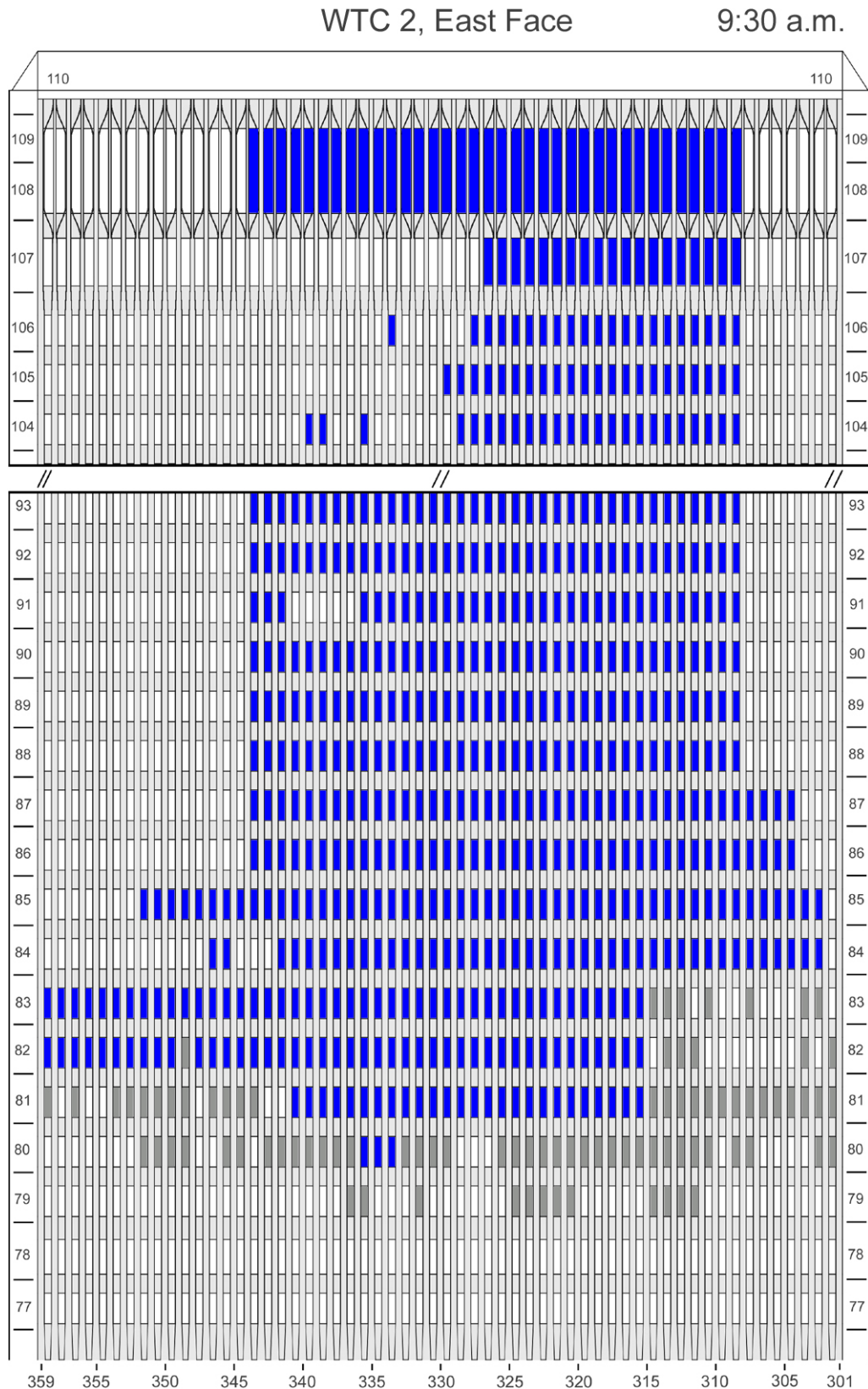


Figure H-30. Diagram of the east face of WTC 2 for floors 77 to 93 and floors 104 to 110 at 9:30 a.m. showing windows where smoke was observed and those hidden from view.

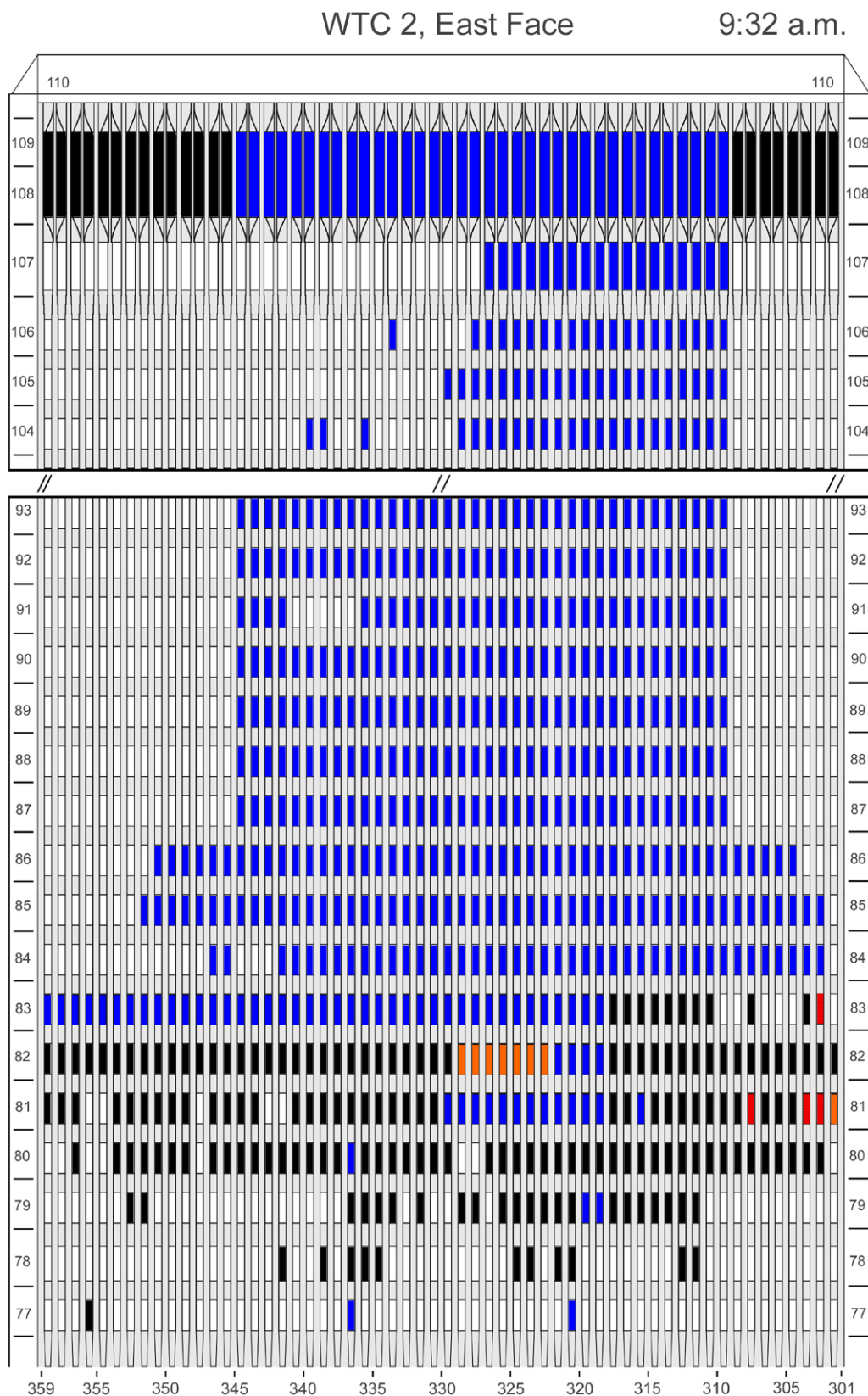


Figure H-31. Diagram of the east face of WTC 2 for floors 77 to 93 and floors 104 to 110 at 9:32 a.m. showing the condition of windows and locations of fires.

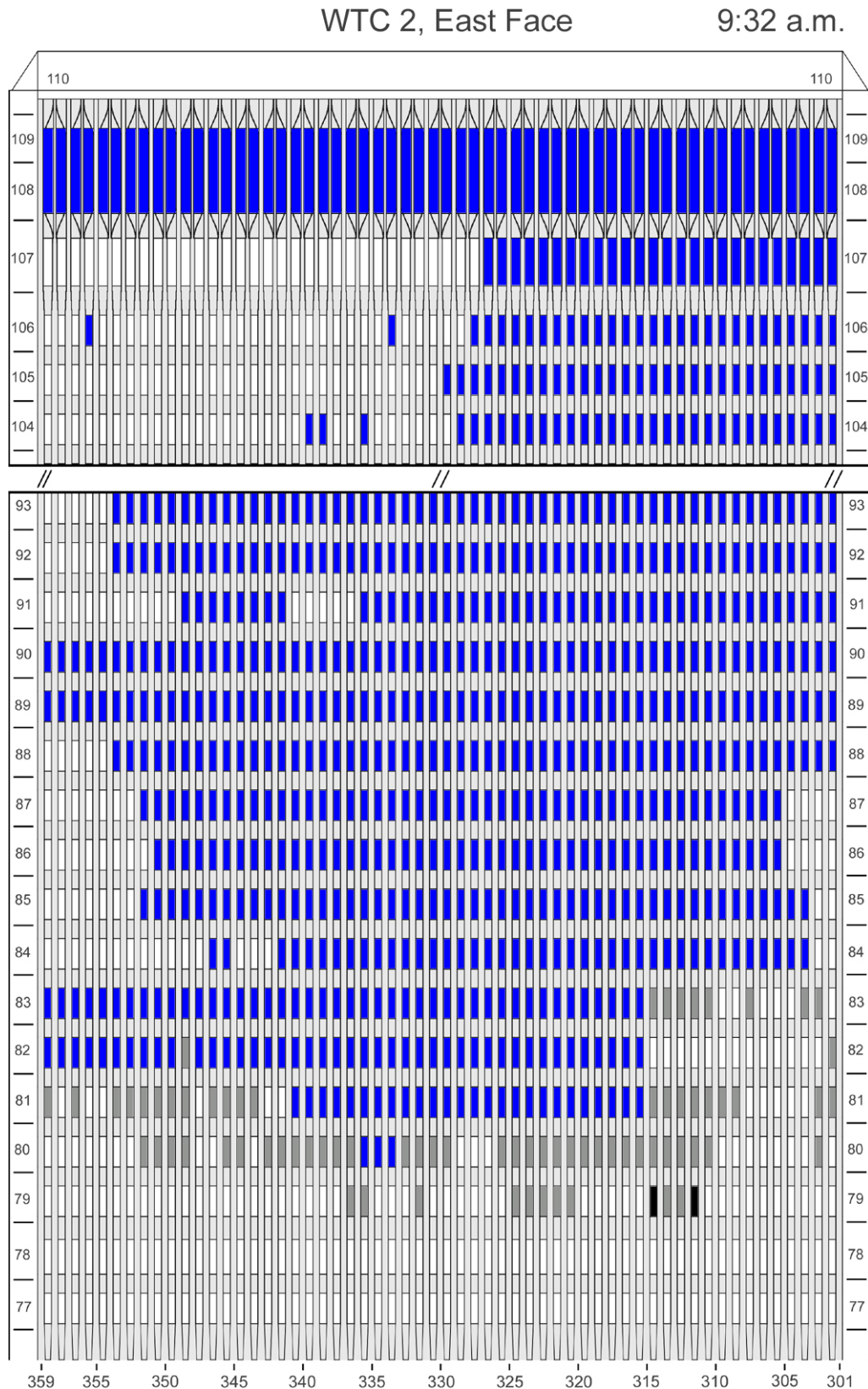


Figure H-32. Diagram of the east face of WTC 2 for floors 77 to 93 and floors 104 to 110 at 9:32 a.m. showing windows where smoke was observed and those hidden from view.

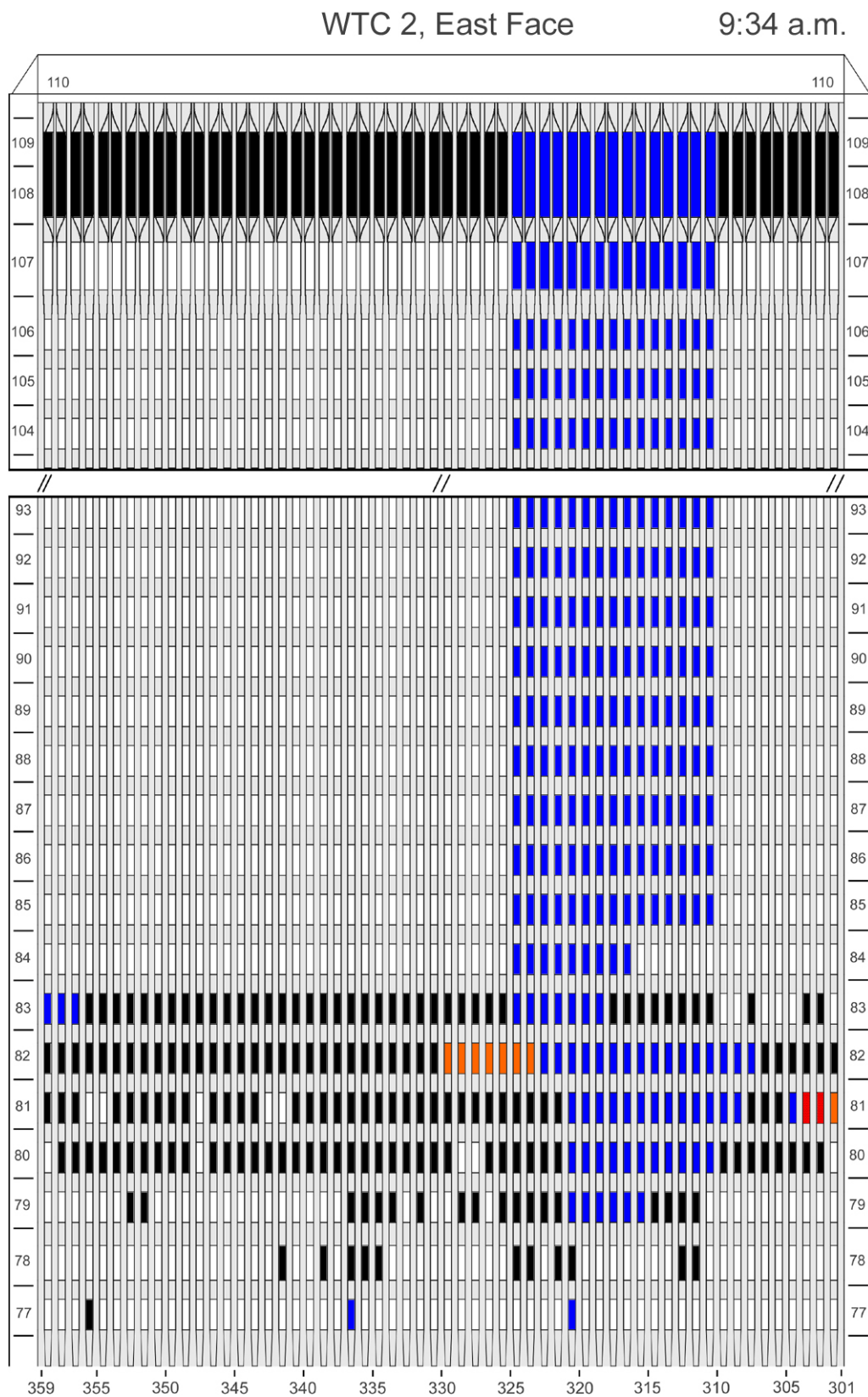


Figure H-33. Diagram of the east face of WTC 2 for floors 77 to 93 and floors 104 to 110 at 9:34 a.m. showing the condition of windows and locations of fires.

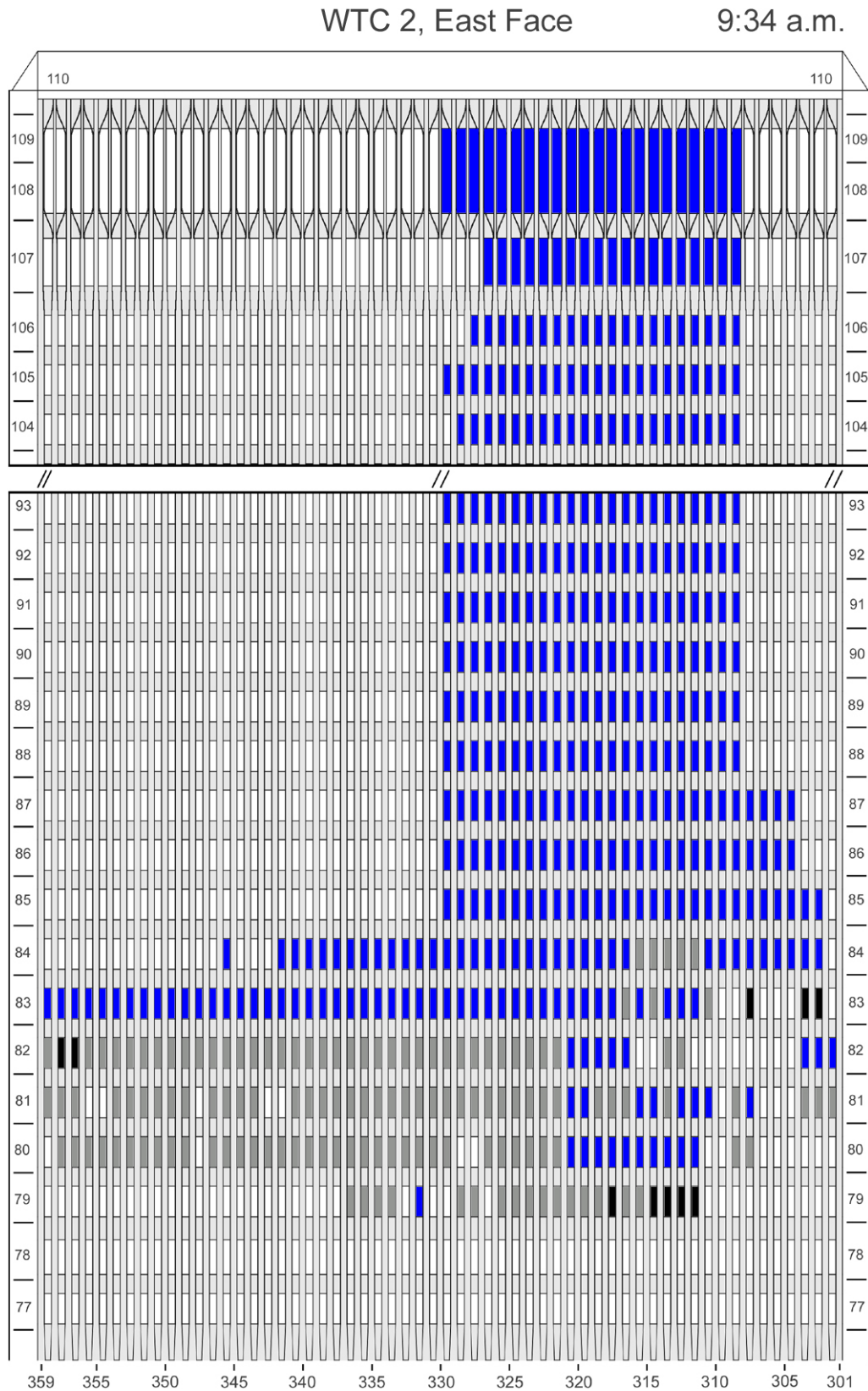


Figure H-34. Diagram of the east face of WTC 2 for floors 77 to 93 and floors 104 to 110 at 9:34 a.m. showing windows where smoke was observed and those hidden from view.

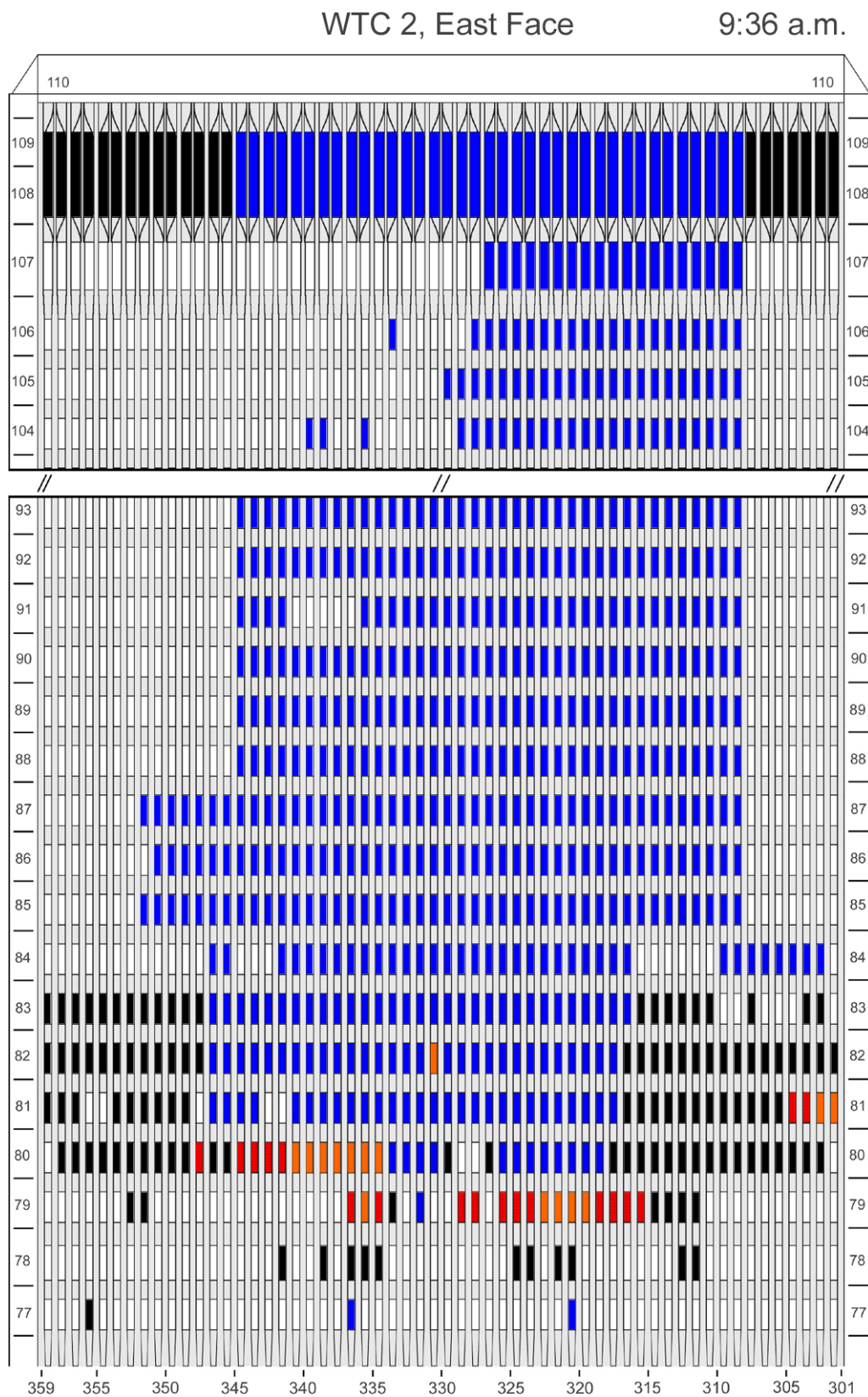


Figure H-35. Diagram of the east face of WTC 2 for floors 77 to 93 and floors 104 to 110 at 9:36 a.m. showing the condition of windows and locations of fires.

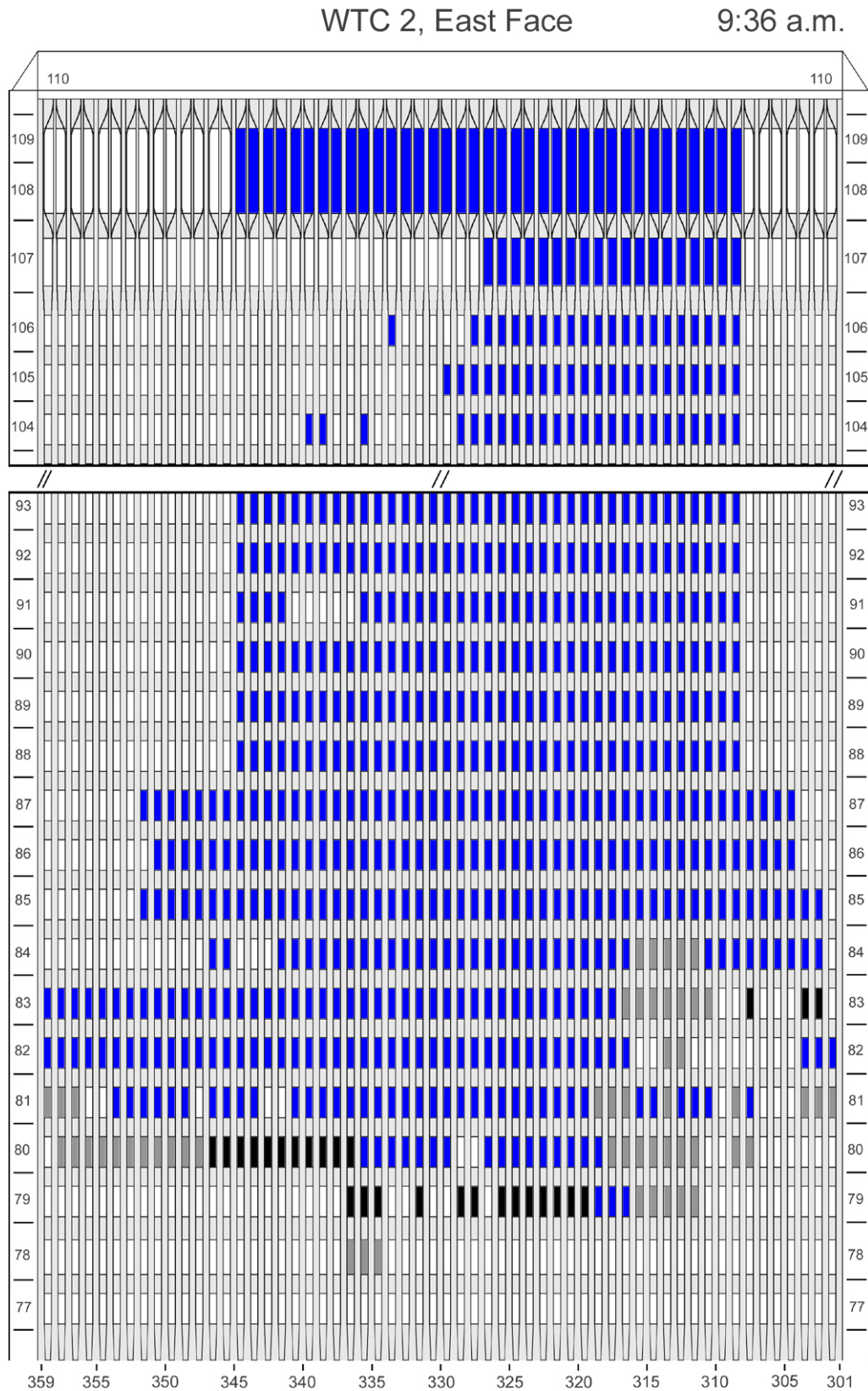


Figure H-36. Diagram of the east face of WTC 2 for floors 77 to 93 and floors 104 to 110 at 9:36 a.m. showing windows where smoke was observed and those hidden from view.

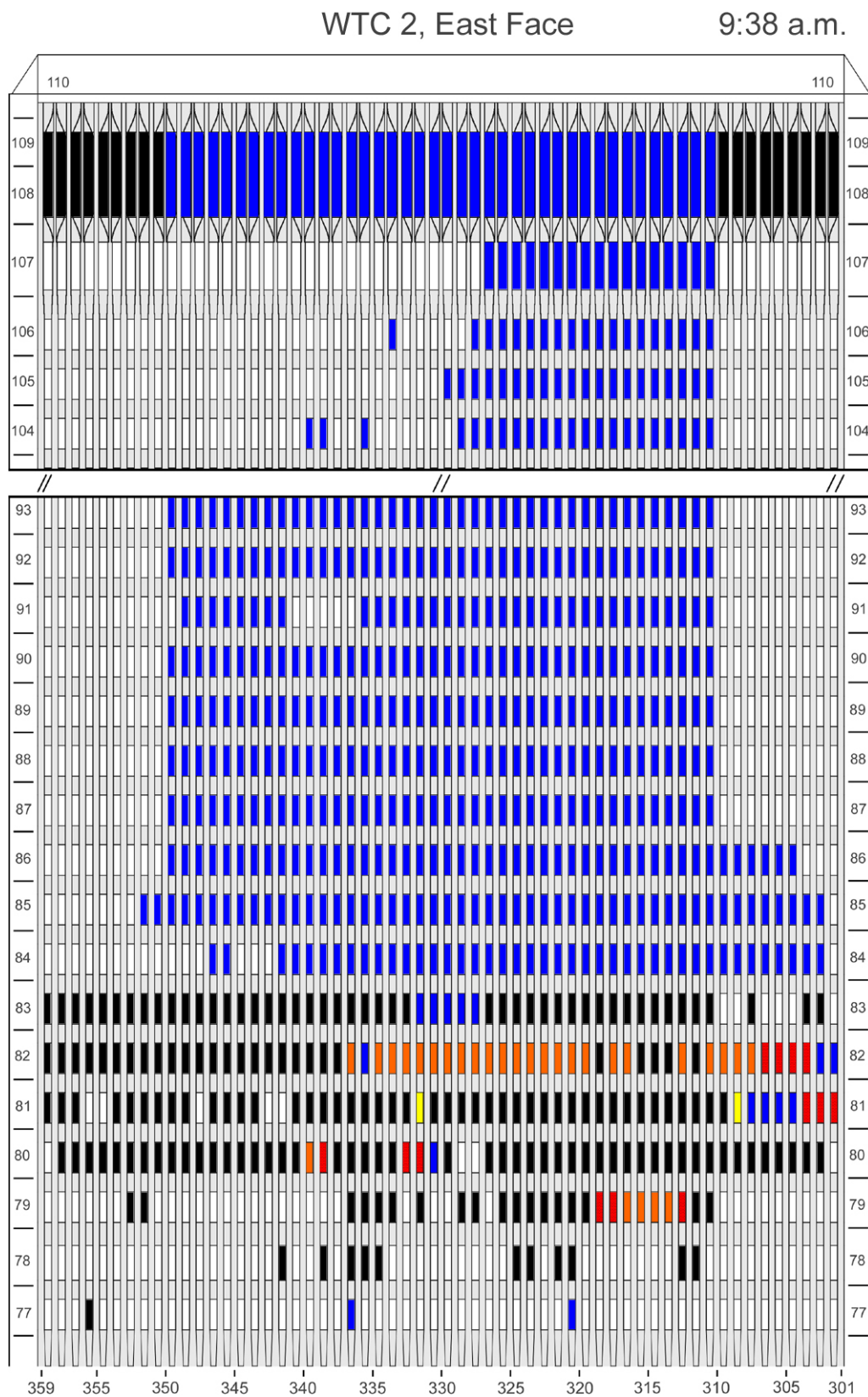


Figure H-37. Diagram of the east face of WTC 2 for floors 77 to 93 and floors 104 to 110 at 9:38 a.m. showing the condition of windows and locations of fires.

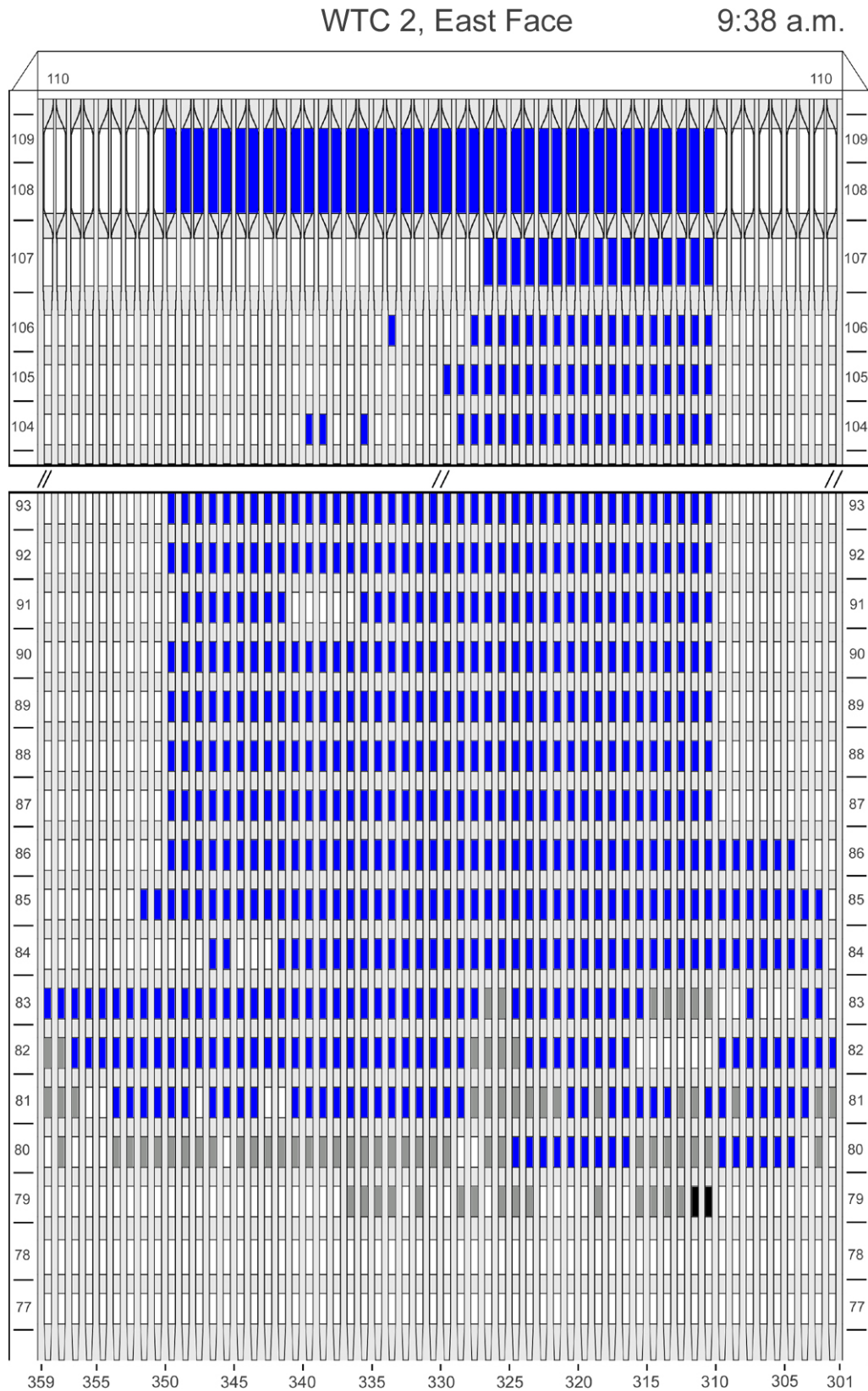


Figure H-38. Diagram of the east face of WTC 2 for floors 77 to 93 and floors 104 to 110 at 9:38 a.m. showing windows where smoke was observed and those hidden from view.

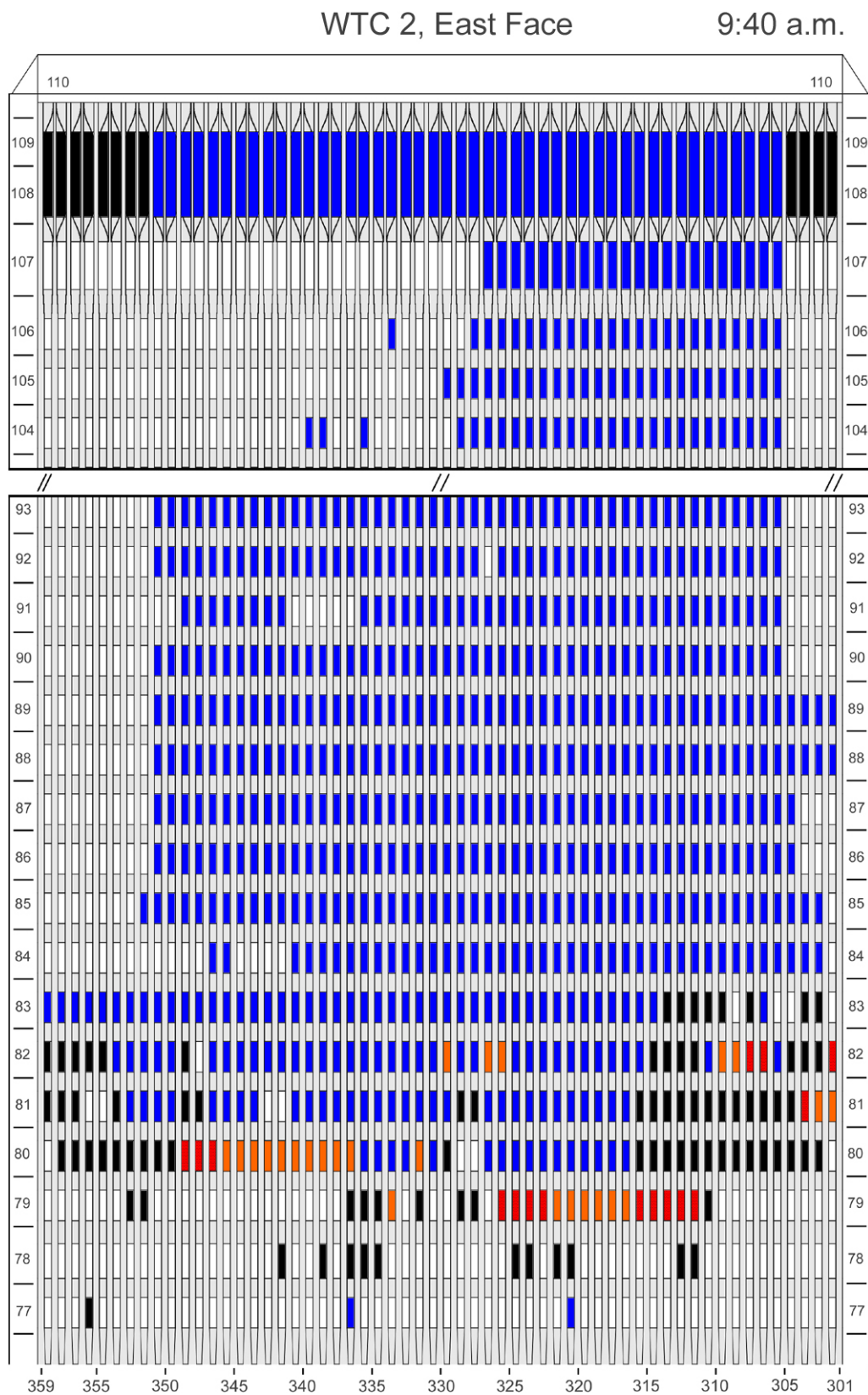


Figure H-39. Diagram of the east face of WTC 2 for floors 77 to 93 and floors 104 to 110 at 9:40 a.m. showing the condition of windows and locations of fires.

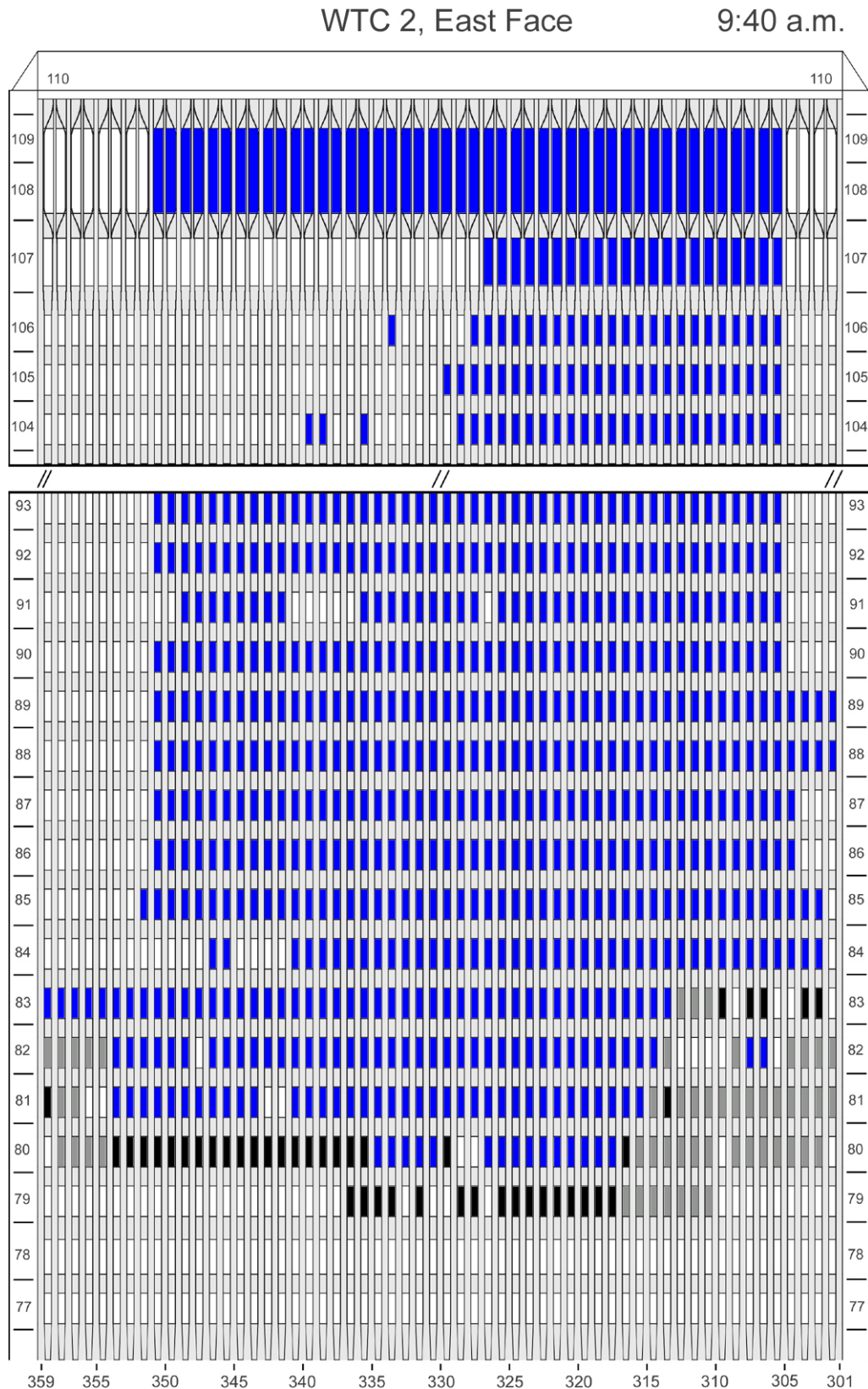


Figure H-40. Diagram of the east face of WTC 2 for floors 77 to 93 and floors 104 to 110 at 9:40 a.m. showing windows where smoke was observed and those hidden from view.

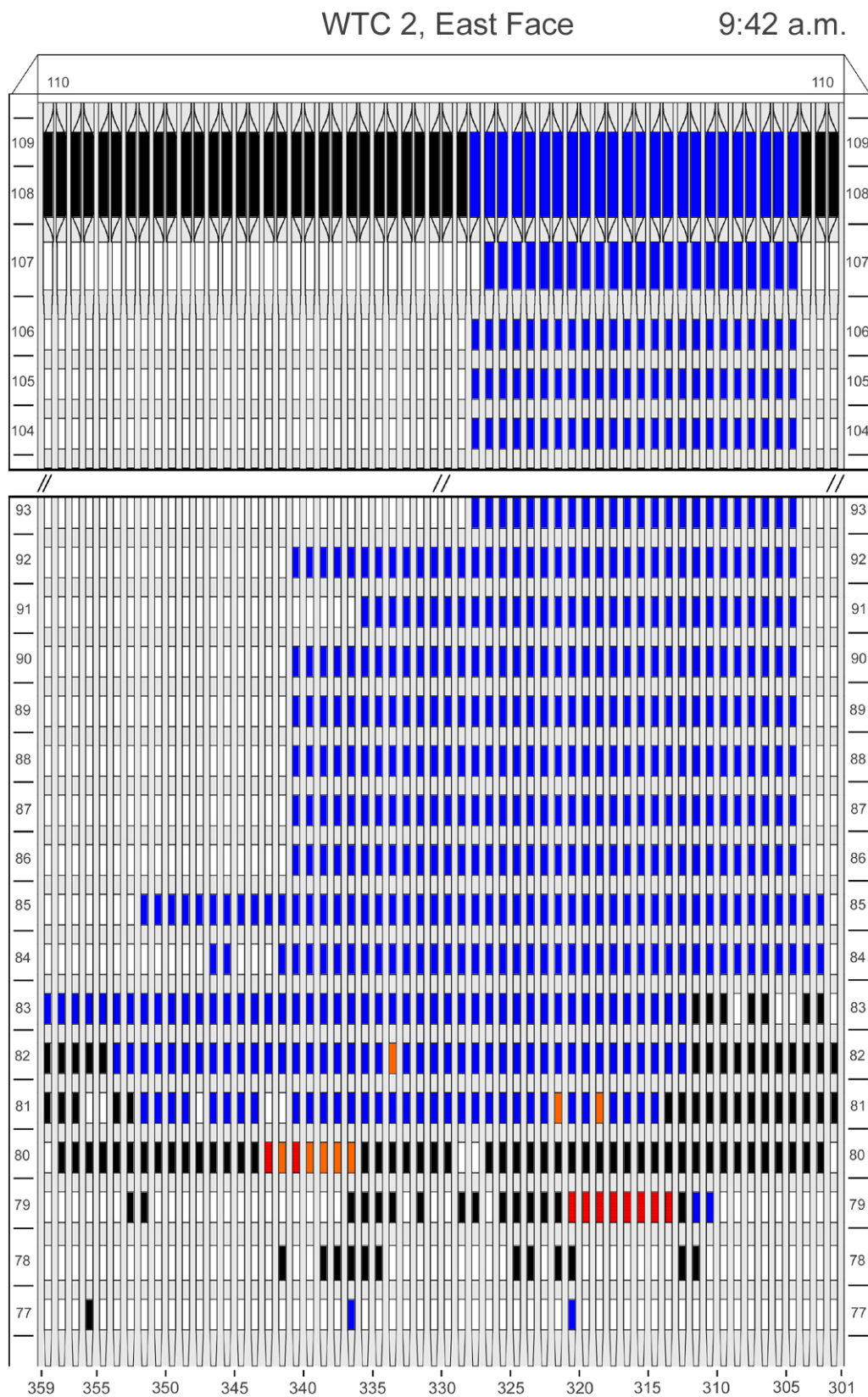


Figure H-41. Diagram of the east face of WTC 2 for floors 77 to 93 and floors 104 to 110 at 9:42 a.m. showing the condition of windows and locations of fires.

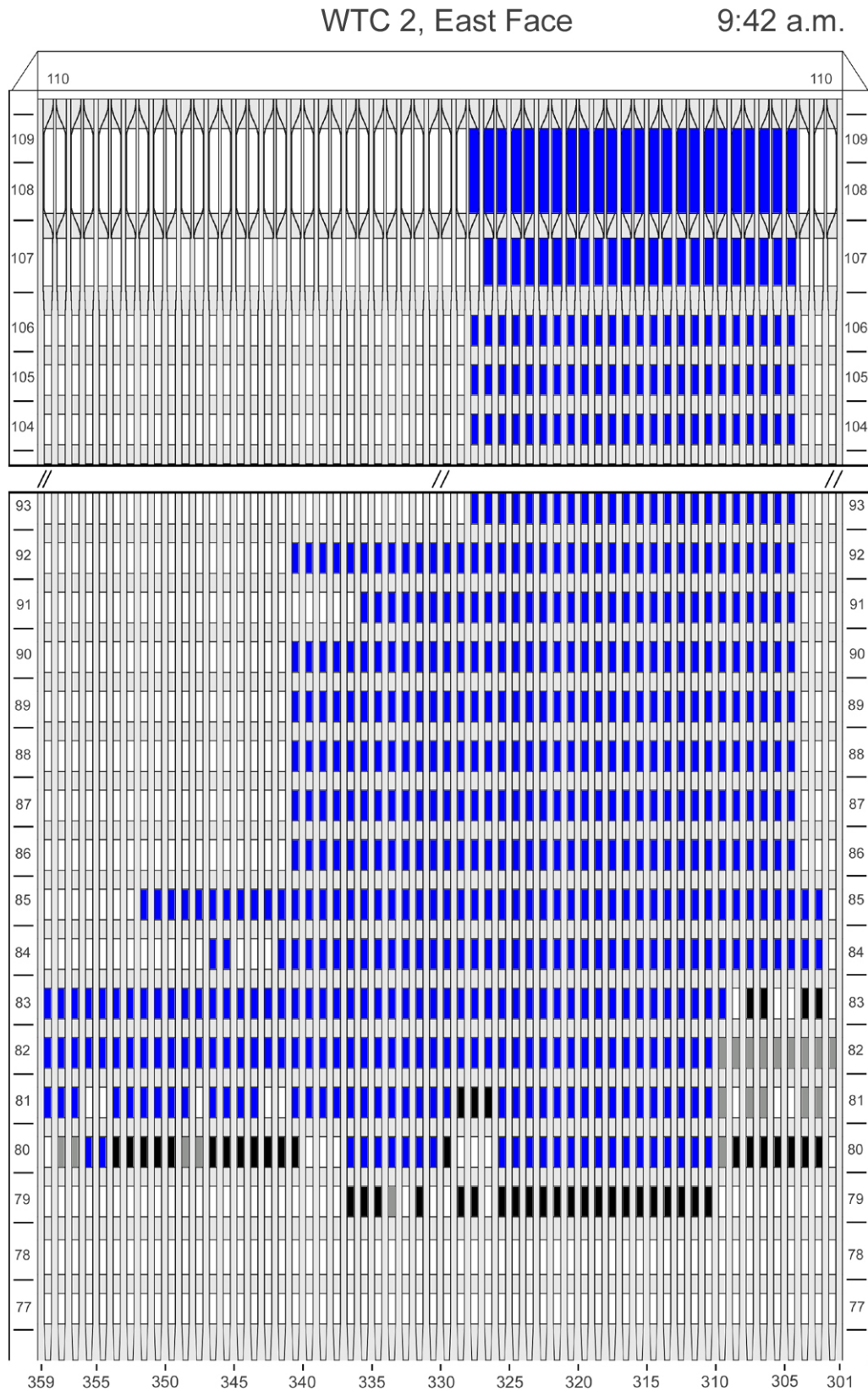


Figure H-42. Diagram of the east face of WTC 2 for floors 77 to 93 and floors 104 to 110 at 9:42 a.m. showing windows where smoke was observed and those hidden from view.

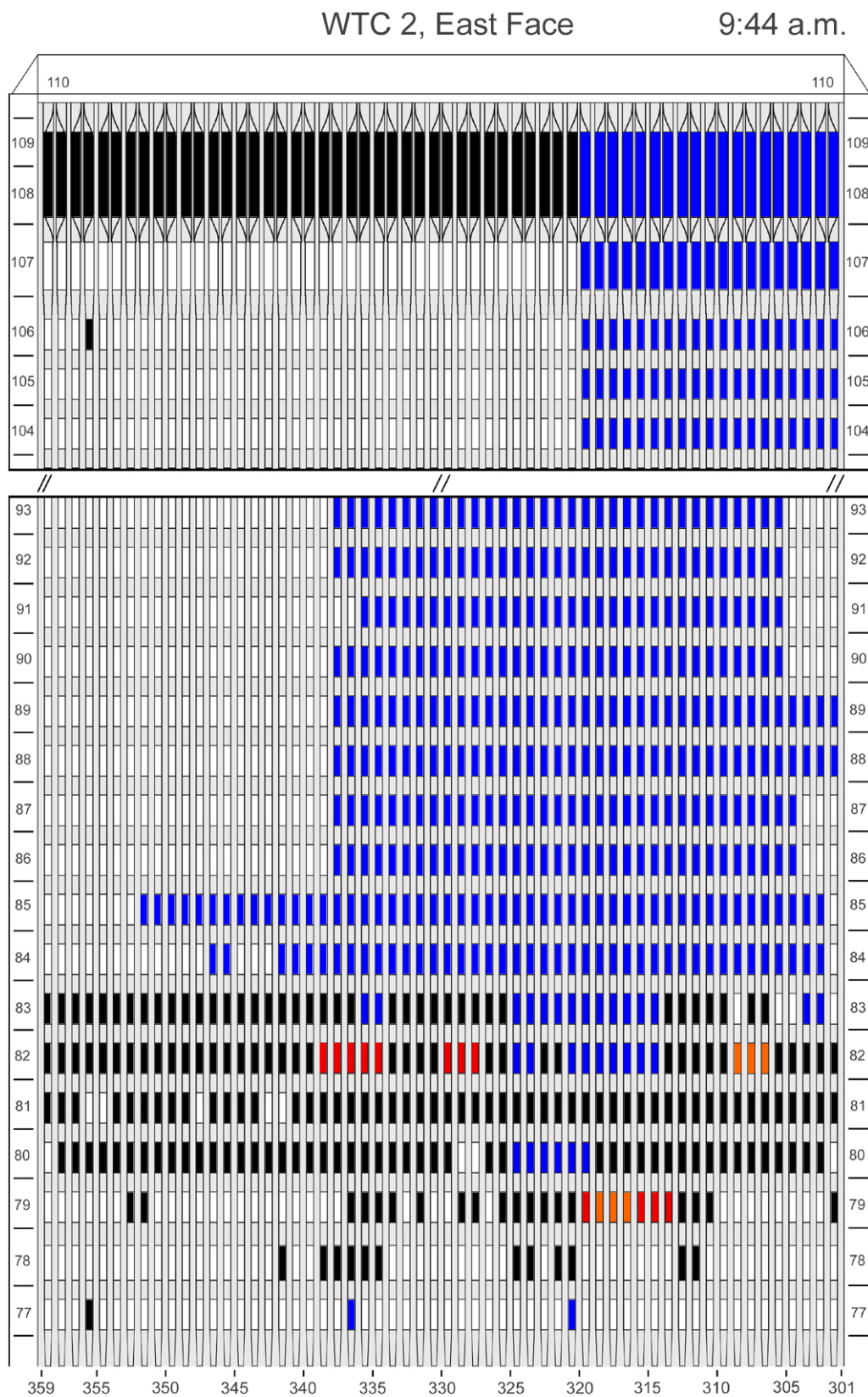


Figure H-43. Diagram of the east face of WTC 2 for floors 77 to 93 and floors 104 to 110 at 9:44 a.m. showing the condition of windows and locations of fires.

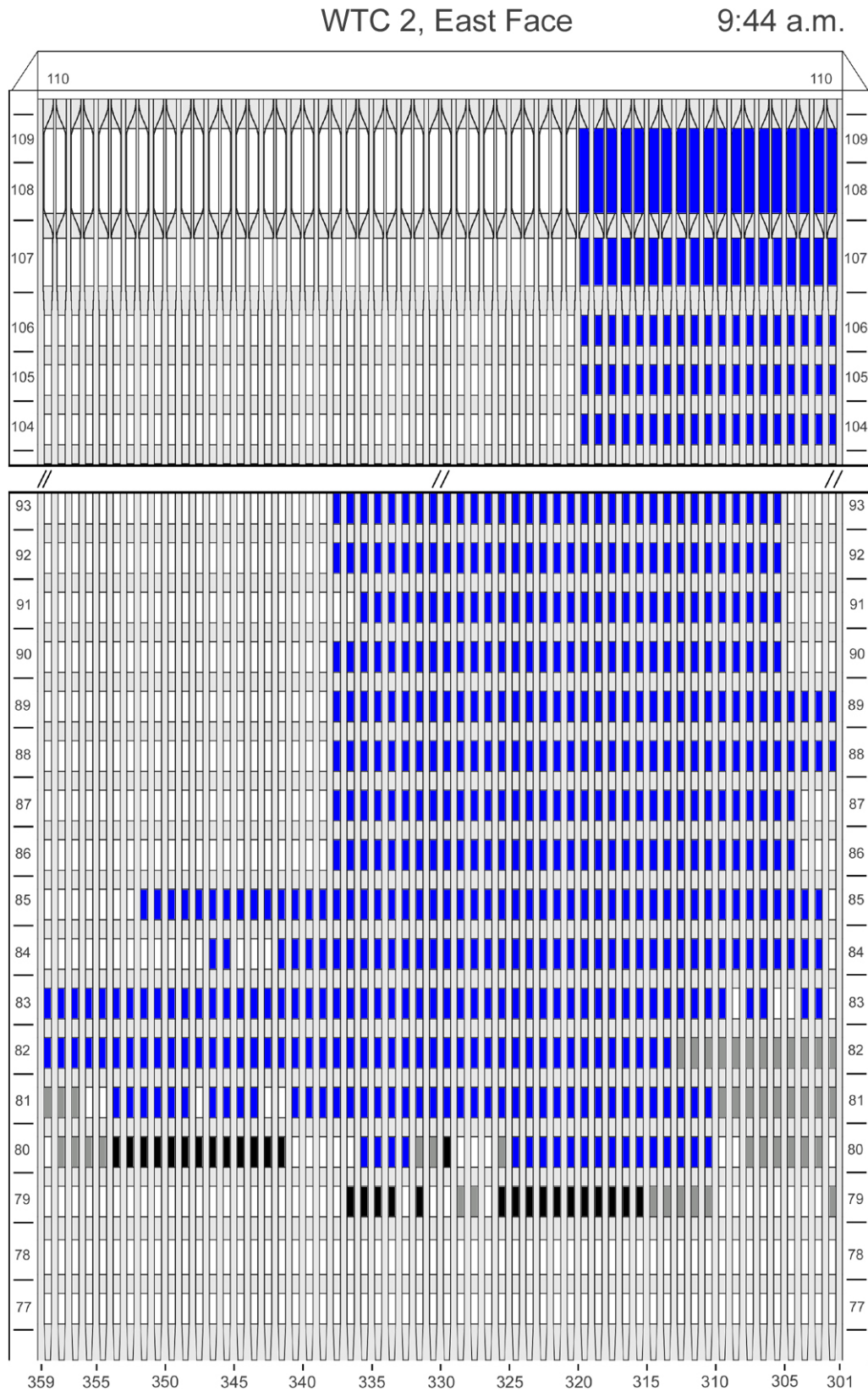


Figure H-44. Diagram of the east face of WTC 2 for floors 77 to 93 and floors 104 to 110 at 9:44 a.m. showing windows where smoke was observed and those hidden from view.

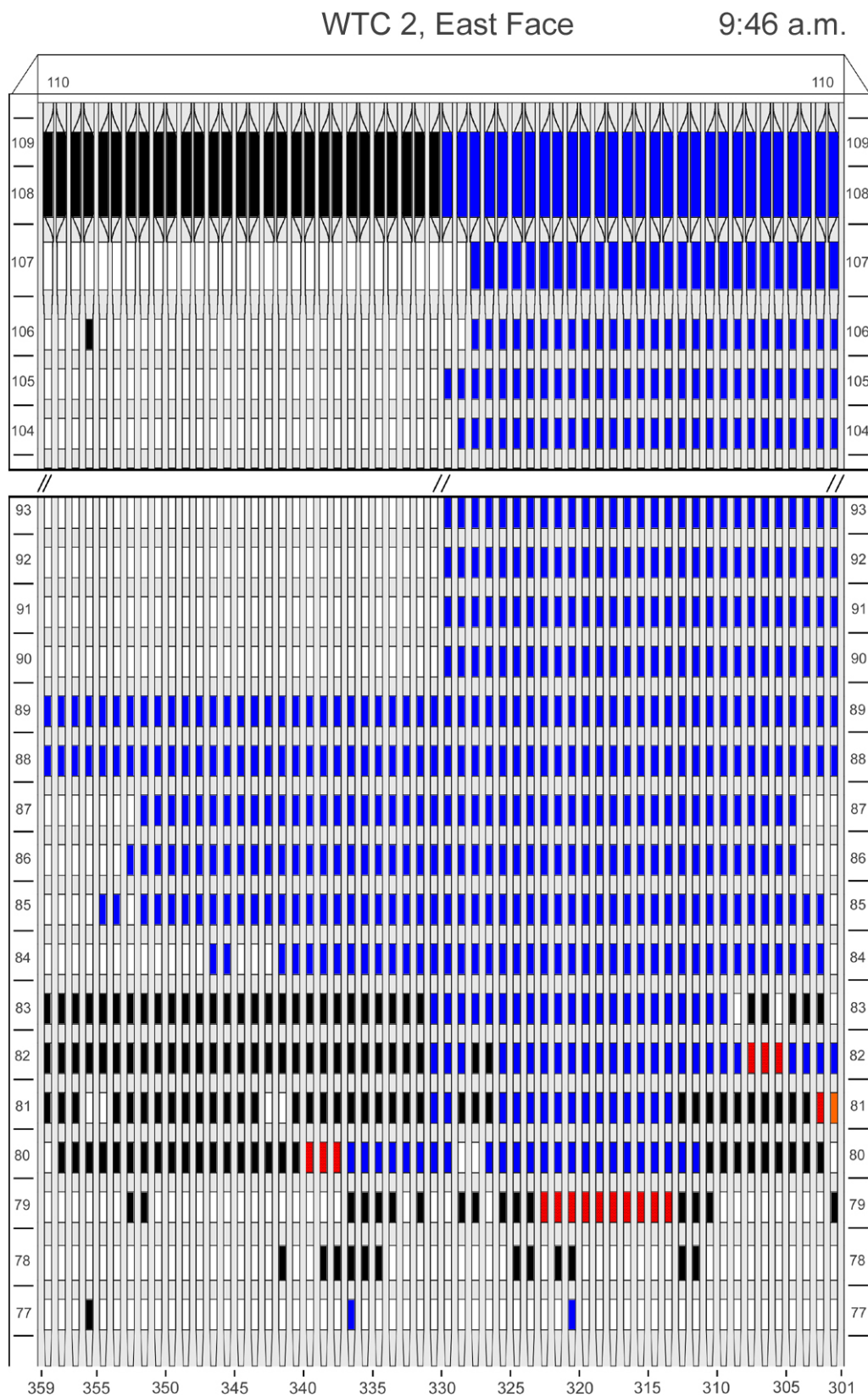


Figure H-45. Diagram of the east face of WTC 2 for floors 77 to 93 and floors 104 to 110 at 9:46 a.m. showing the condition of windows and locations of fires.

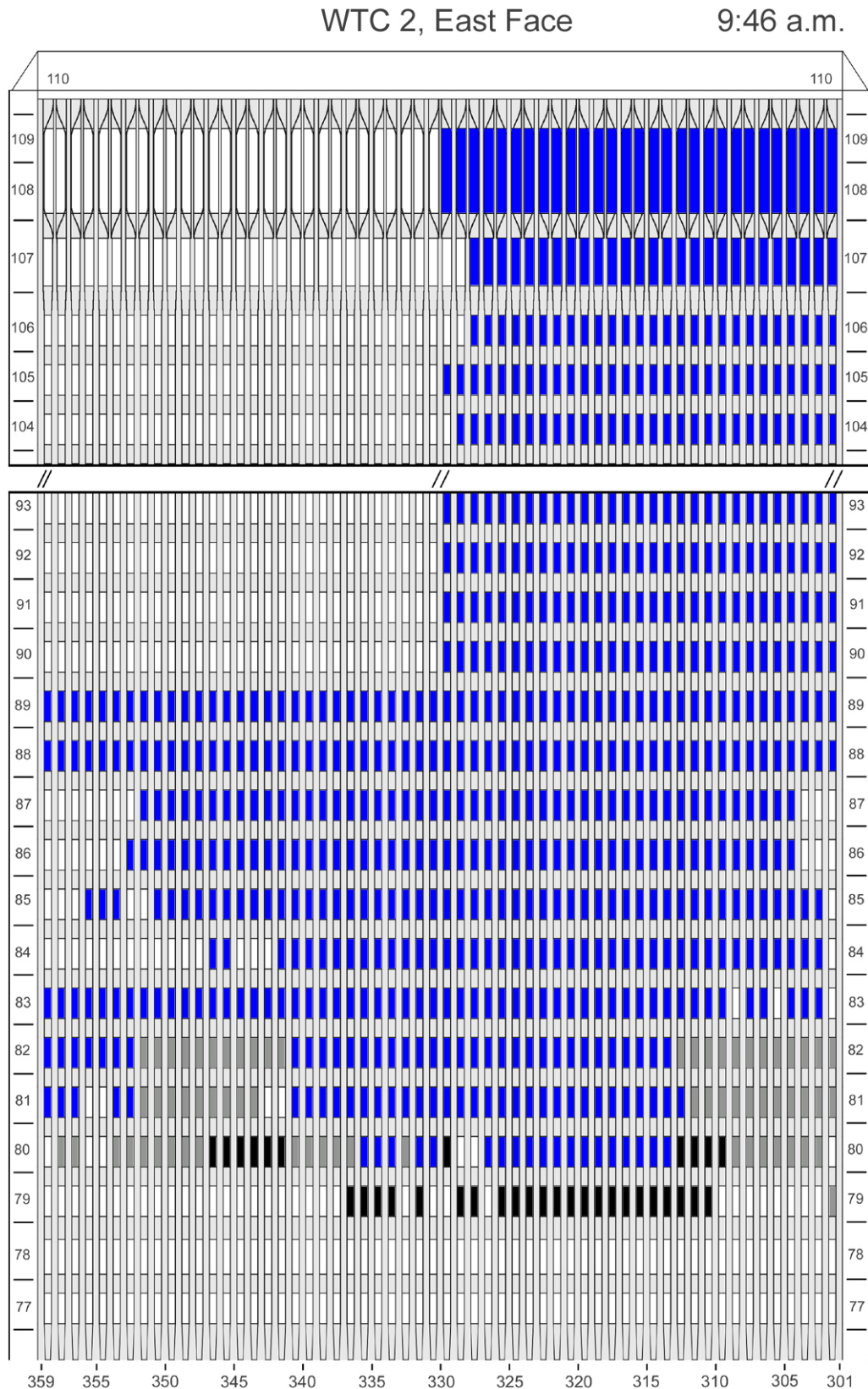


Figure H-46. Diagram of the east face of WTC 2 for floors 77 to 93 and floors 104 to 110 at 9:46 a.m. showing windows where smoke was observed and those hidden from view.

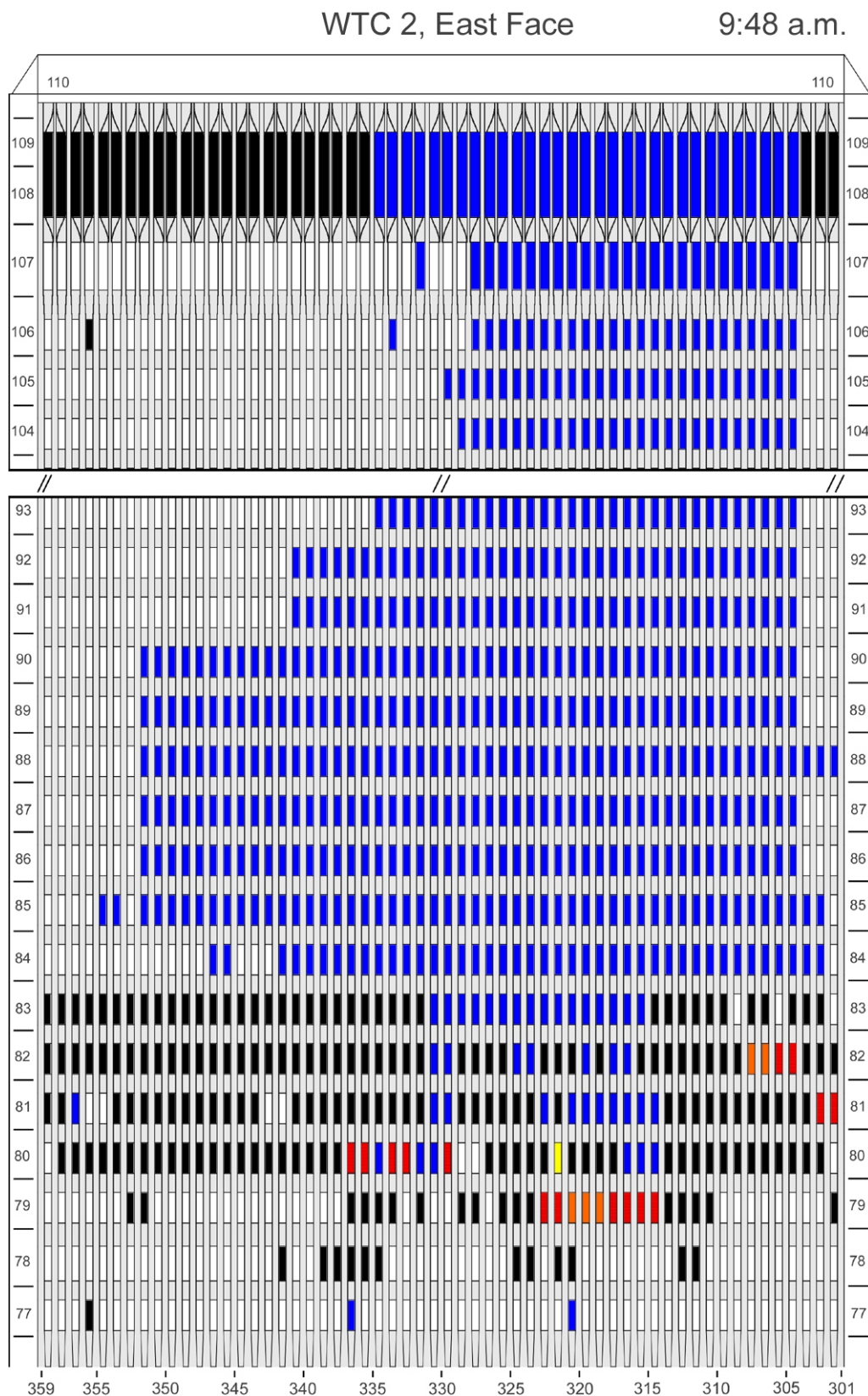


Figure H-47. Diagram of the east face of WTC 2 for floors 77 to 93 and floors 104 to 110 at 9:48 a.m. showing the condition of windows and locations of fires.

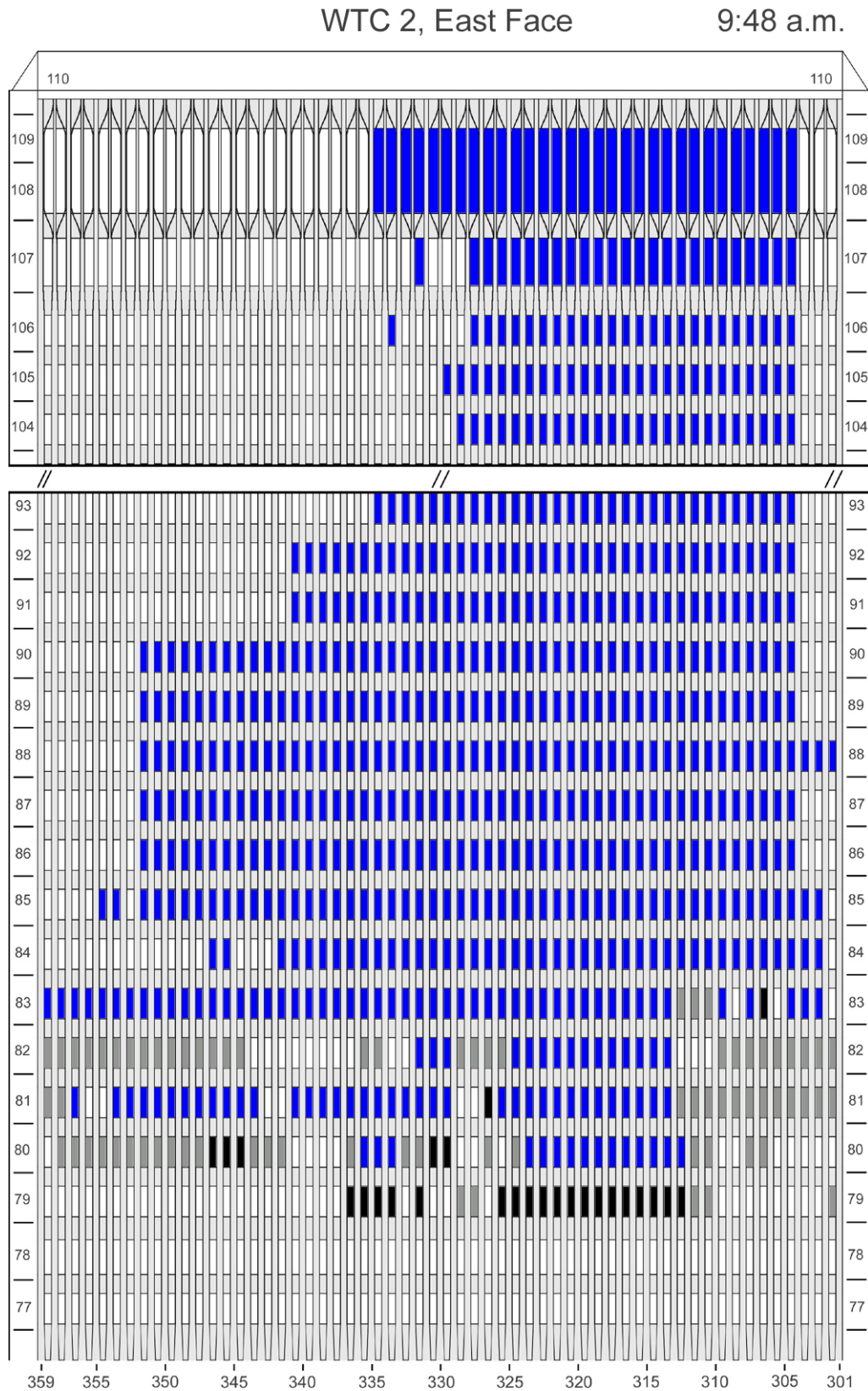


Figure H- 48. Diagram of the east face of WTC 2 for floors 77 to 93 and floors 104 to 110 at 9:48 a.m. showing windows where smoke was observed and those hidden from view.

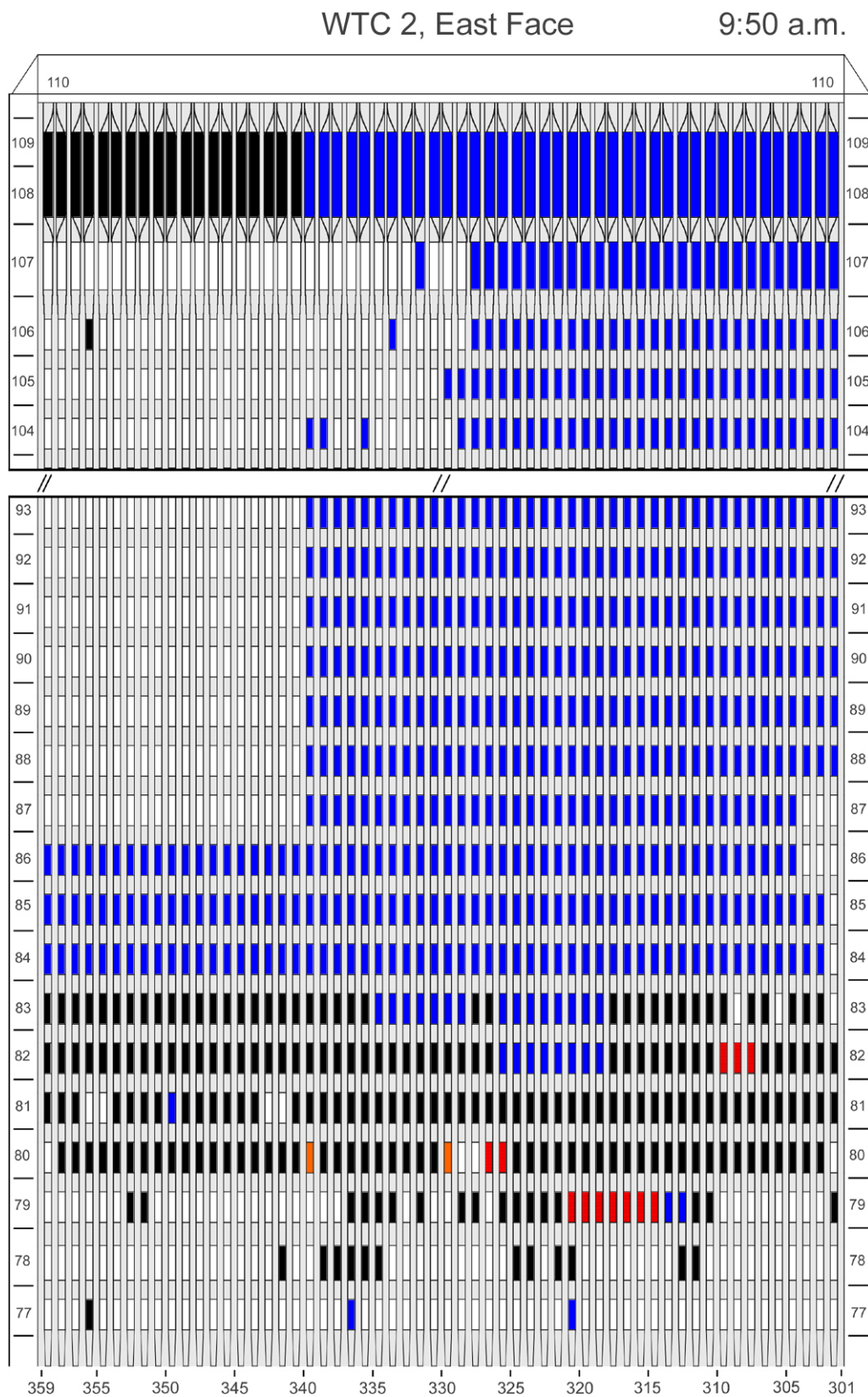


Figure H-49. Diagram of the east face of WTC 2 for floors 77 to 93 and floors 104 to 110 at 9:50 a.m. showing the condition of windows and locations of fires.

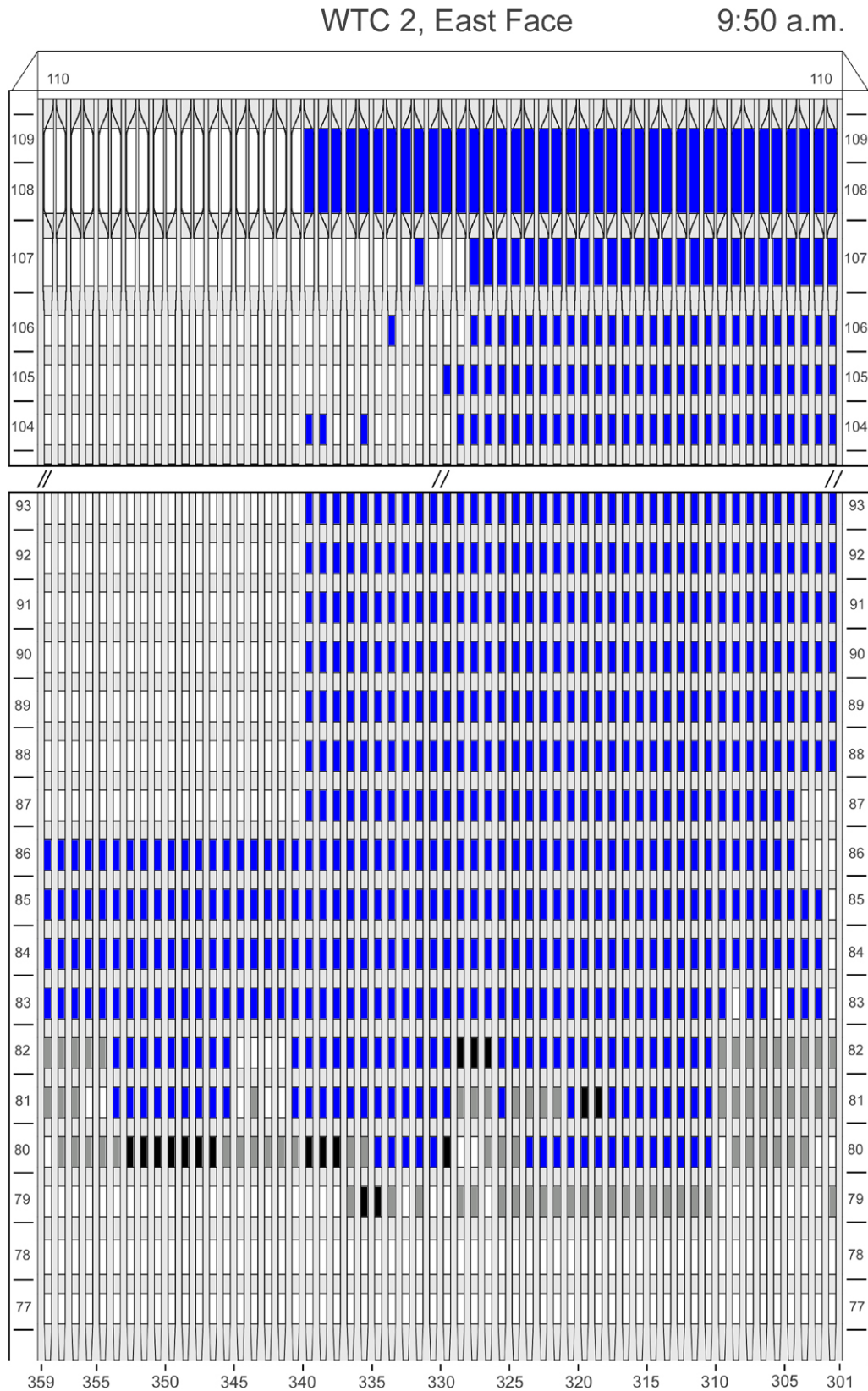


Figure H-50. Diagram of the east face of WTC 2 for floors 77 to 93 and floors 104 to 110 at 9:50 a.m. showing windows where smoke was observed and those hidden from view.

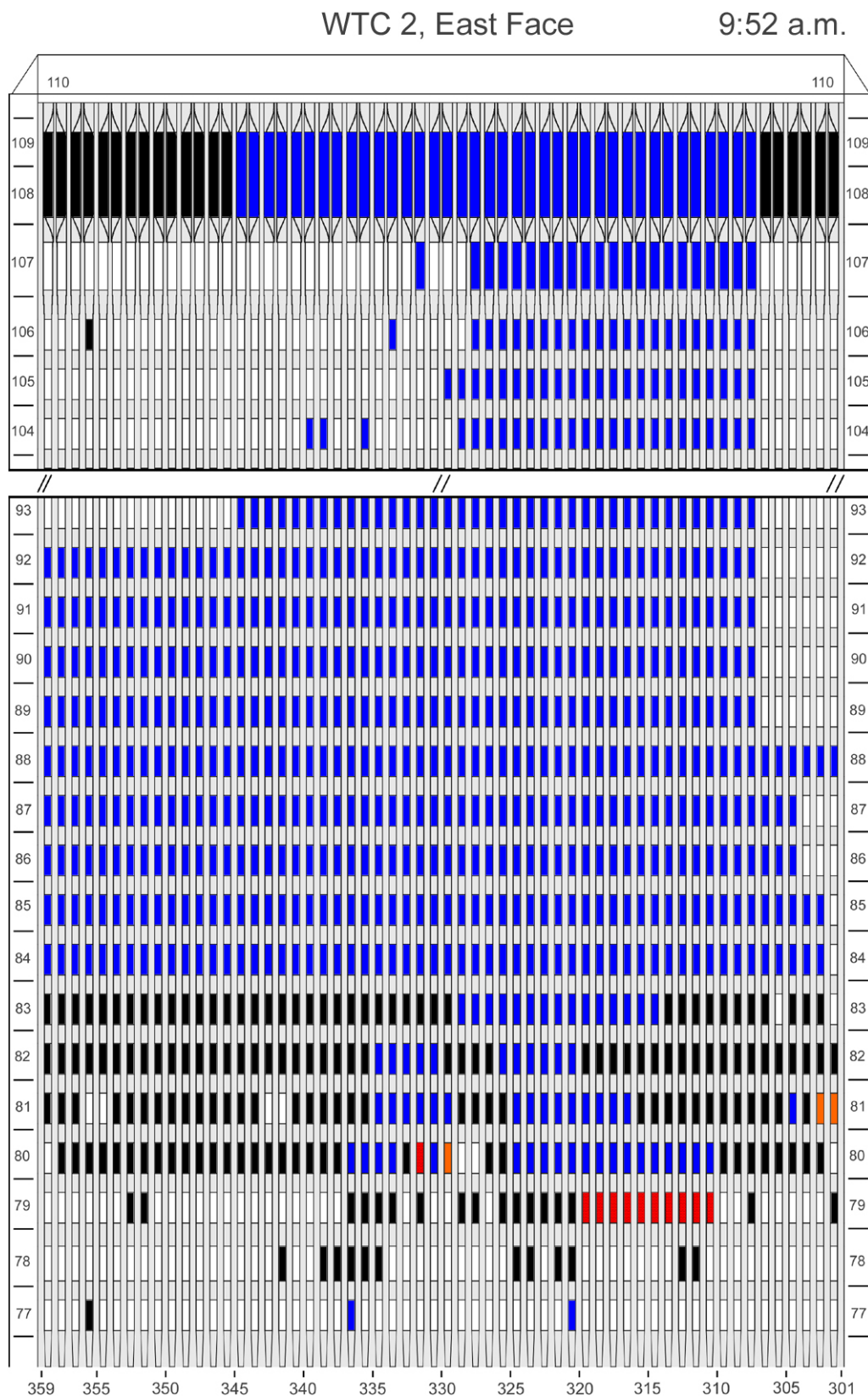


Figure H-51. Diagram of the east face of WTC 2 for floors 77 to 93 and floors 104 to 110 at 9:52 a.m. showing the condition of windows and locations of fires.

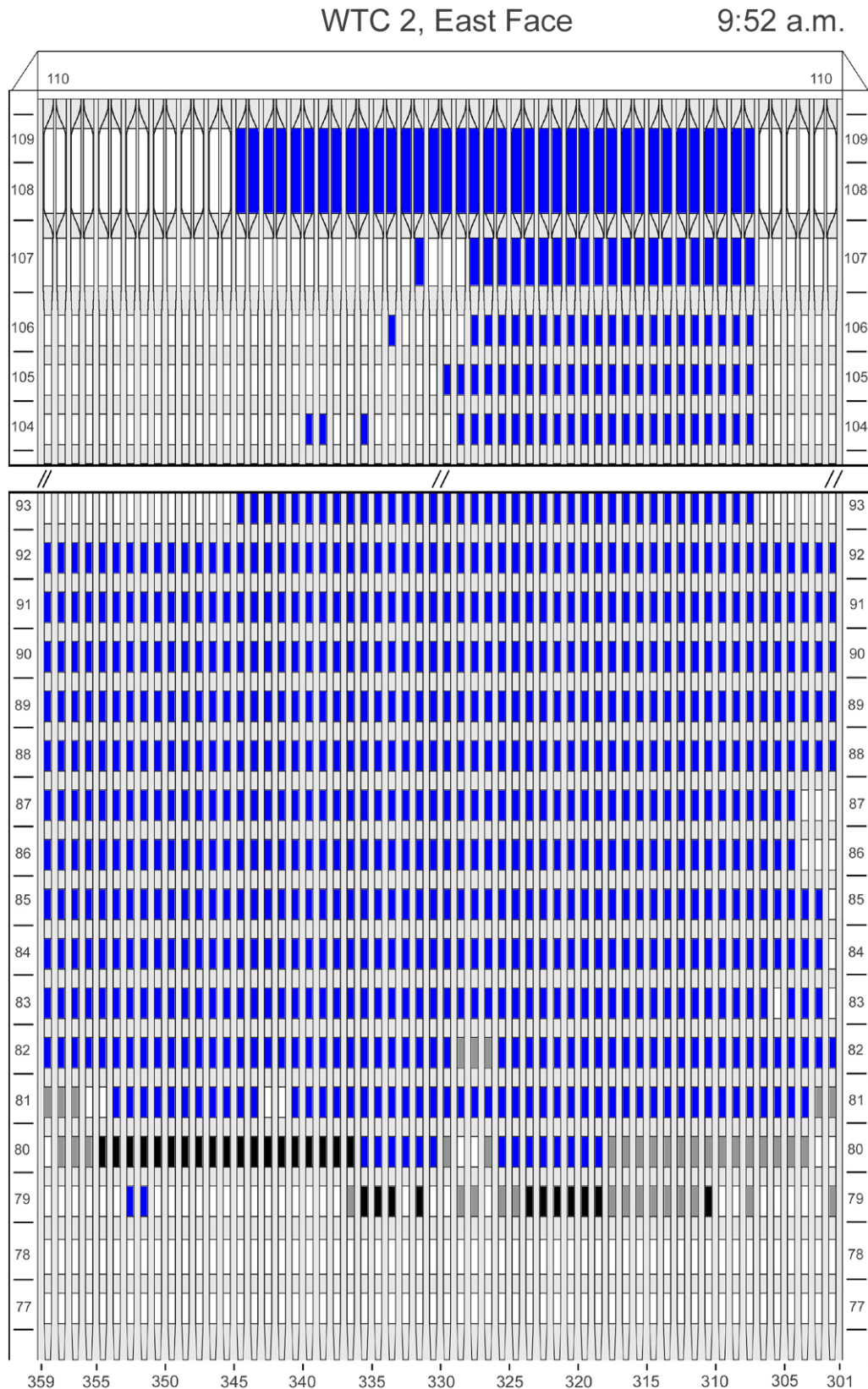


Figure H-52. Diagram of the east face of WTC 2 for floors 77 to 93 and floors 104 to 110 at 9:52 a.m. showing windows where smoke was observed and those hidden from view.

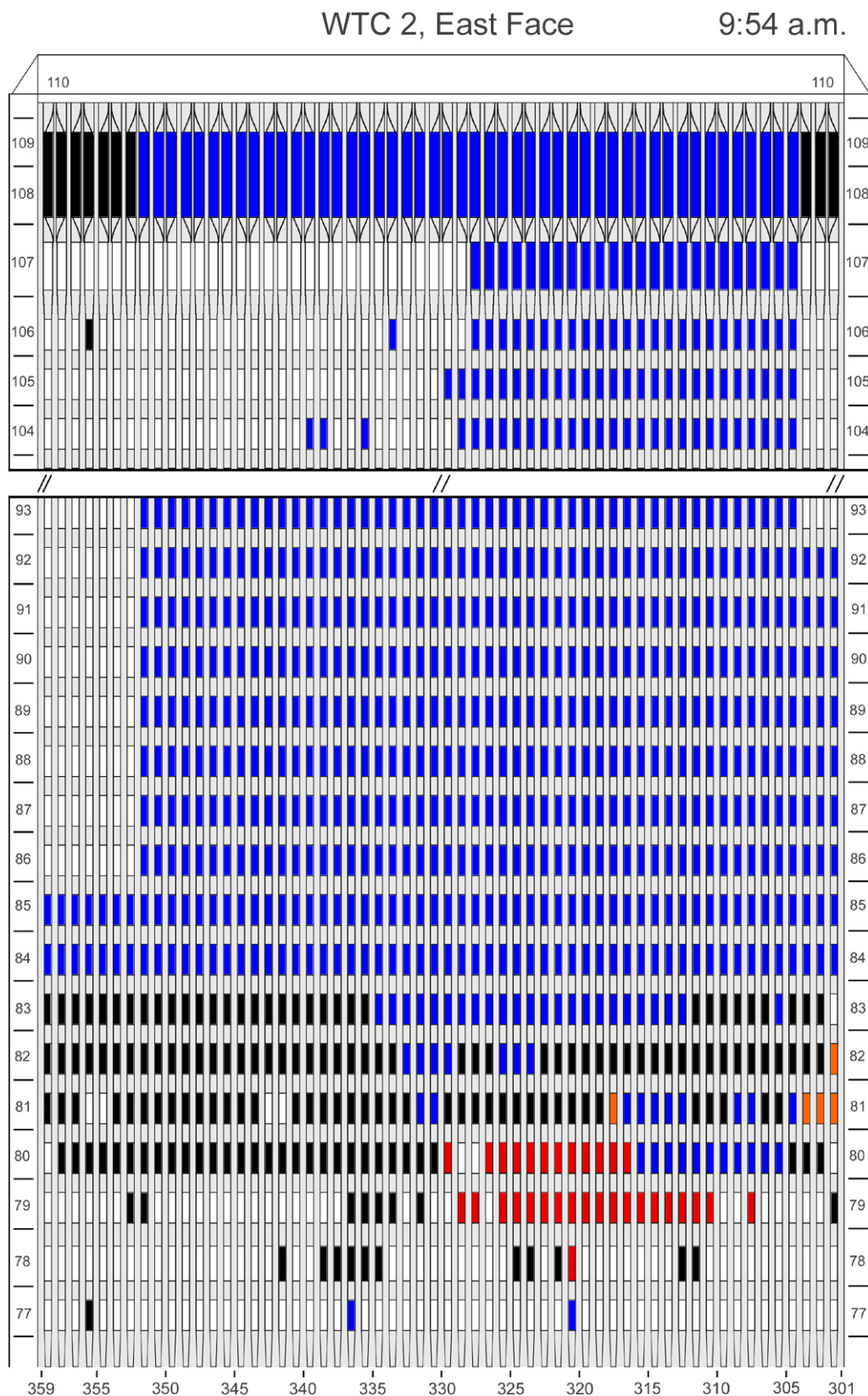


Figure H-53. Diagram of the east face of WTC 2 for floors 77 to 93 and floors 104 to 110 at 9:54 a.m. showing the condition of windows and locations of fires.

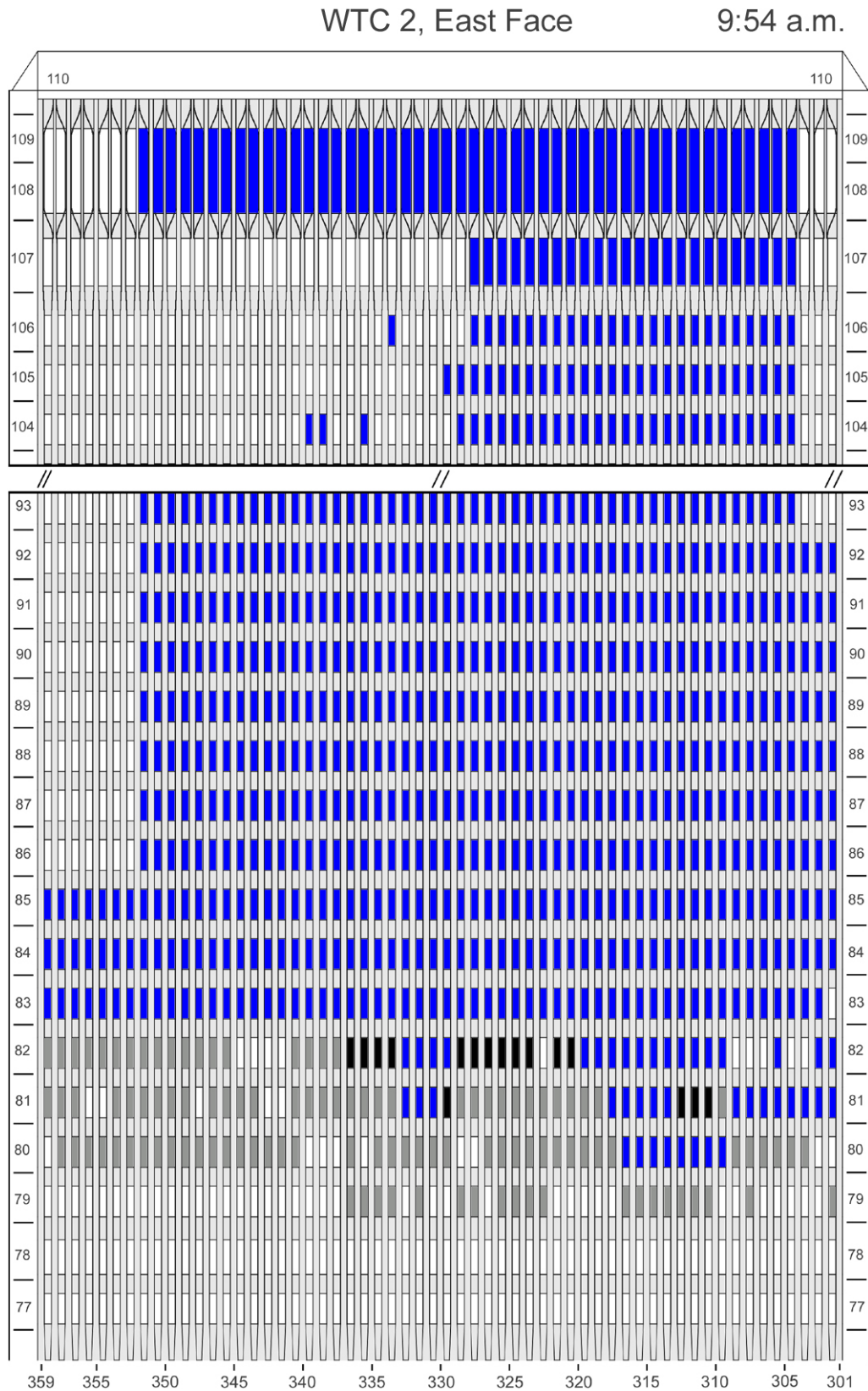


Figure H-54. Diagram of the east face of WTC 2 for floors 77 to 93 and floors 104 to 110 at 9:54 a.m. showing windows where smoke was observed and those hidden from view.

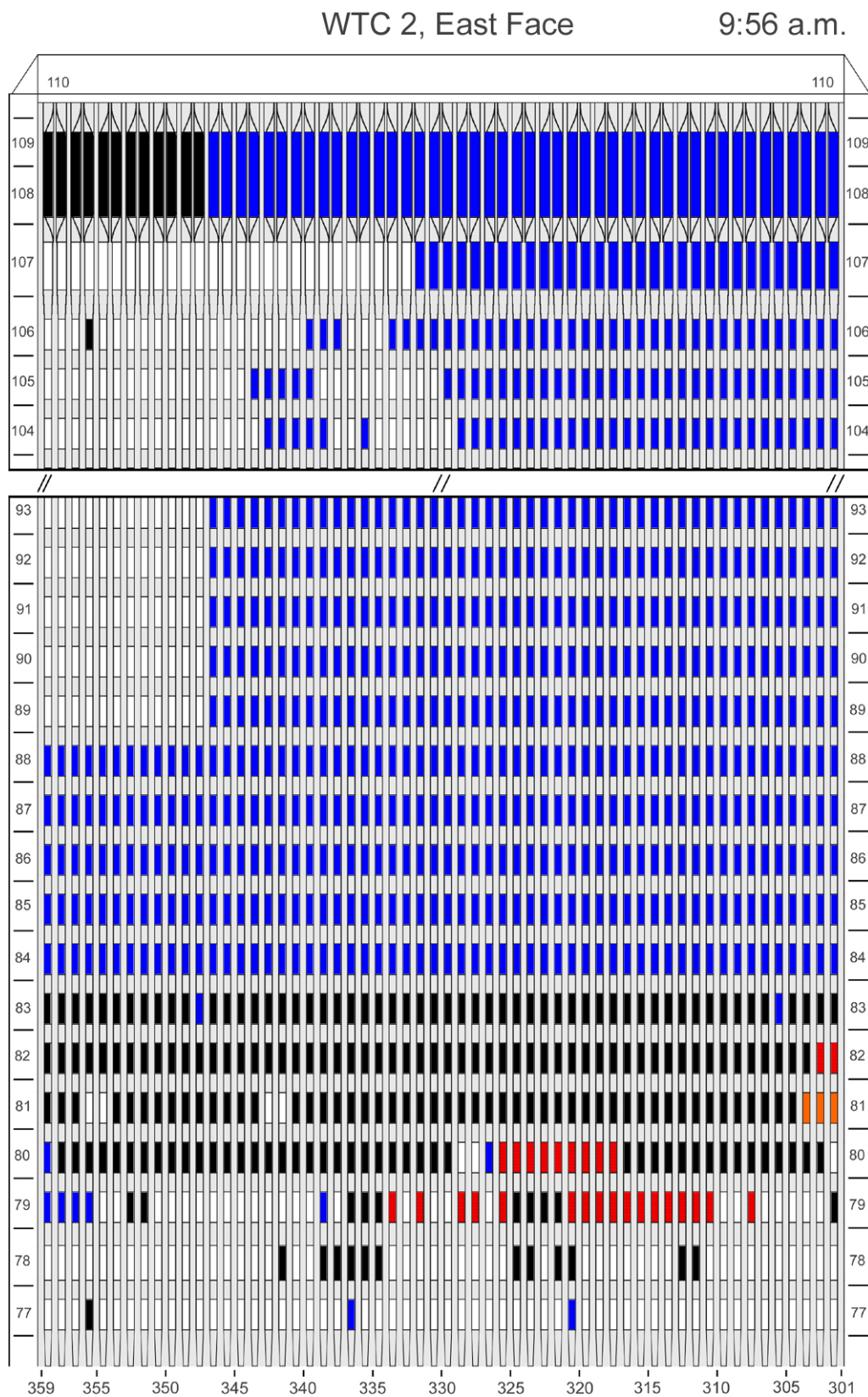


Figure H-55. Diagram of the east face of WTC 2 for floors 77 to 93 and floors 104 to 110 at 9:56 a.m. showing the condition of windows and locations of fires.

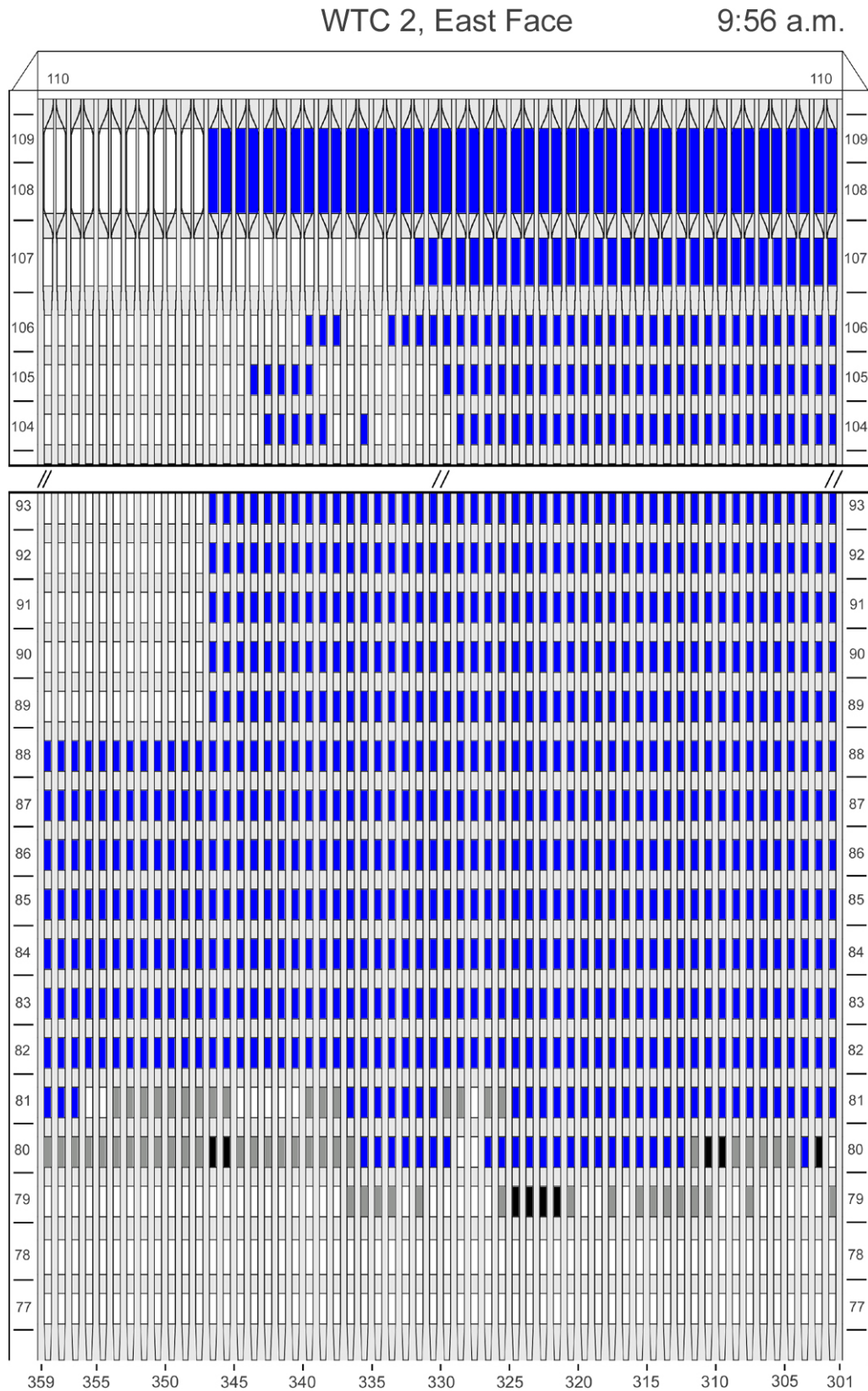


Figure H-56. Diagram of the east face of WTC 2 for floors 77 to 93 and floors 104 to 110 at 9:56 a.m. showing windows where smoke was observed and those hidden from view.

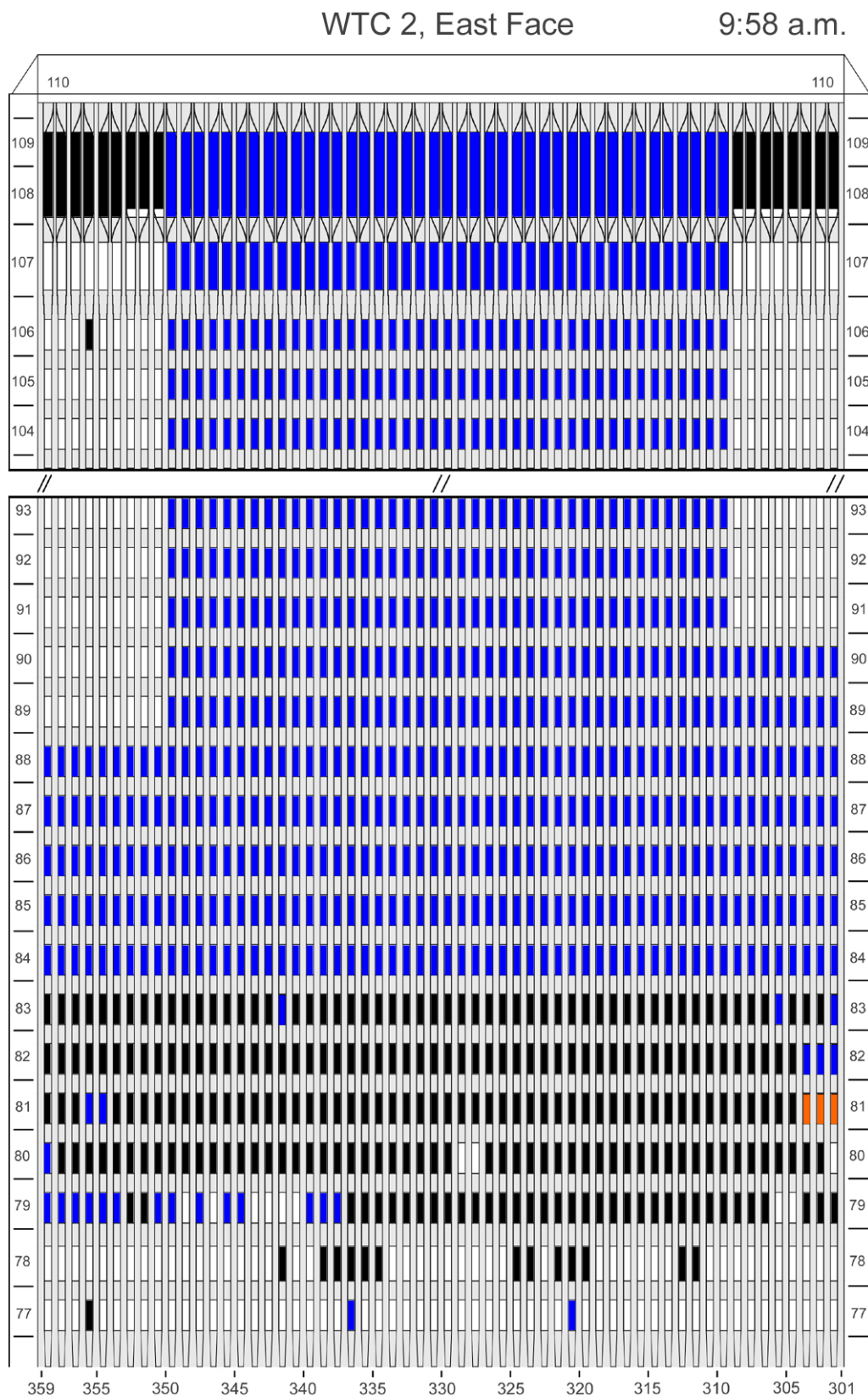


Figure H-57. Diagram of the east face of WTC 2 for floors 77 to 93 and floors 104 to 110 at 9:58 a.m. showing the condition of windows and locations of fires.

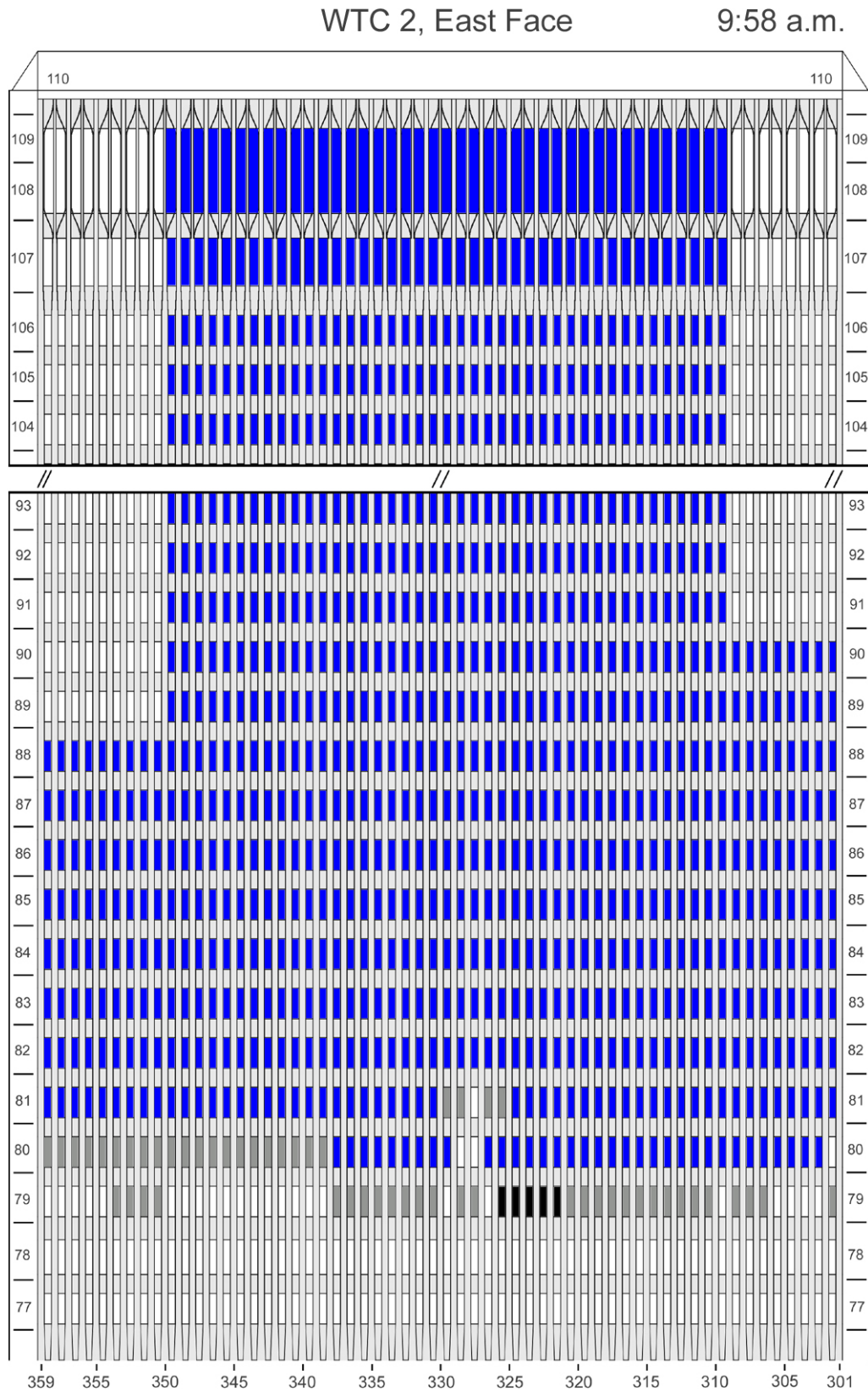












Figure H-58. Diagram of the east face of WTC 2 for floors 77 to 93 and floors 104 to 110 at 9:58 a.m. showing windows where smoke was observed and those hidden from view.

This page intentionally left blank.

Appendix I

WTC 2 SOUTH FACE COMBINED FIRE AND WINDOW CONDITION AND WINDOW SMOKE CONDITION

This appendix provides visual representations of the data contained in data sheets describing observations of fire, smoke, and window condition on a window-by-window basis as a function of time for the south face of WTC 2. The data for window condition and fire observations are combined into single representations, with the data for fire taking precedence. Observations are represented using the key provided in Figure 5-1 as follows:  - window glass in place,  - window open,  - spot fire,  - fire visible inside,  - external flaming, and  - not visible. The data for smoke are shown in separate figures using the key from Figure 5-1 as follows:  - no smoke visible,  - light smoke,  - heavy smoke, and  - not visible. For a given time, the window condition and fire data are shown first.

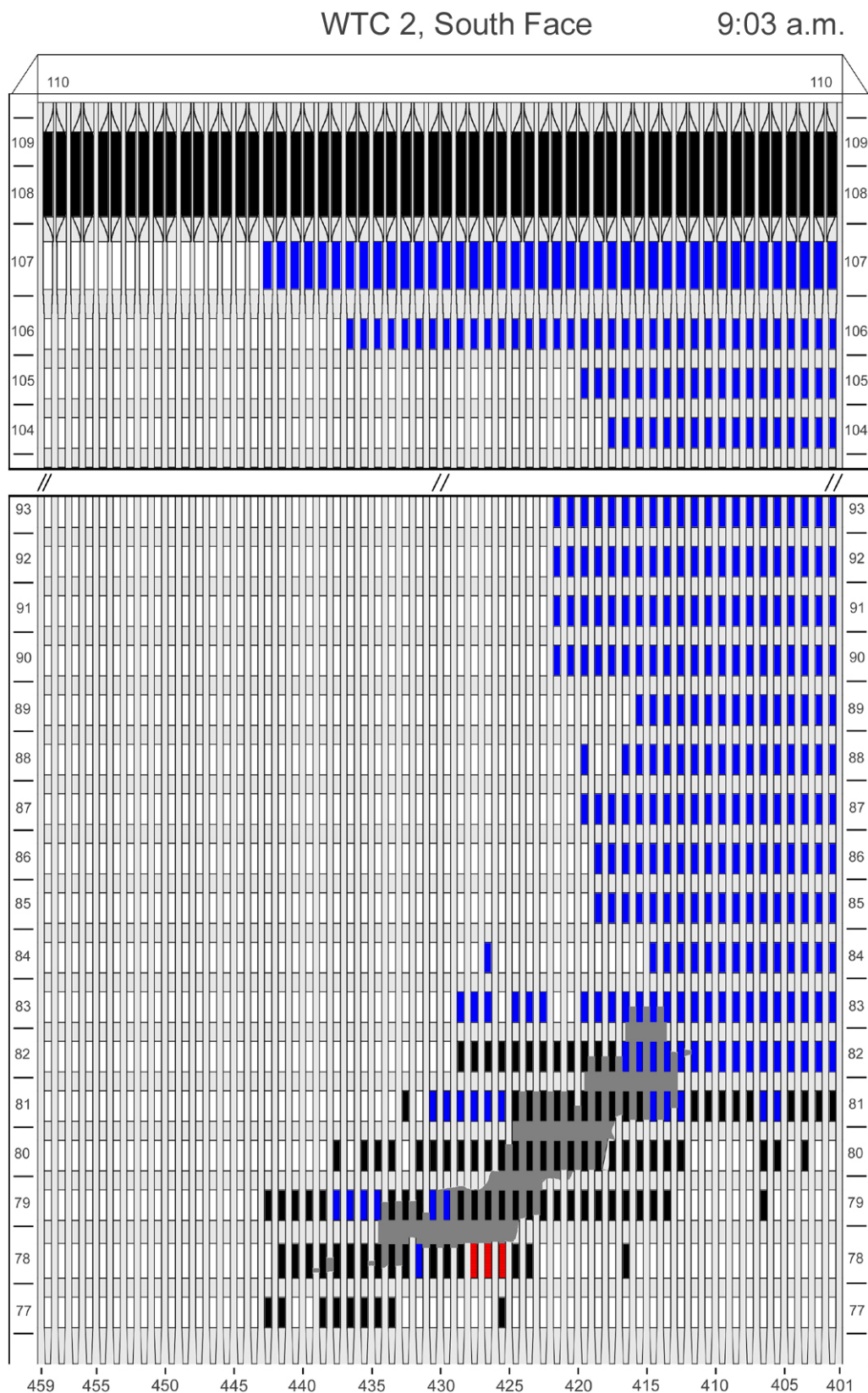


Figure I-1. Diagram of the south face of WTC 2 for floors 77 to 93 and floors 104 to 110 at 9:03 a.m. showing the condition of windows and locations of fires.

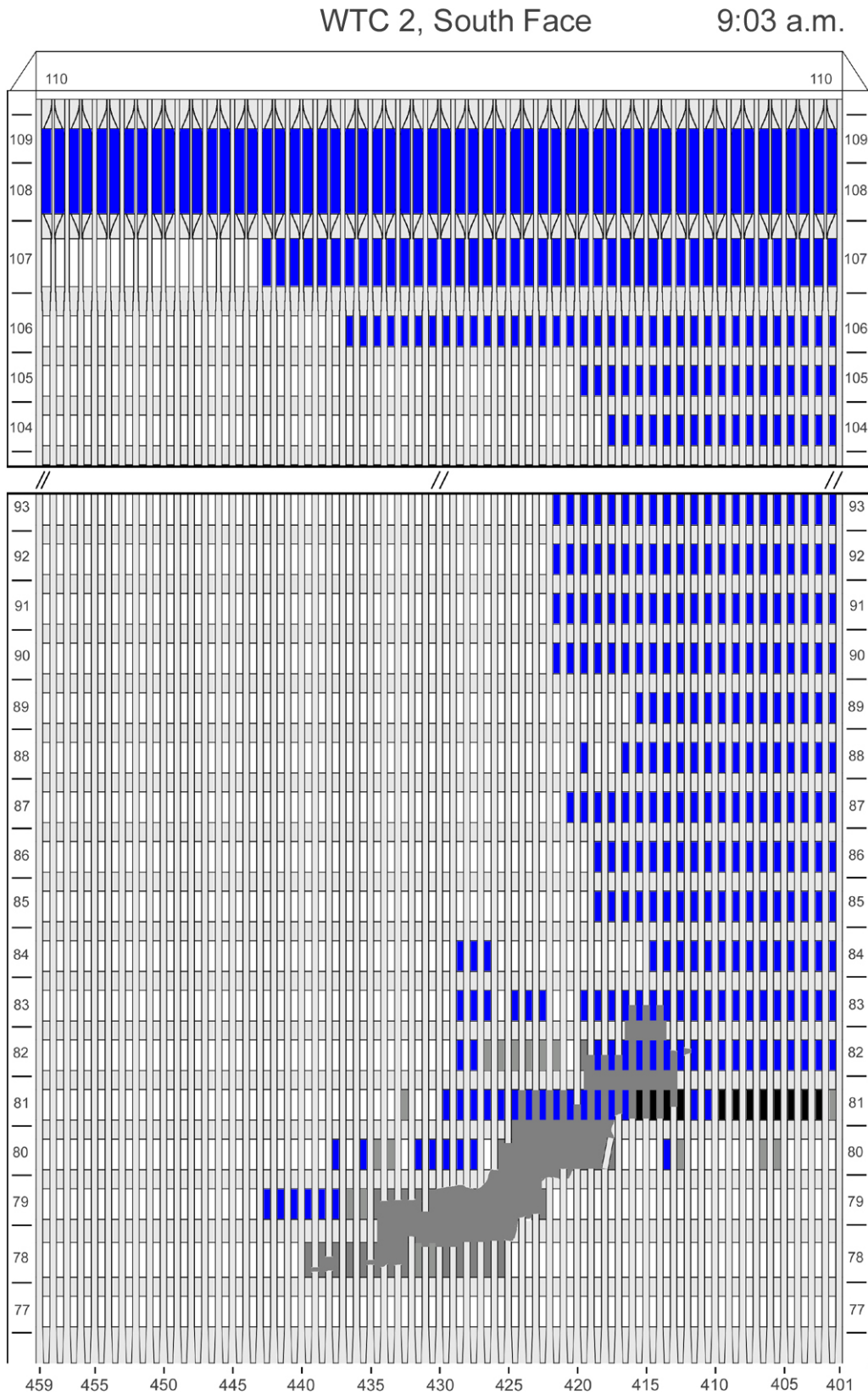


Figure I-2. Diagram of the south face of WTC 2 for floors 77 to 93 and floors 104 to 110 at 9:03 a.m. showing windows where smoke was observed and those hidden from view.

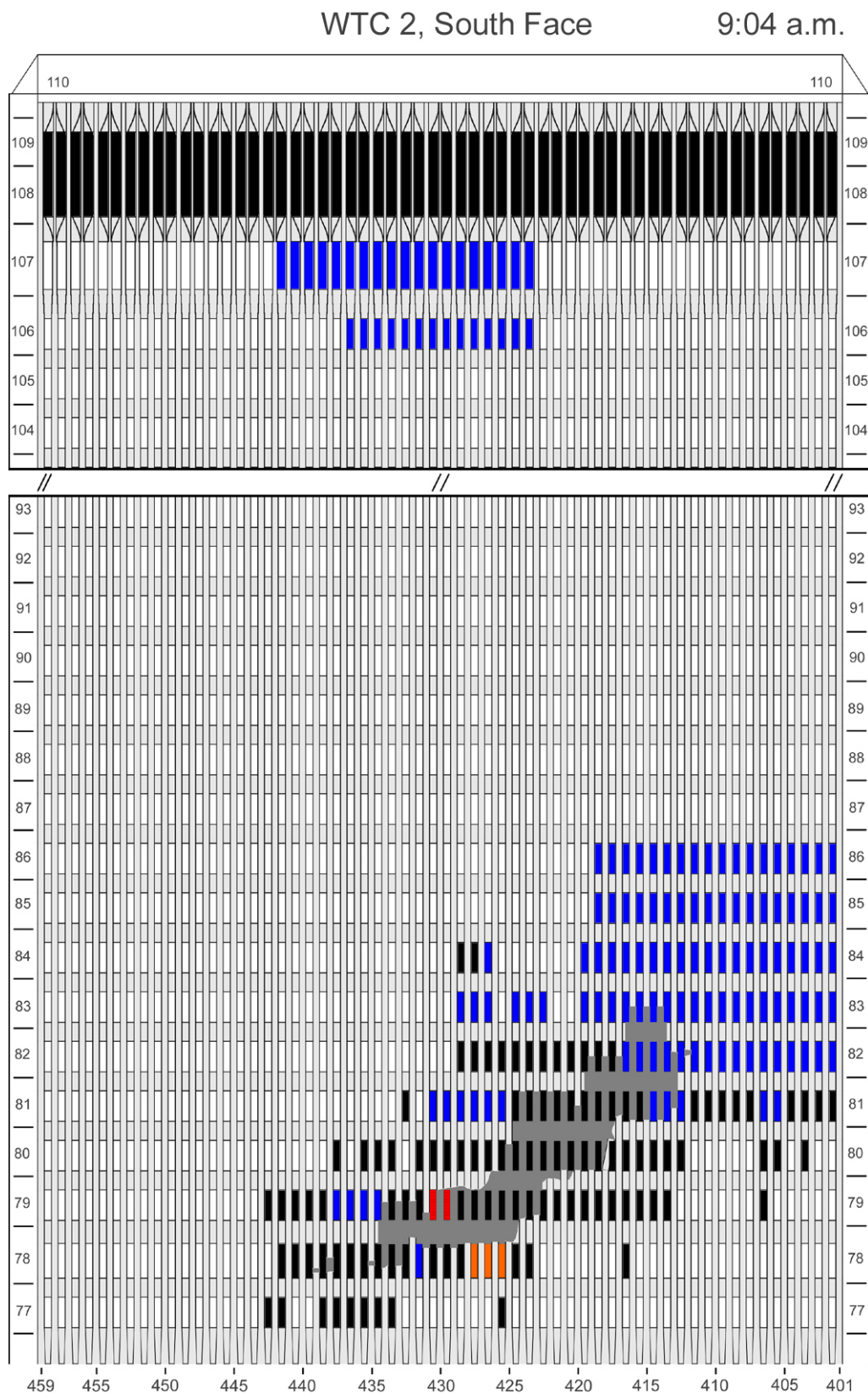


Figure I-3. Diagram of the south face of WTC 2 for floors 77 to 93 and floors 104 to 110 at 9:04 a.m. showing the condition of windows and locations of fires.

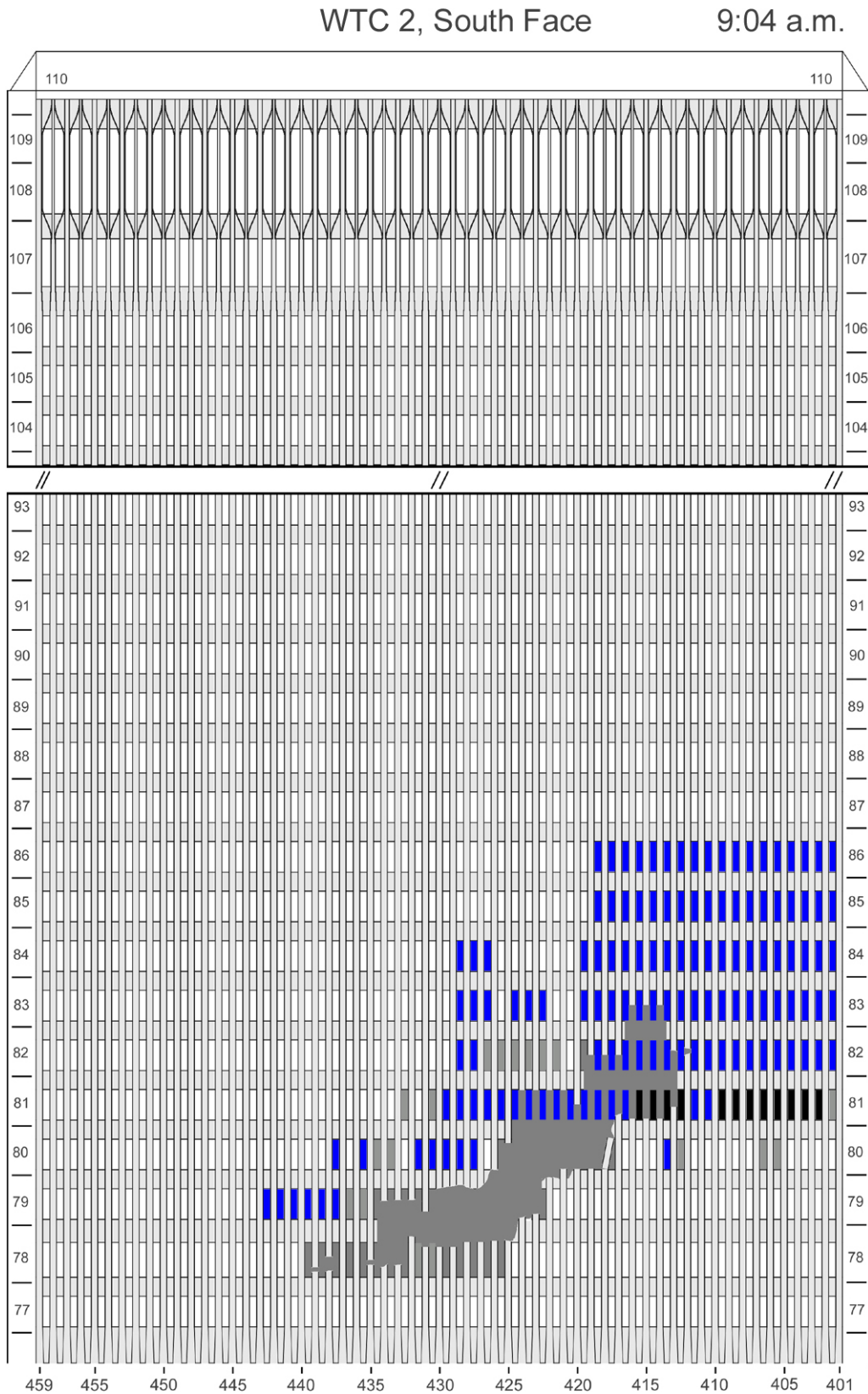


Figure I-4. Diagram of the south face of WTC 2 for floors 77 to 93 and floors 104 to 110 at 9:04 a.m. showing windows where smoke was observed and those hidden from view.

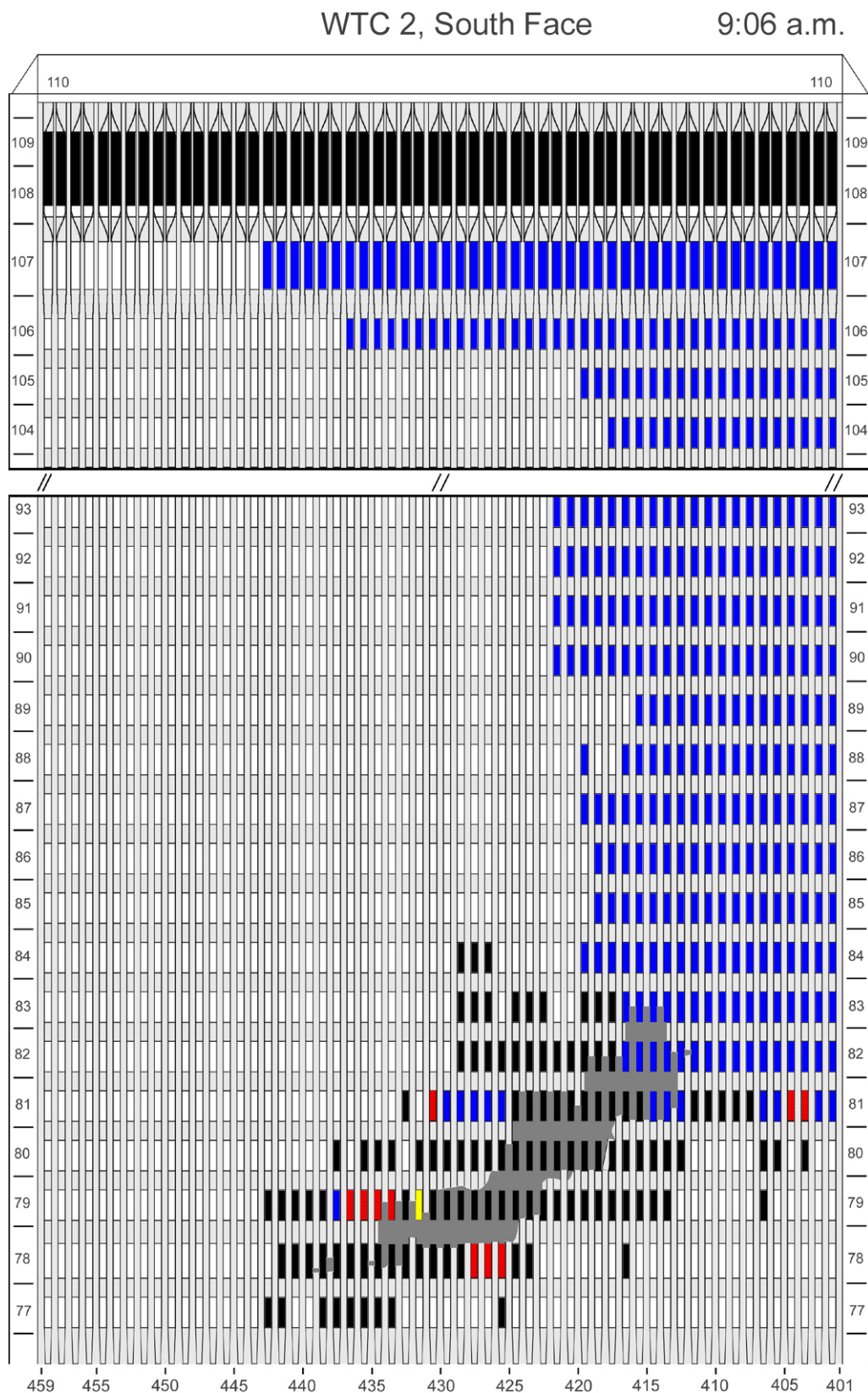


Figure I-5. Diagram of the south face of WTC 2 for floors 77 to 93 and floors 104 to 110 at 9:06 a.m. showing the condition of windows and locations of fires.

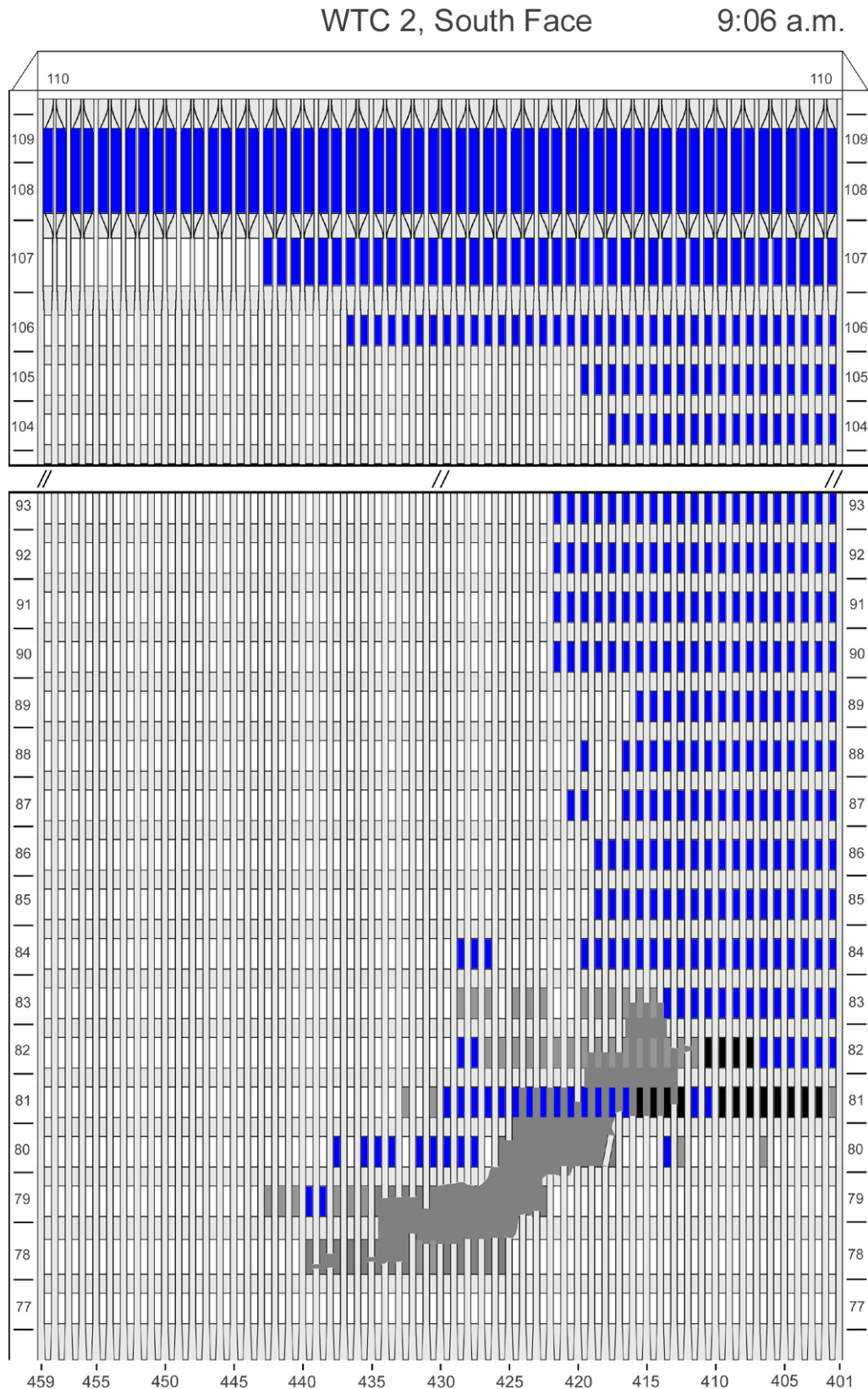


Figure I-6. Diagram of the south face of WTC 2 for floors 77 to 93 and floors 104 to 110 at 9:06 a.m. showing windows where smoke was observed and those hidden from view.

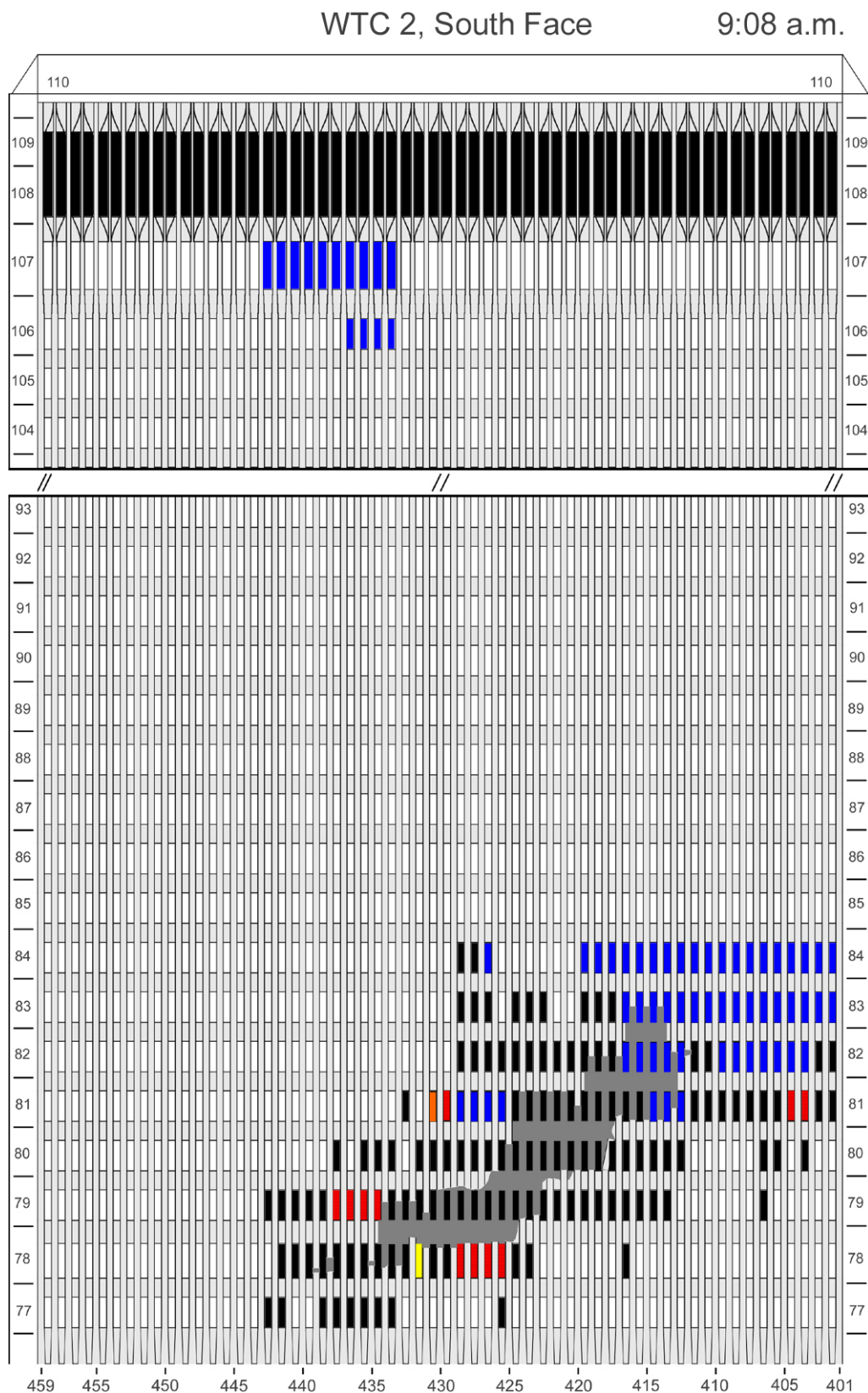


Figure I-7. Diagram of the south face of WTC 2 for floors 77 to 93 and floors 104 to 110 at 9:08 a.m. showing the condition of windows and locations of fires.

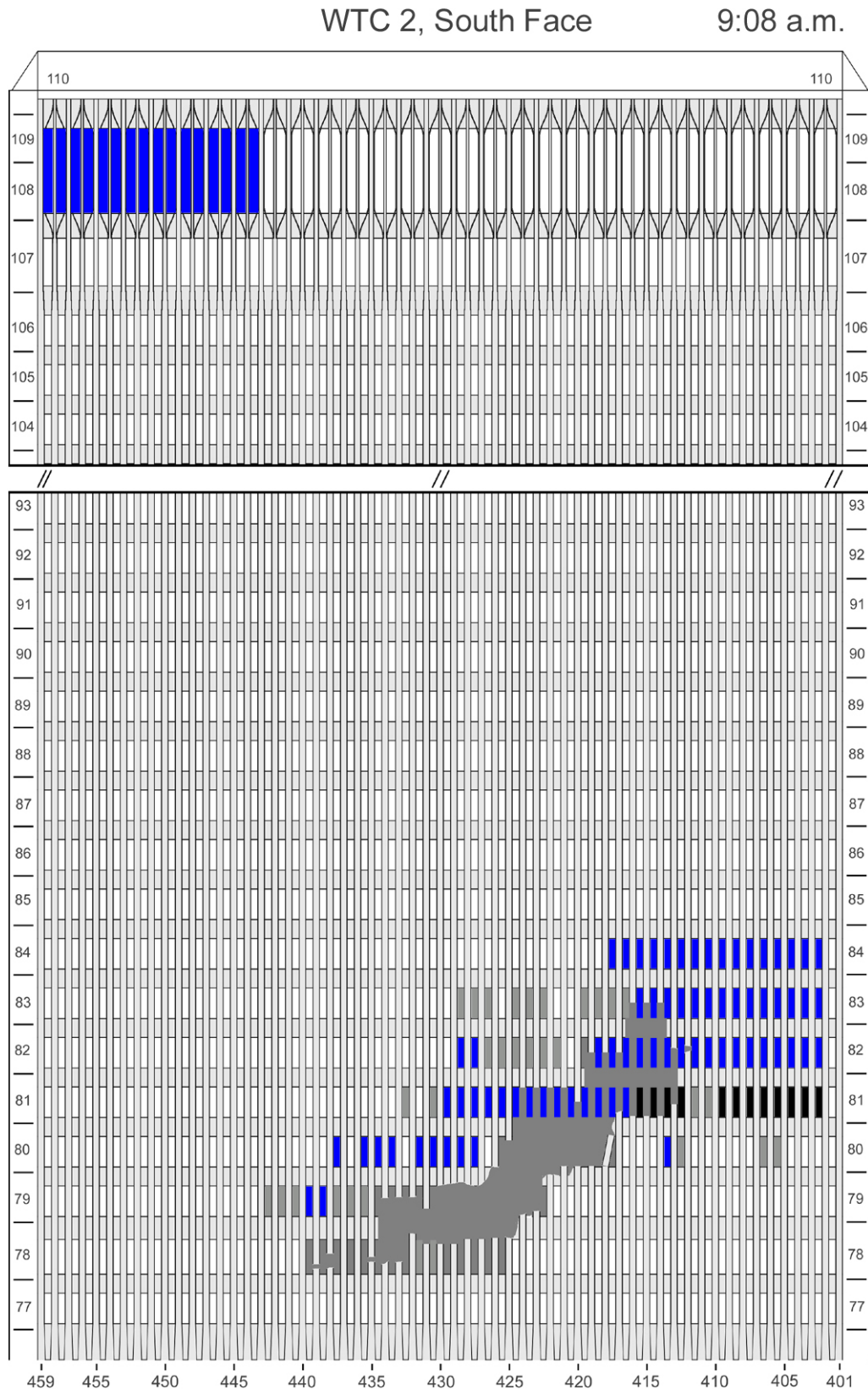


Figure I-8. Diagram of the south face of WTC 2 for floors 77 to 93 and floors 104 to 110 at 9:08 a.m. showing windows where smoke was observed and those hidden from view.

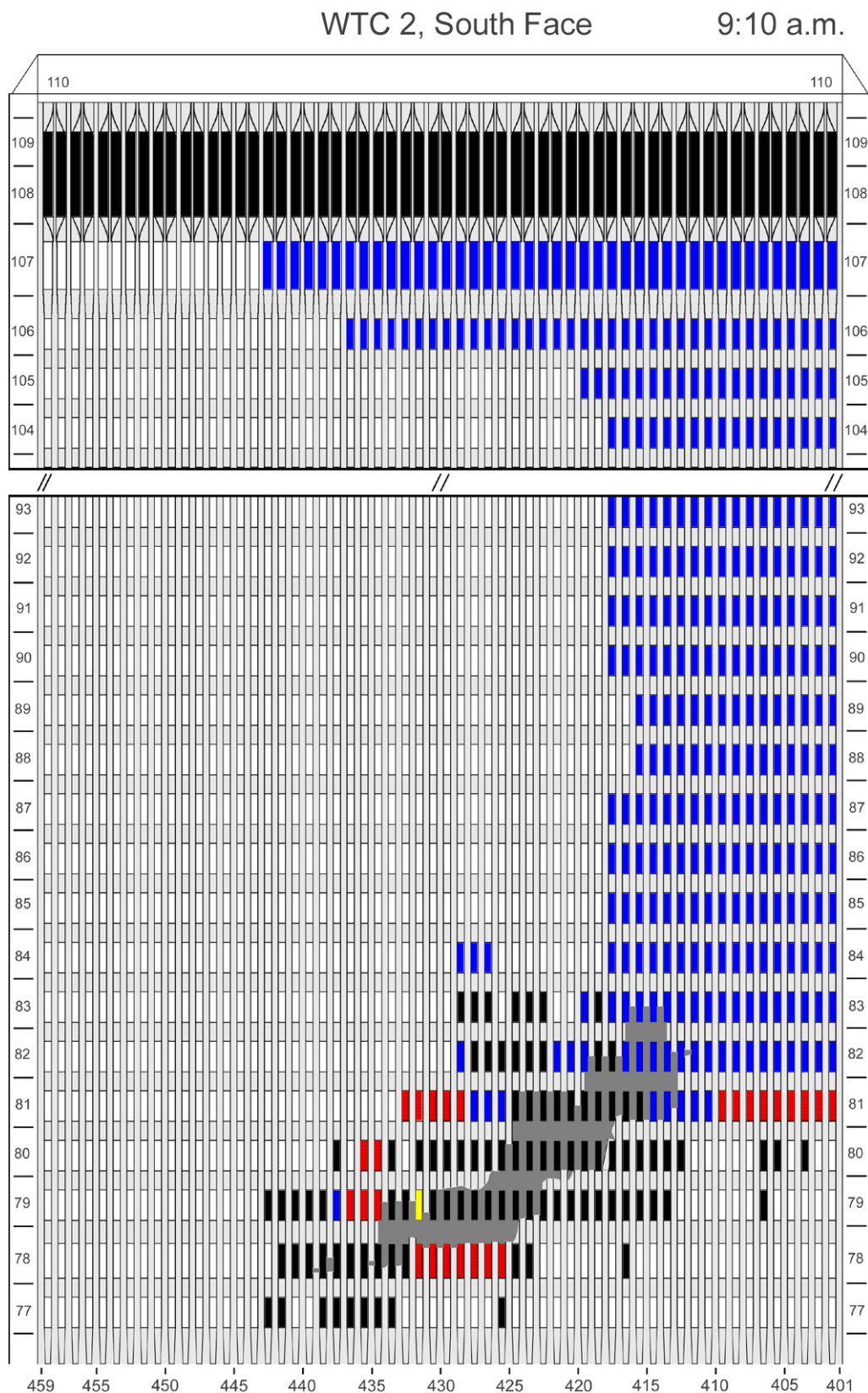


Figure I-9. Diagram of the south face of WTC 2 for floors 77 to 93 and floors 104 to 110 at 9:10 a.m. showing the condition of windows and locations of fires.

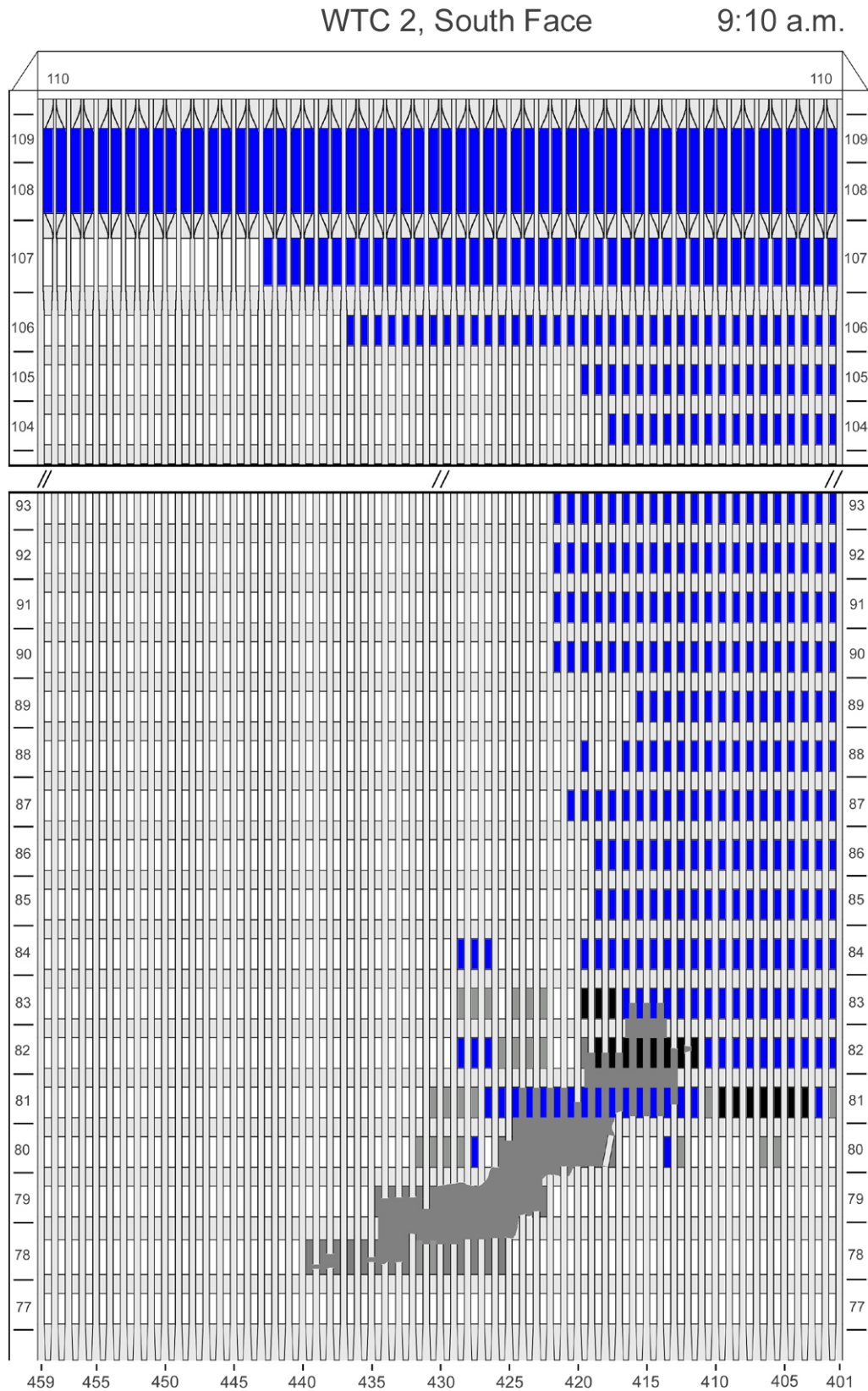


Figure I-10. Diagram of the south face of WTC 2 for floors 77 to 93 and floors 104 to 110 at 9:10 a.m. showing windows where smoke was observed and those hidden from view.

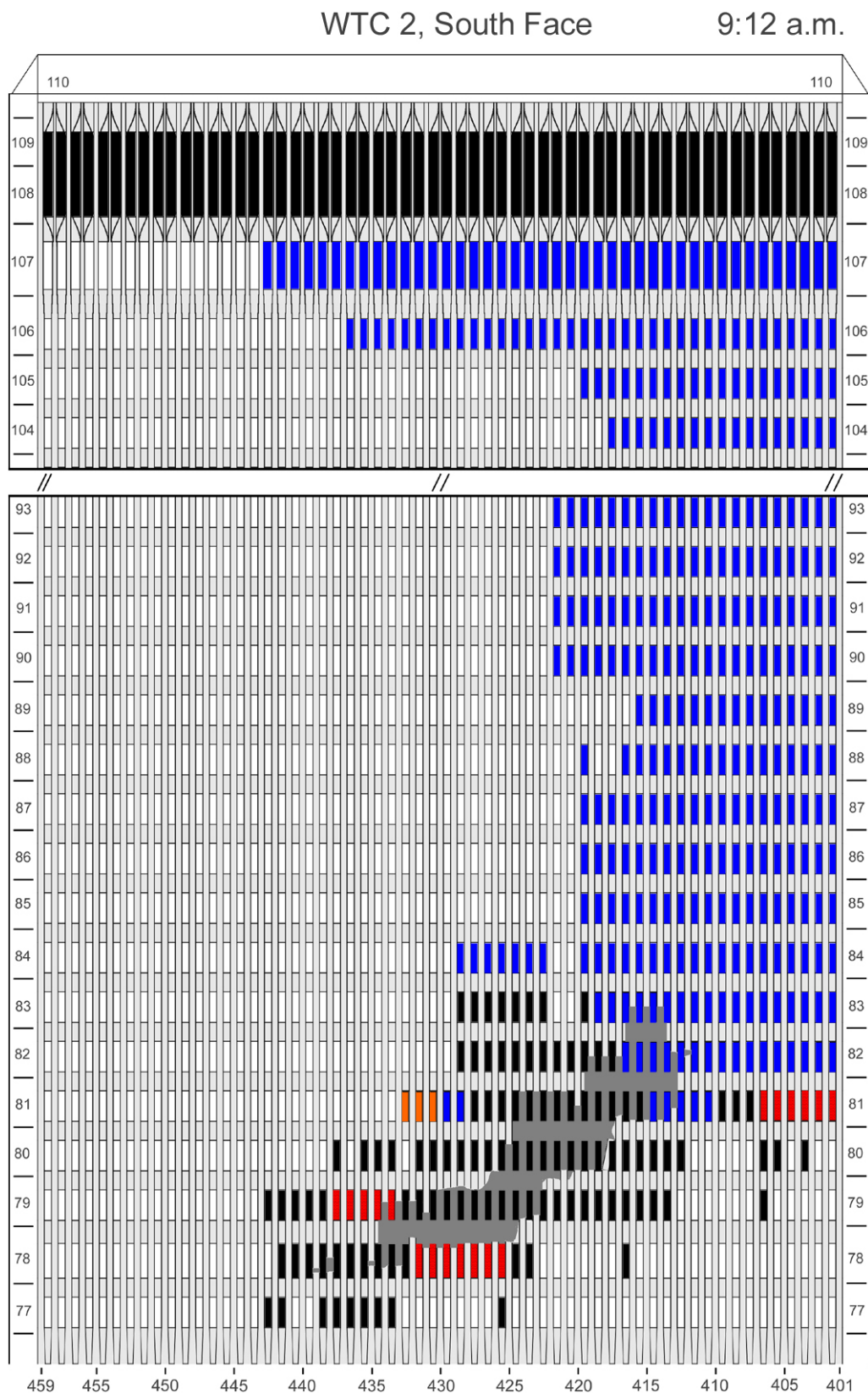


Figure I-11. Diagram of the south face of WTC 2 for floors 77 to 93 and floors 104 to 110 at 9:12 a.m. showing the condition of windows and locations of fires.

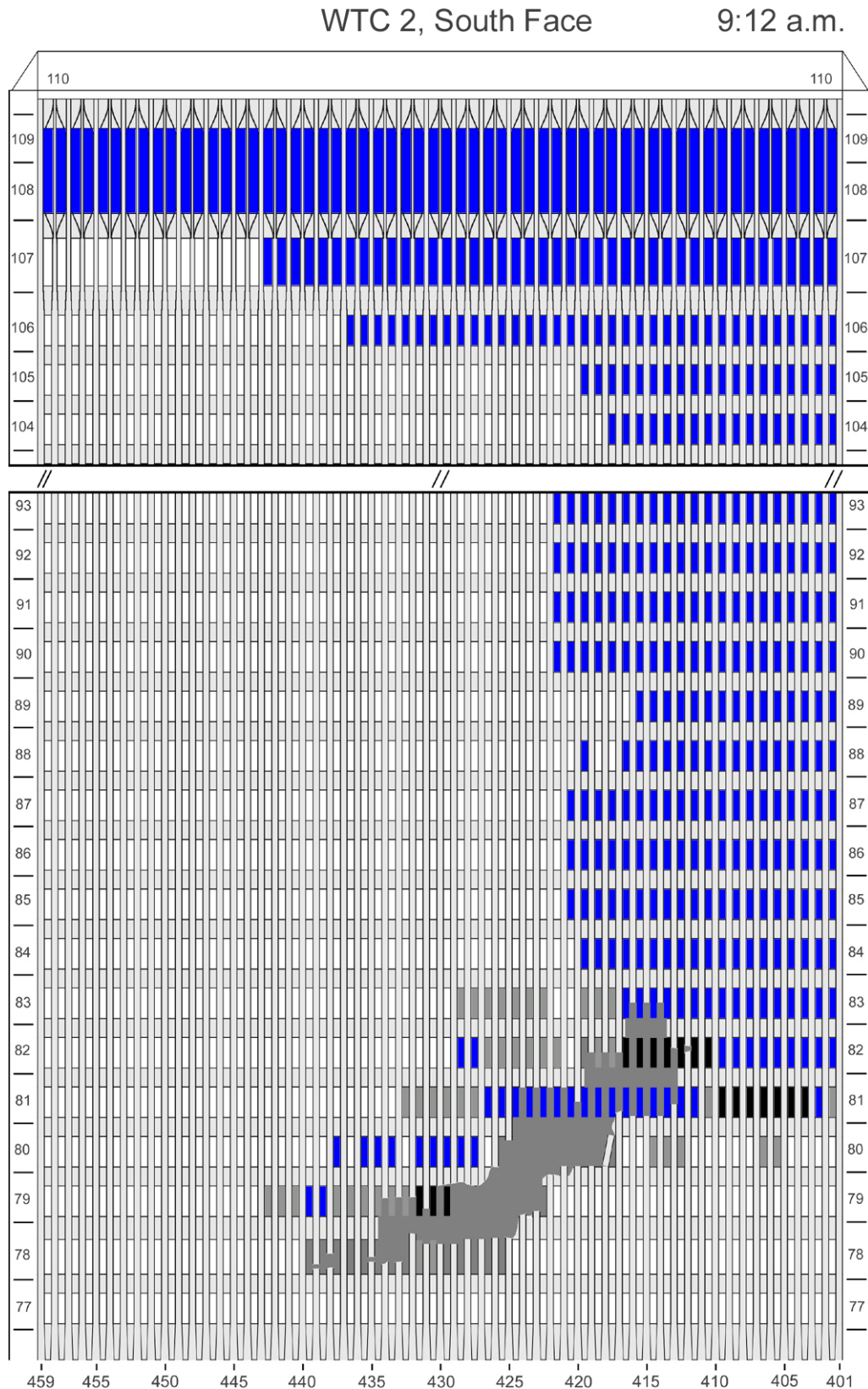


Figure I-12. Diagram of the south face of WTC 2 for floors 77 to 93 and floors 104 to 110 at 9:12 a.m. showing windows where smoke was observed and those hidden from view.

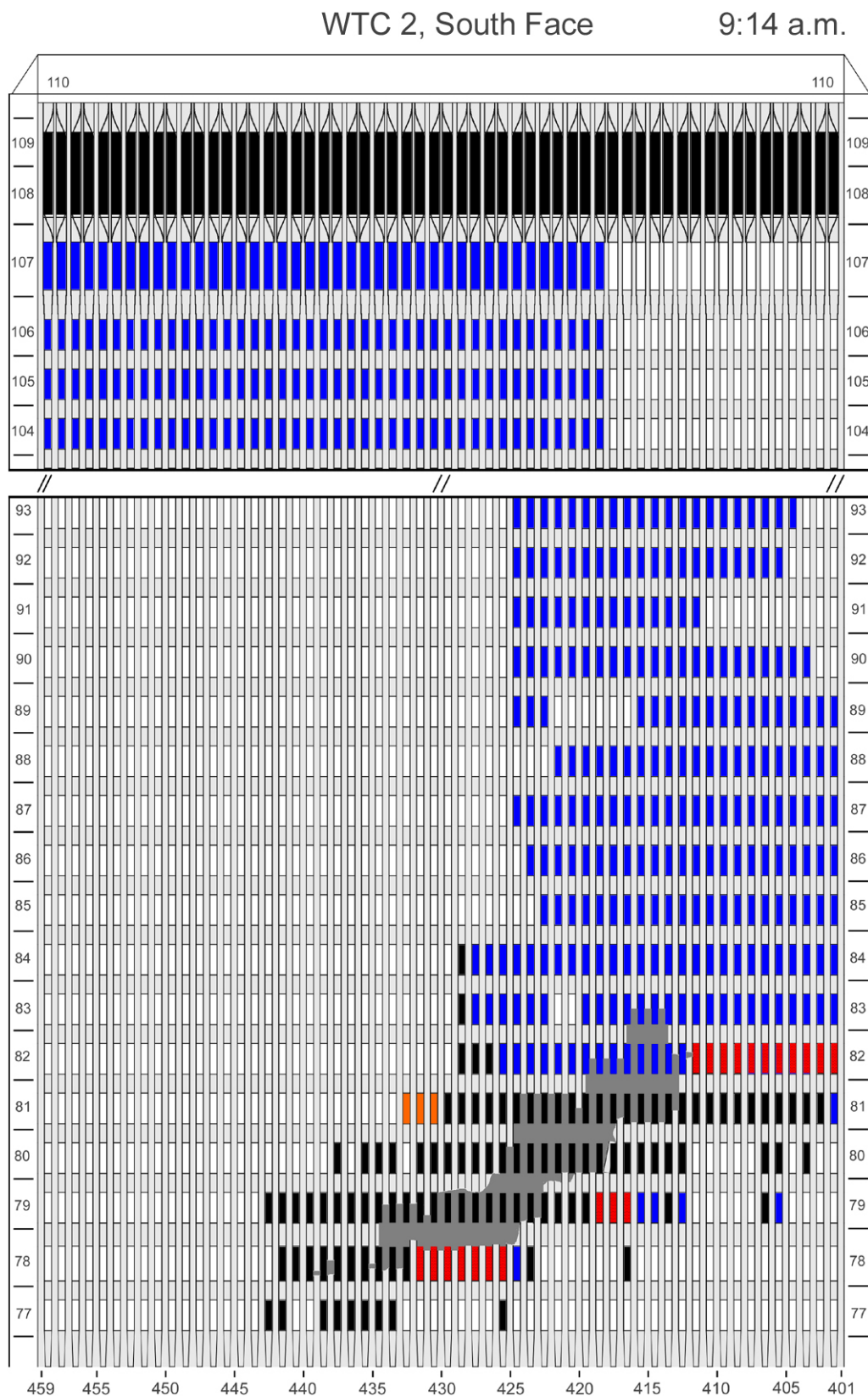


Figure I-13. Diagram of the south face of WTC 2 for floors 77 to 93 and floors 104 to 110 at 9:14 a.m. showing the condition of windows and locations of fires.

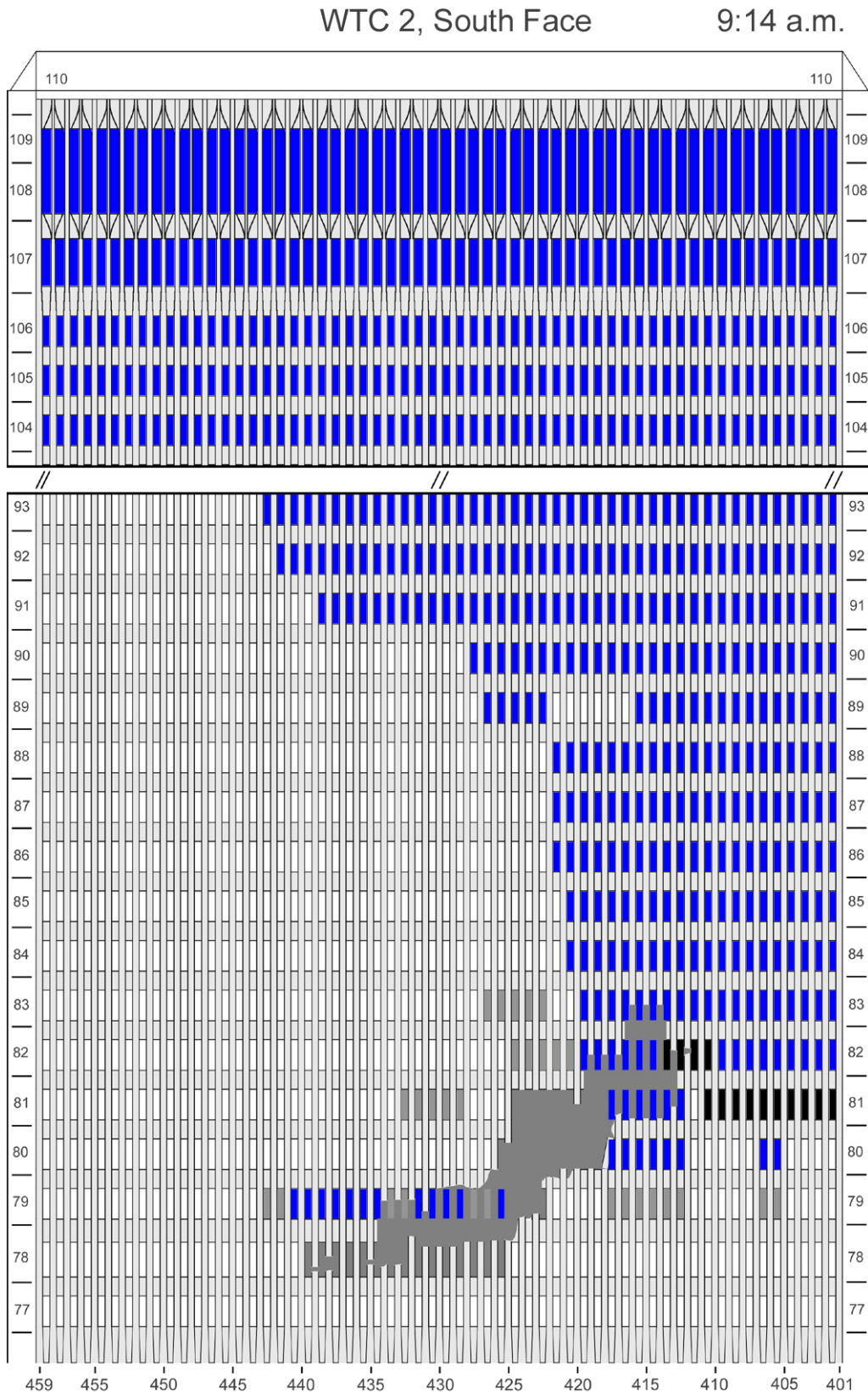


Figure I-14. Diagram of the south face of WTC 2 for floors 77 to 93 and floors 104 to 110 at 9:14 a.m. showing windows where smoke was observed and those hidden from view.

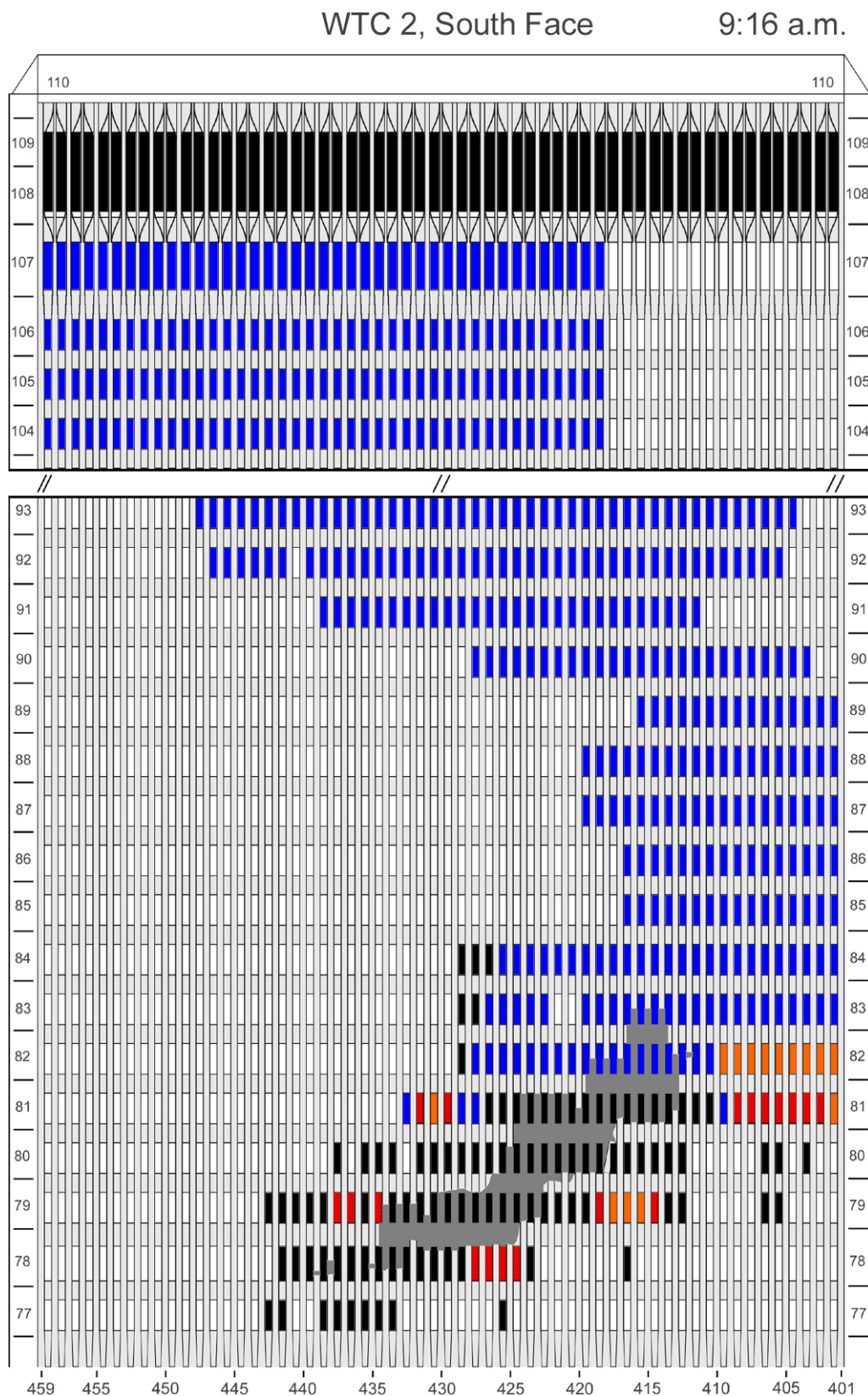


Figure I-15. Diagram of the south face of WTC 2 for floors 77 to 93 and floors 104 to 110 at 9:16 a.m. showing the condition of windows and locations of fires.

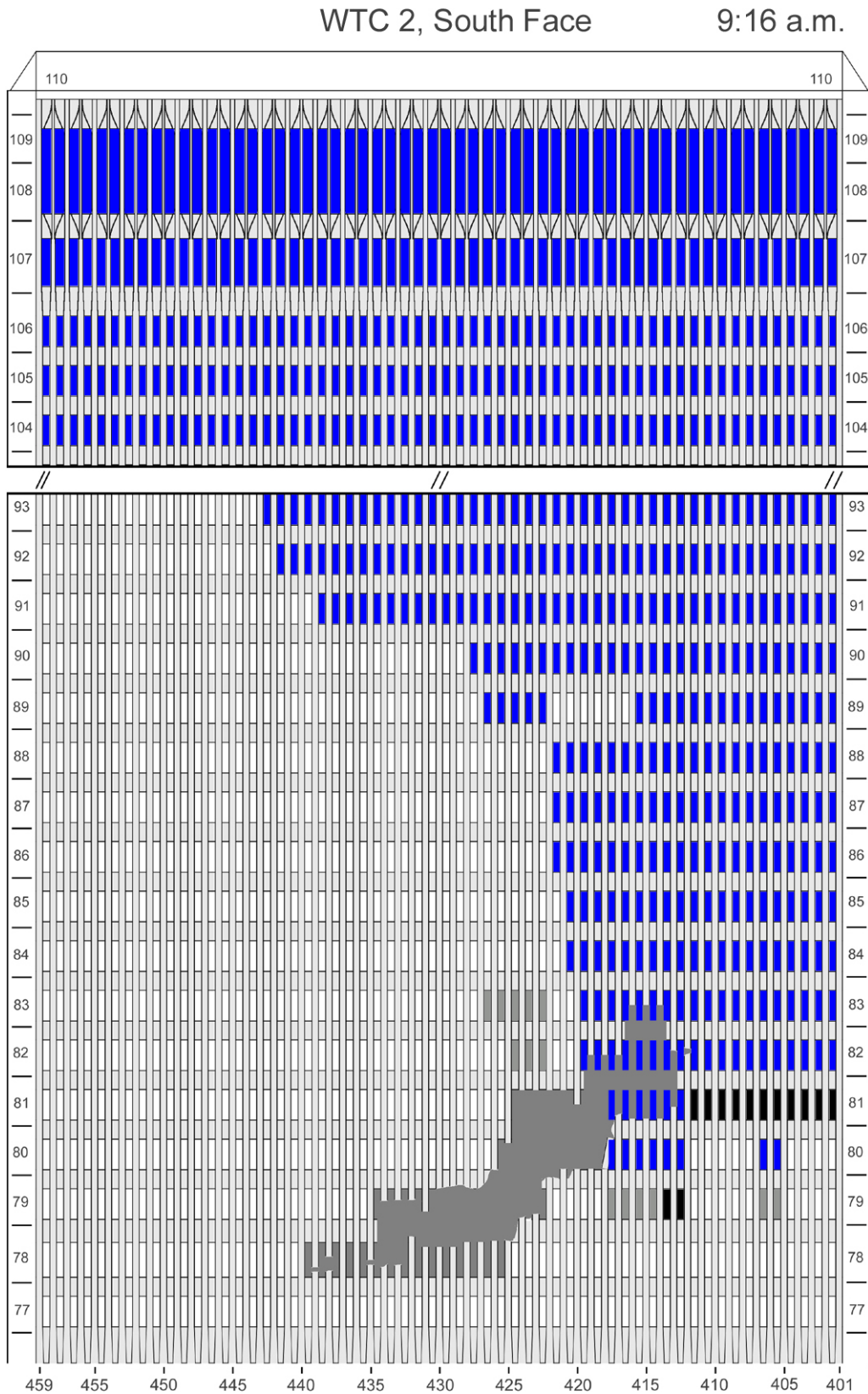


Figure I-16. Diagram of the south face of WTC 2 for floors 77 to 93 and floors 104 to 110 at 9:16 a.m. showing windows where smoke was observed and those hidden from view.

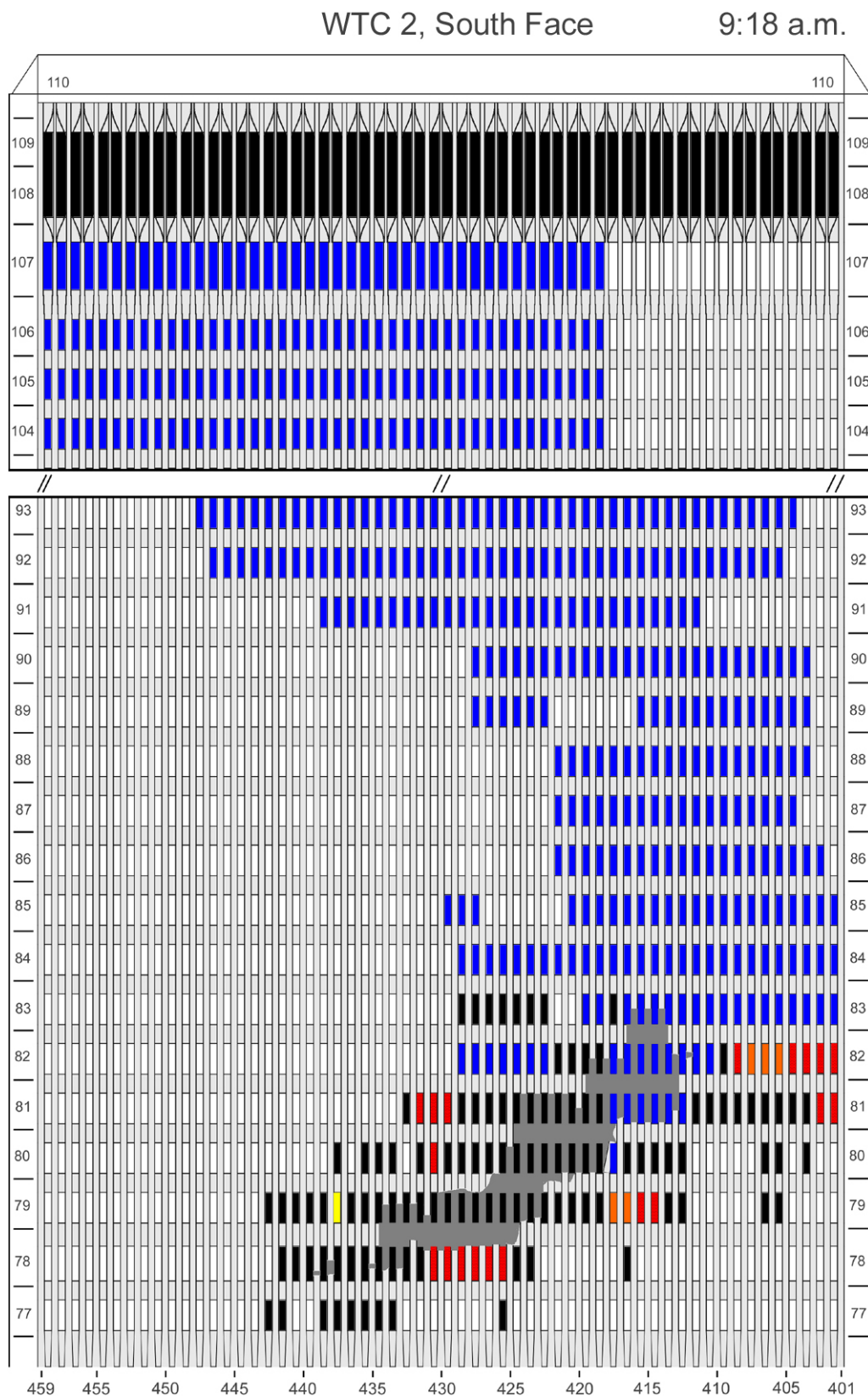


Figure I-17. Diagram of the south face of WTC 2 for floors 77 to 93 and floors 104 to 110 at 9:18 a.m. showing the condition of windows and locations of fires.

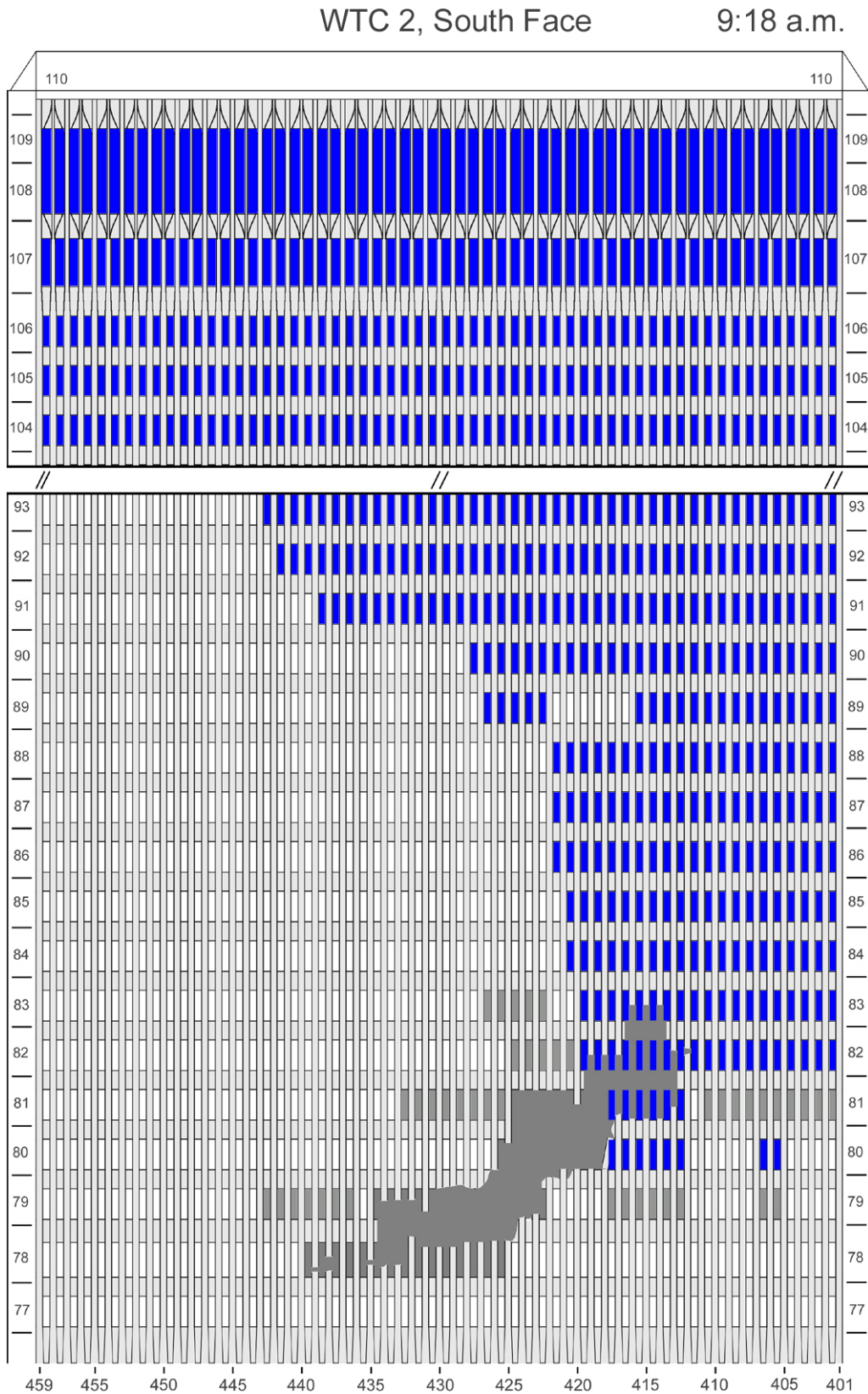


Figure I-18. Diagram of the south face of WTC 2 for floors 77 to 93 and floors 104 to 110 at 9:18 a.m. showing windows where smoke was observed and those hidden from view.

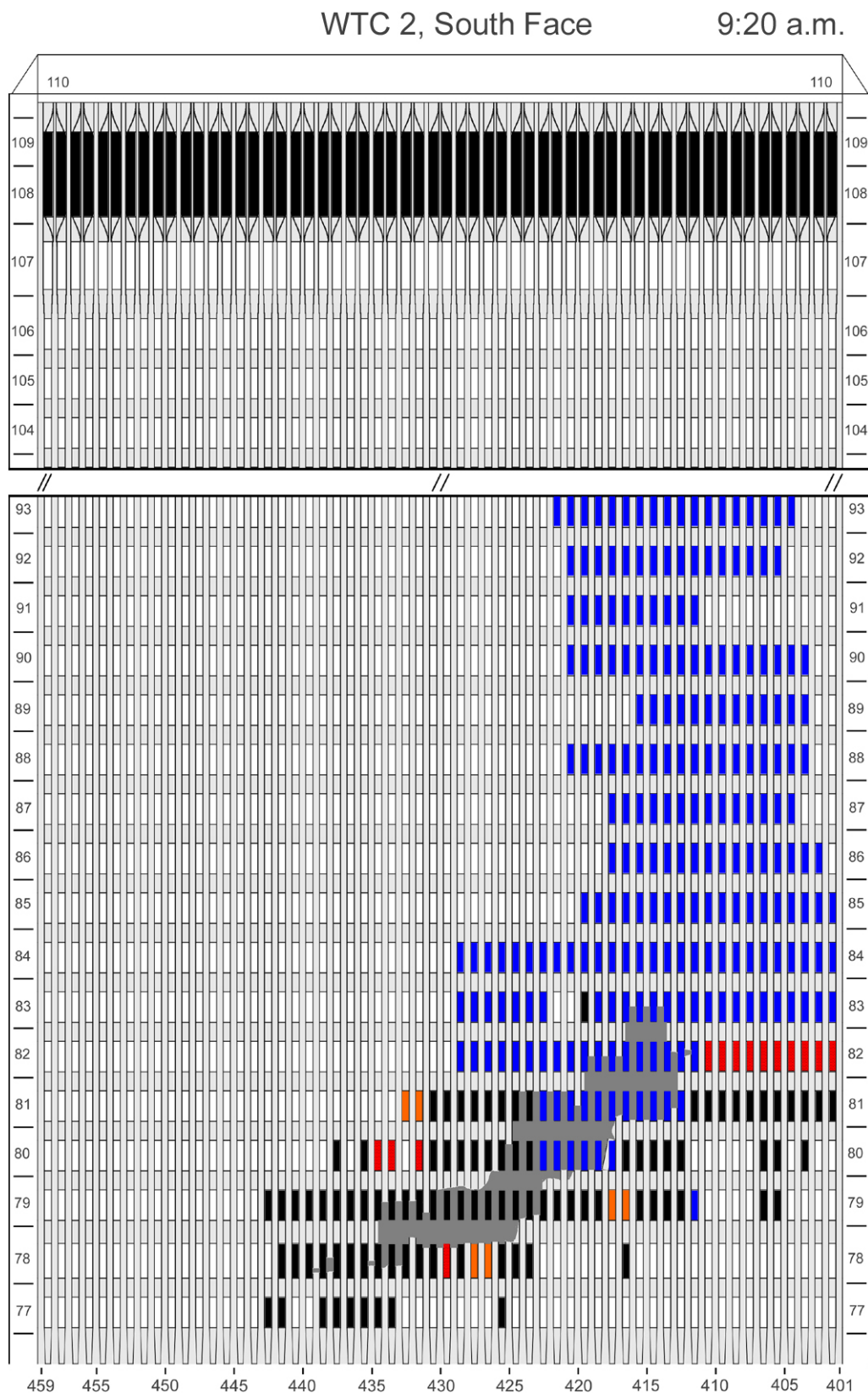


Figure I-19. Diagram of the south face of WTC 2 for floors 77 to 93 and floors 104 to 110 at 9:20 a.m. showing the condition of windows and locations of fires.

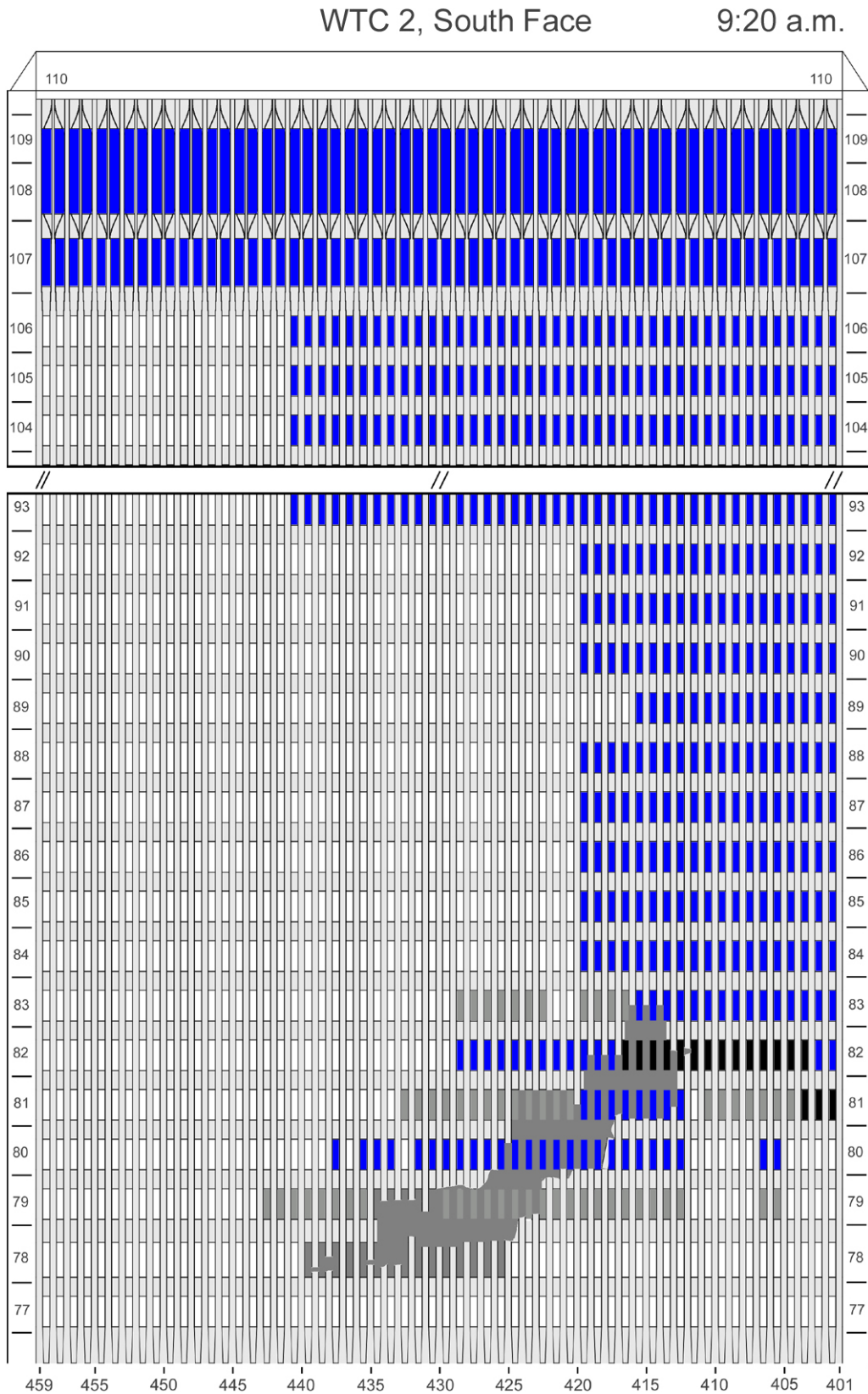


Figure I-20. Diagram of the south face of WTC 2 for floors 77 to 93 and floors 104 to 110 at 9:20 a.m. showing windows where smoke was observed and those hidden from view.

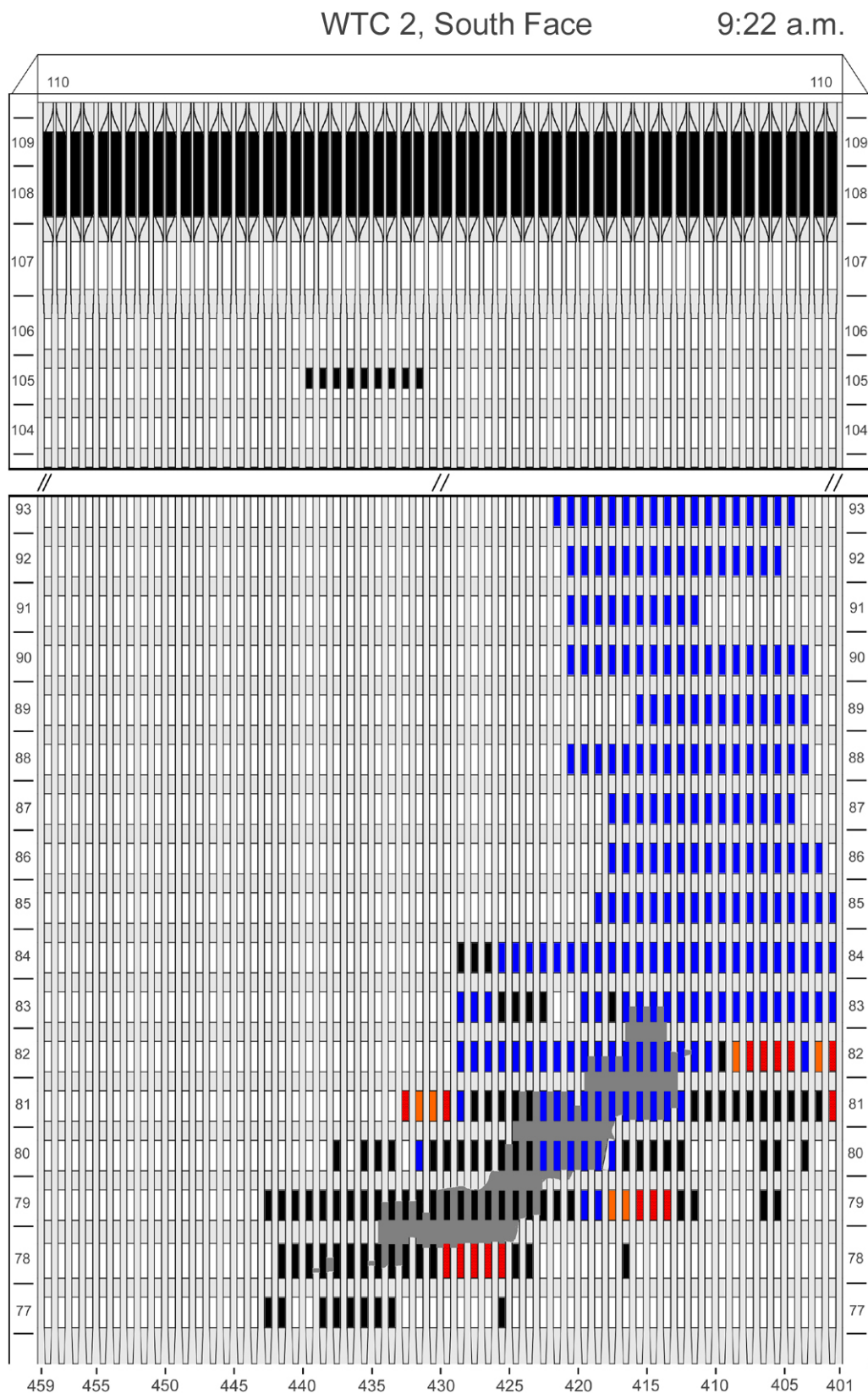


Figure I-21. Diagram of the south face of WTC 2 for floors 77 to 93 and floors 104 to 110 at 9:22 a.m. showing the condition of windows and locations of fires.

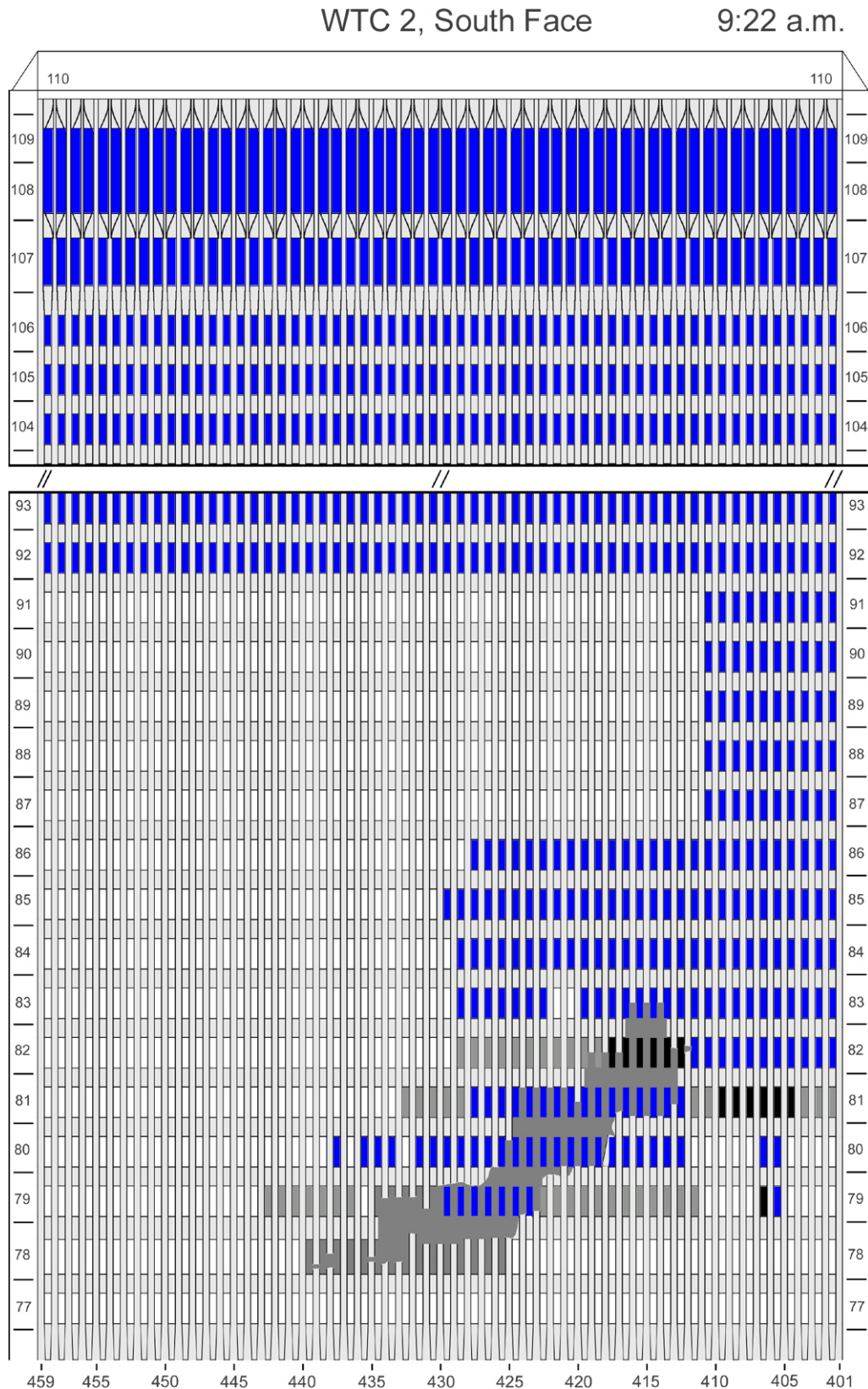


Figure I-22. Diagram of the south face of WTC 2 for floors 77 to 93 and floors 104 to 110 at 9:22 a.m. showing windows where smoke was observed and those hidden from view.

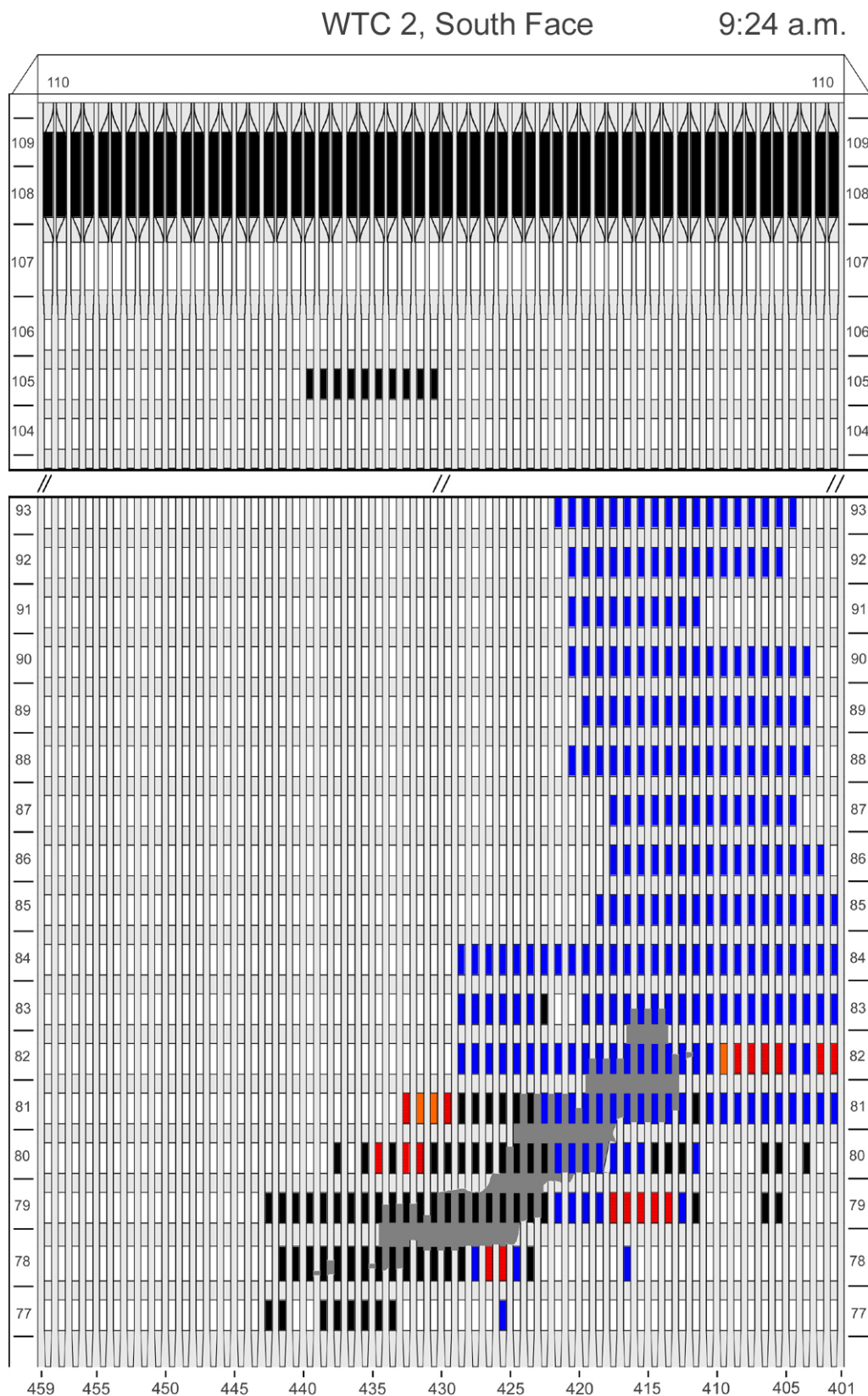


Figure I-23. Diagram of the south face of WTC 2 for floors 77 to 93 and floors 104 to 110 at 9:24 a.m. showing the condition of windows and locations of fires.

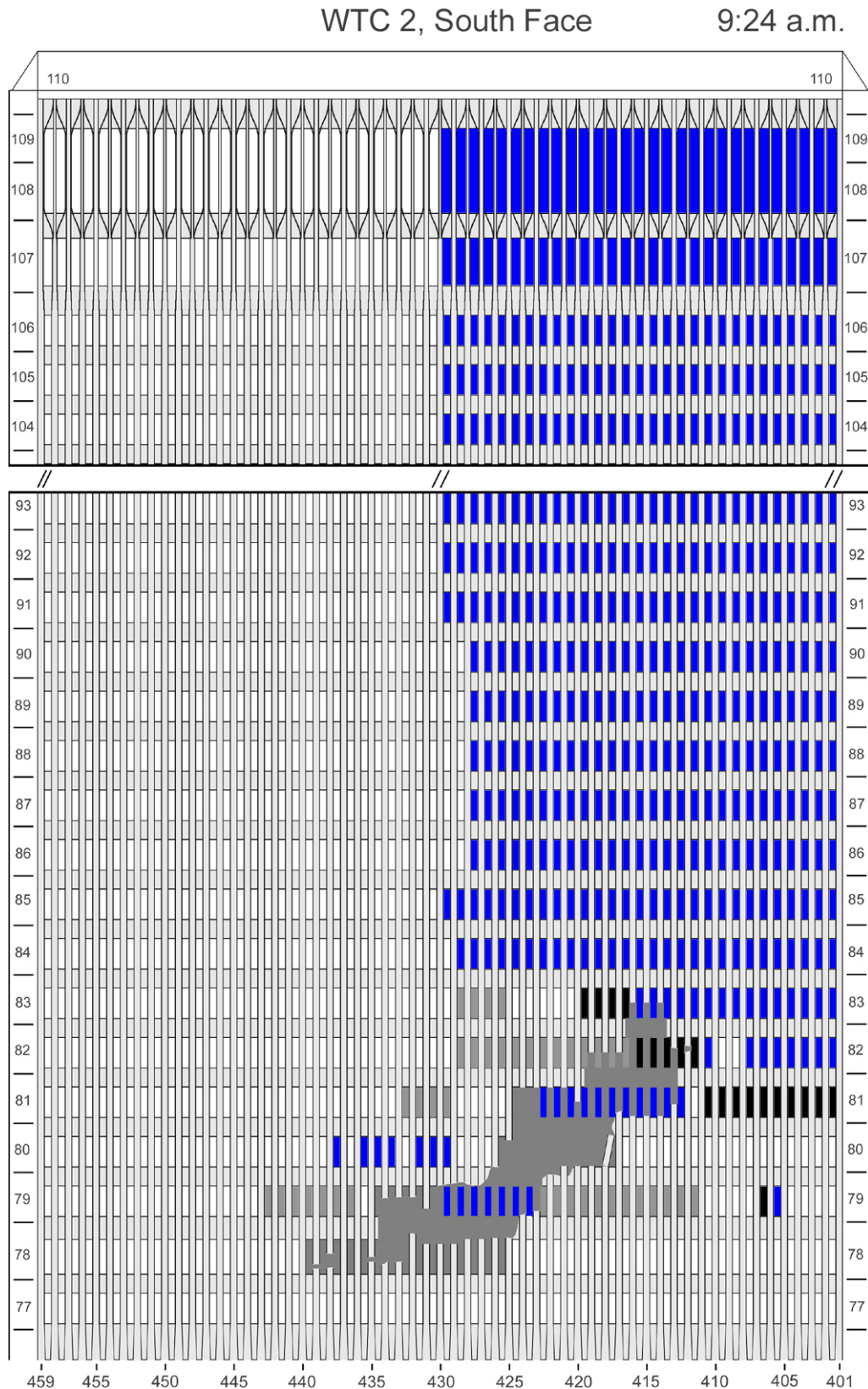


Figure I-24. Diagram of the south face of WTC 2 for floors 77 to 93 and floors 104 to 110 at 9:24 a.m. showing windows where smoke was observed and those hidden from view.

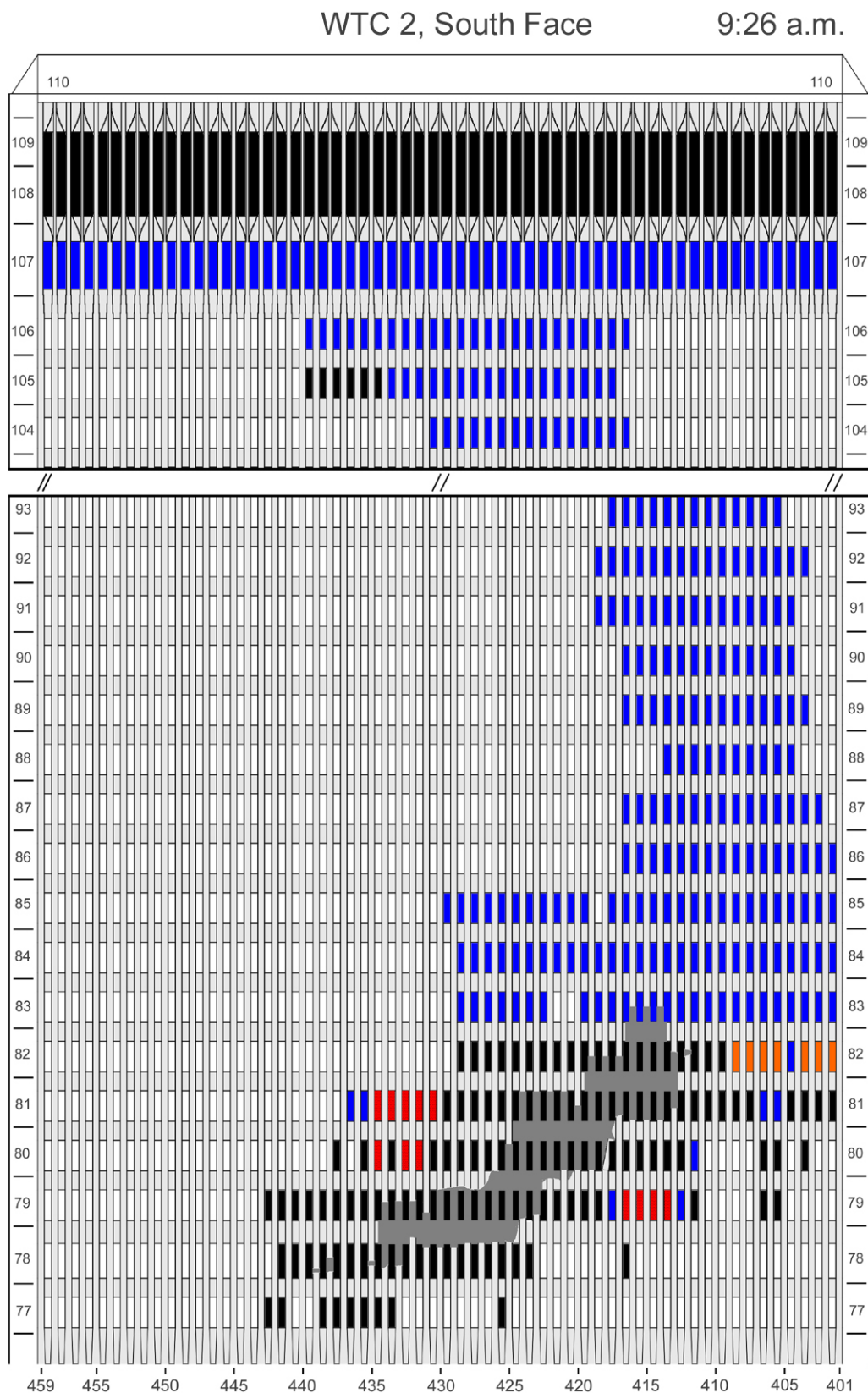


Figure I-25. Diagram of the south face of WTC 2 for floors 77 to 93 and floors 104 to 110 at 9:26 a.m. showing the condition of windows and locations of fires.

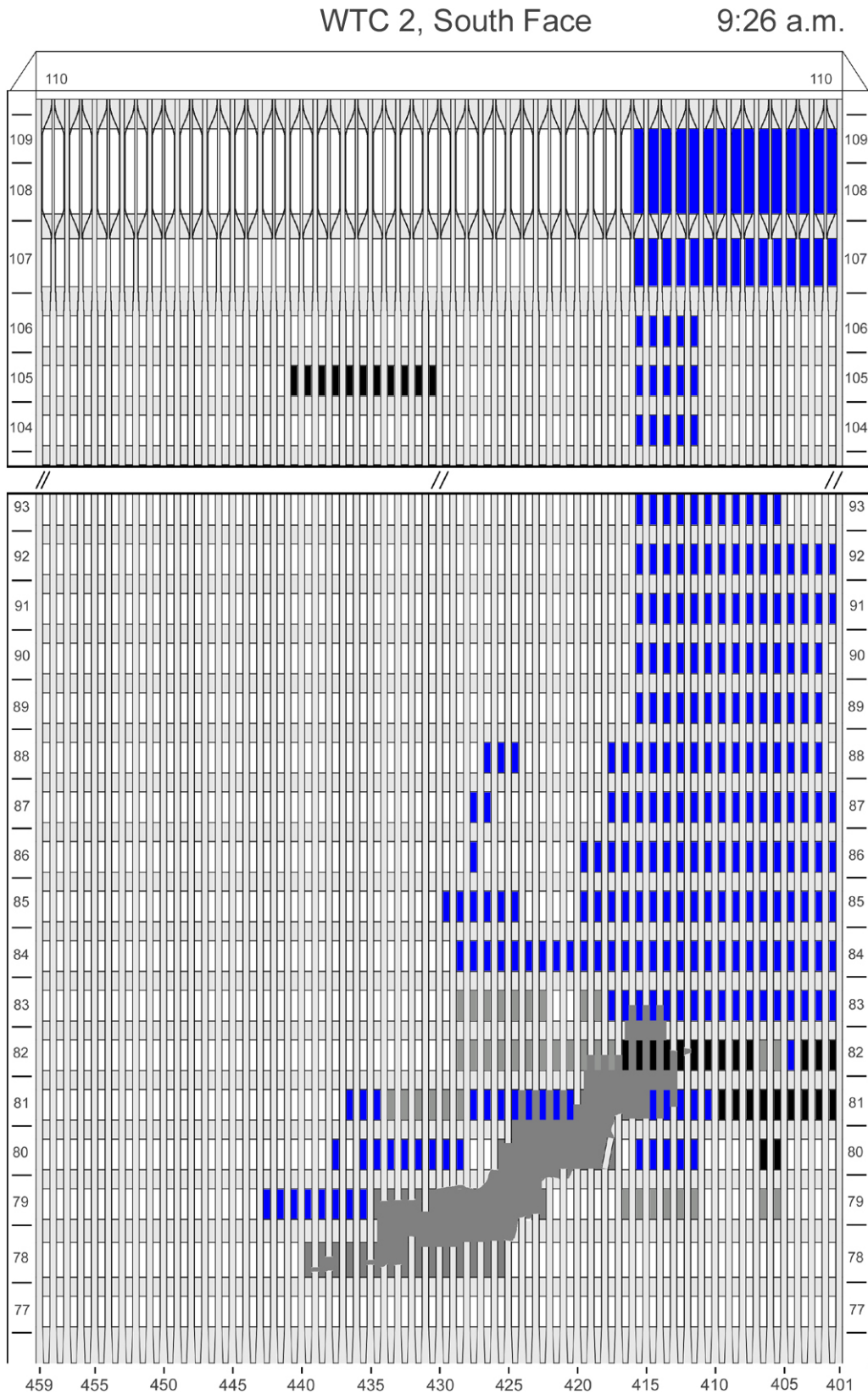


Figure I-26. Diagram of the south face of WTC 2 for floors 77 to 93 and floors 104 to 110 at 9:26 a.m. showing windows where smoke was observed and those hidden from view.

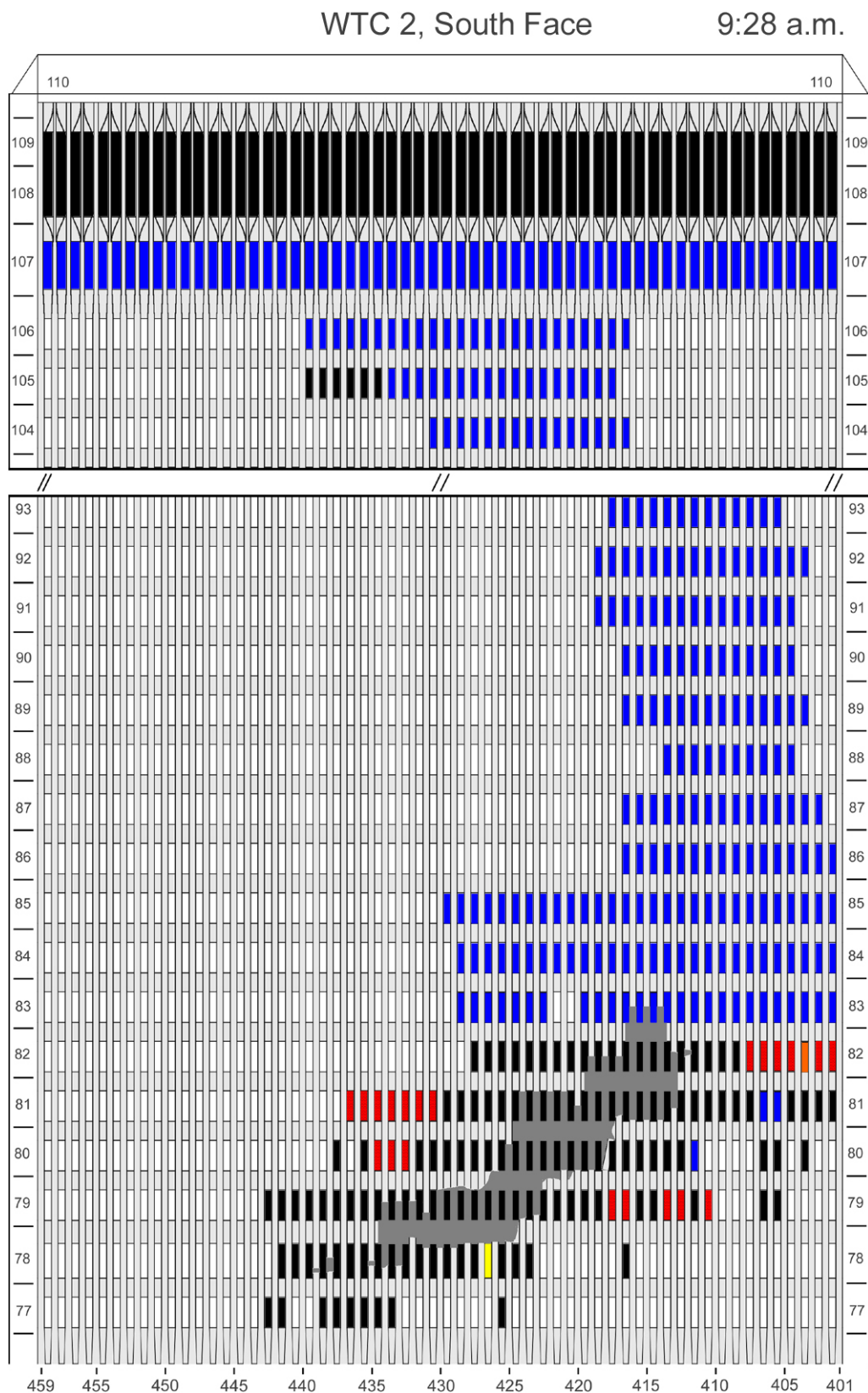


Figure I-27. Diagram of the south face of WTC 2 for floors 77 to 93 and floors 104 to 110 at 9:28 a.m. showing the condition of windows and locations of fires.

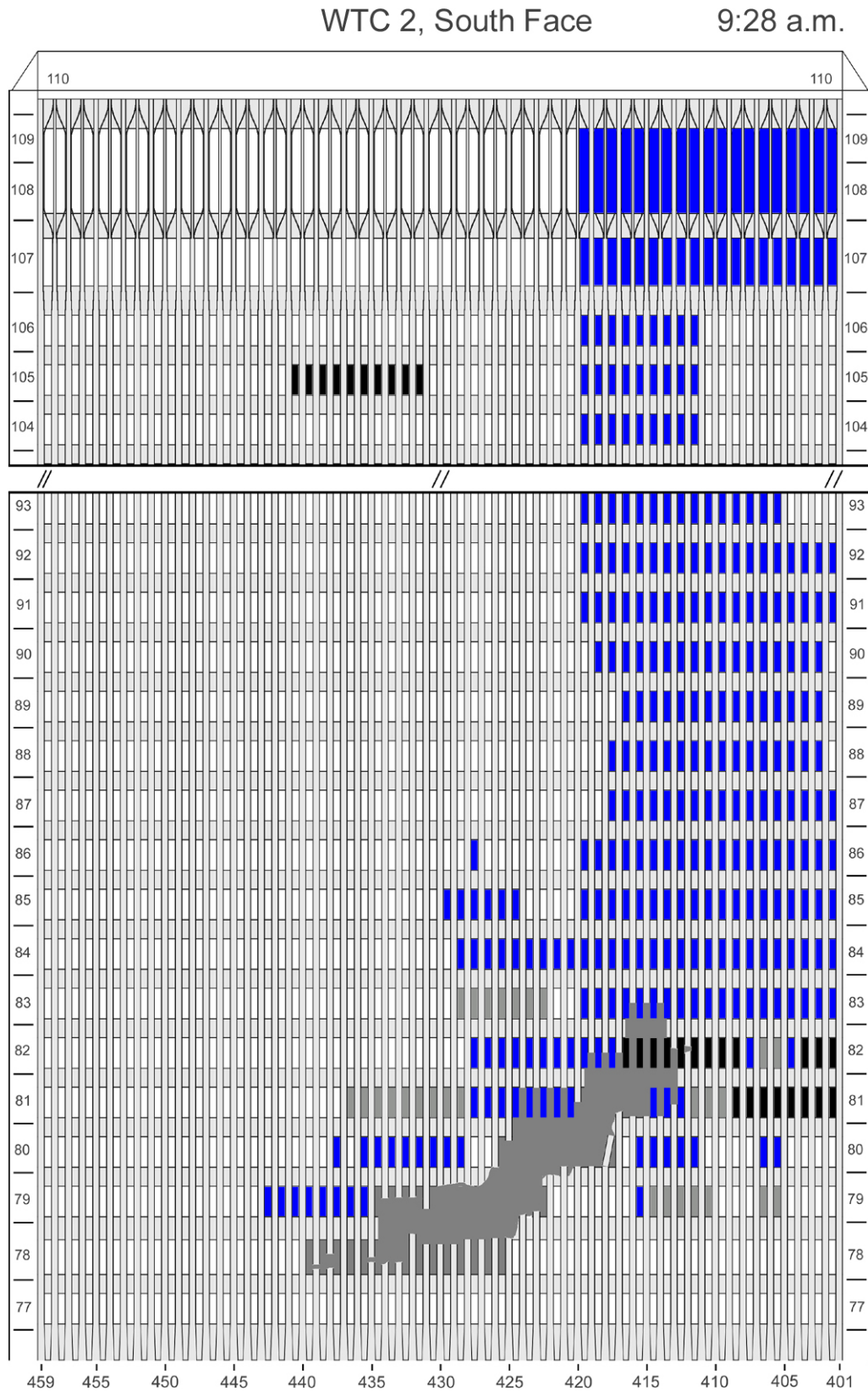


Figure I-28. Diagram of the south face of WTC 2 for floors 77 to 93 and floors 104 to 110 at 9:28 a.m. showing windows where smoke was observed and those hidden from view.

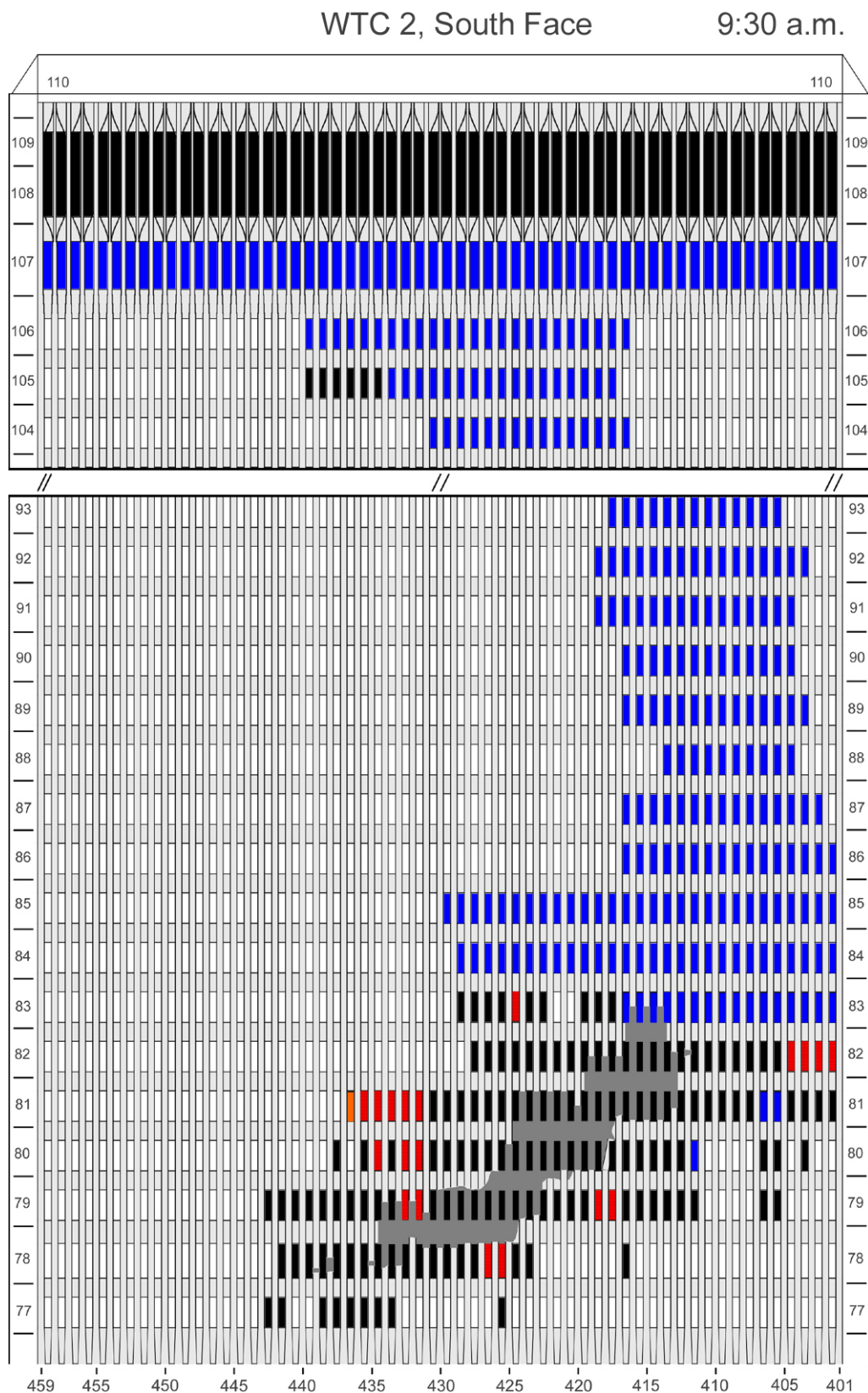


Figure I-29. Diagram of the south face of WTC 2 for floors 77 to 93 and floors 104 to 110 at 9:30 a.m. showing the condition of windows and locations of fires.

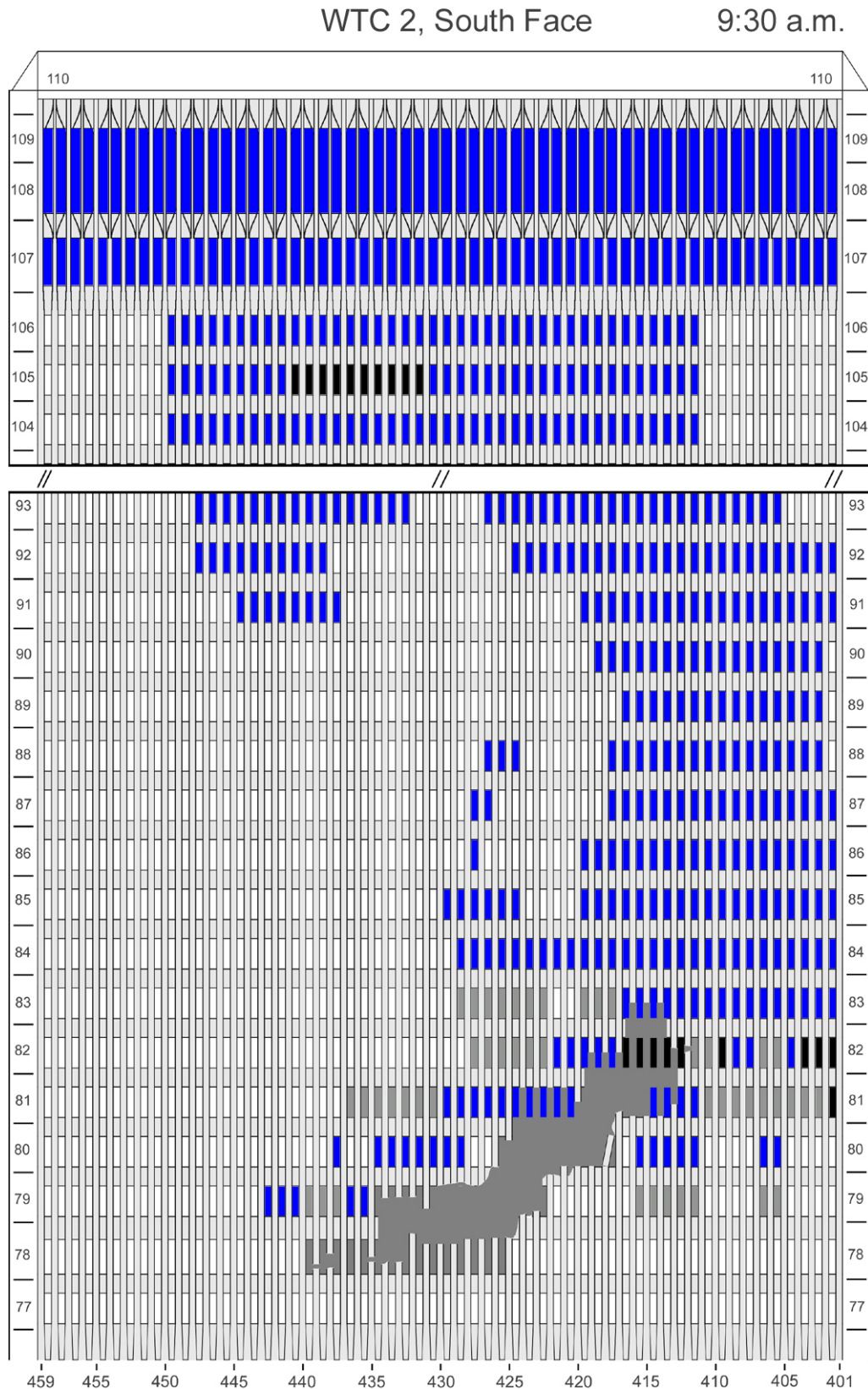


Figure I-30. Diagram of the south face of WTC 2 for floors 77 to 93 and floors 104 to 110 at 9:30 a.m. showing windows where smoke was observed and those hidden from view.

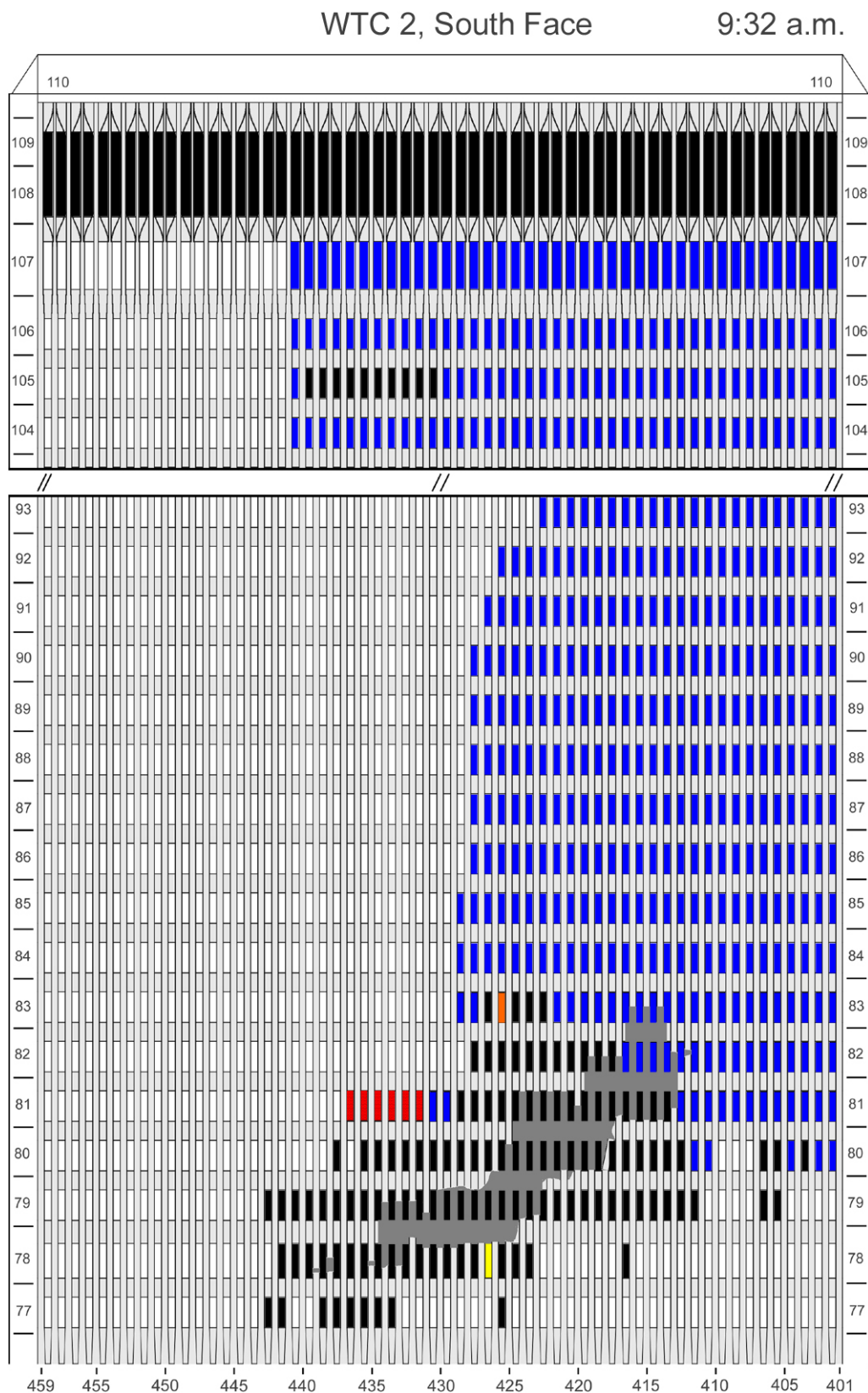


Figure I-31. Diagram of the south face of WTC 2 for floors 77 to 93 and floors 104 to 110 at 9:32 a.m. showing the condition of windows and locations of fires.

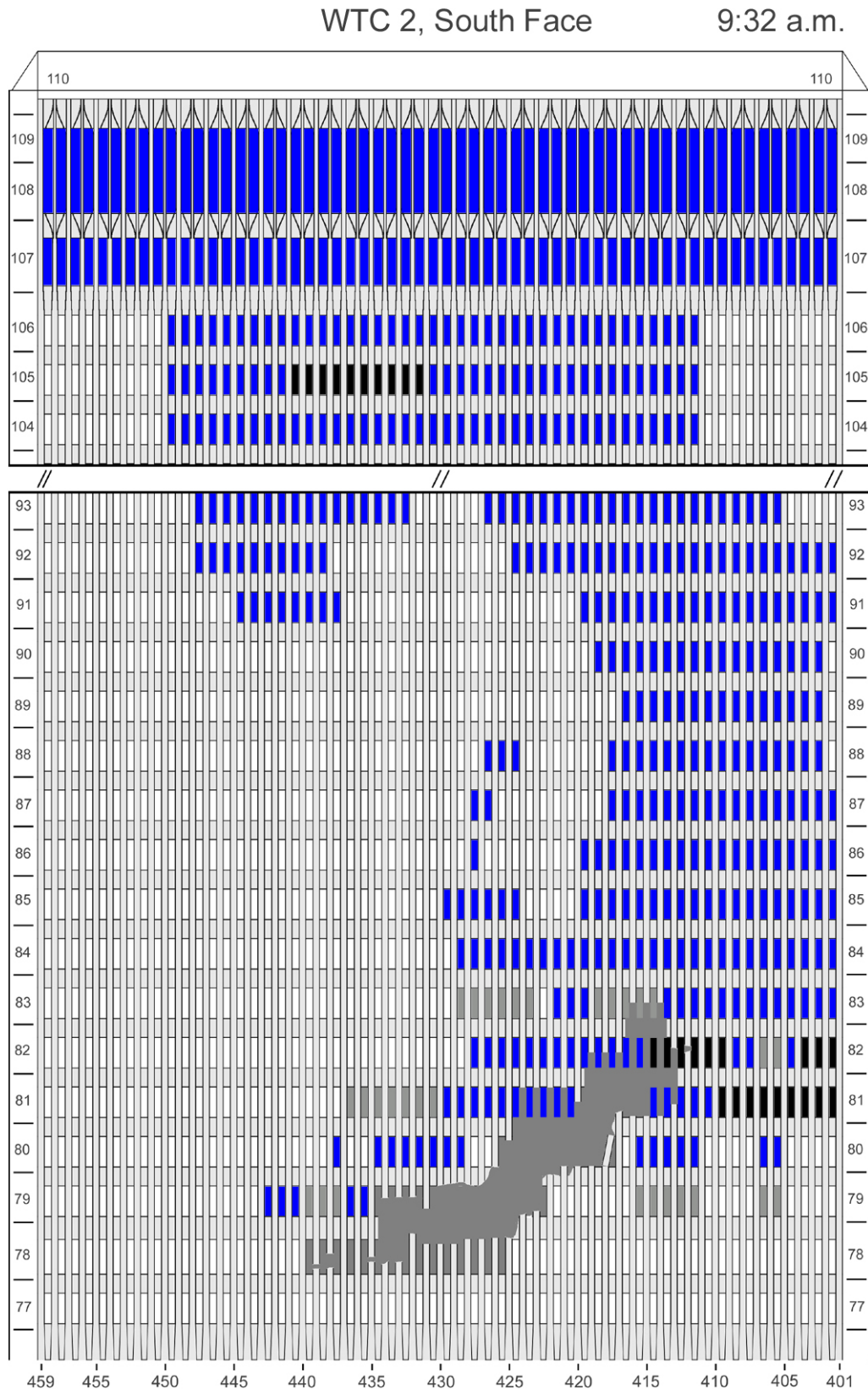


Figure I-32. Diagram of the south face of WTC 2 for floors 77 to 93 and floors 104 to 110 at 9:32 a.m. showing windows where smoke was observed and those hidden from view.

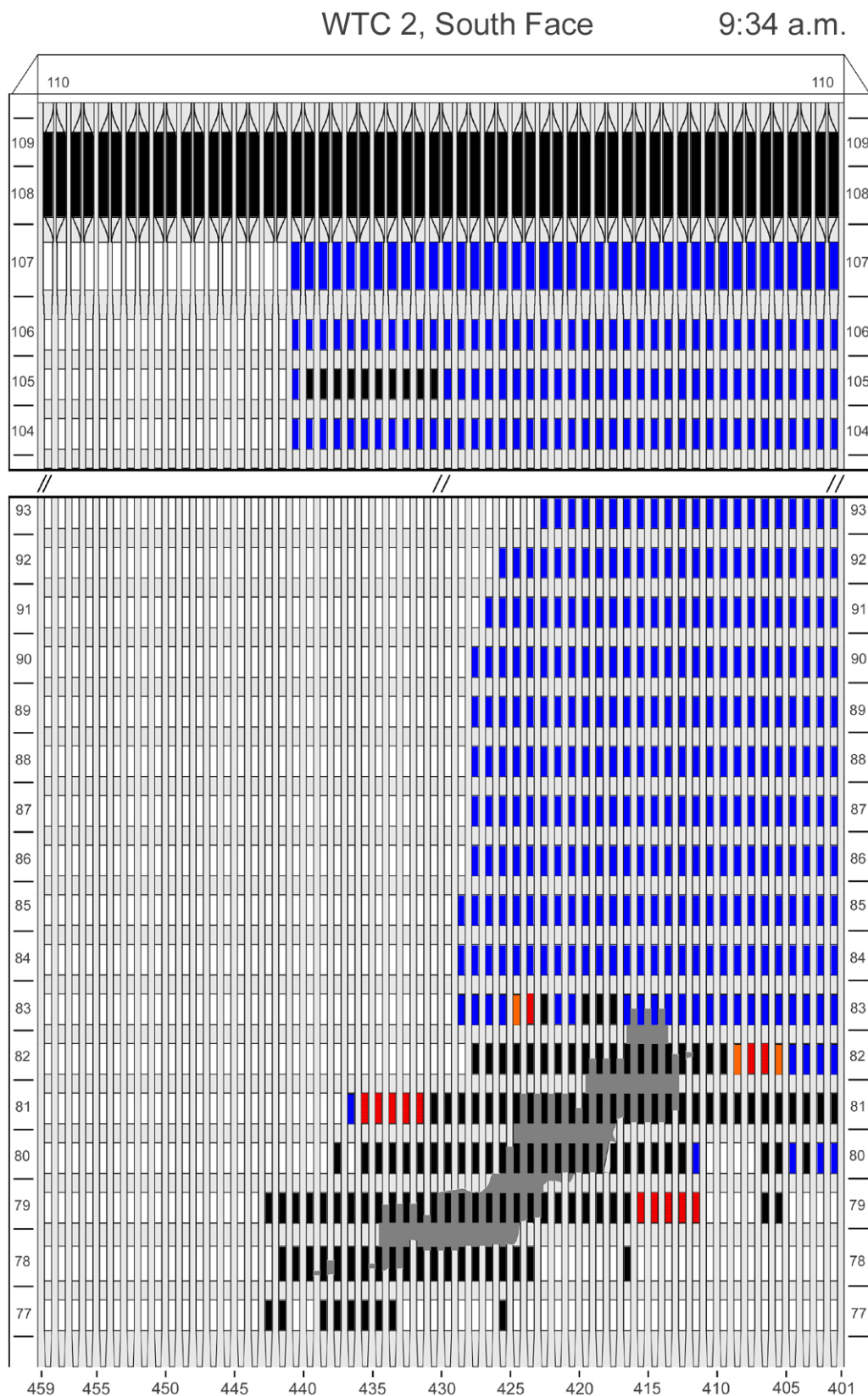


Figure I-33. Diagram of the south face of WTC 2 for floors 77 to 93 and floors 104 to 110 at 9:34 a.m. showing the condition of windows and locations of fires.

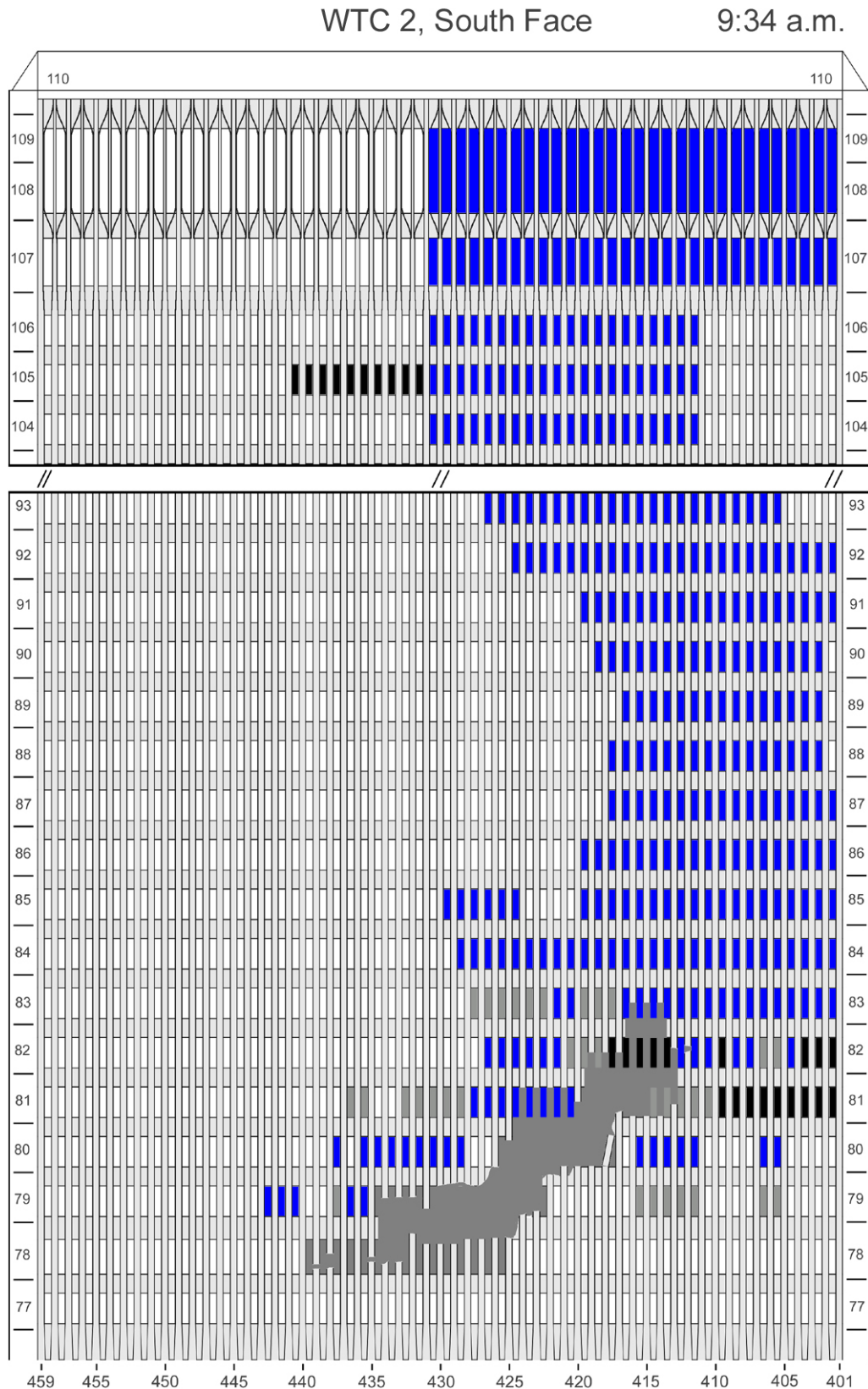


Figure I-34. Diagram of the south face of WTC 2 for floors 77 to 93 and floors 104 to 110 at 9:34 a.m. showing windows where smoke was observed and those hidden from view.

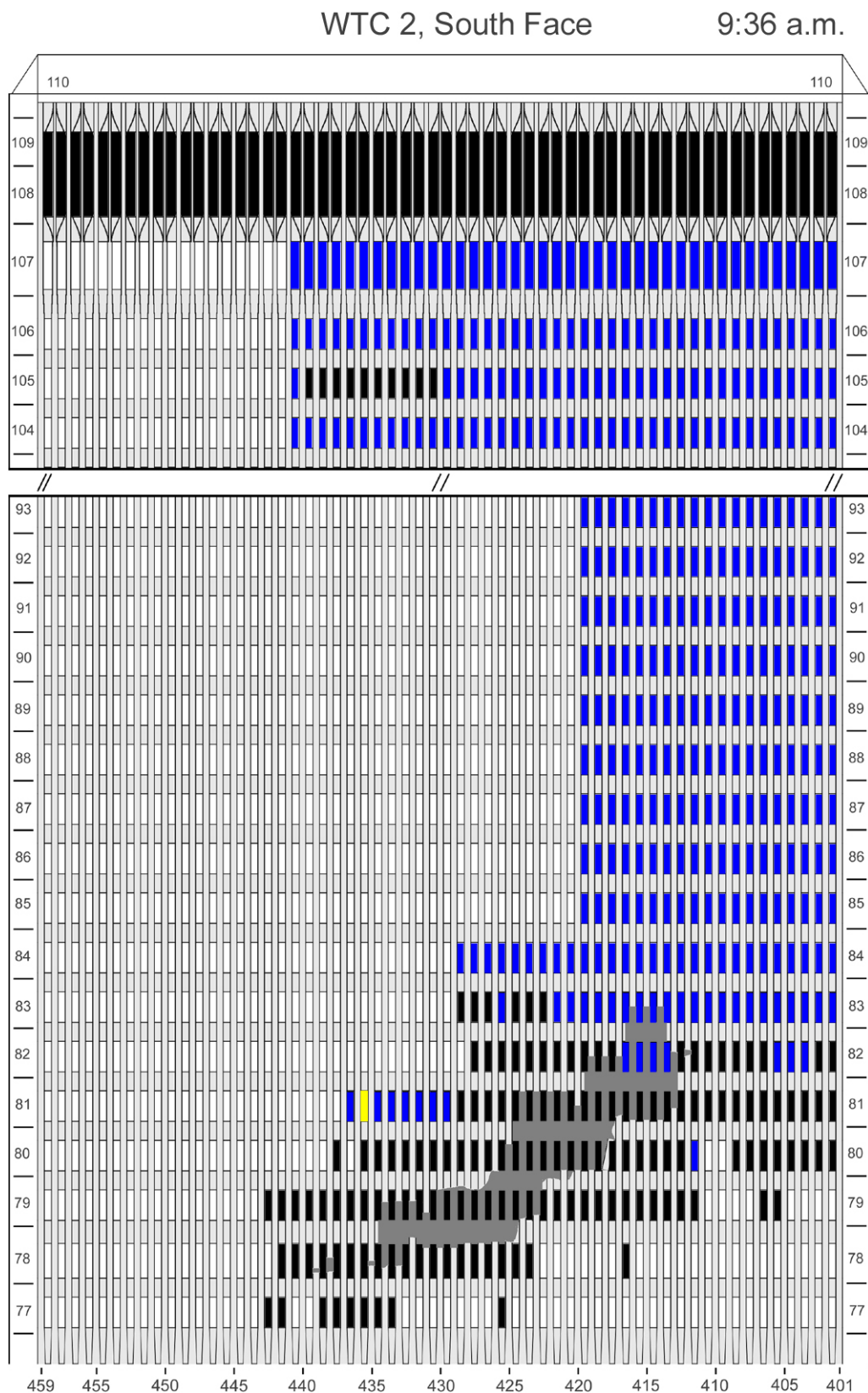


Figure I-35. Diagram of the south face of WTC 2 for floors 77 to 93 and floors 104 to 110 at 9:36 a.m. showing the condition of windows and locations of fires.

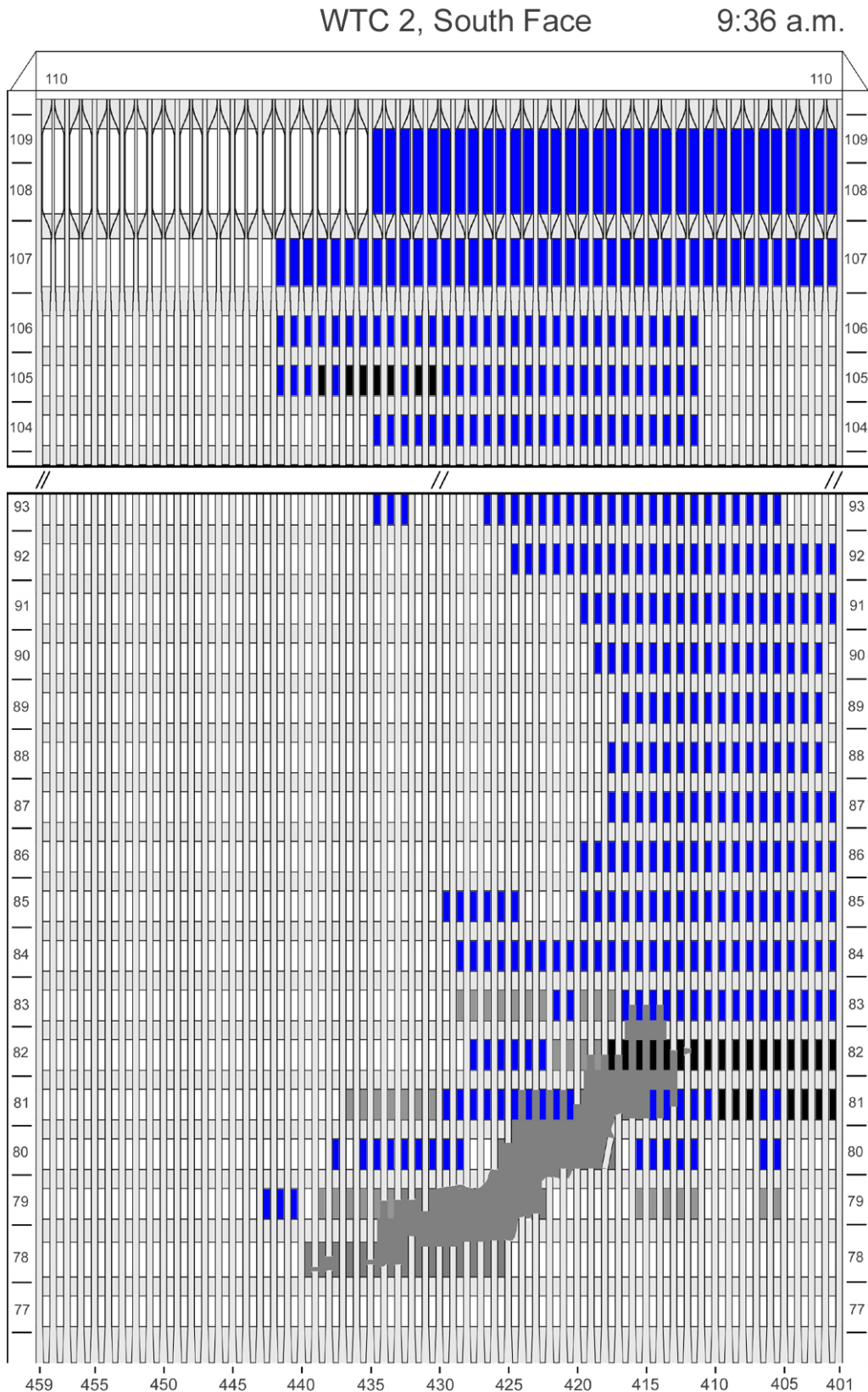


Figure I-36. Diagram of the south face of WTC 2 for floors 77 to 93 and floors 104 to 110 at 9:36 a.m. showing windows where smoke was observed and those hidden from view.

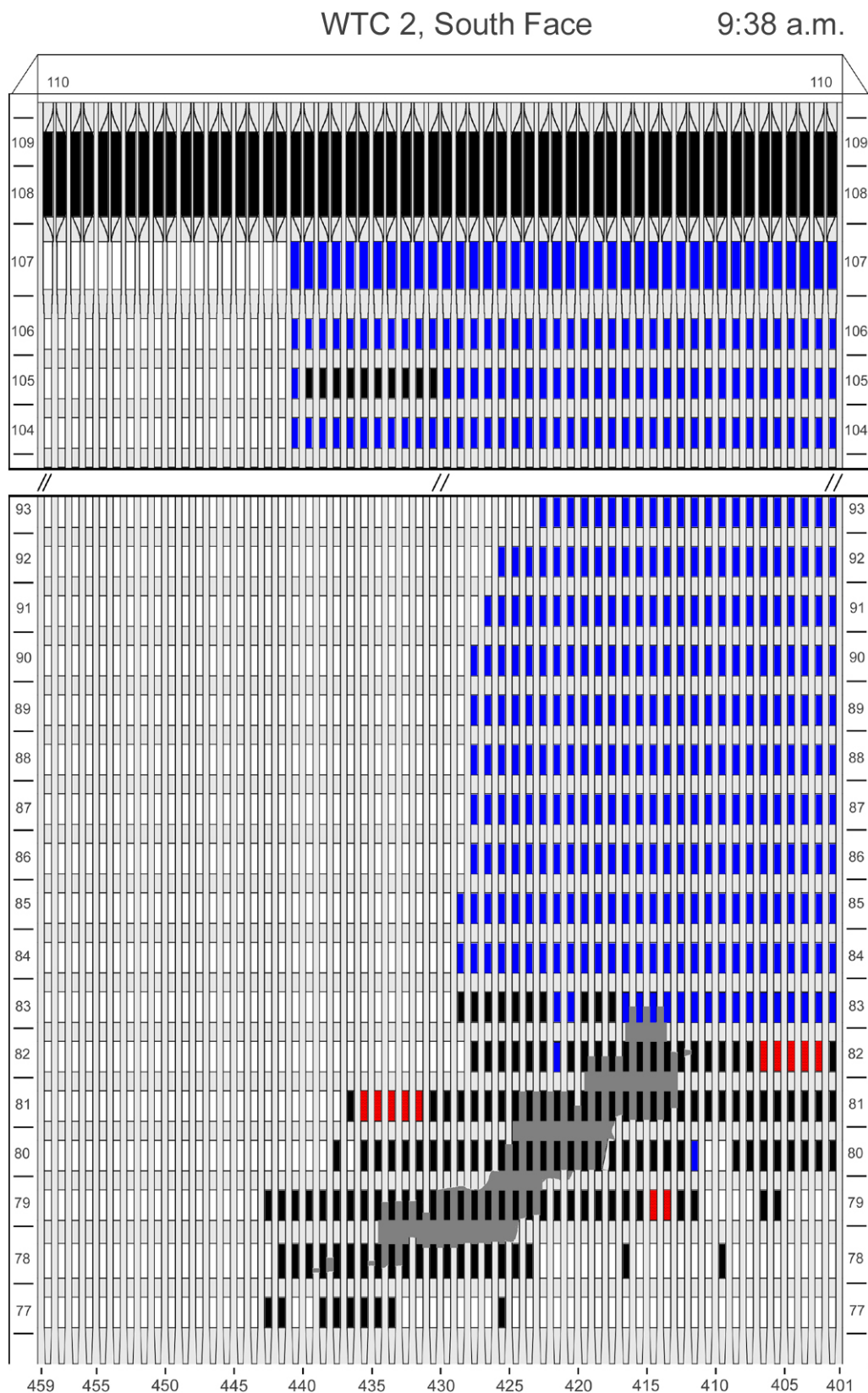


Figure I-37. Diagram of the south face of WTC 2 for floors 77 to 93 and floors 104 to 110 at 9:38 a.m. showing the condition of windows and locations of fires.

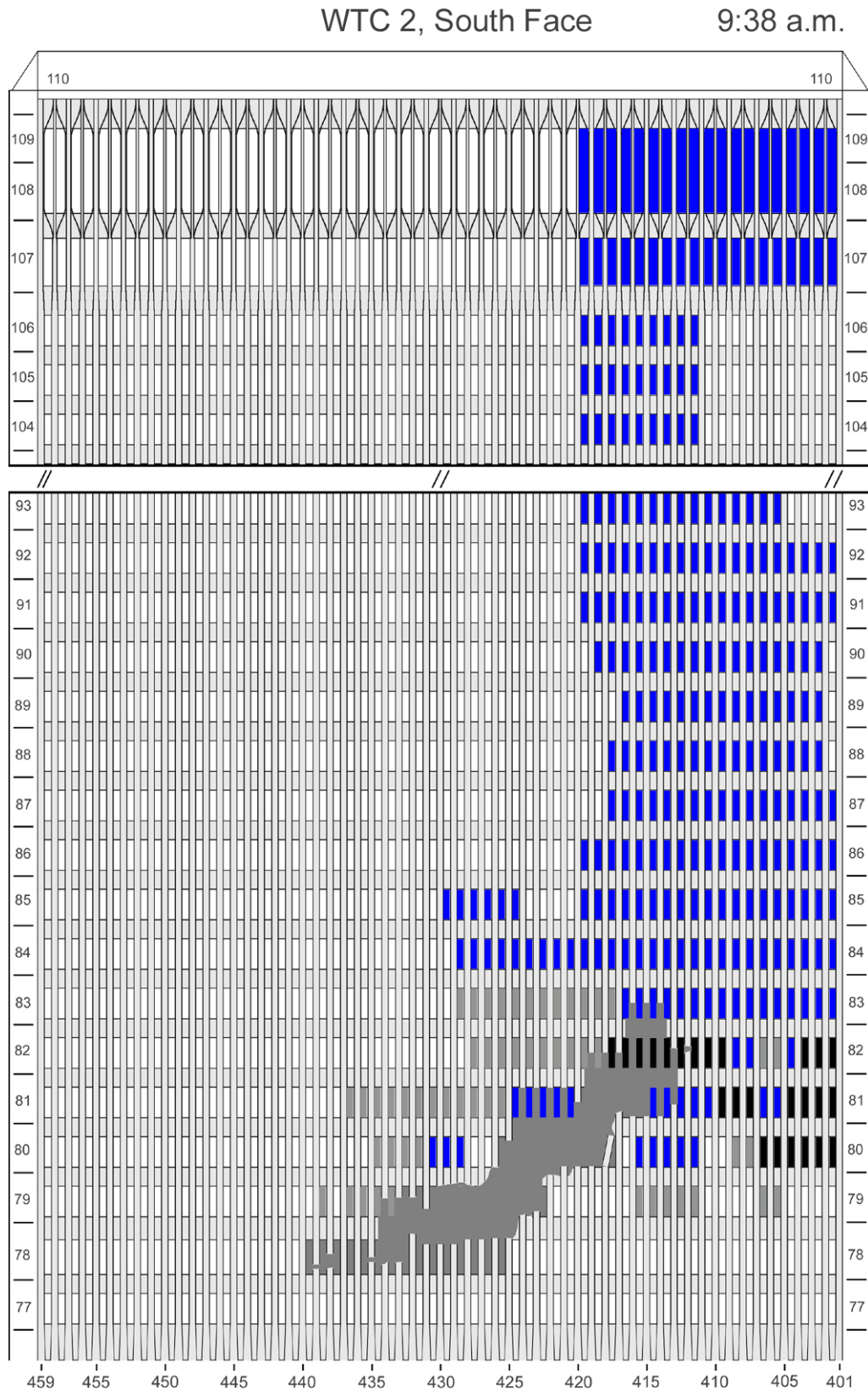


Figure I-38. Diagram of the south face of WTC 2 for floors 77 to 93 and floors 104 to 110 at 9:38 a.m. showing windows where smoke was observed and those hidden from view.

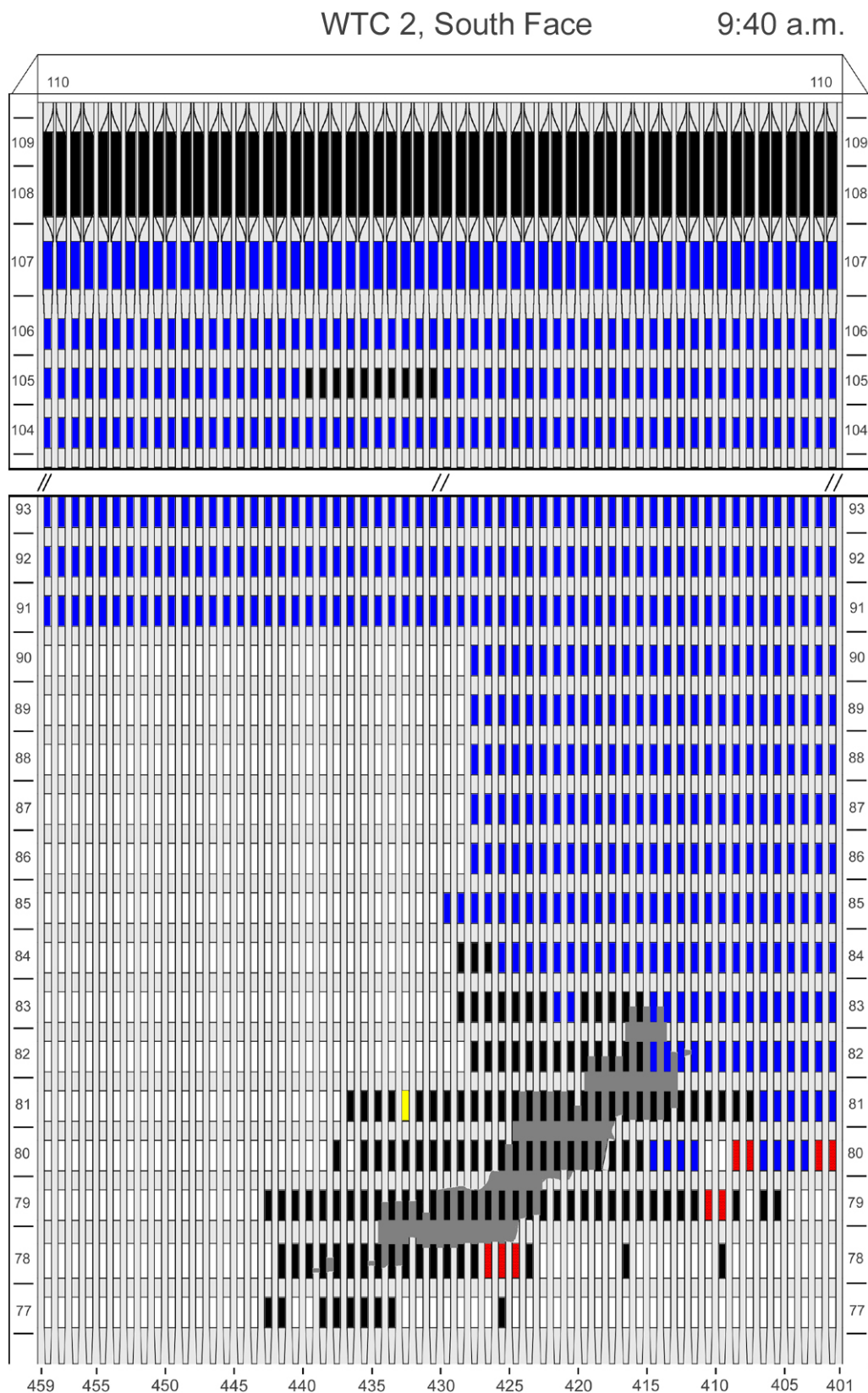


Figure I-39. Diagram of the south face of WTC 2 for floors 77 to 93 and floors 104 to 110 at 9:40 a.m. showing the condition of windows and locations of fires.

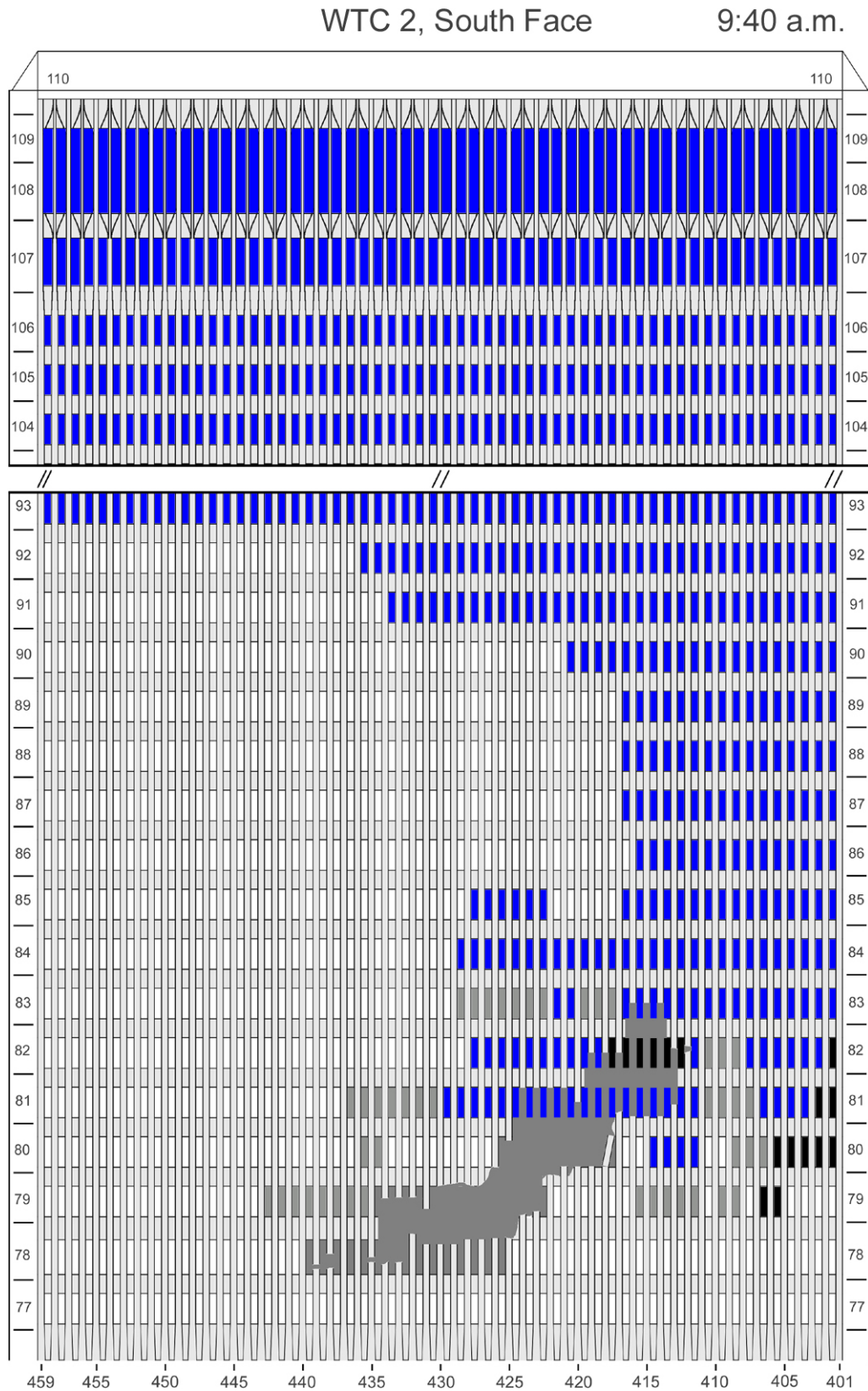


Figure I-40. Diagram of the south face of WTC 2 for floors 77 to 93 and floors 104 to 110 at 9:40 a.m. showing windows where smoke was observed and those hidden from view.

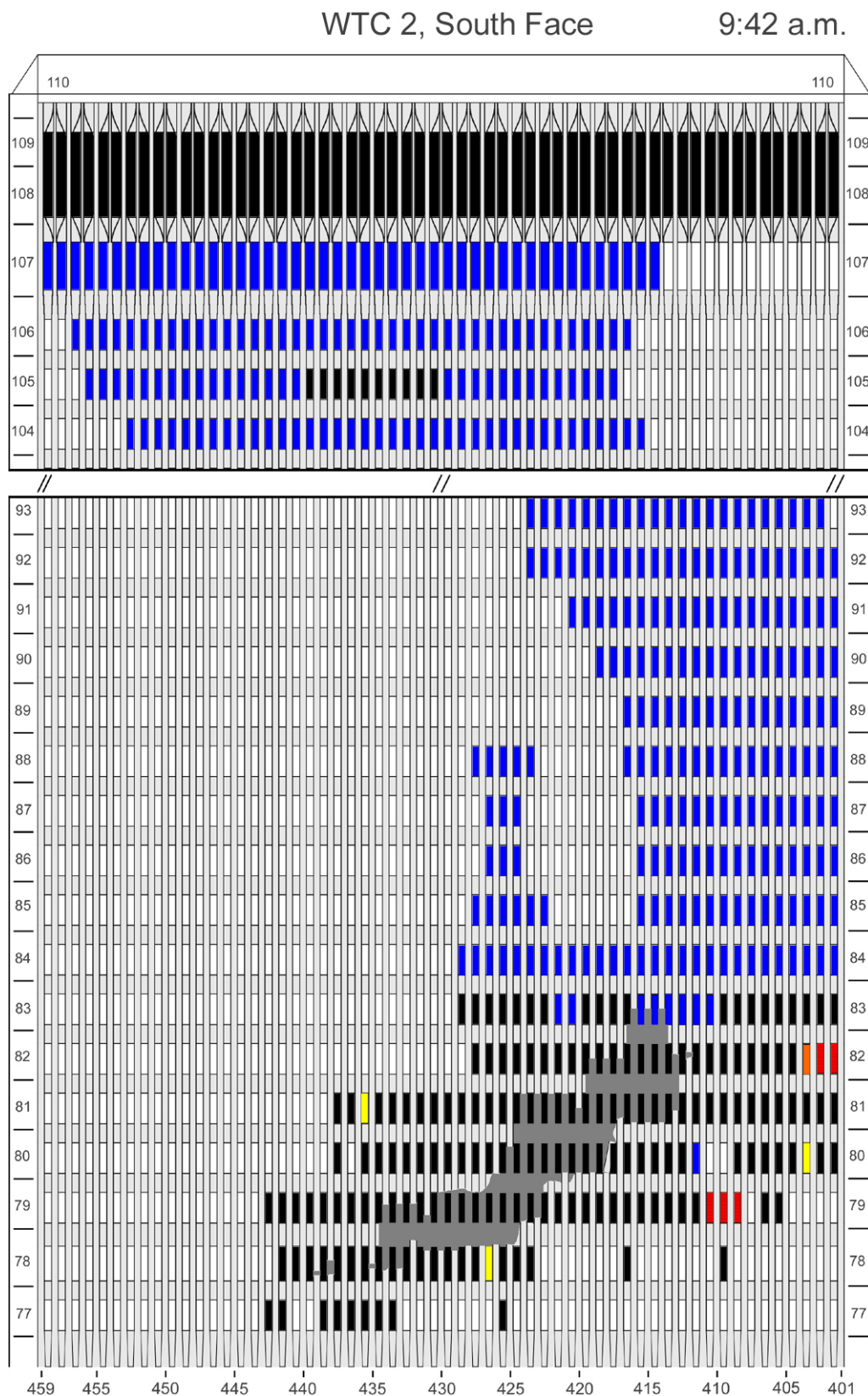


Figure I-41. Diagram of the south face of WTC 2 for floors 77 to 93 and floors 104 to 110 at 9:42 a.m. showing the condition of windows and locations of fires.

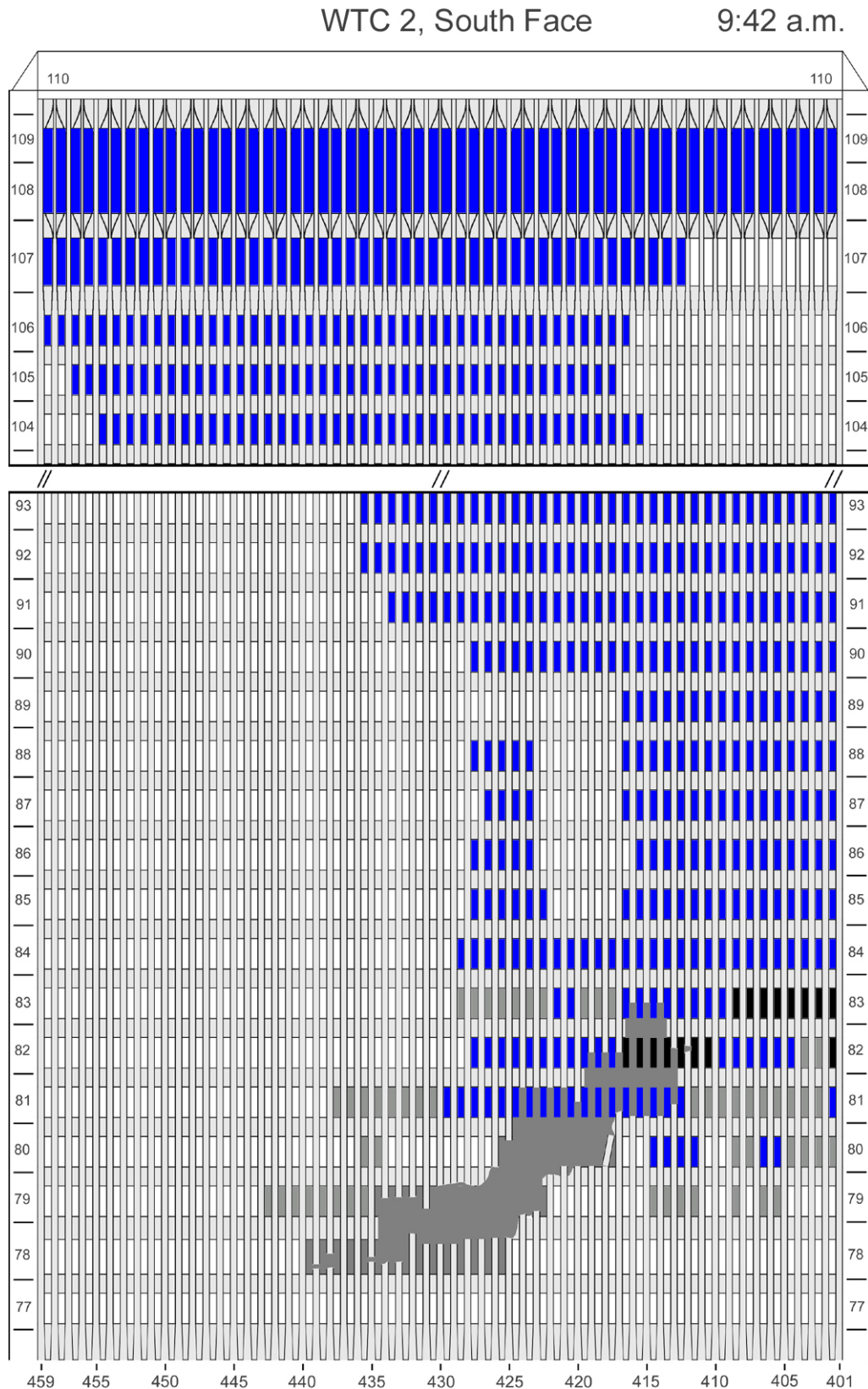


Figure I-42. Diagram of the south face of WTC 2 for floors 77 to 93 and floors 104 to 110 at 9:42 a.m. showing windows where smoke was observed and those hidden from view.

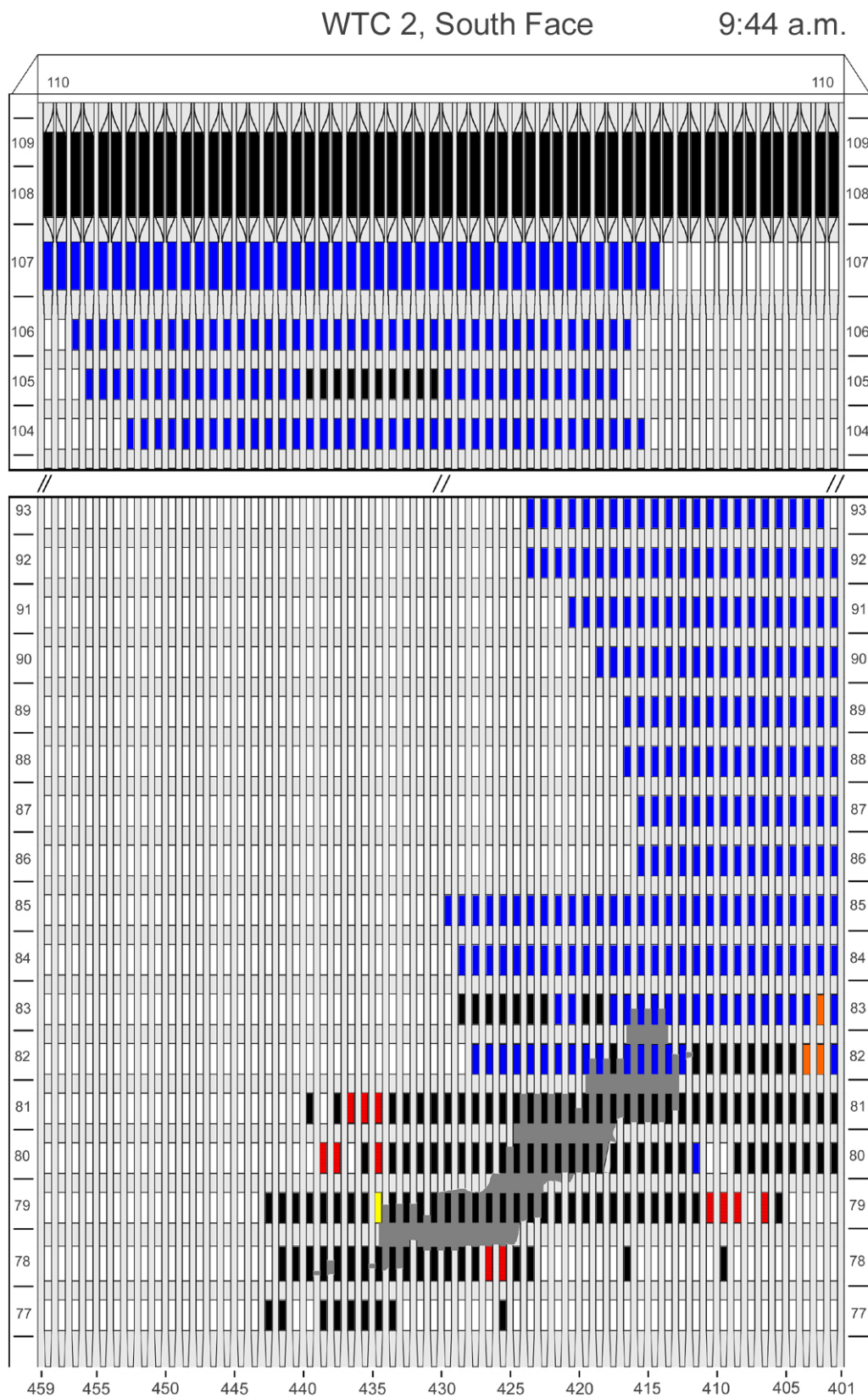


Figure I-43. Diagram of the south face of WTC 2 for floors 77 to 93 and floors 104 to 110 at 9:44 a.m. showing the condition of windows and locations of fires.

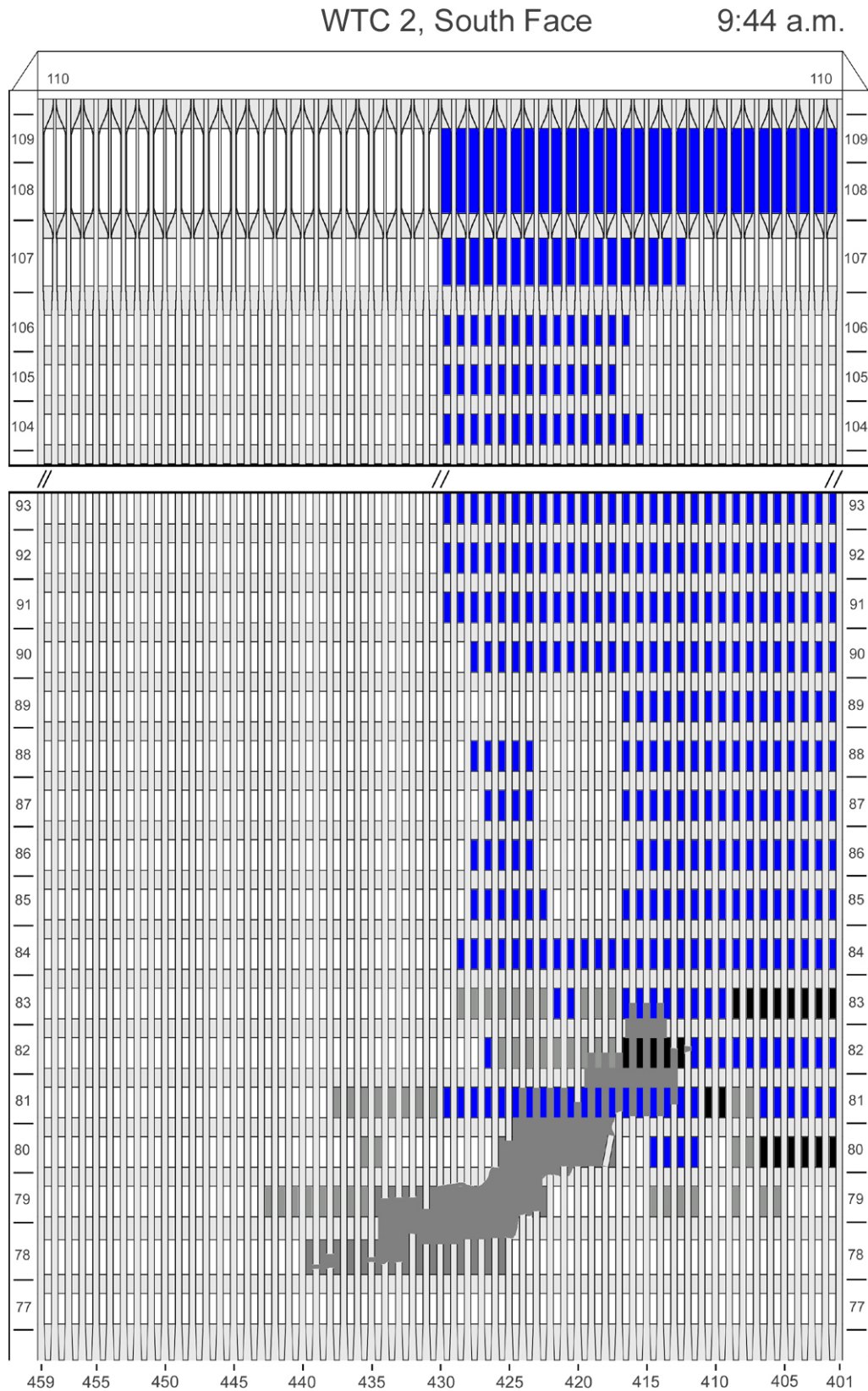


Figure I-44. Diagram of the south face of WTC 2 for floors 77 to 93 and floors 104 to 110 at 9:44 a.m. showing windows where smoke was observed and those hidden from view.

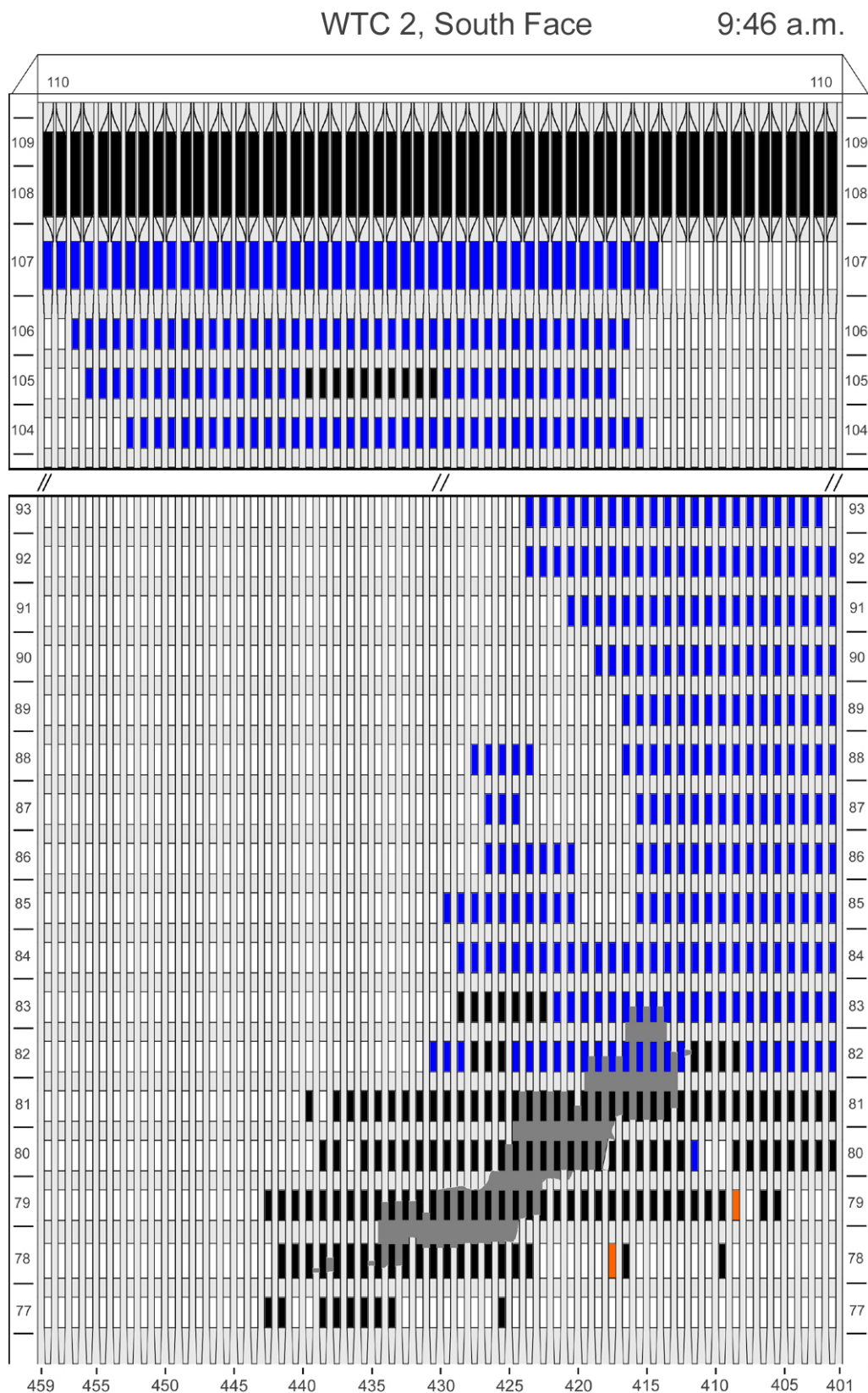


Figure I-45. Diagram of the south face of WTC 2 for floors 77 to 93 and floors 104 to 110 at 9:46 a.m. showing the condition of windows and locations of fires.

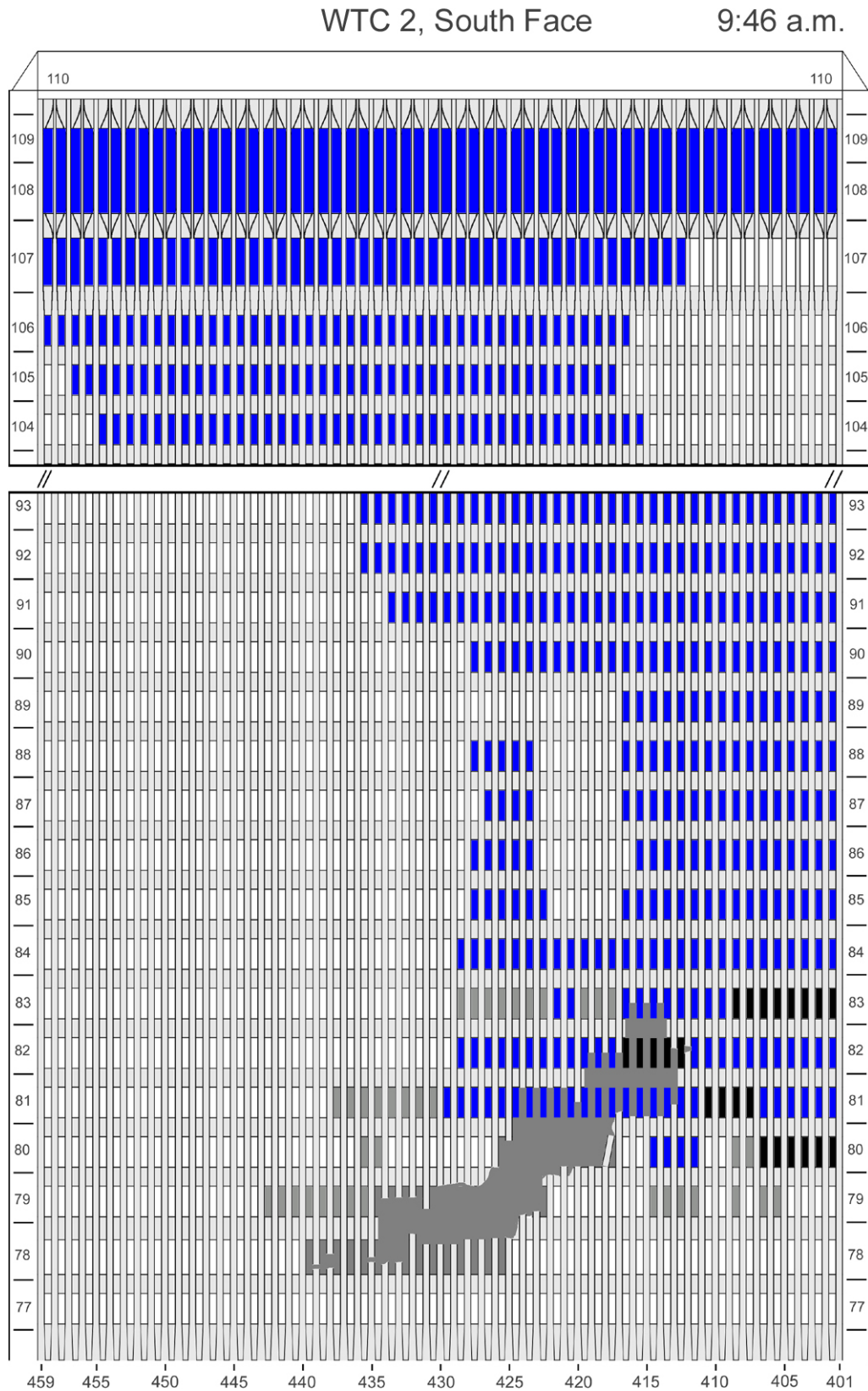


Figure I-46. Diagram of the south face of WTC 2 for floors 77 to 93 and floors 104 to 110 at 9:46 a.m. showing windows where smoke was observed and those hidden from view.

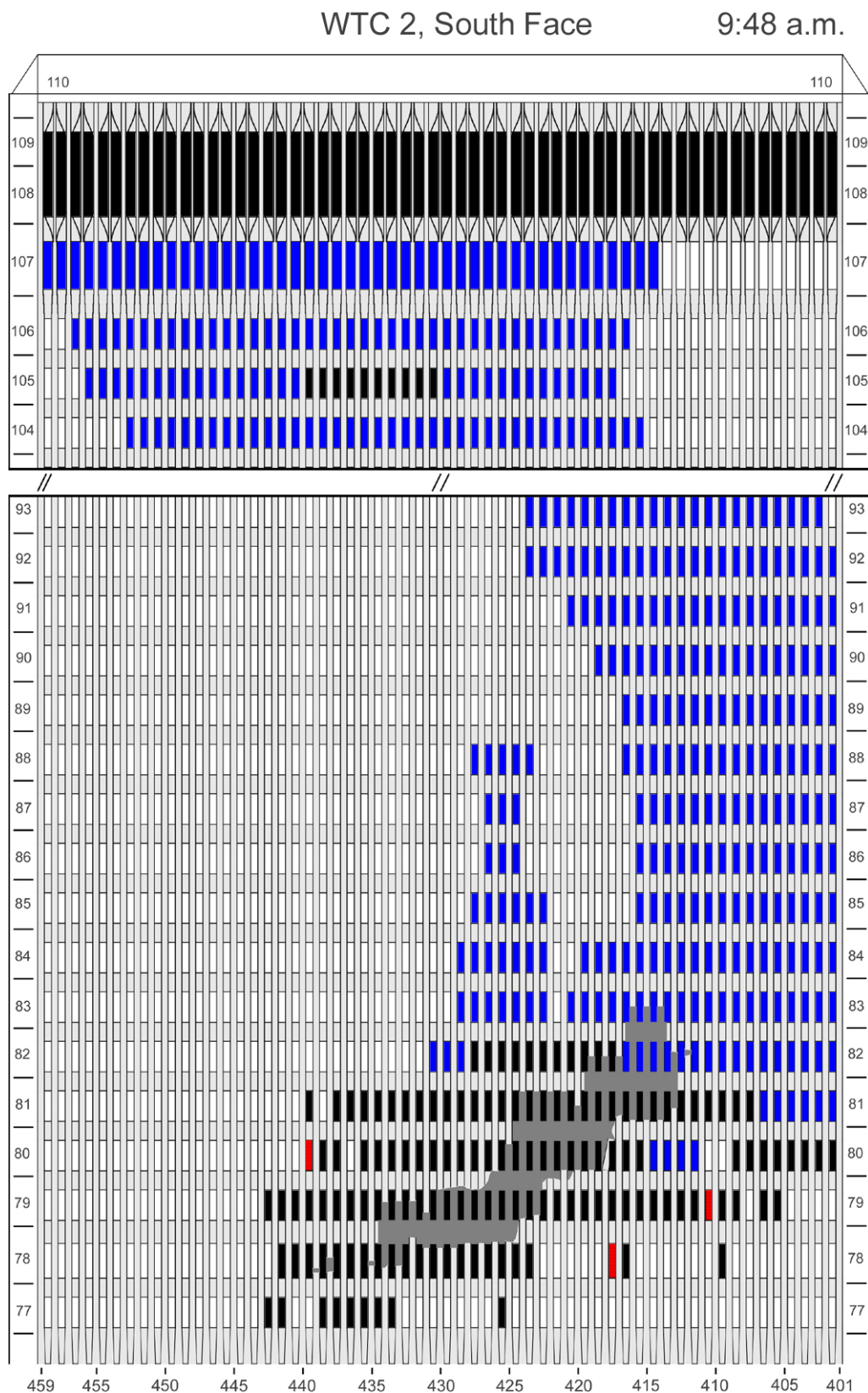


Figure I-47. Diagram of the south face of WTC 2 for floors 77 to 93 and floors 104 to 110 at 9:48 a.m. showing the condition of windows and locations of fires.

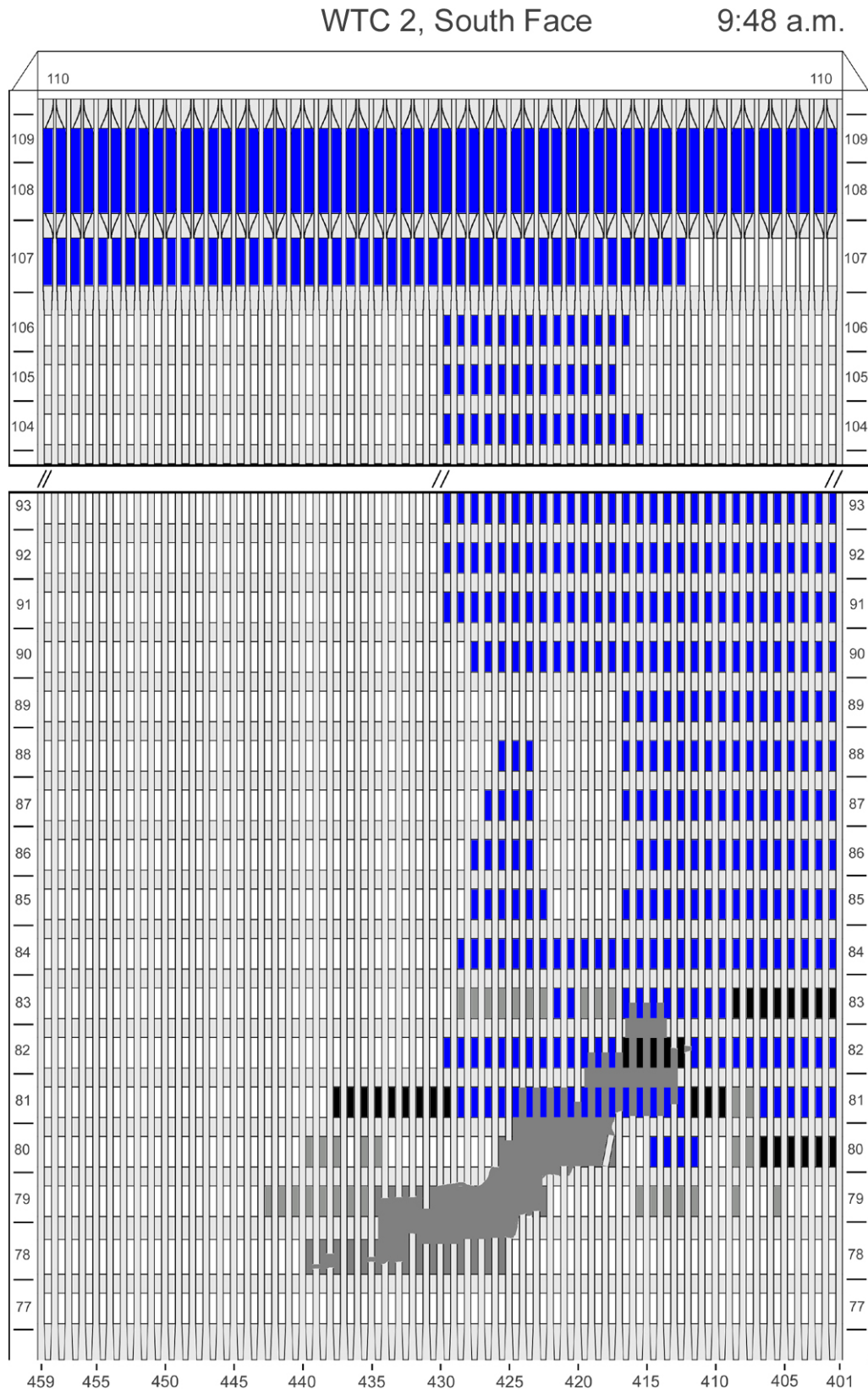


Figure I- 48. Diagram of the south face of WTC 2 for floors 77 to 93 and floors 104 to 110 at 9:48 a.m. showing windows where smoke was observed and those hidden from view.

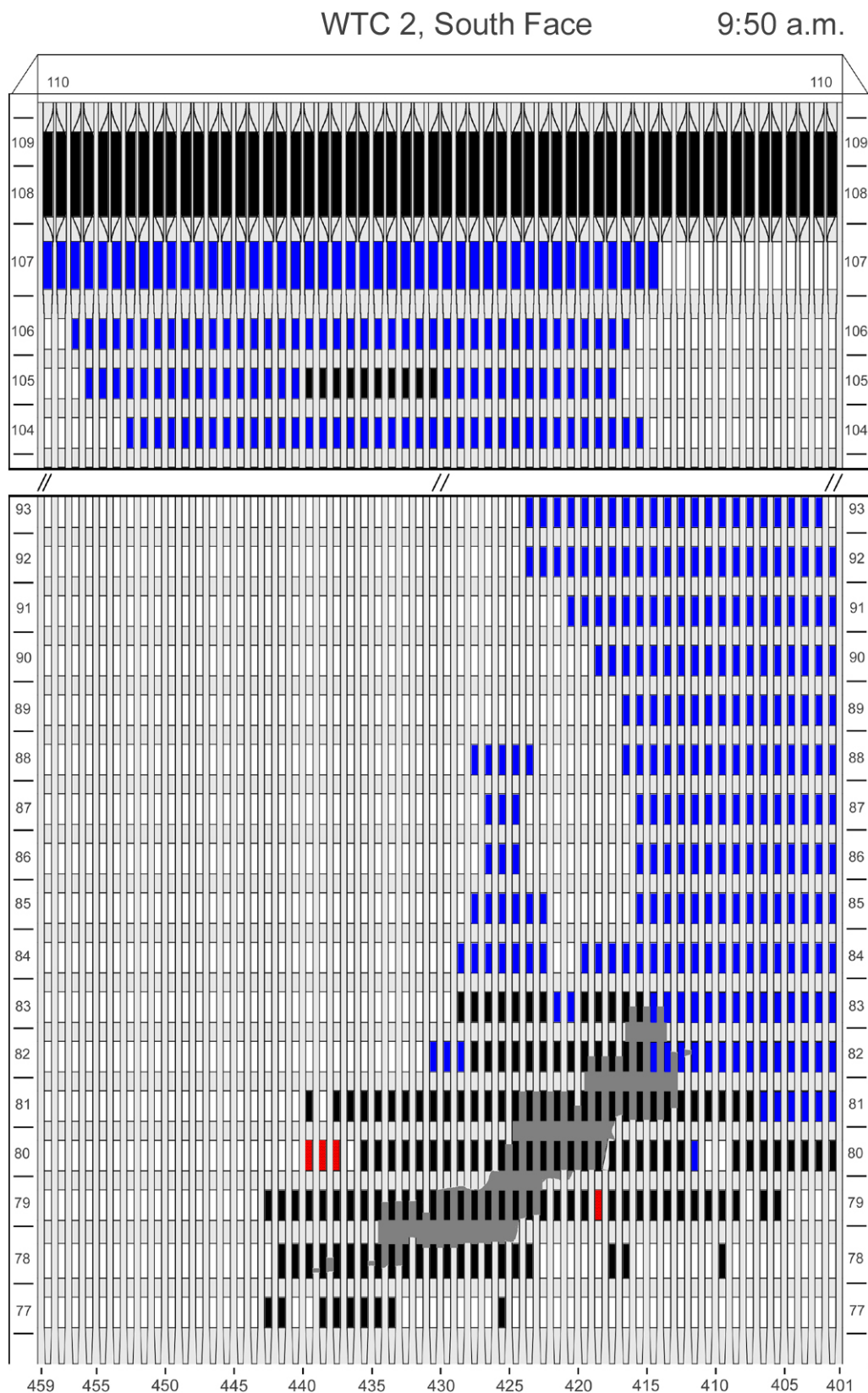


Figure I-49. Diagram of the south face of WTC 2 for floors 77 to 93 and floors 104 to 110 at 9:50 a.m. showing the condition of windows and locations of fires.

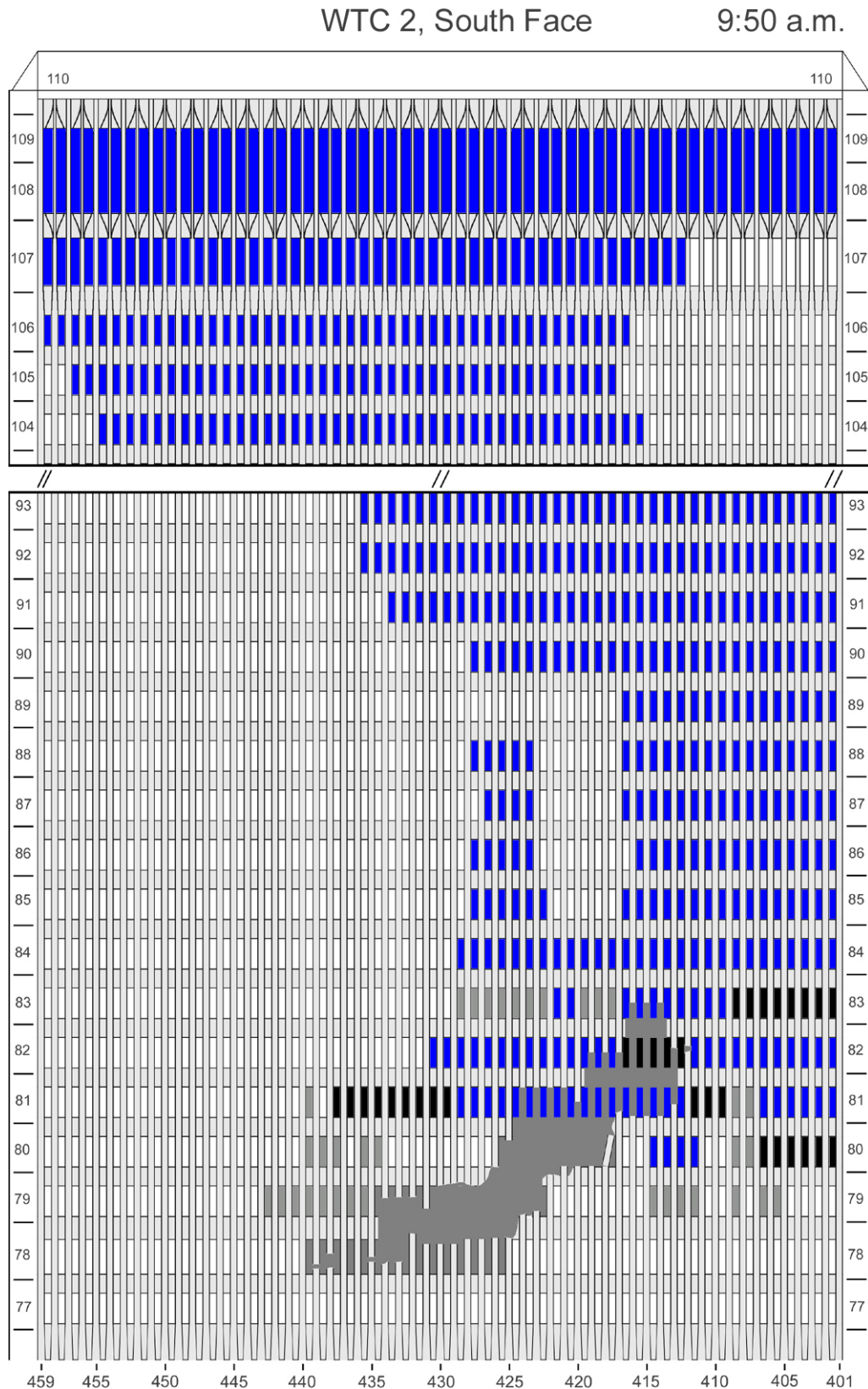


Figure I-50. Diagram of the south face of WTC 2 for floors 77 to 93 and floors 104 to 110 at 9:50 a.m. showing windows where smoke was observed and those hidden from view.

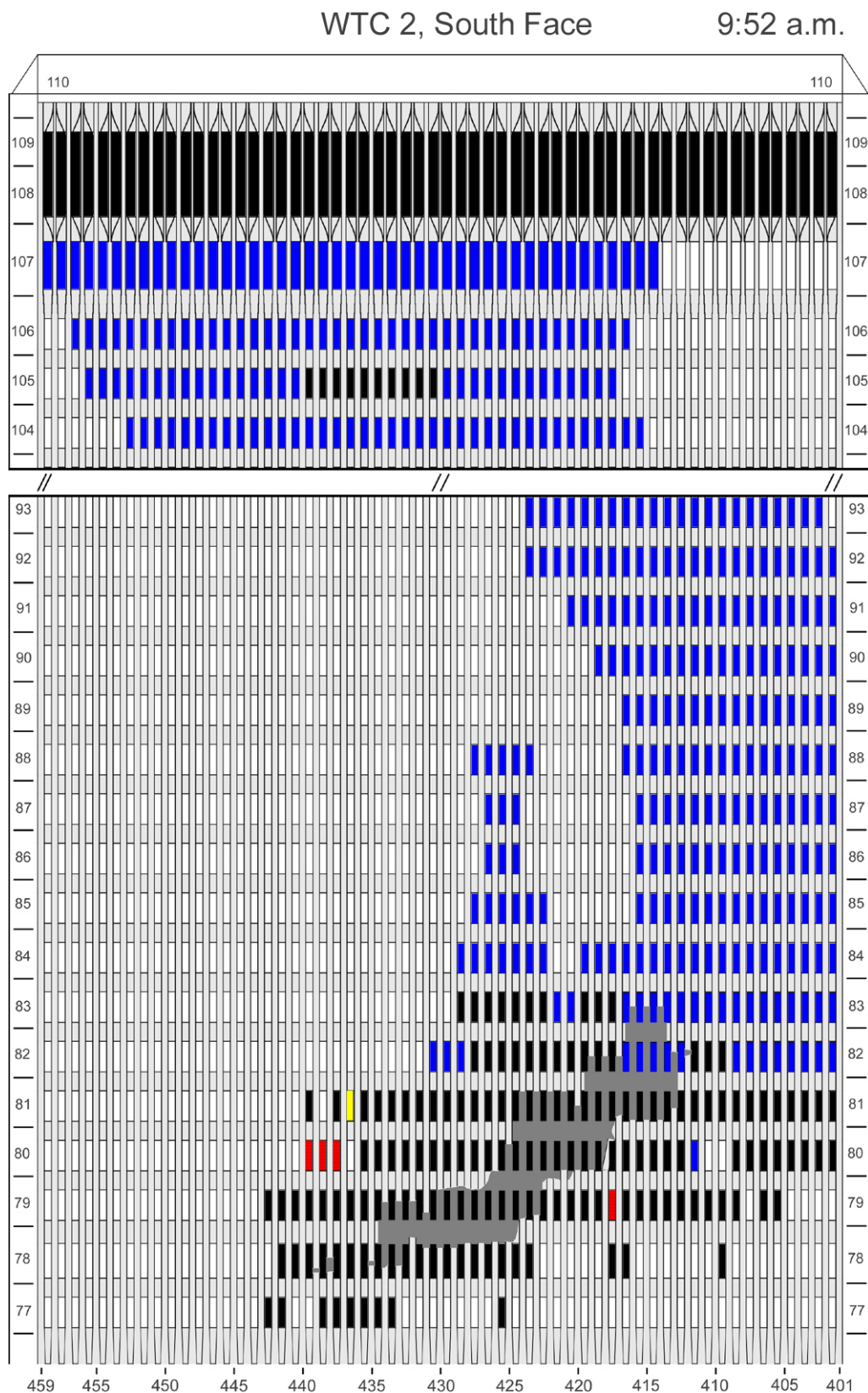


Figure I-51. Diagram of the south face of WTC 2 for floors 77 to 93 and floors 104 to 110 at 9:52 a.m. showing the condition of windows and locations of fires.

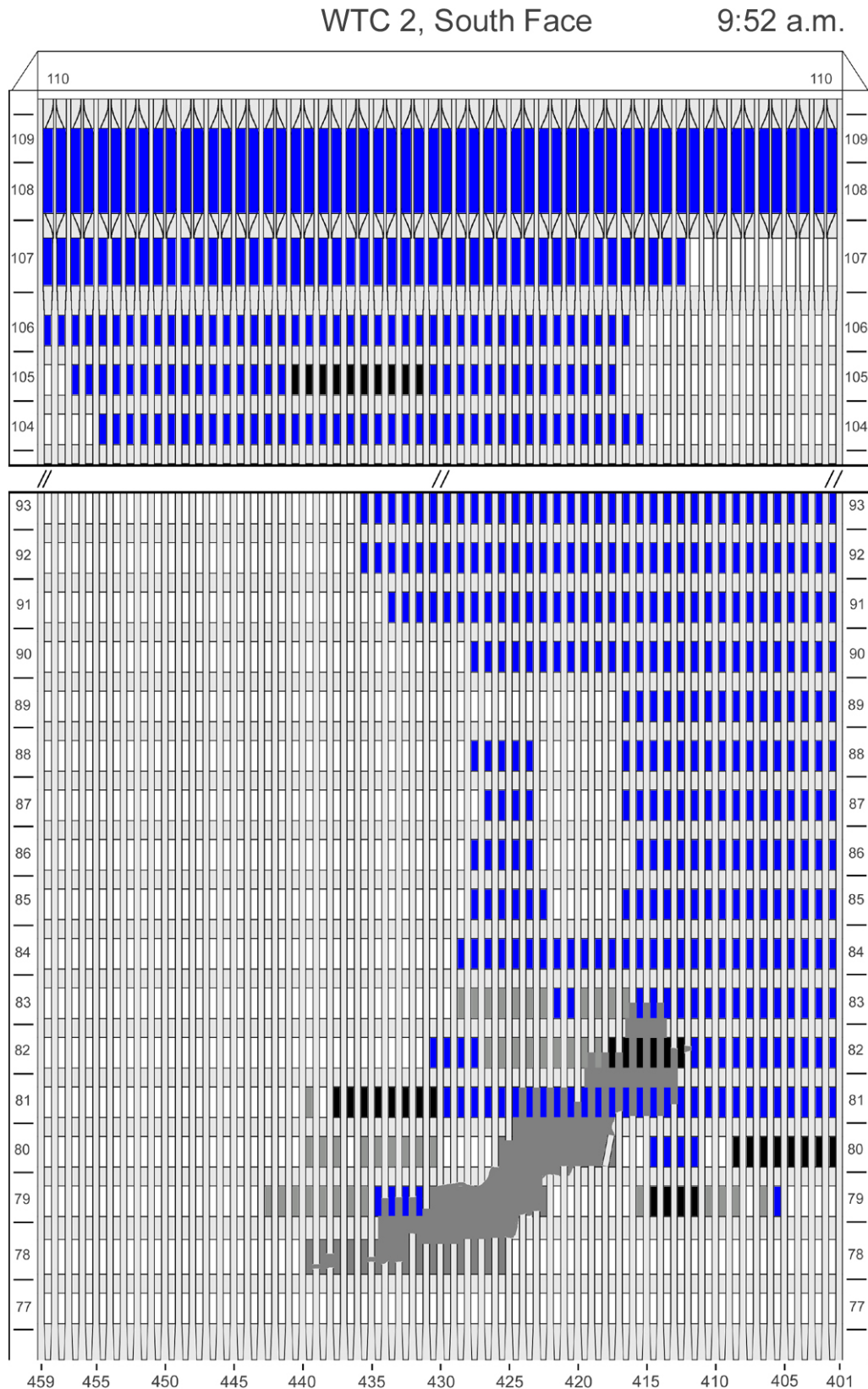


Figure I-52. Diagram of the south face of WTC 2 for floors 77 to 93 and floors 104 to 110 at 9:52 a.m. showing windows where smoke was observed and those hidden from view.

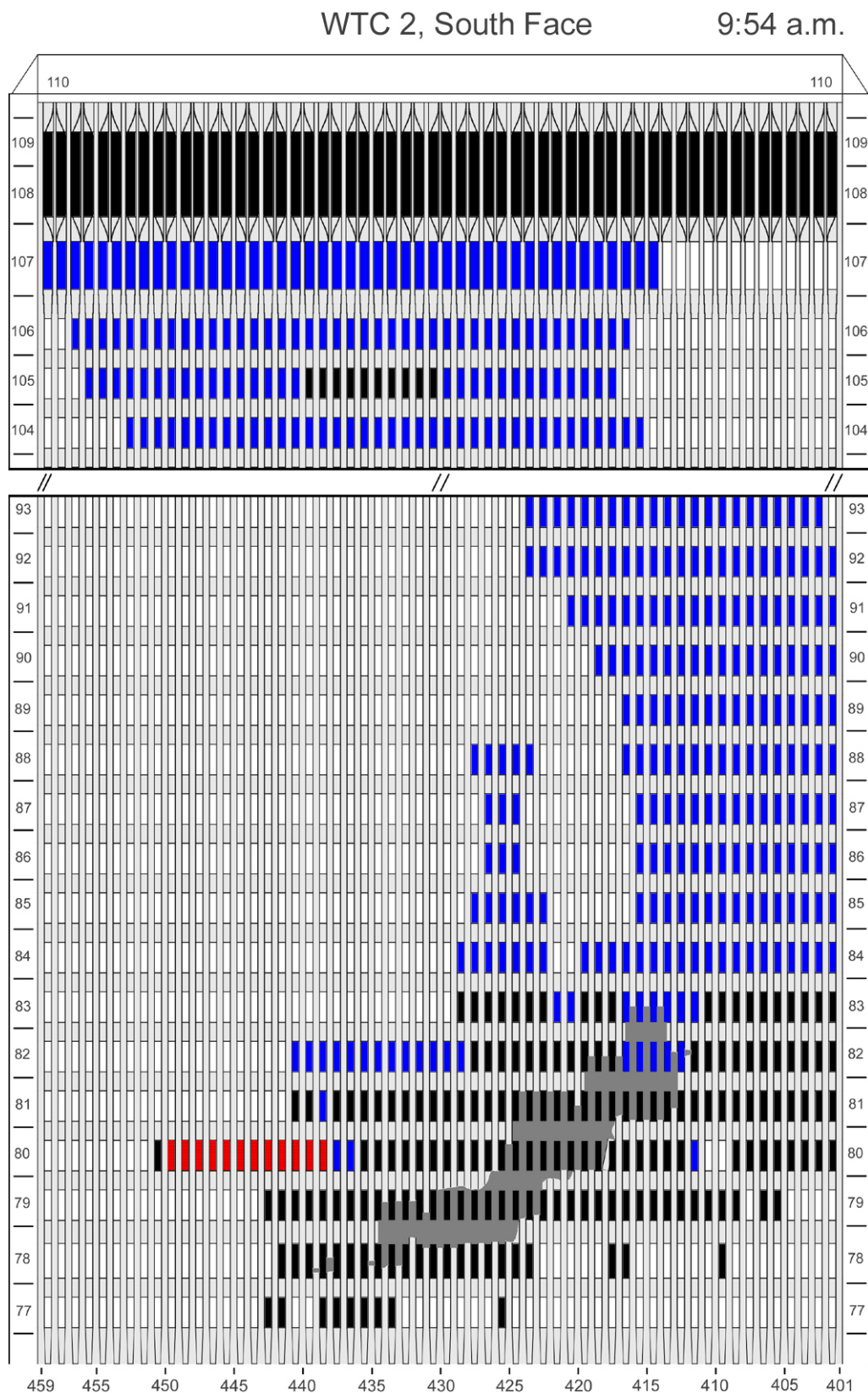


Figure I-53. Diagram of the south face of WTC 2 for floors 77 to 93 and floors 104 to 110 at 9:54 a.m. showing the condition of windows and locations of fires.

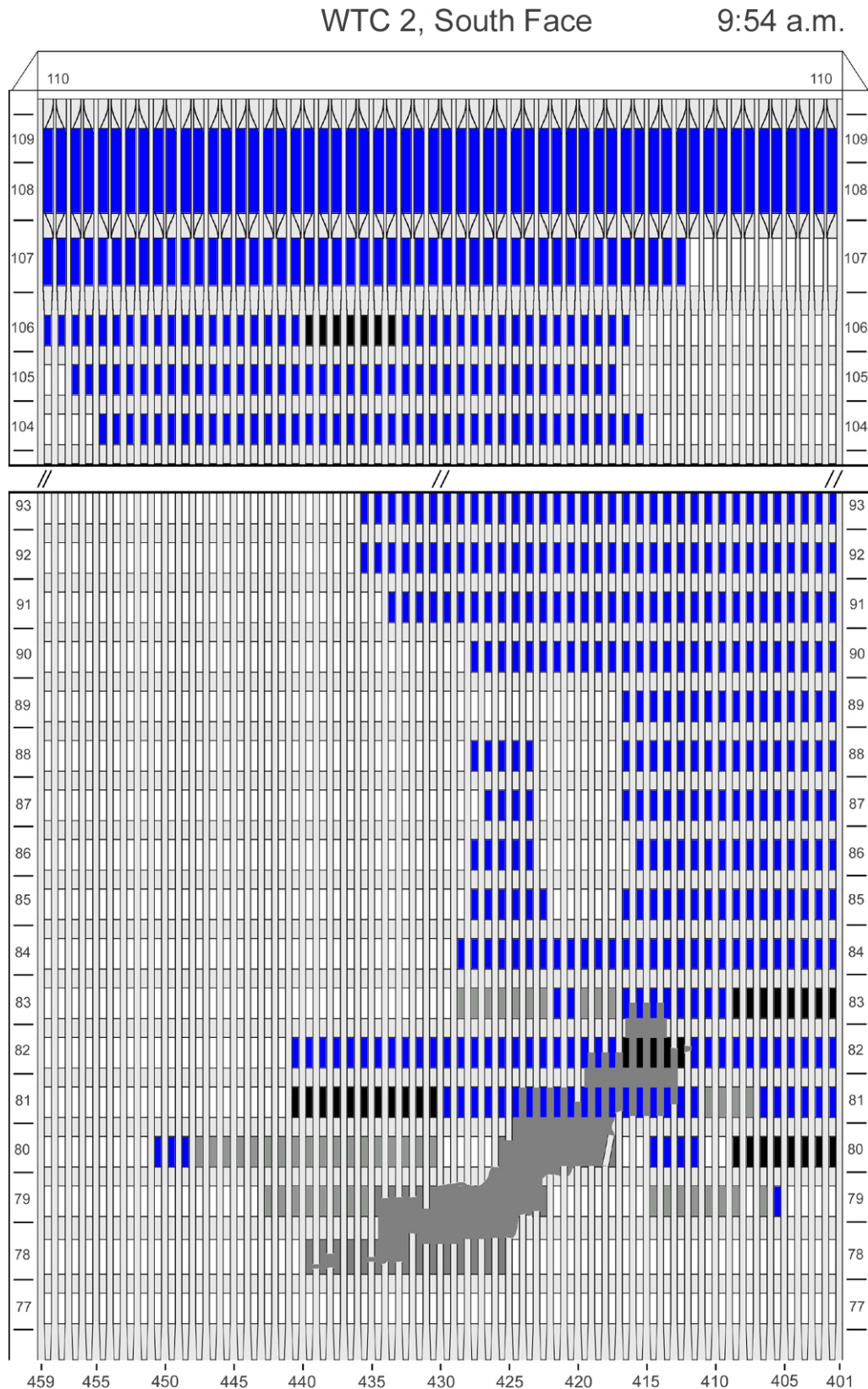


Figure I-54. Diagram of the south face of WTC 2 for floors 77 to 93 and floors 104 to 110 at 9:54 a.m. showing windows where smoke was observed and those hidden from view.

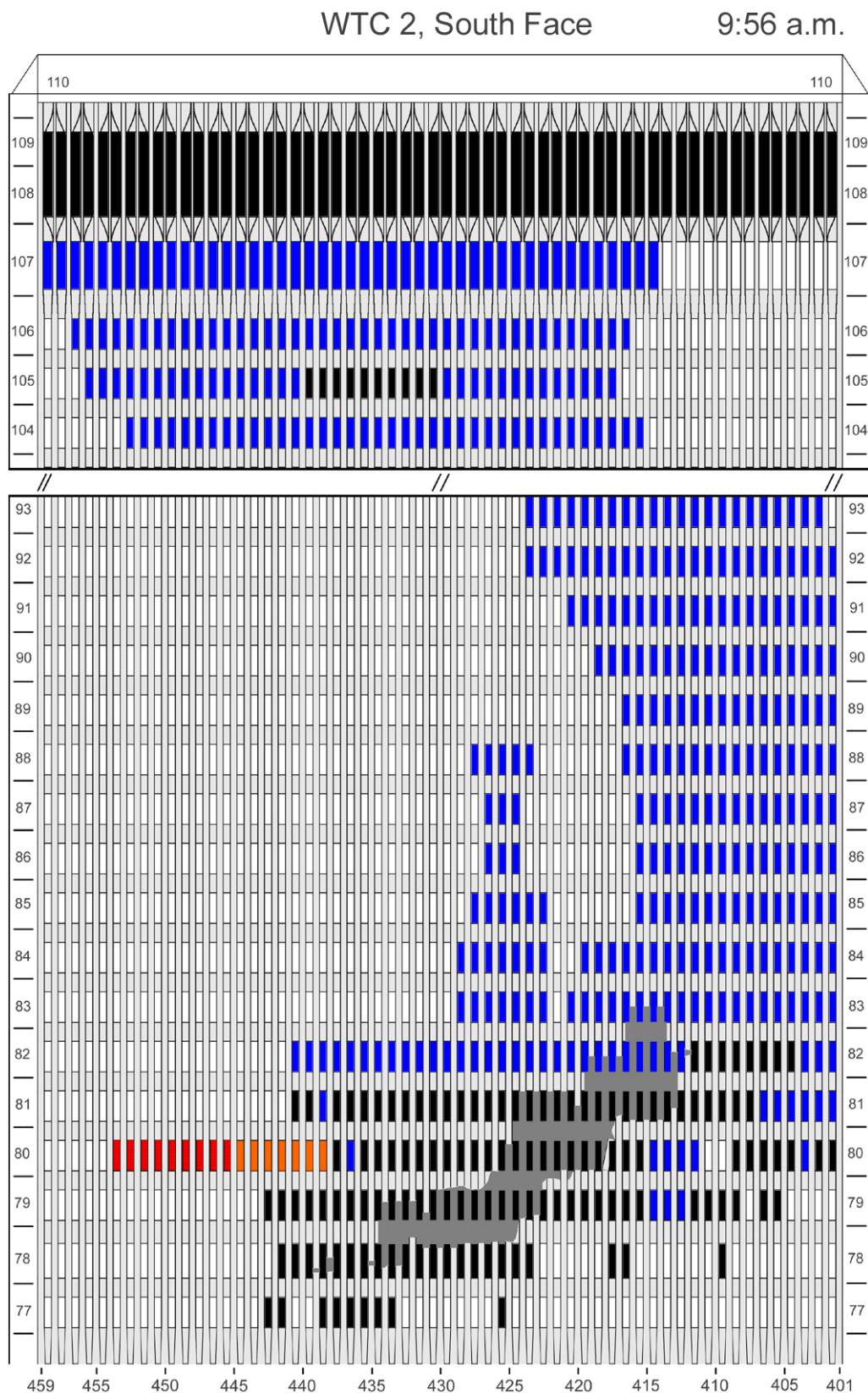


Figure I-55. Diagram of the south face of WTC 2 for floors 77 to 93 and floors 104 to 110 at 9:56 a.m. showing the condition of windows and locations of fires.

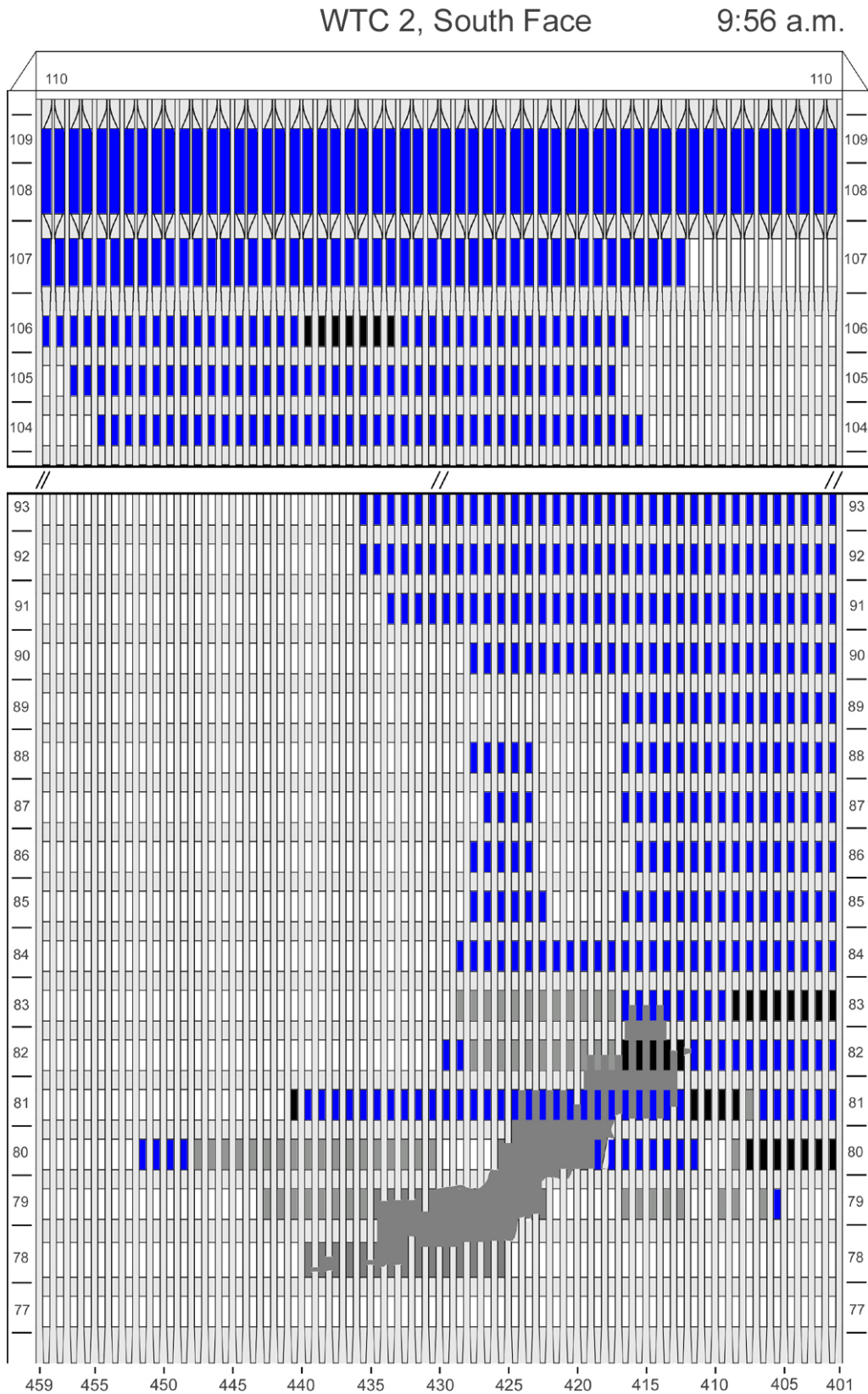


Figure I-56. Diagram of the south face of WTC 2 for floors 77 to 93 and floors 104 to 110 at 9:56 a.m. showing windows where smoke was observed and those hidden from view.

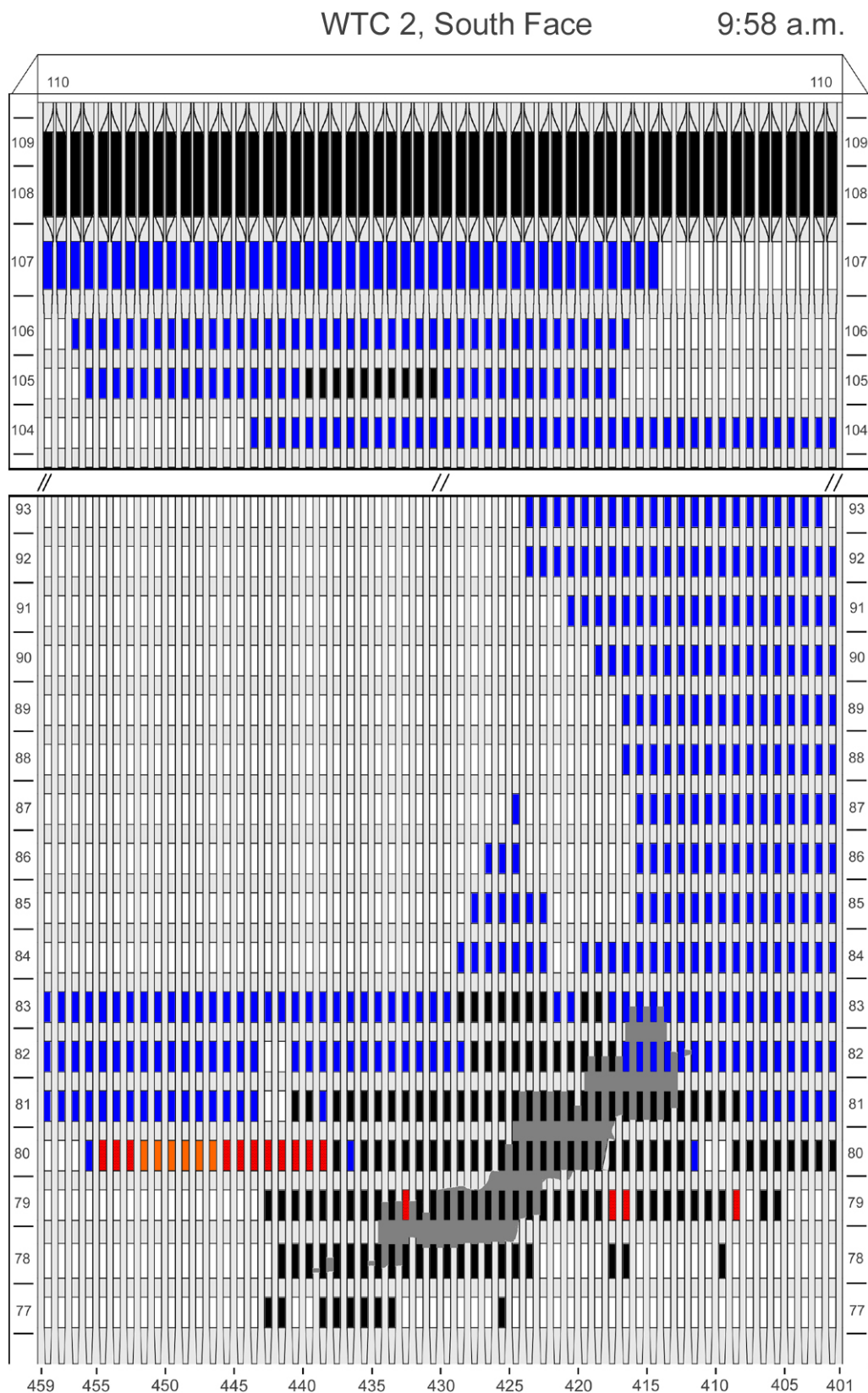


Figure I-57. Diagram of the south face of WTC 2 for floors 77 to 93 and floors 104 to 110 at 9:58 a.m. showing the condition of windows and locations of fires.

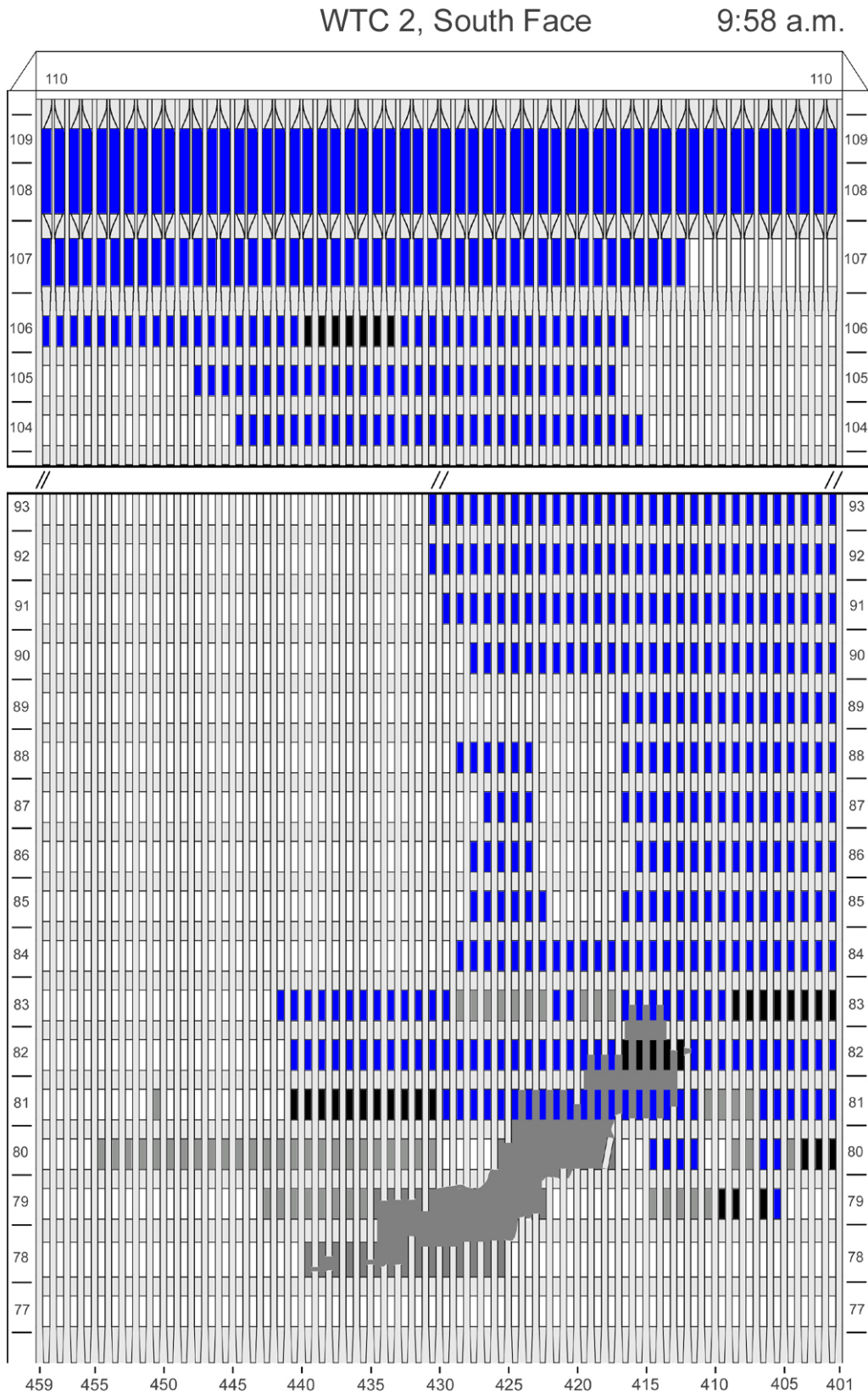












Figure I-58. Diagram of the south face of WTC 2 for floors 77 to 93 and floors 104 to 110 at 9:58 a.m. showing windows where smoke was observed and those hidden from view.

This page intentionally left blank.

Appendix J

WTC 2 WEST FACE COMBINED FIRE AND WINDOW CONDITION AND WINDOW SMOKE CONDITION

This appendix provides visual representations of the data contained in data sheets describing observations of fire, smoke, and window condition on a window-by-window basis as a function of time for the west face of WTC 2. The data for window condition and fire observations are combined into single representations, with the data for fire taking precedence. Observations are represented using the key provided in Figure 5-1 as follows:  - window glass in place,  - window open,  - spot fire,  - fire visible inside,  - external flaming, and  - not visible. The data for smoke are shown in separate figures using the key from Figure 5-1 as follows:  - no smoke visible,  - light smoke,  - heavy smoke, and  - not visible. For a given time, the window condition and fire data are shown first.

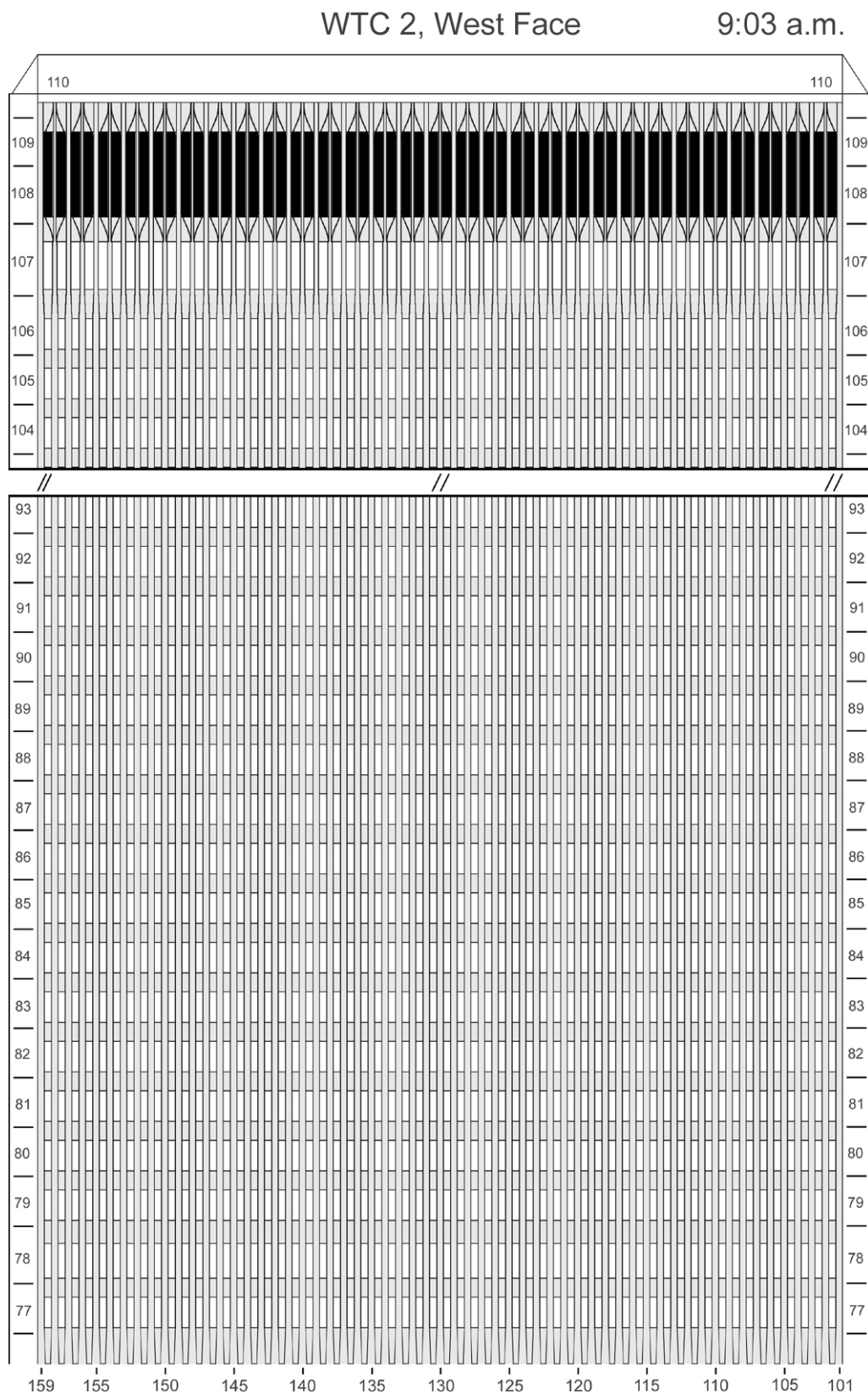


Figure J-1. Diagram of the west face of WTC 2 for floors 77 to 93 and floors 104 to 110 at 9:03 a.m. showing the condition of windows and locations of fires.

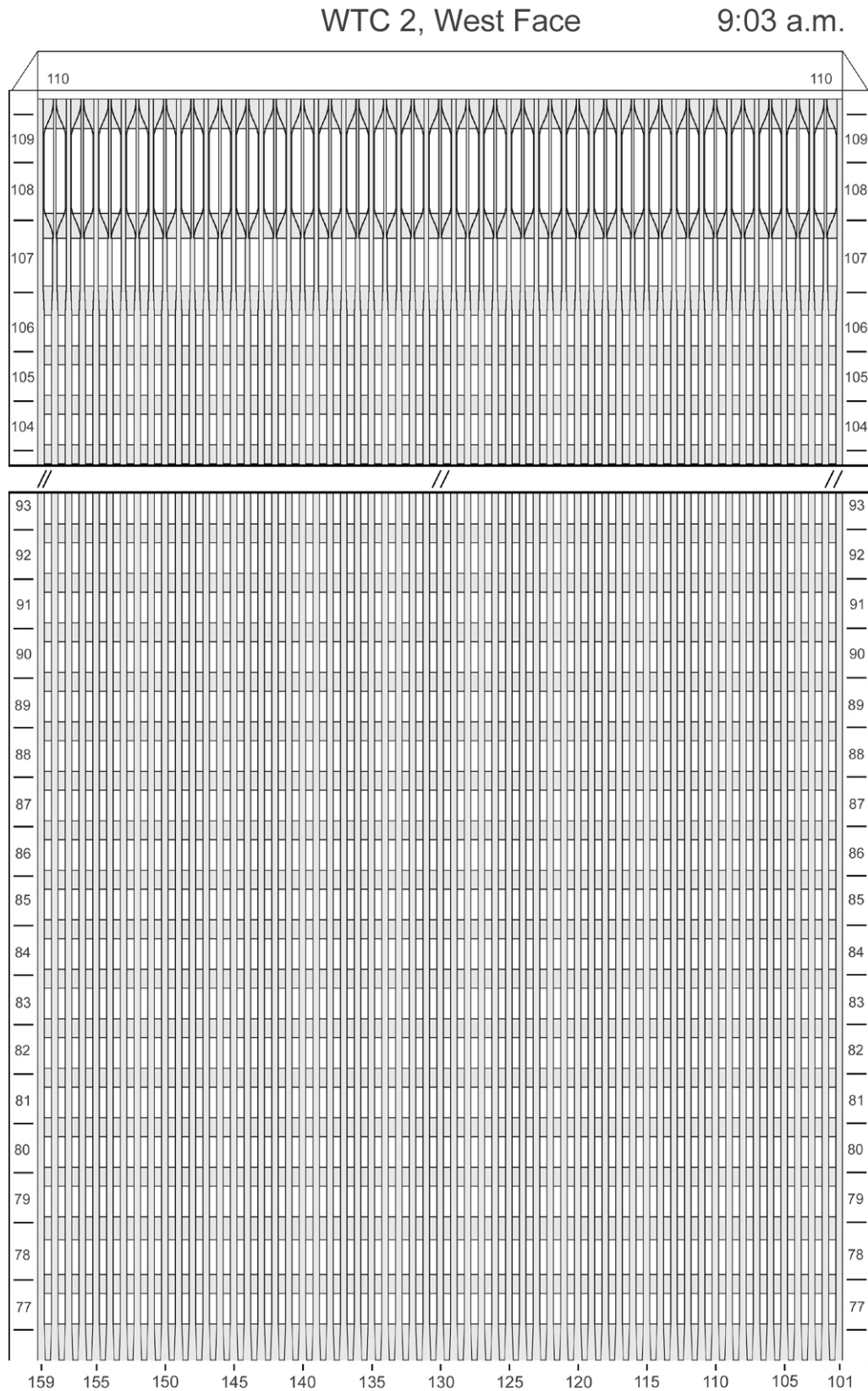


Figure J-2. Diagram of the west face of WTC 2 for floors 77 to 93 and floors 104 to 110 at 9:03 a.m. showing windows where smoke was observed and those hidden from view.

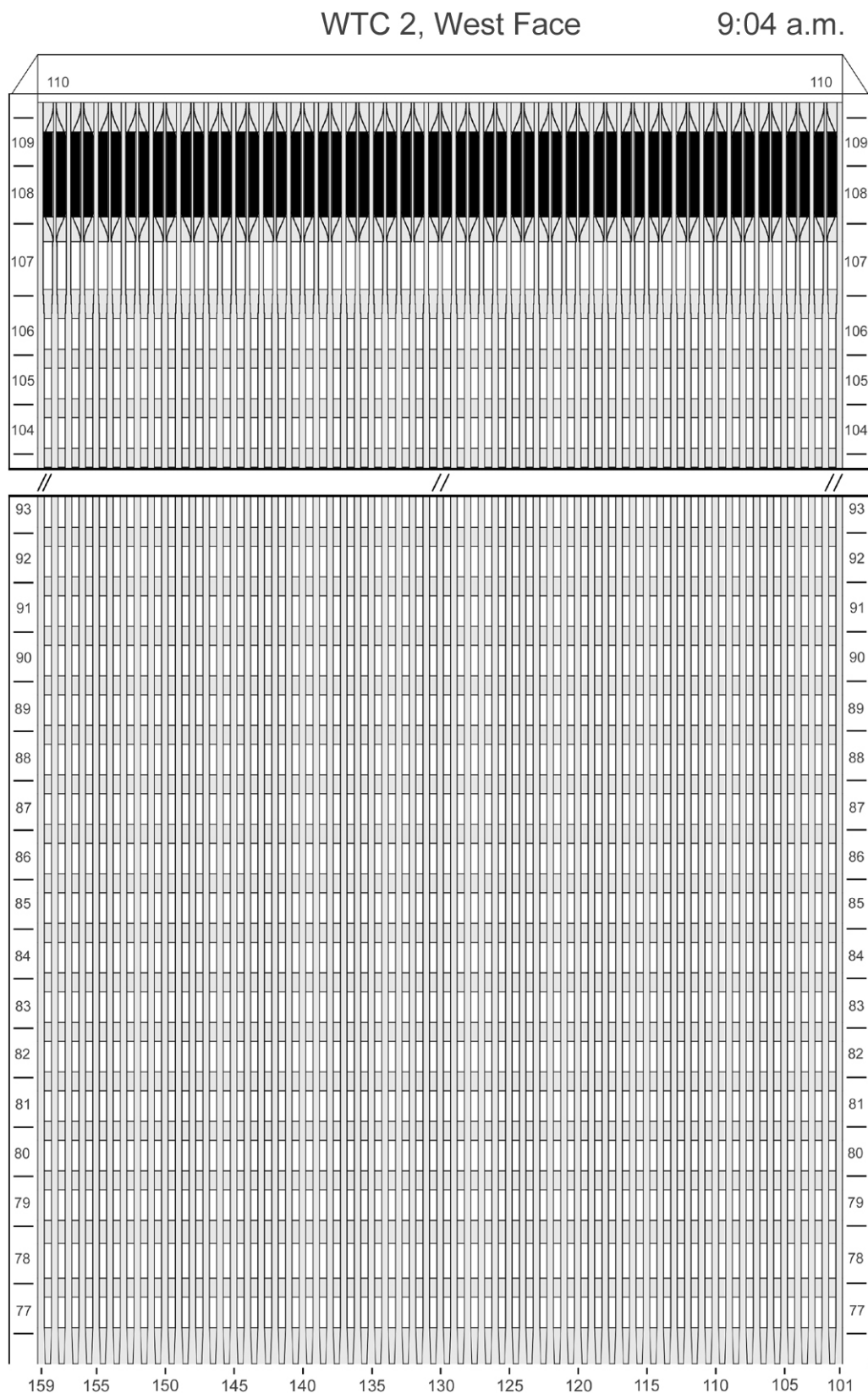


Figure J-3. Diagram of the west face of WTC 2 for floors 77 to 93 and floors 104 to 110 at 9:04 a.m. showing the condition of windows and locations of fires.

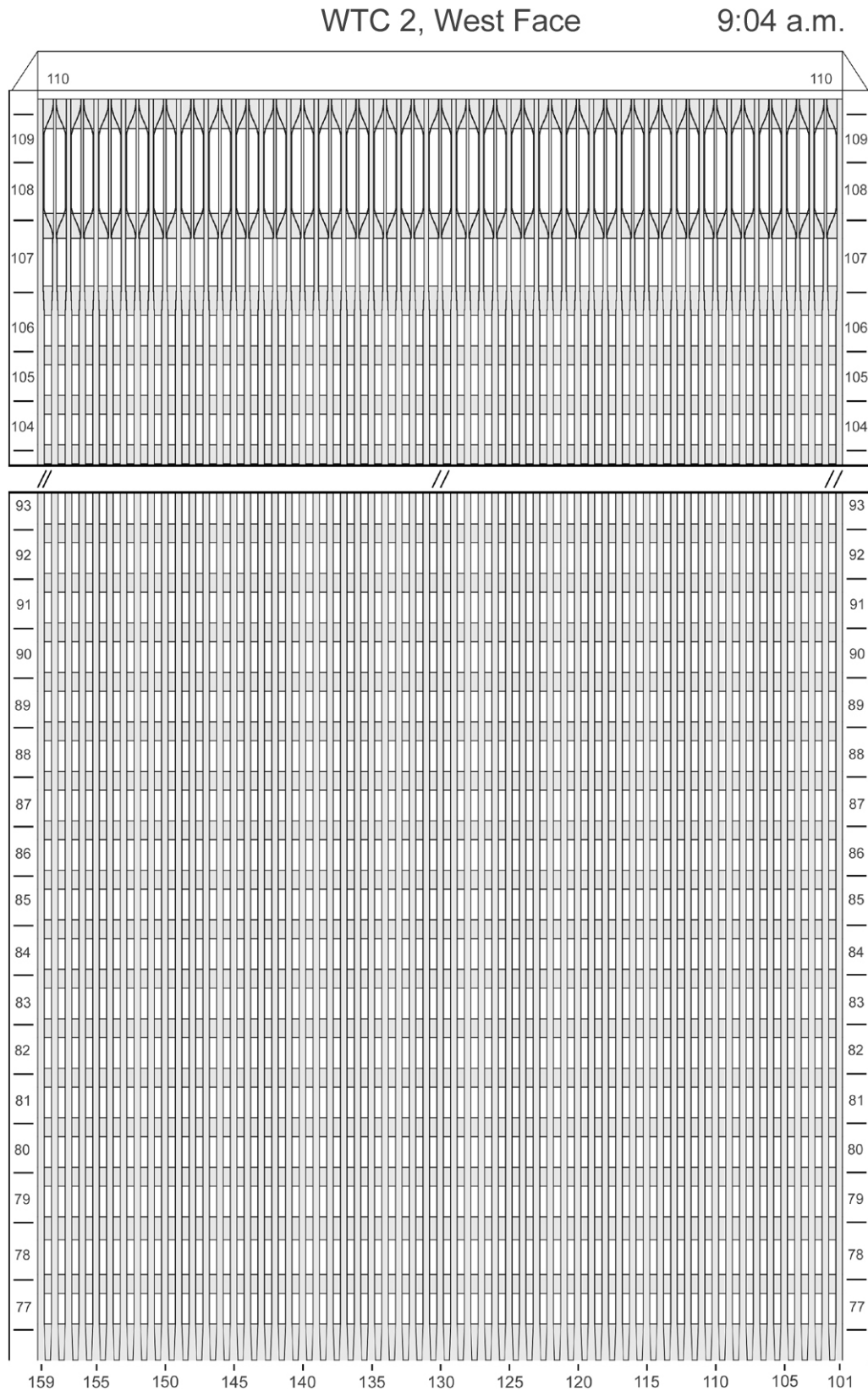


Figure J-4. Diagram of the west face of WTC 2 for floors 77 to 93 and floors 104 to 110 at 9:04 a.m. showing windows where smoke was observed and those hidden from view.

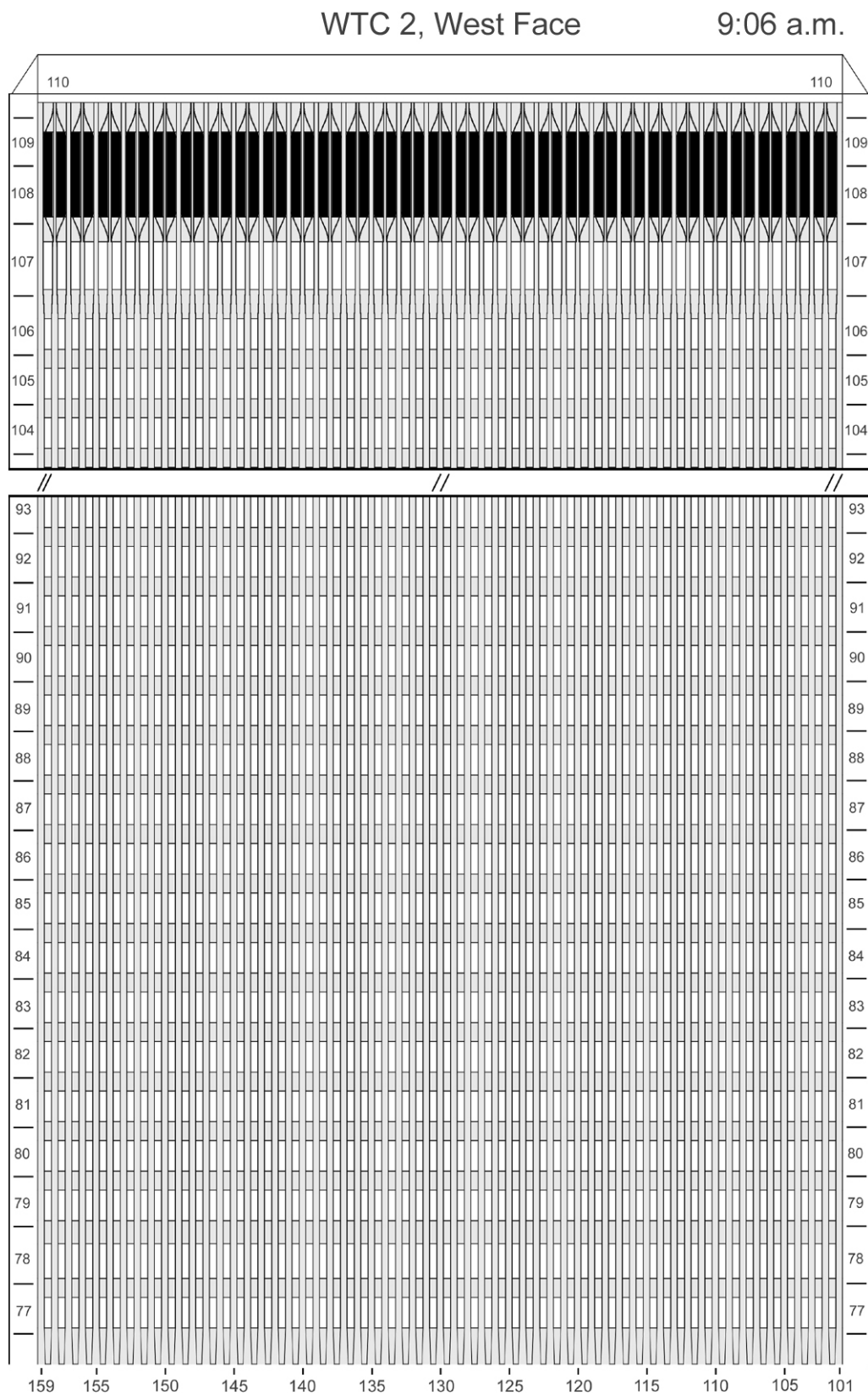


Figure J-5. Diagram of the west face of WTC 2 for floors 77 to 93 and floors 104 to 110 at 9:06 a.m. showing the condition of windows and locations of fires.

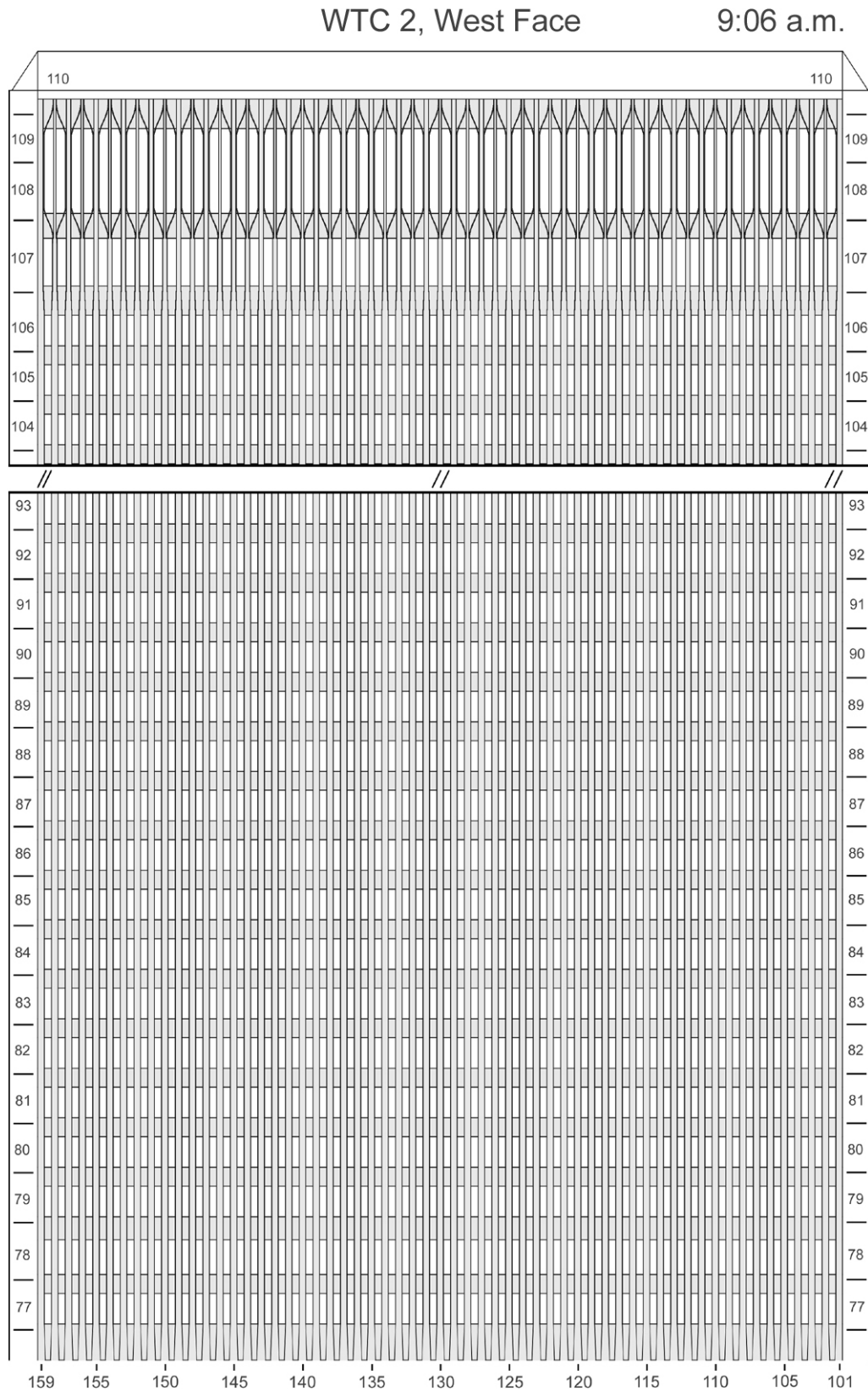


Figure J-6. Diagram of the west face of WTC 2 for floors 77 to 93 and floors 104 to 110 at 9:06 a.m. showing windows where smoke was observed and those hidden from view.

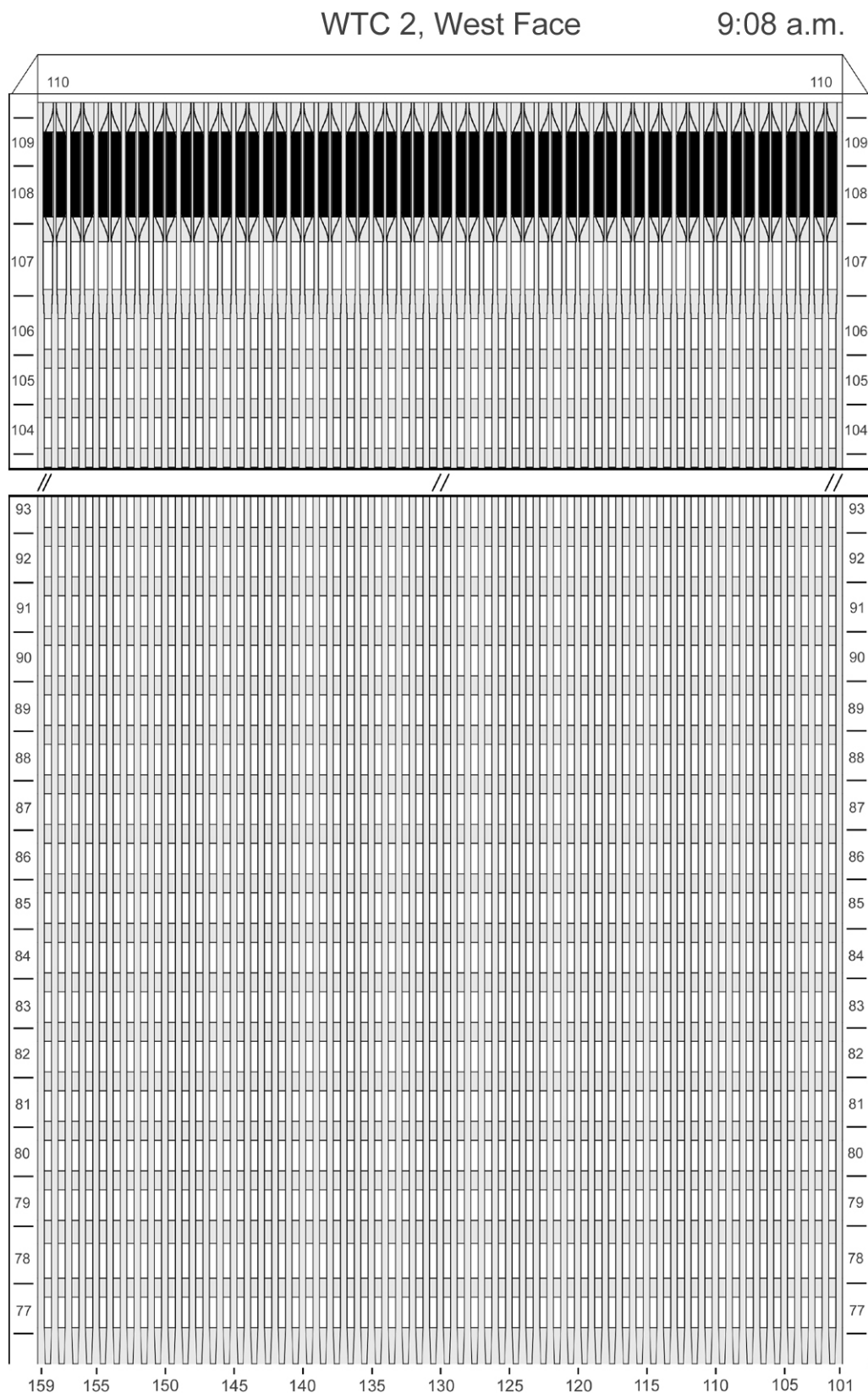


Figure J-7. Diagram of the west face of WTC 2 for floors 77 to 93 and floors 104 to 110 at 9:08 a.m. showing the condition of windows and locations of fires.

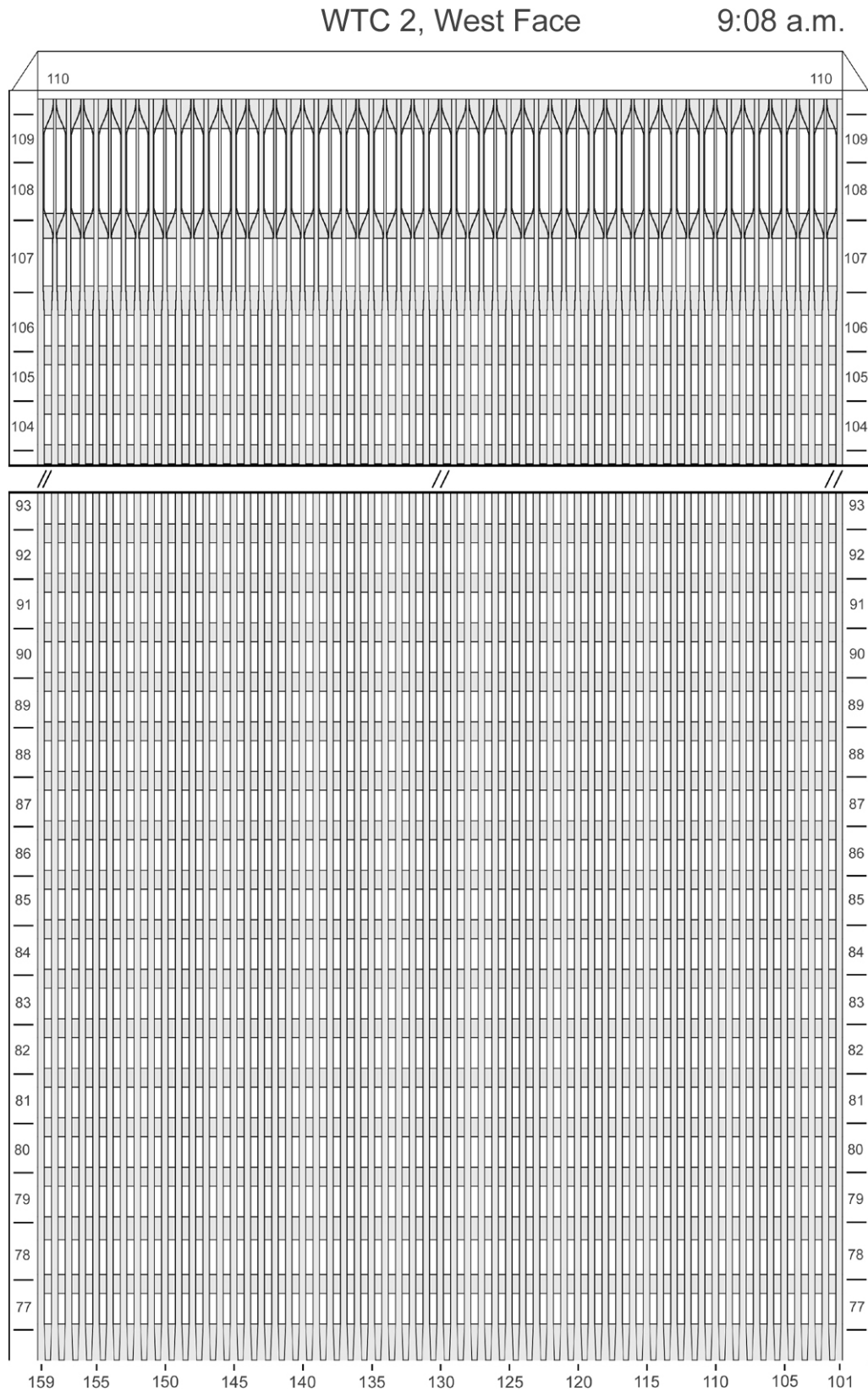


Figure J-8. Diagram of the west face of WTC 2 for floors 77 to 93 and floors 104 to 110 at 9:08 a.m. showing windows where smoke was observed and those hidden from view.

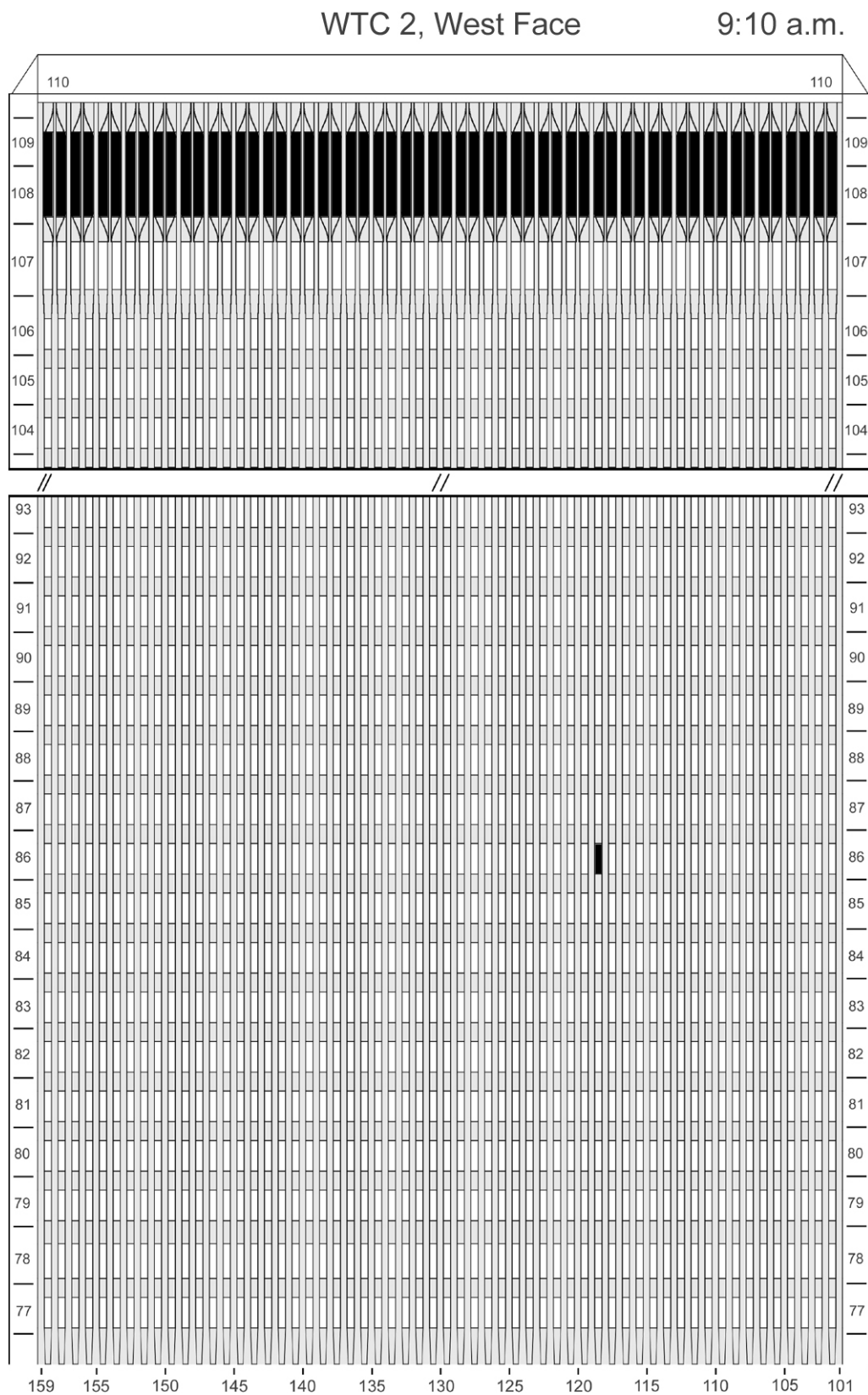


Figure J-9. Diagram of the west face of WTC 2 for floors 77 to 93 and floors 104 to 110 at 9:10 a.m. showing the condition of windows and locations of fires.

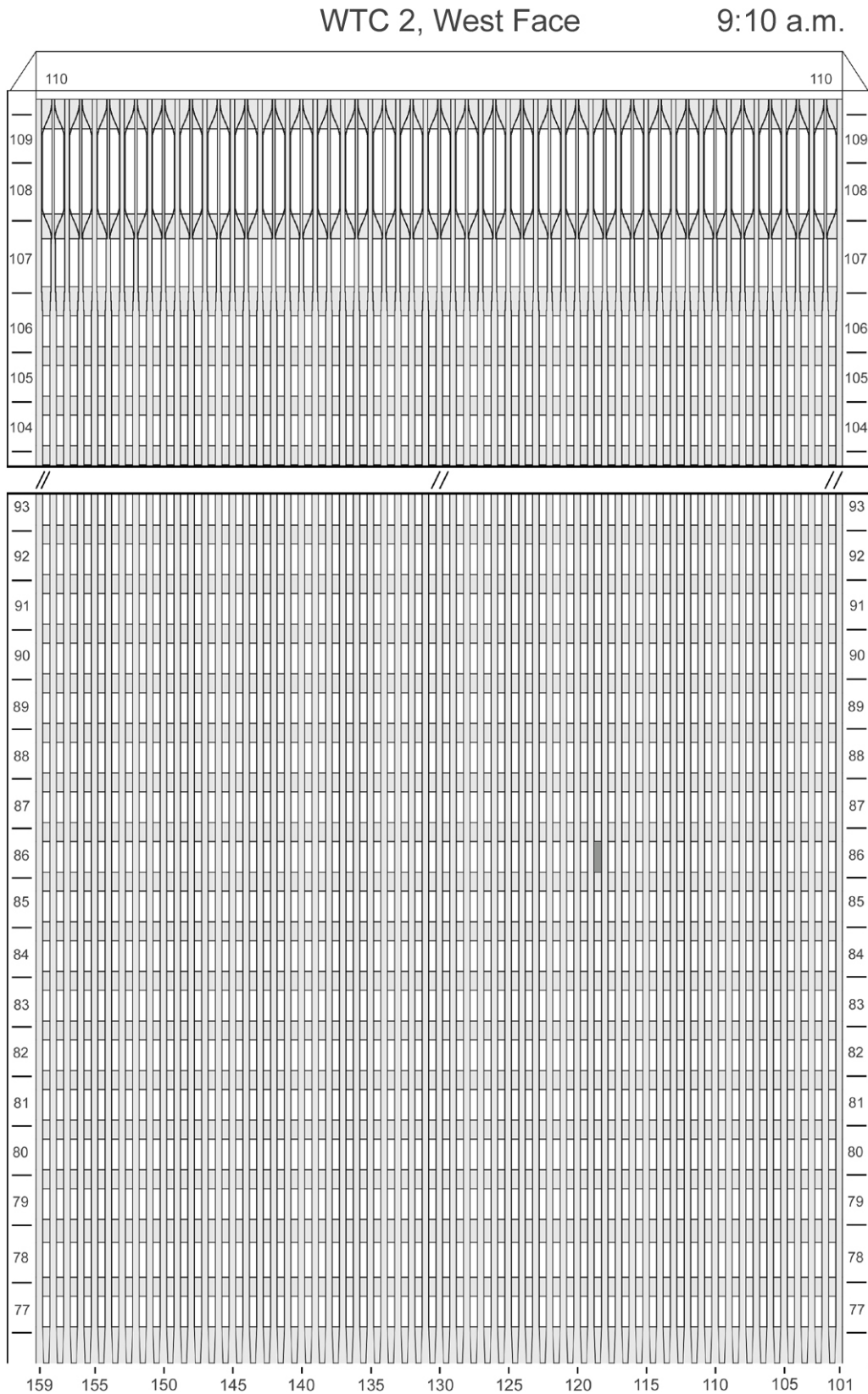
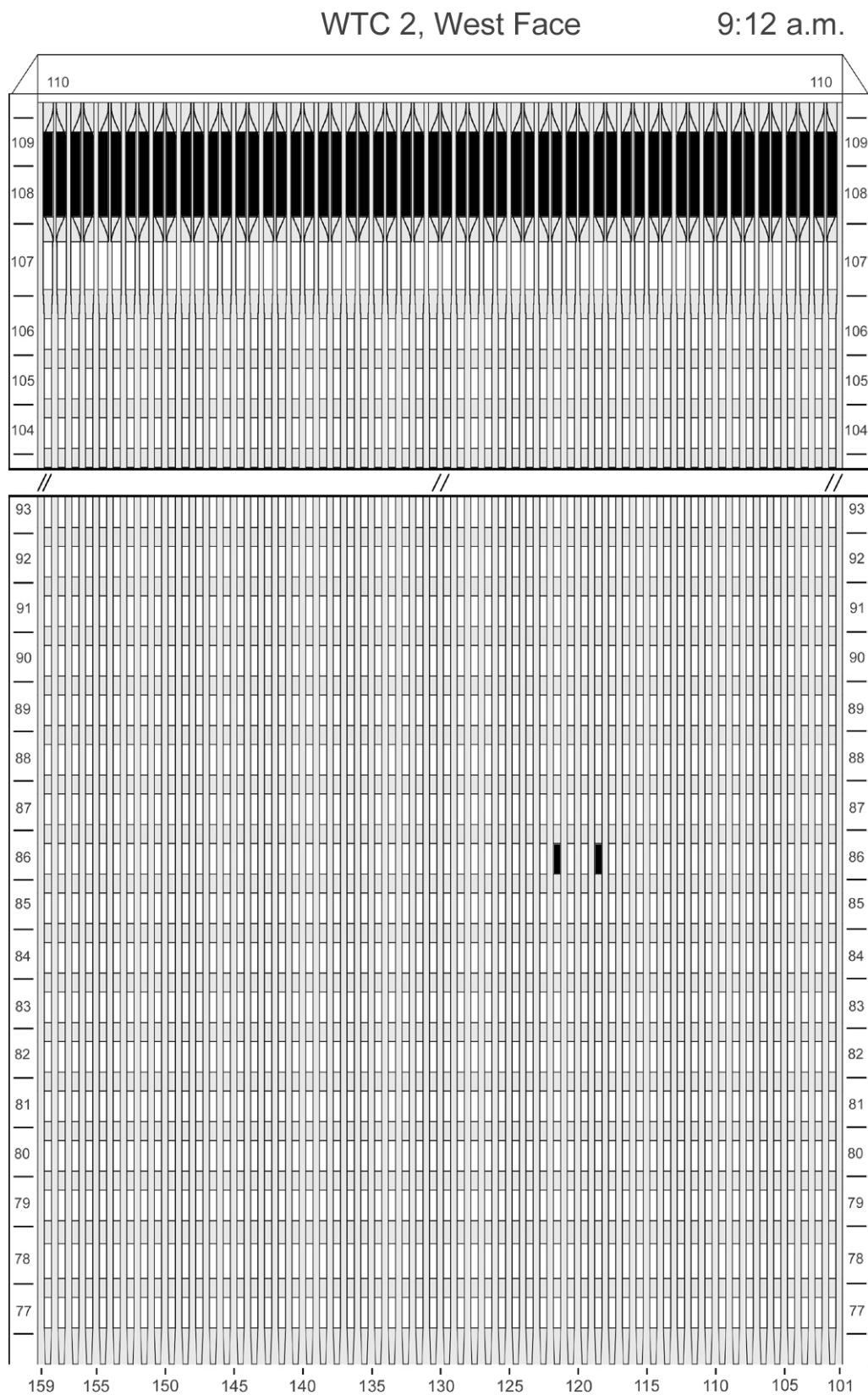


Figure J-10. Diagram of the west face of WTC 2 for floors 77 to 93 and floors 104 to 110 at 9:10 a.m. showing windows where smoke was observed and those hidden from view.



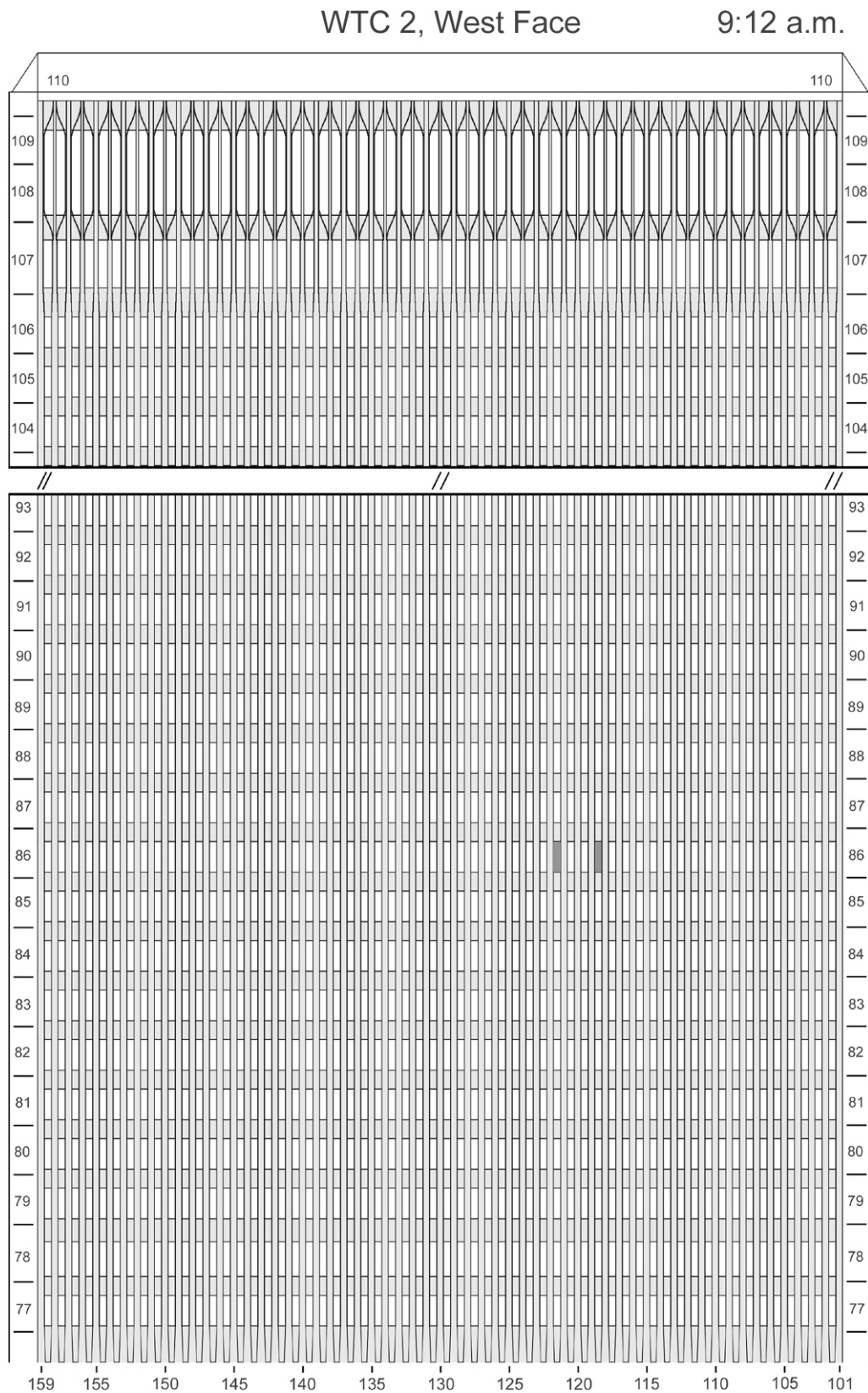


Figure J-12. Diagram of the west face of WTC 2 for floors 77 to 93 and floors 104 to 110 at 9:12 a.m. showing windows where smoke was observed and those hidden from view.

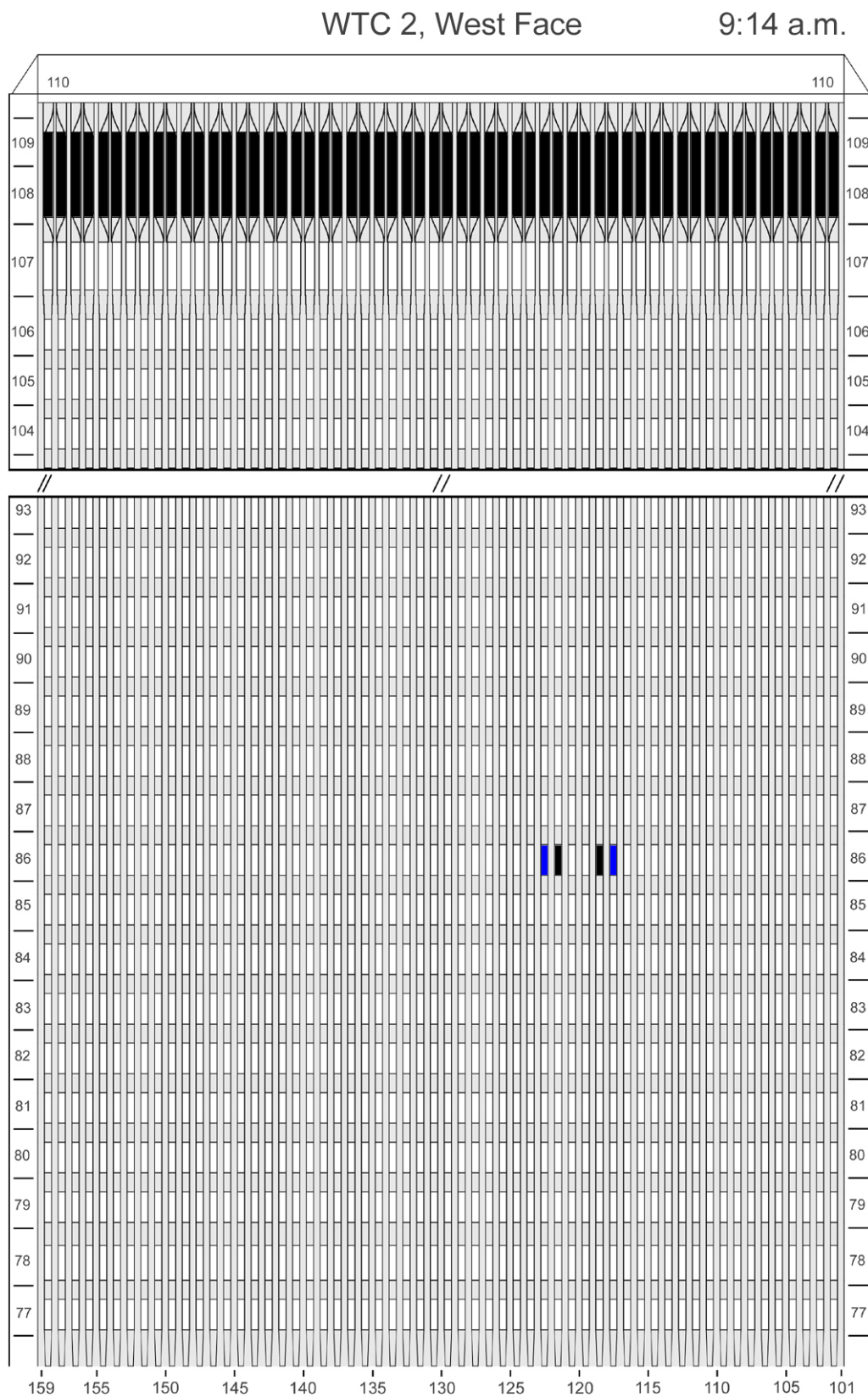


Figure J-13. Diagram of the west face of WTC 2 for floors 77 to 93 and floors 104 to 110 at 9:14 a.m. showing the condition of windows and locations of fires.

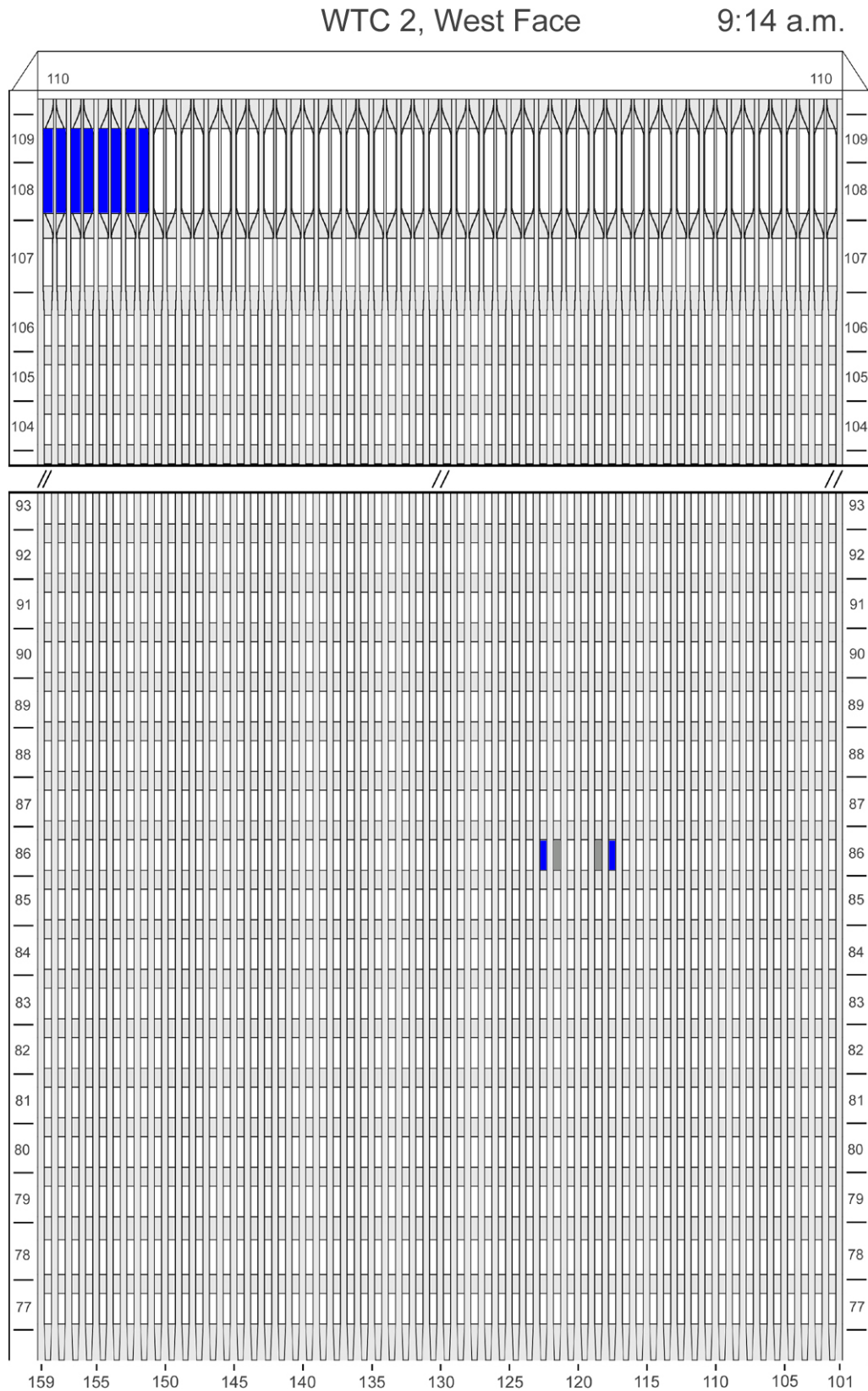


Figure J-14. Diagram of the west face of WTC 2 for floors 77 to 93 and floors 104 to 110 at 9:14 a.m. showing windows where smoke was observed and those hidden from view.

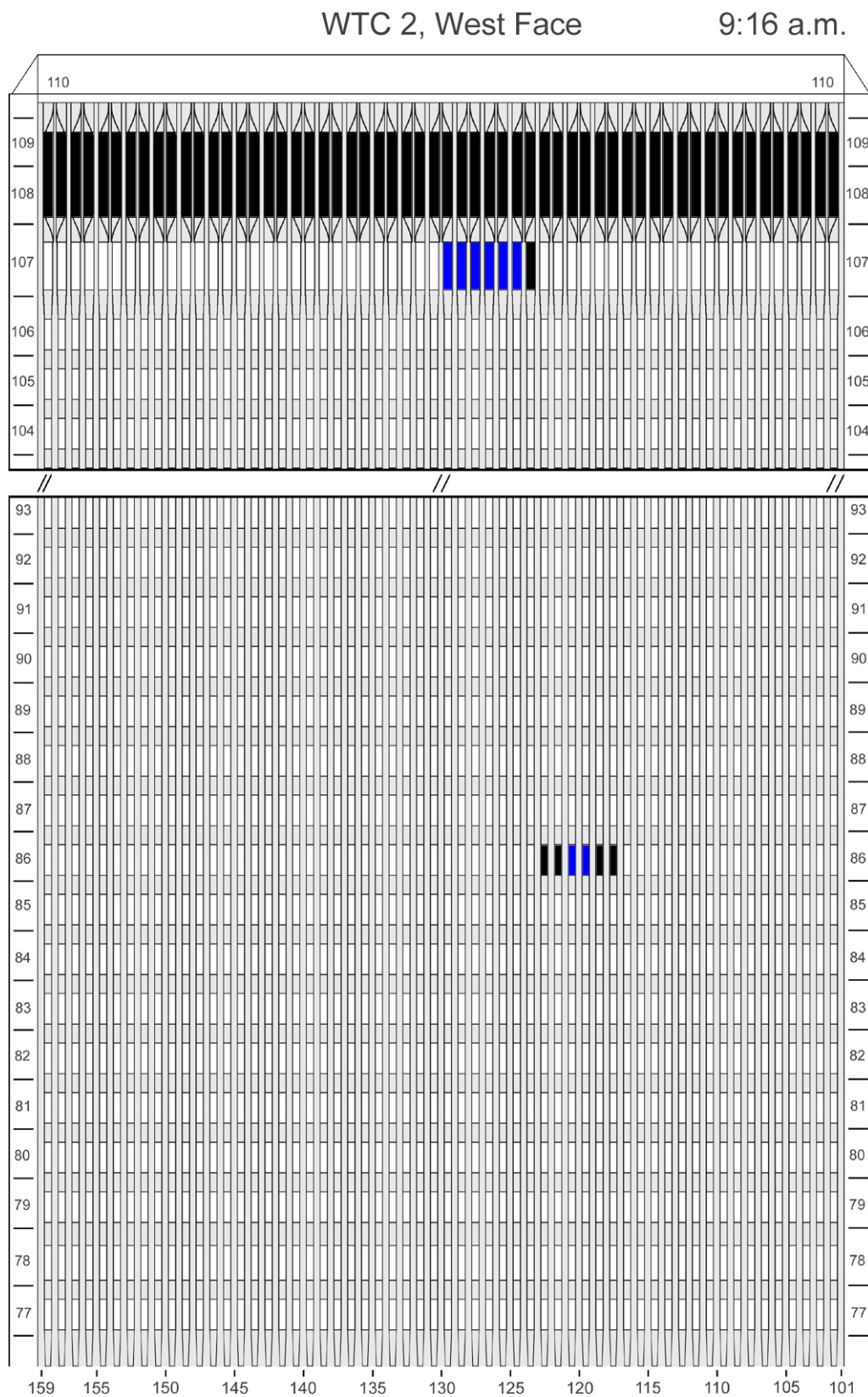


Figure J-15. Diagram of the west face of WTC 2 for floors 77 to 93 and floors 104 to 110 at 9:16 a.m. showing the condition of windows and locations of fires.

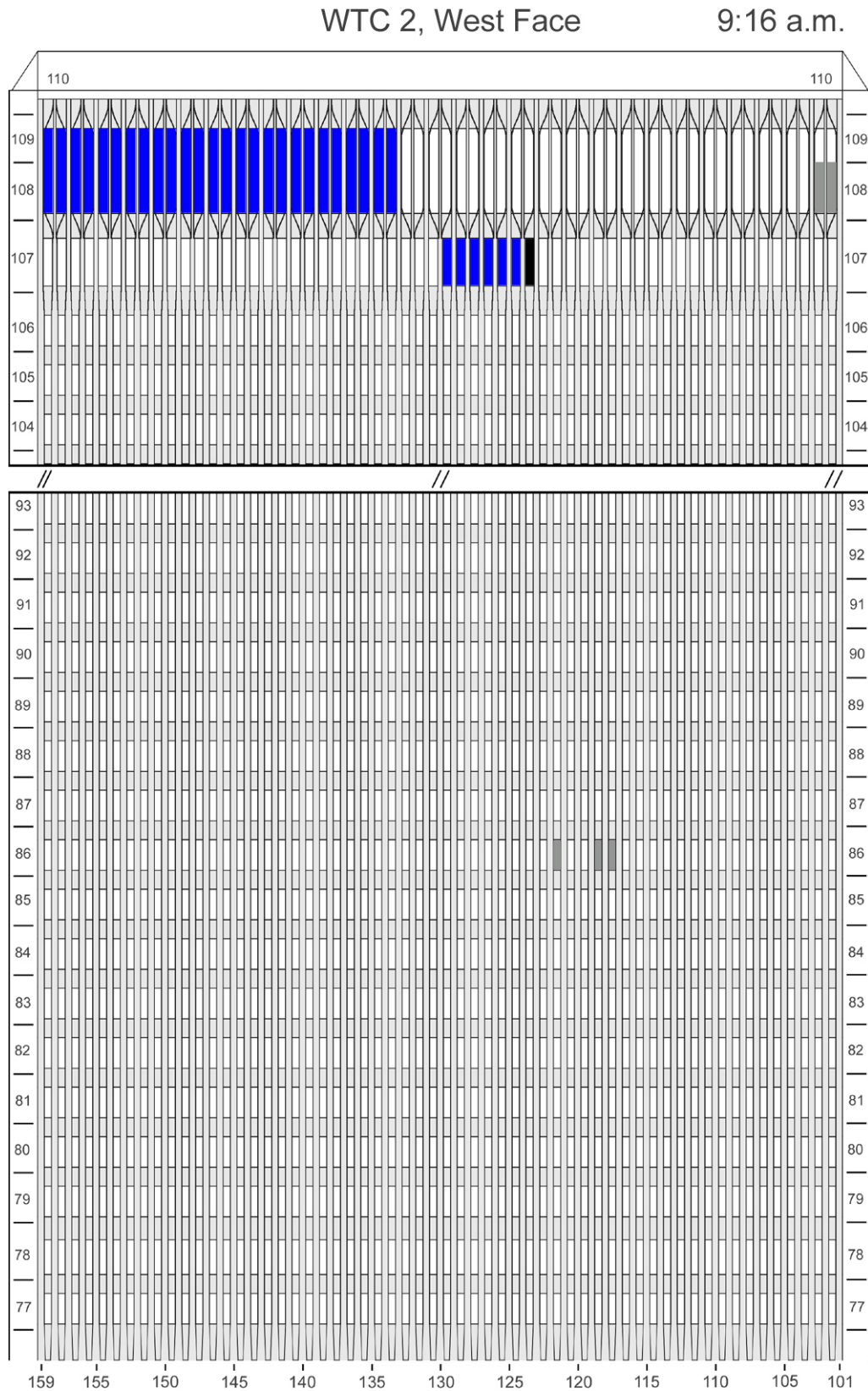


Figure J-16. Diagram of the west face of WTC 2 for floors 77 to 93 and floors 104 to 110 at 9:16 a.m. showing windows where smoke was observed and those hidden from view.

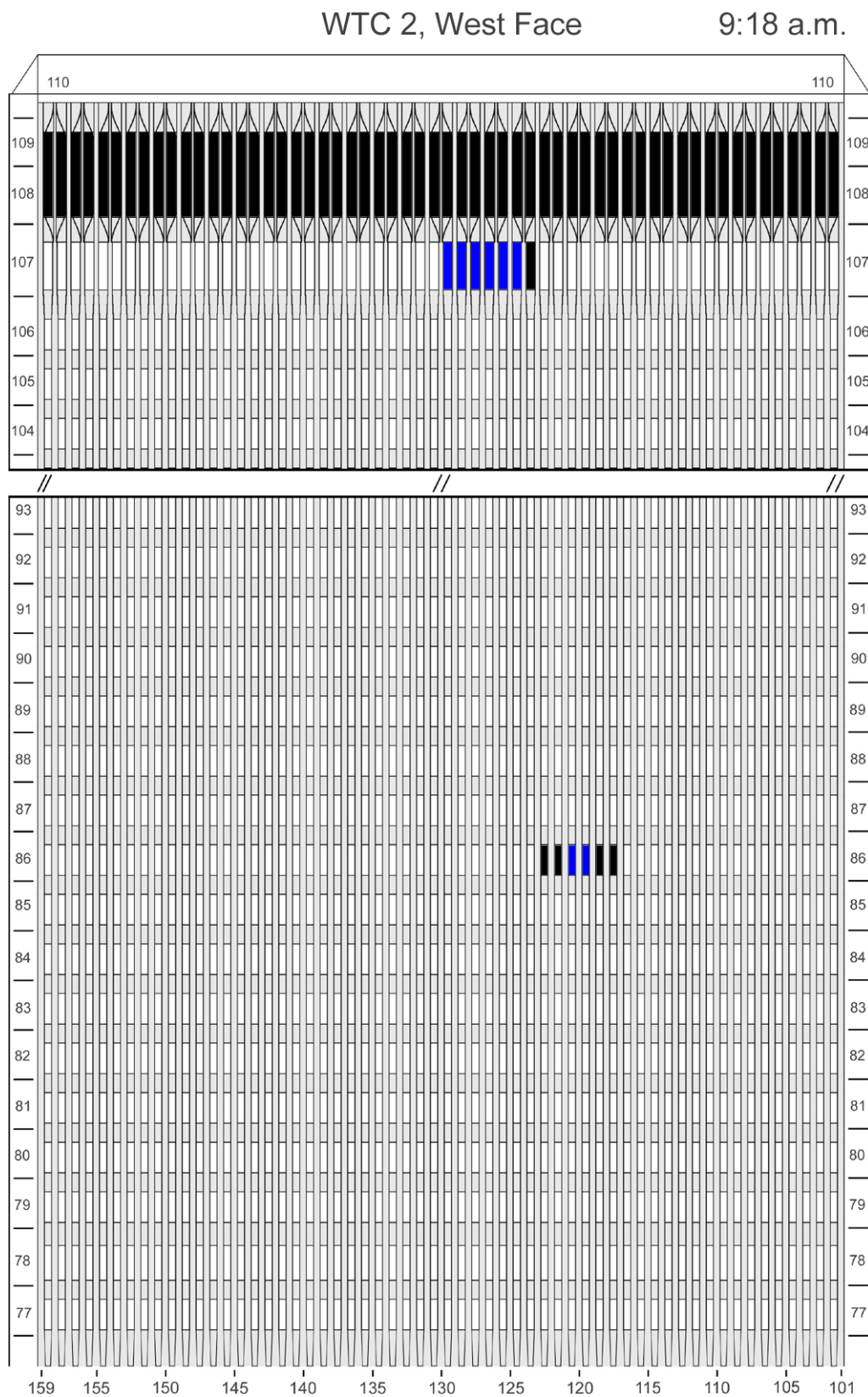


Figure J-17. Diagram of the west face of WTC 2 for floors 77 to 93 and floors 104 to 110 at 9:18 a.m. showing the condition of windows and locations of fires.

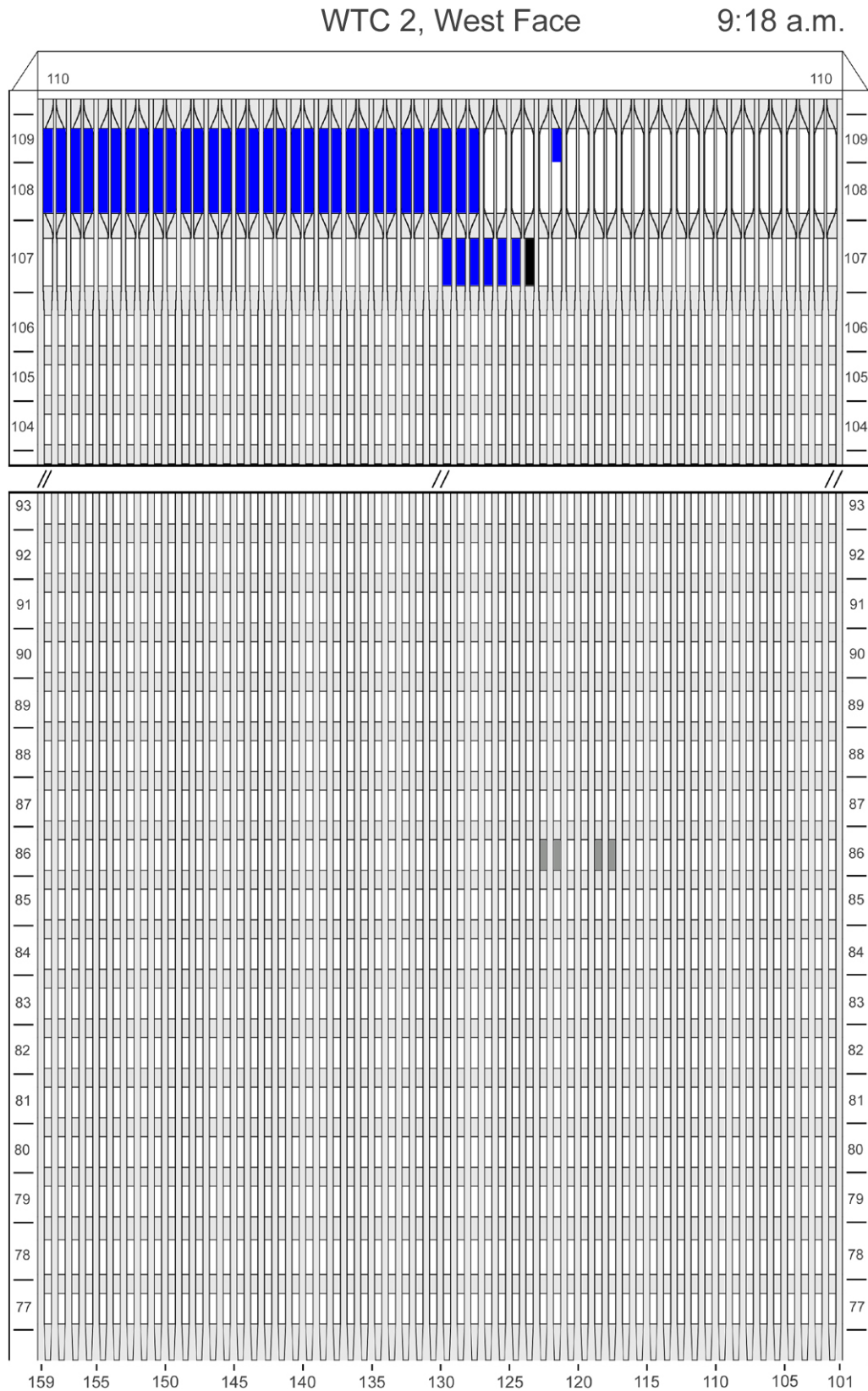


Figure J-18. Diagram of the west face of WTC 2 for floors 77 to 93 and floors 104 to 110 at 9:18 a.m. showing windows where smoke was observed and those hidden from view.

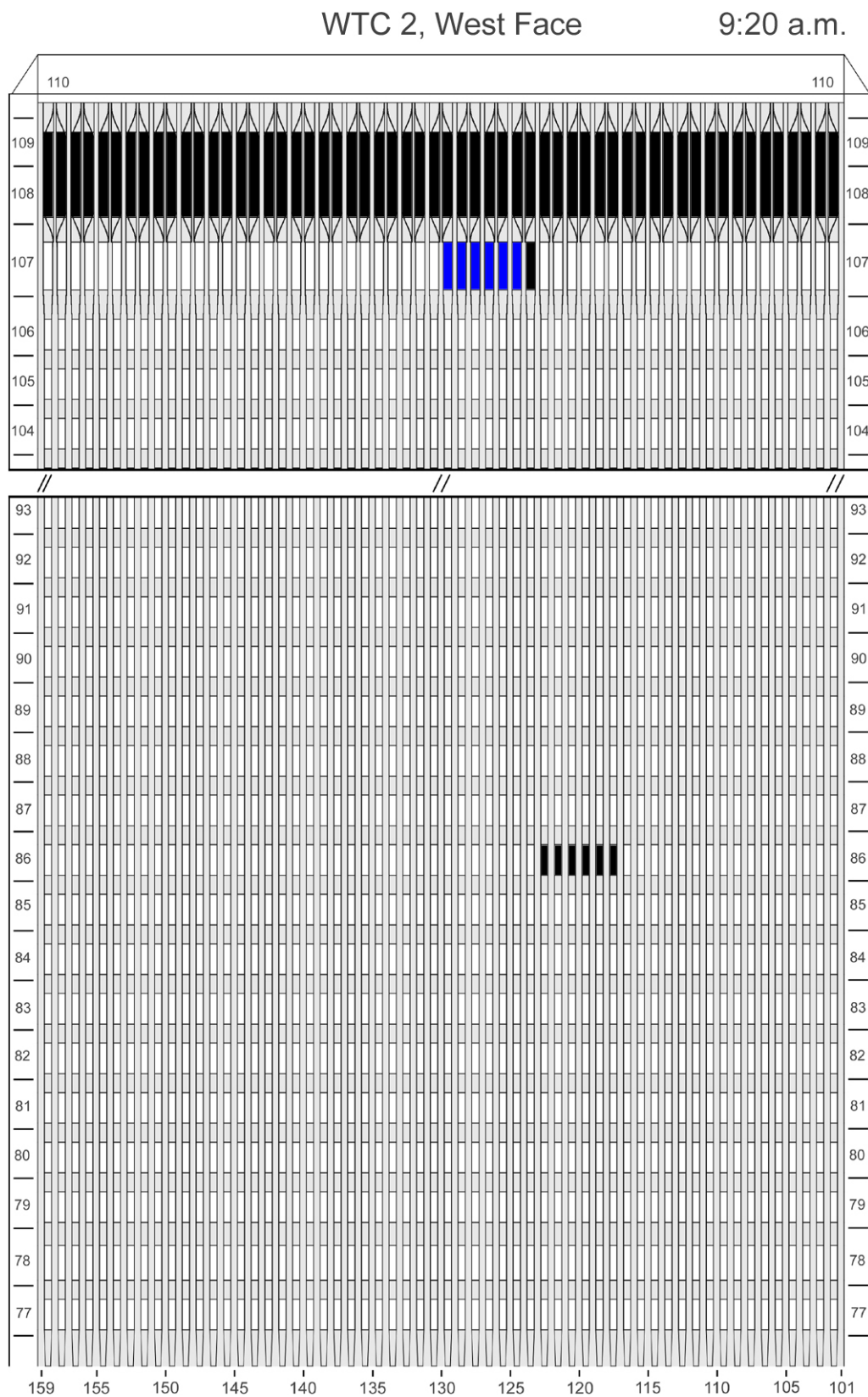


Figure J-19. Diagram of the west face of WTC 2 for floors 77 to 93 and floors 104 to 110 at 9:20 a.m. showing the condition of windows and locations of fires.

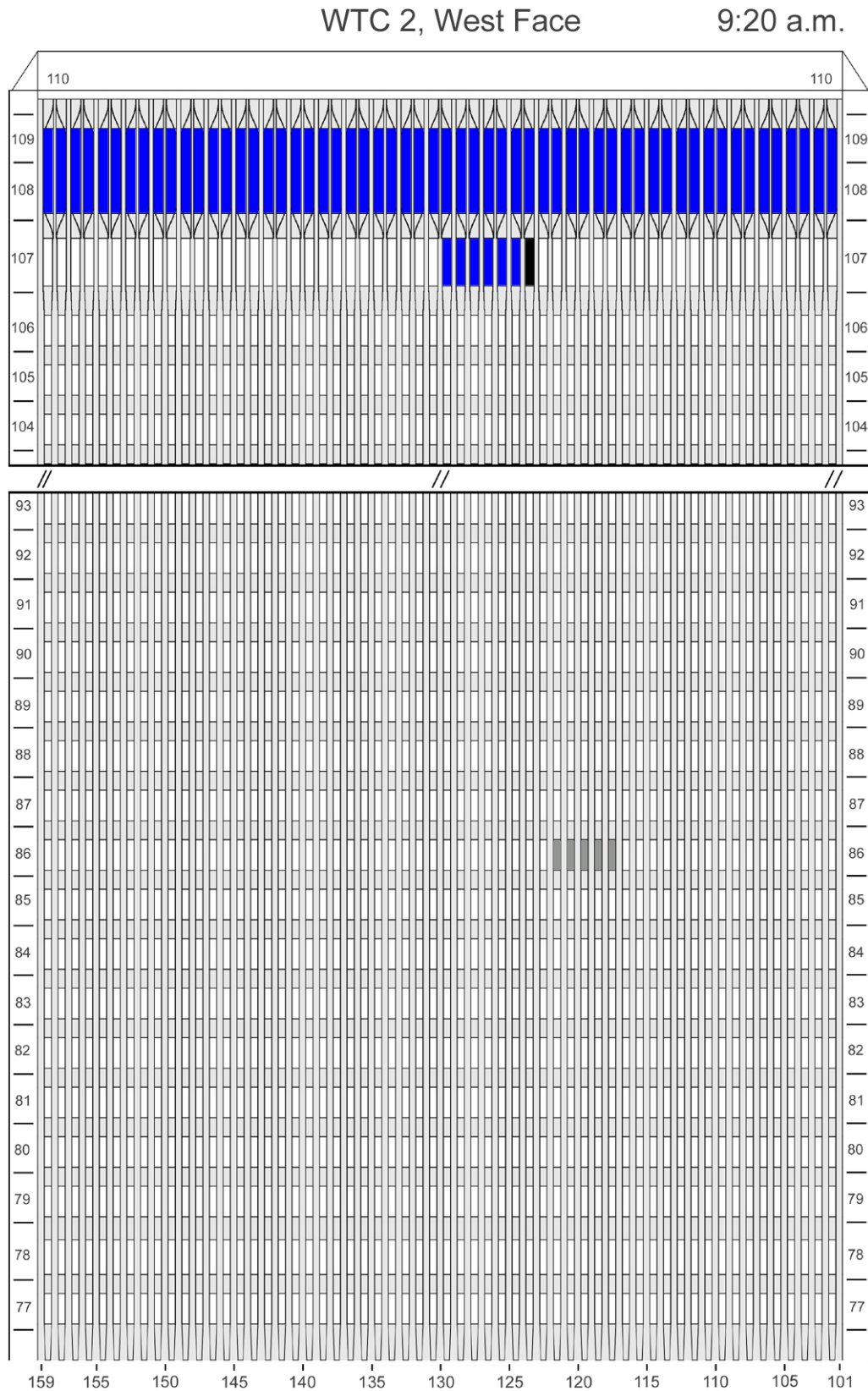


Figure J-20. Diagram of the west face of WTC 2 for floors 77 to 93 and floors 104 to 110 at 9:20 a.m. showing windows where smoke was observed and those hidden from view.

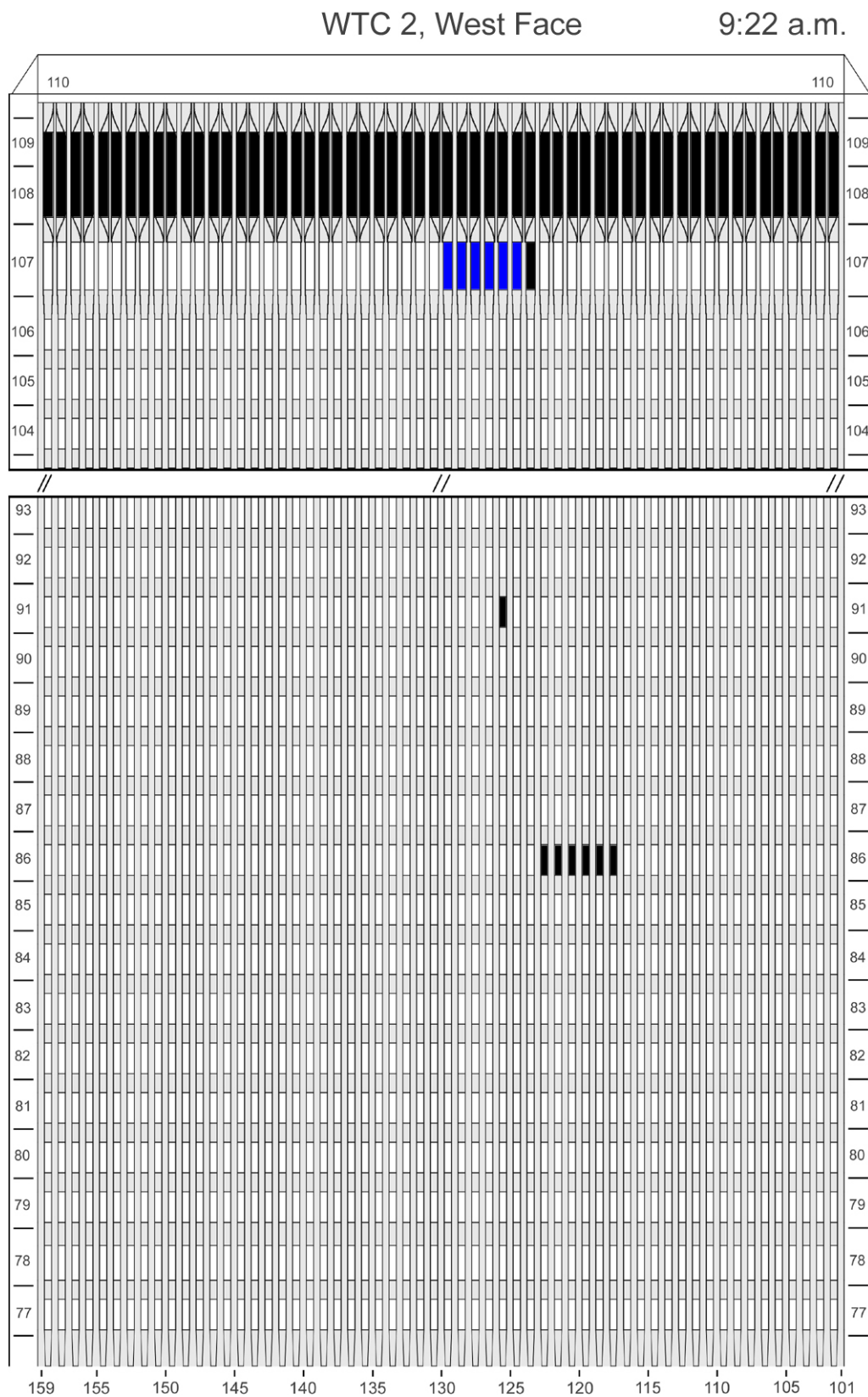


Figure J-21. Diagram of the west face of WTC 2 for floors 77 to 93 and floors 104 to 110 at 9:22 a.m. showing the condition of windows and locations of fires.

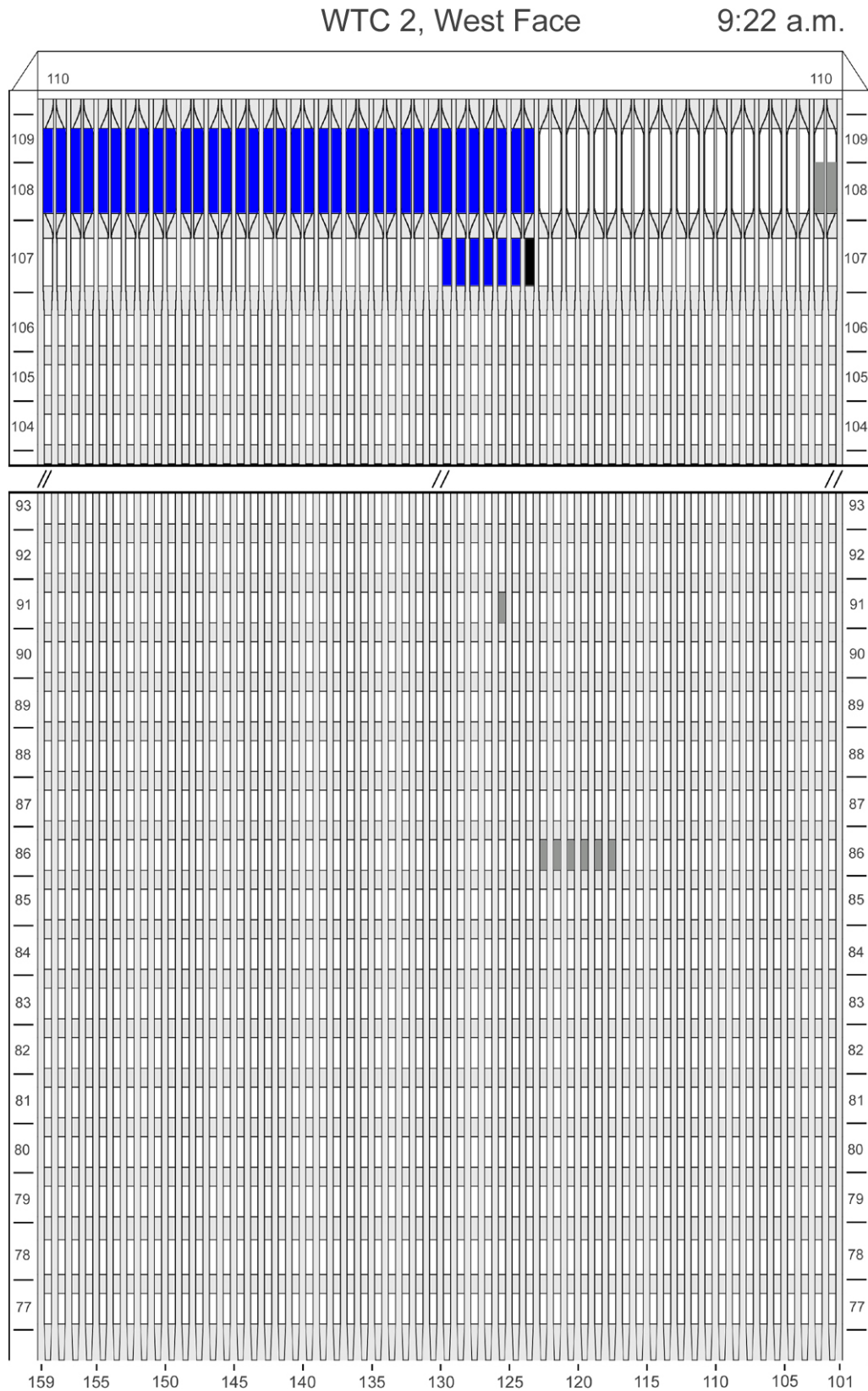


Figure J-22. Diagram of the west face of WTC 2 for floors 77 to 93 and floors 104 to 110 at 9:22 a.m. showing windows where smoke was observed and those hidden from view.

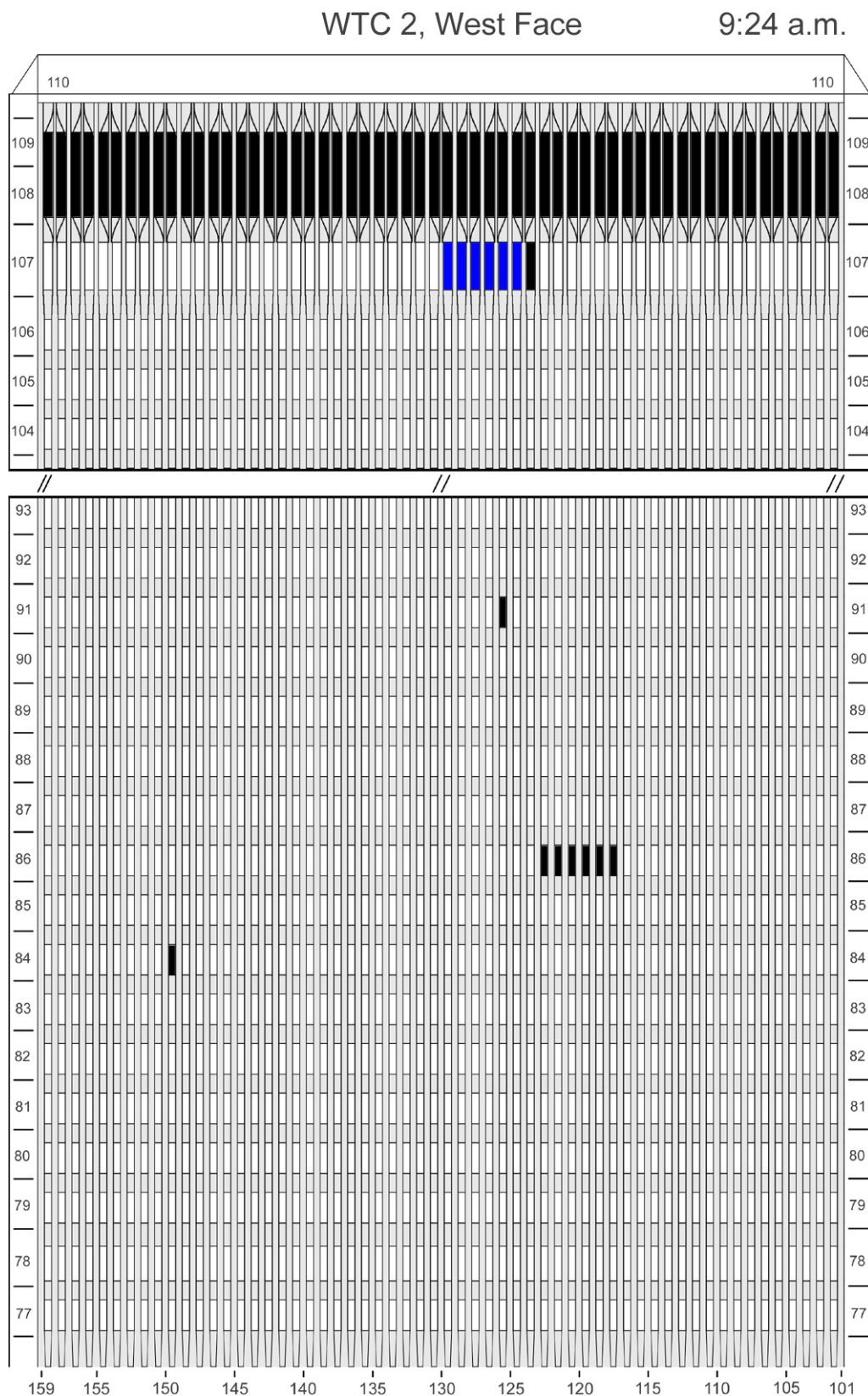


Figure J-23. Diagram of the west face of WTC 2 for floors 77 to 93 and floors 104 to 110 at 9:24 a.m. showing the condition of windows and locations of fires.

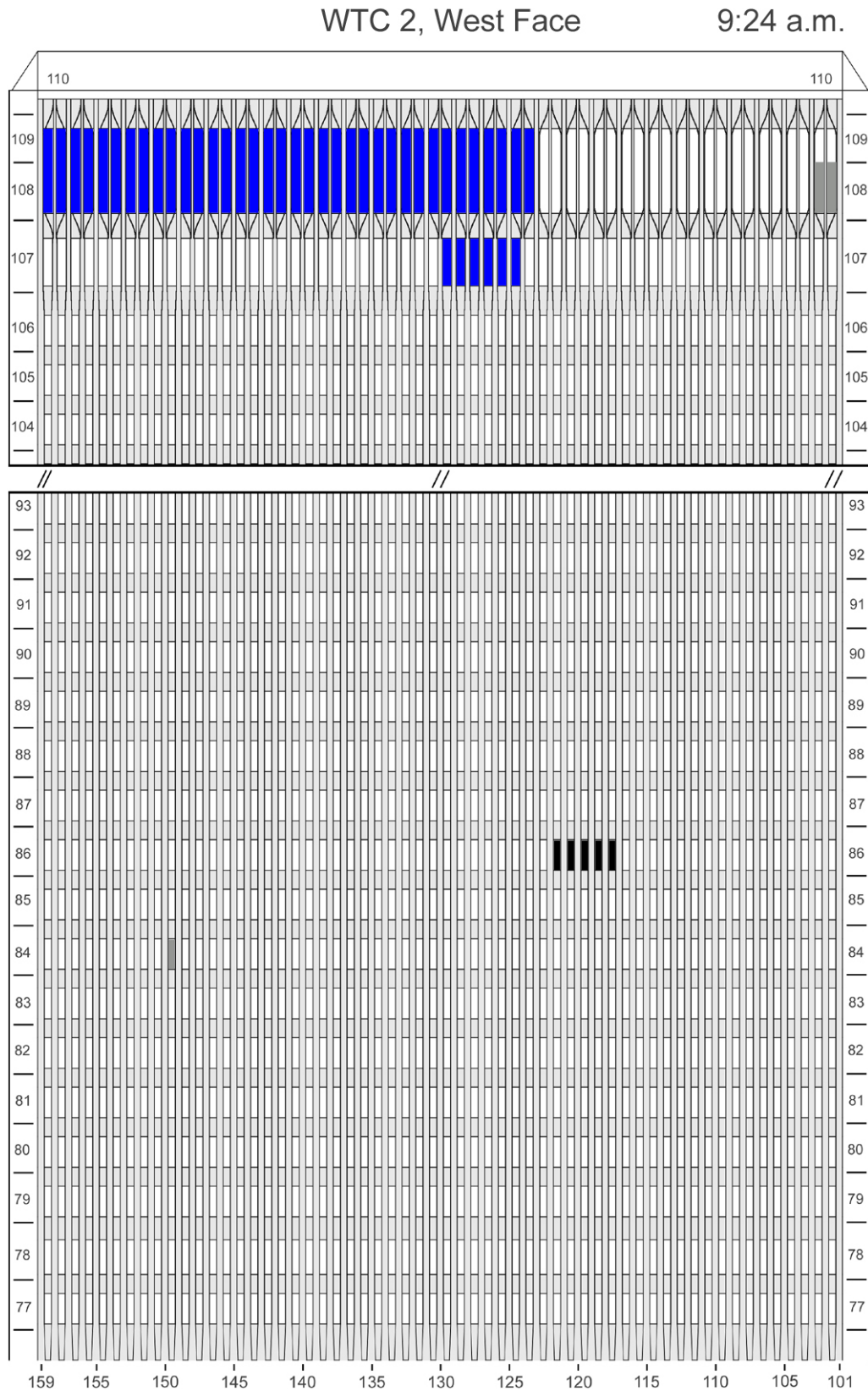


Figure J-24. Diagram of the west face of WTC 2 for floors 77 to 93 and floors 104 to 110 at 9:24 a.m. showing windows where smoke was observed and those hidden from view.

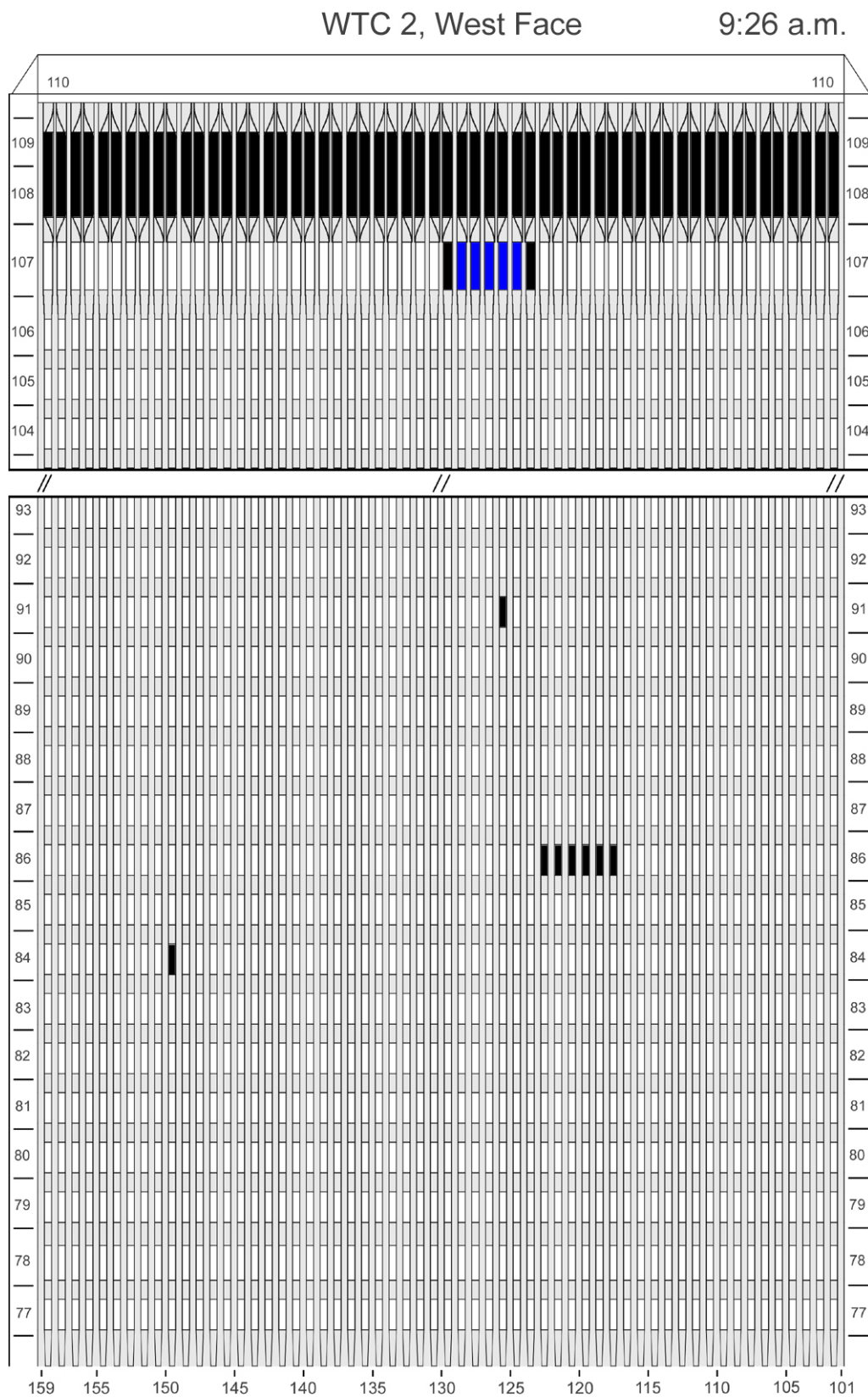


Figure J-25. Diagram of the west face of WTC 2 for floors 77 to 93 and floors 104 to 110 at 9:26 a.m. showing the condition of windows and locations of fires.

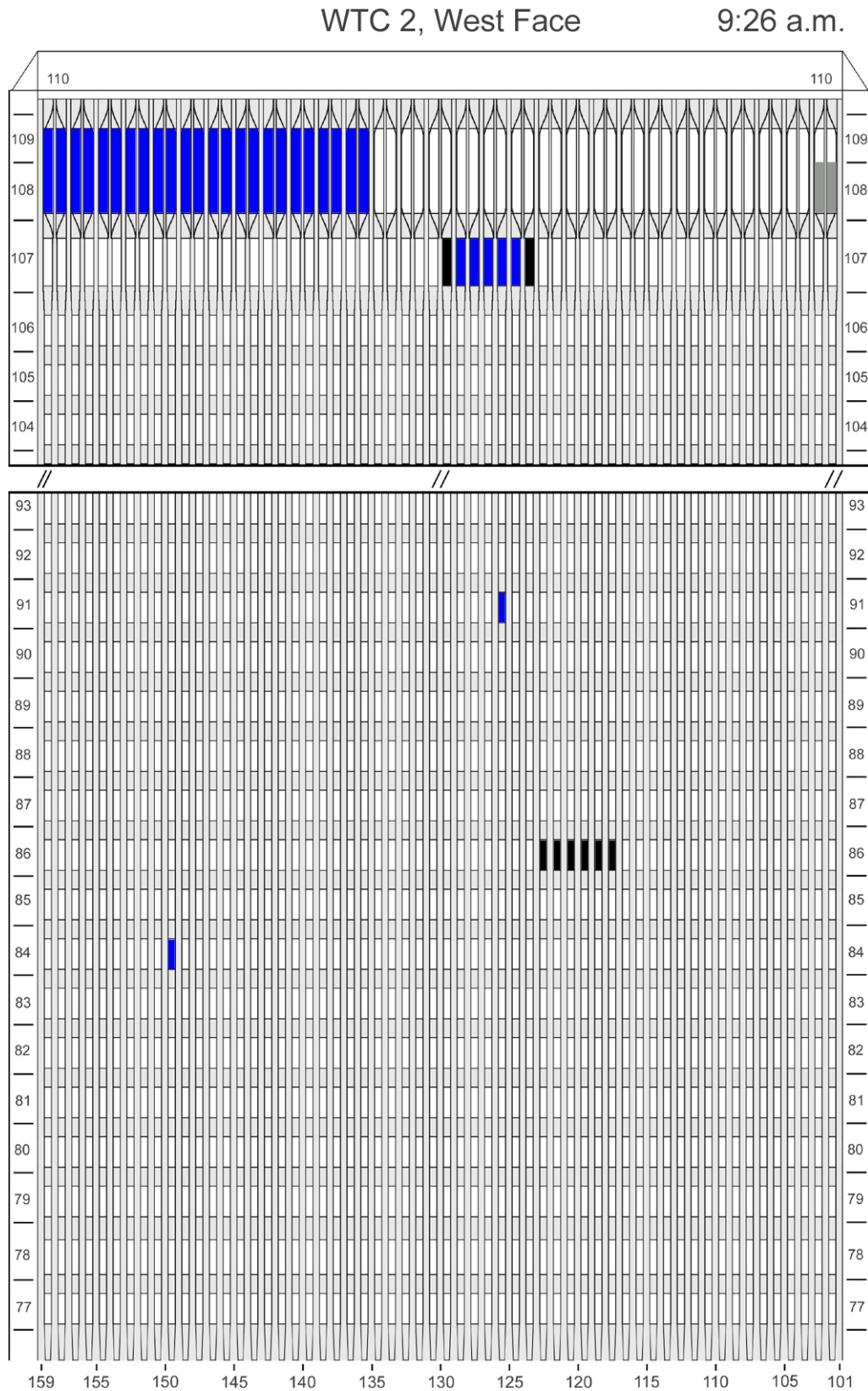


Figure J-26. Diagram of the west face of WTC 2 for floors 77 to 93 and floors 104 to 110 at 9:26 a.m. showing windows where smoke was observed and those hidden from view.

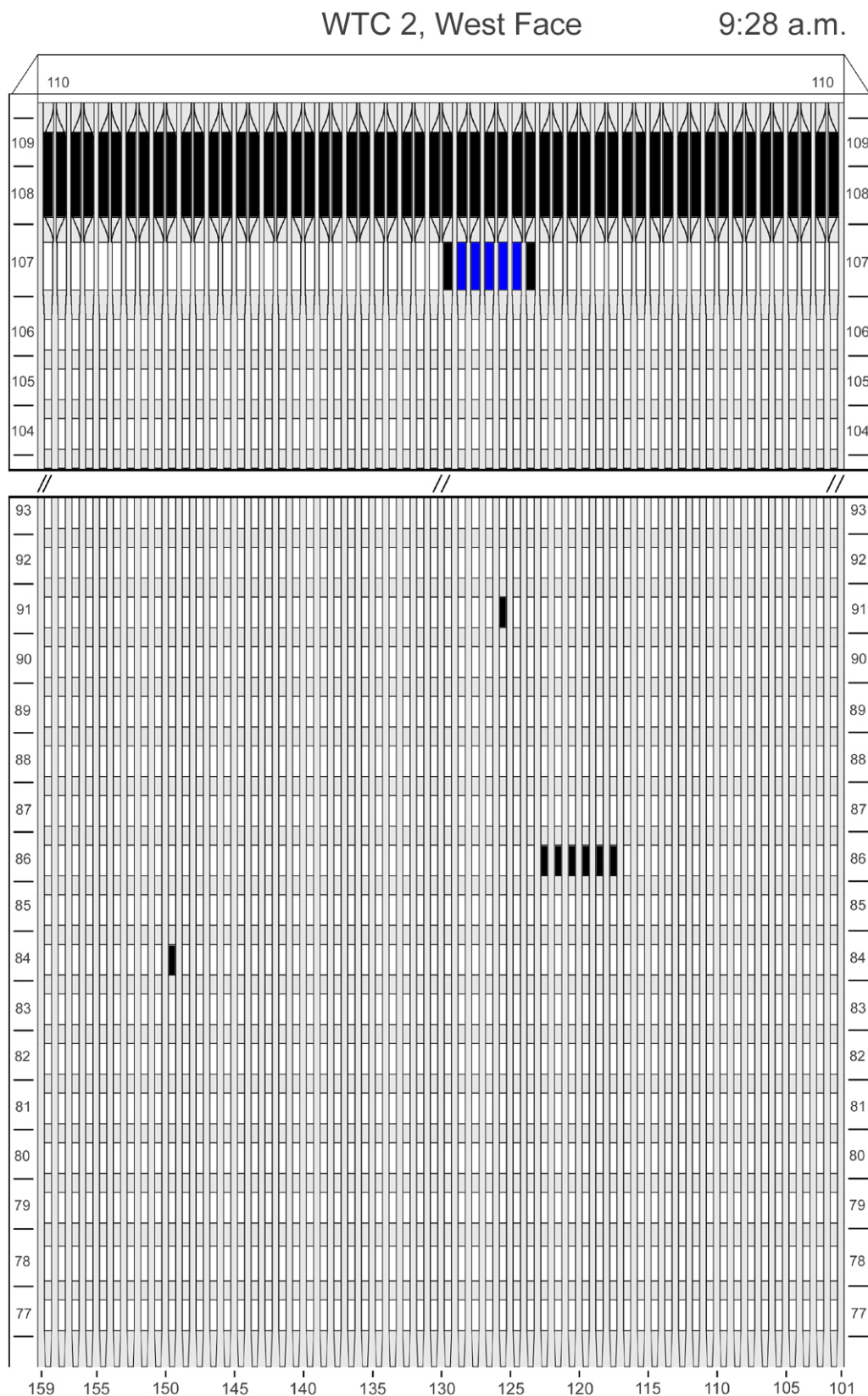


Figure J-27. Diagram of the west face of WTC 2 for floors 77 to 93 and floors 104 to 110 at 9:28 a.m. showing the condition of windows and locations of fires.

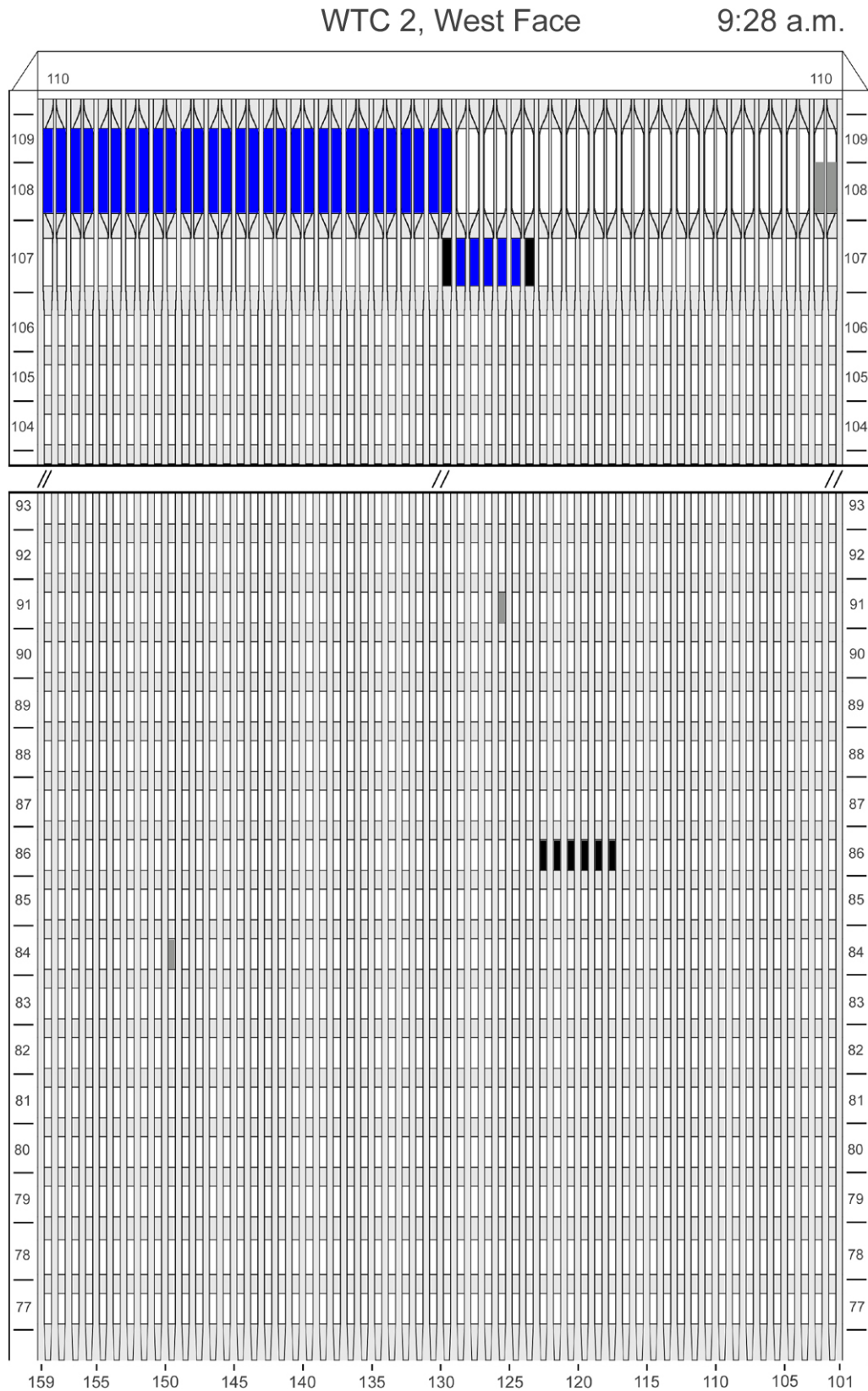


Figure J-28. Diagram of the west face of WTC 2 for floors 77 to 93 and floors 104 to 110 at 9:28 a.m. showing windows where smoke was observed and those hidden from view.

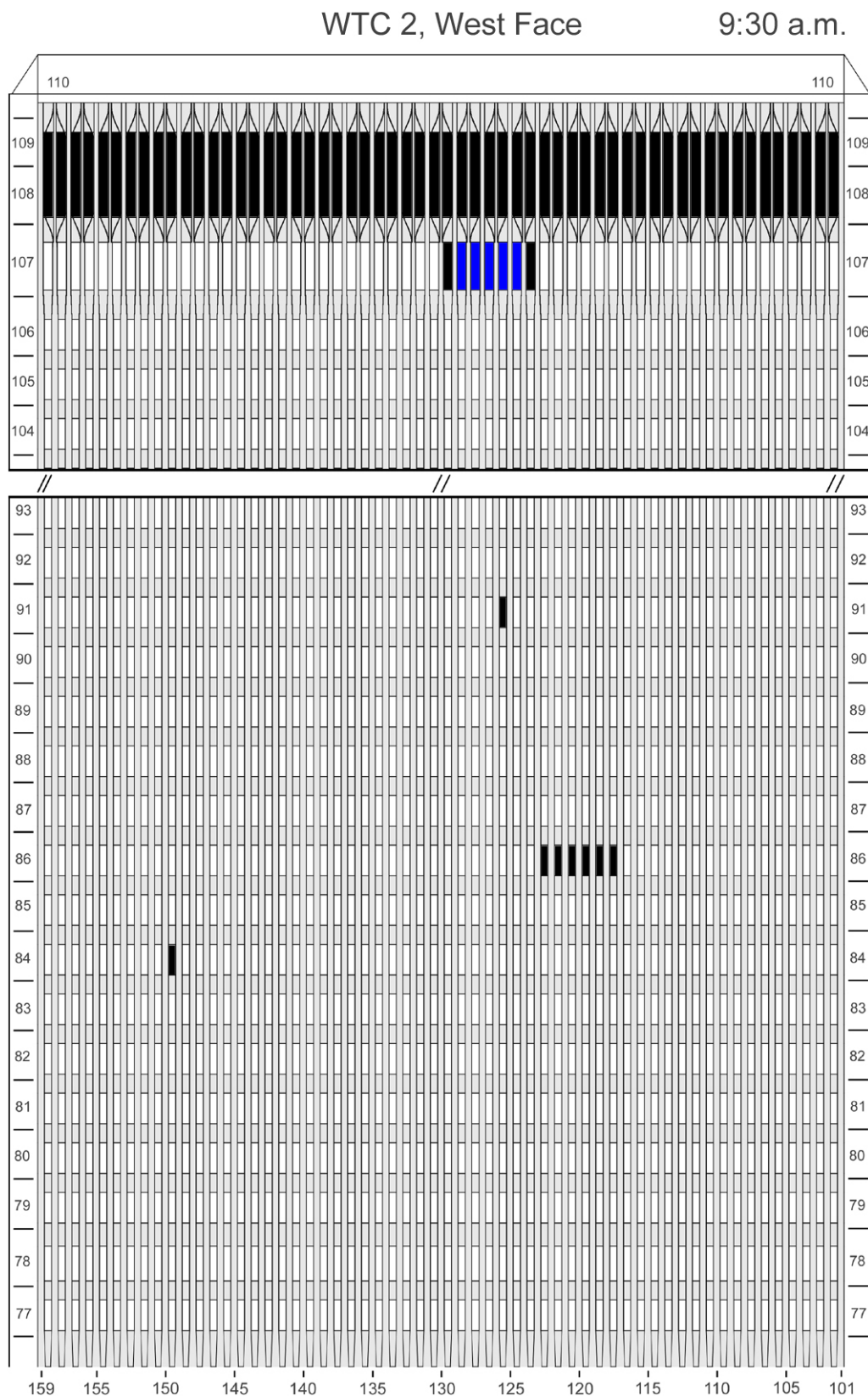


Figure J-29. Diagram of the west face of WTC 2 for floors 77 to 93 and floors 104 to 110 at 9:30 a.m. showing the condition of windows and locations of fires.

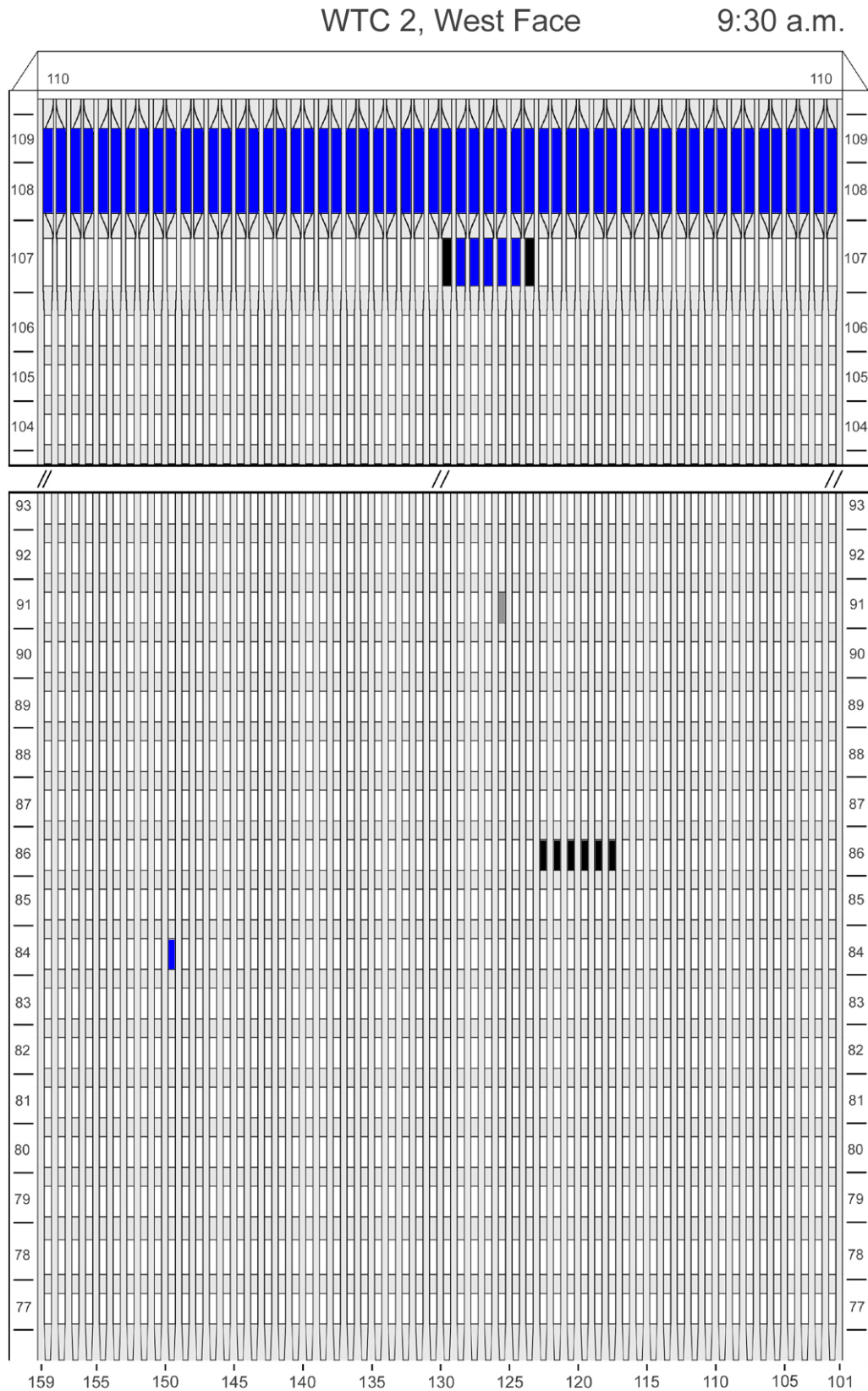


Figure J-30. Diagram of the west face of WTC 2 for floors 77 to 93 and floors 104 to 110 at 9:30 a.m. showing windows where smoke was observed and those hidden from view.

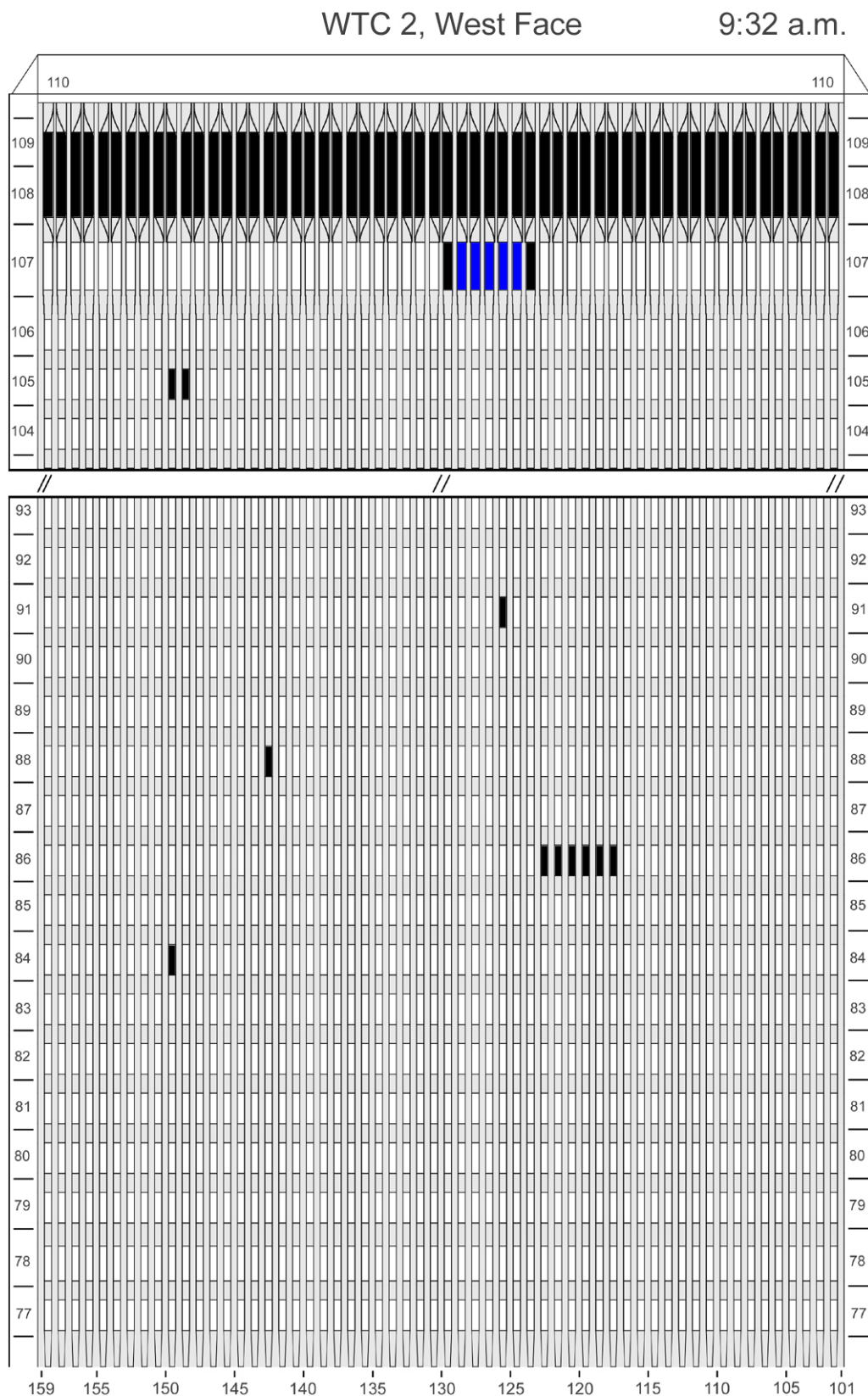


Figure J-31. Diagram of the west face of WTC 2 for floors 77 to 93 and floors 104 to 110 at 9:32 a.m. showing the condition of windows and locations of fires.

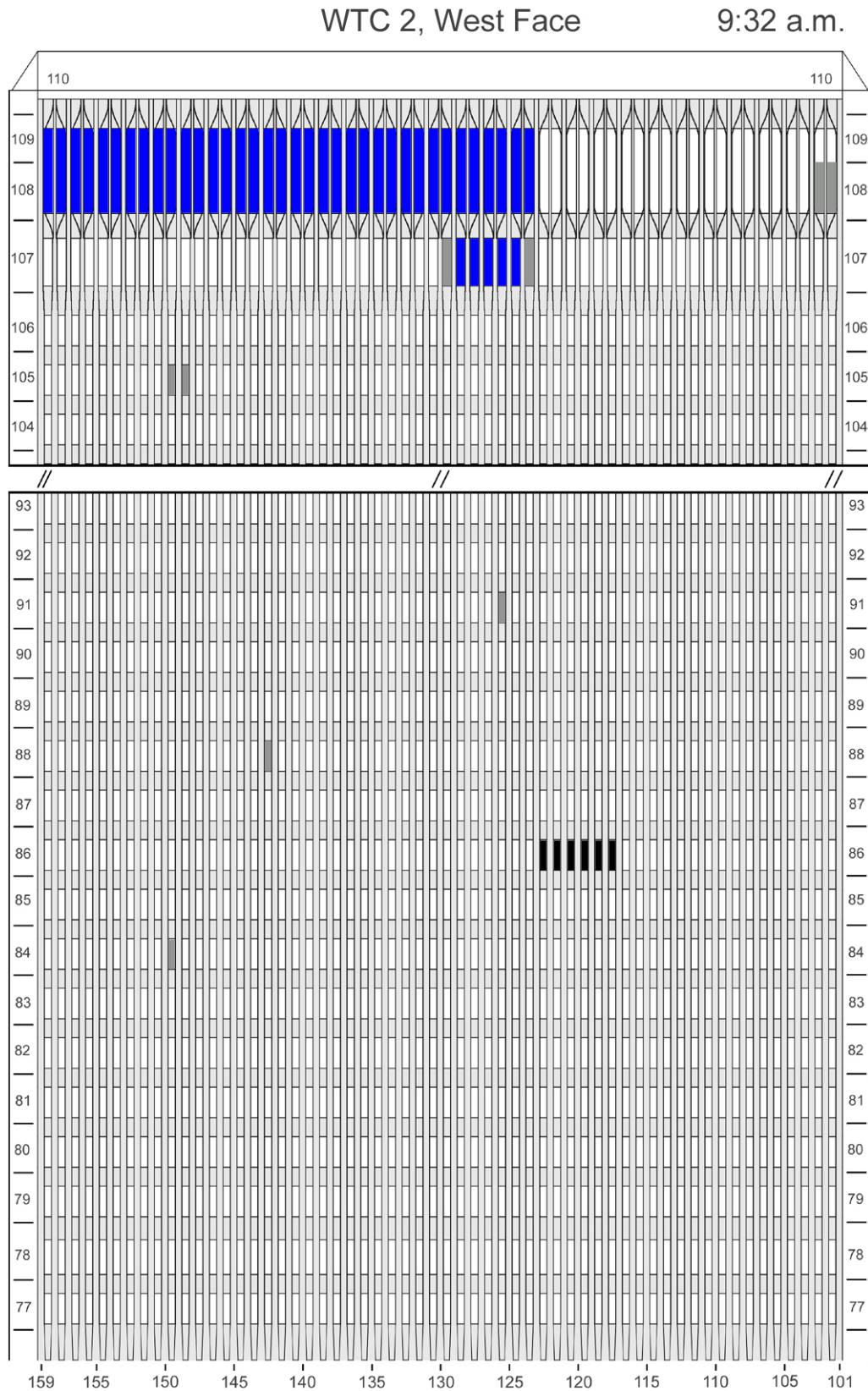


Figure J-32. Diagram of the west face of WTC 2 for floors 77 to 93 and floors 104 to 110 at 9:32 a.m. showing windows where smoke was observed and those hidden from view.

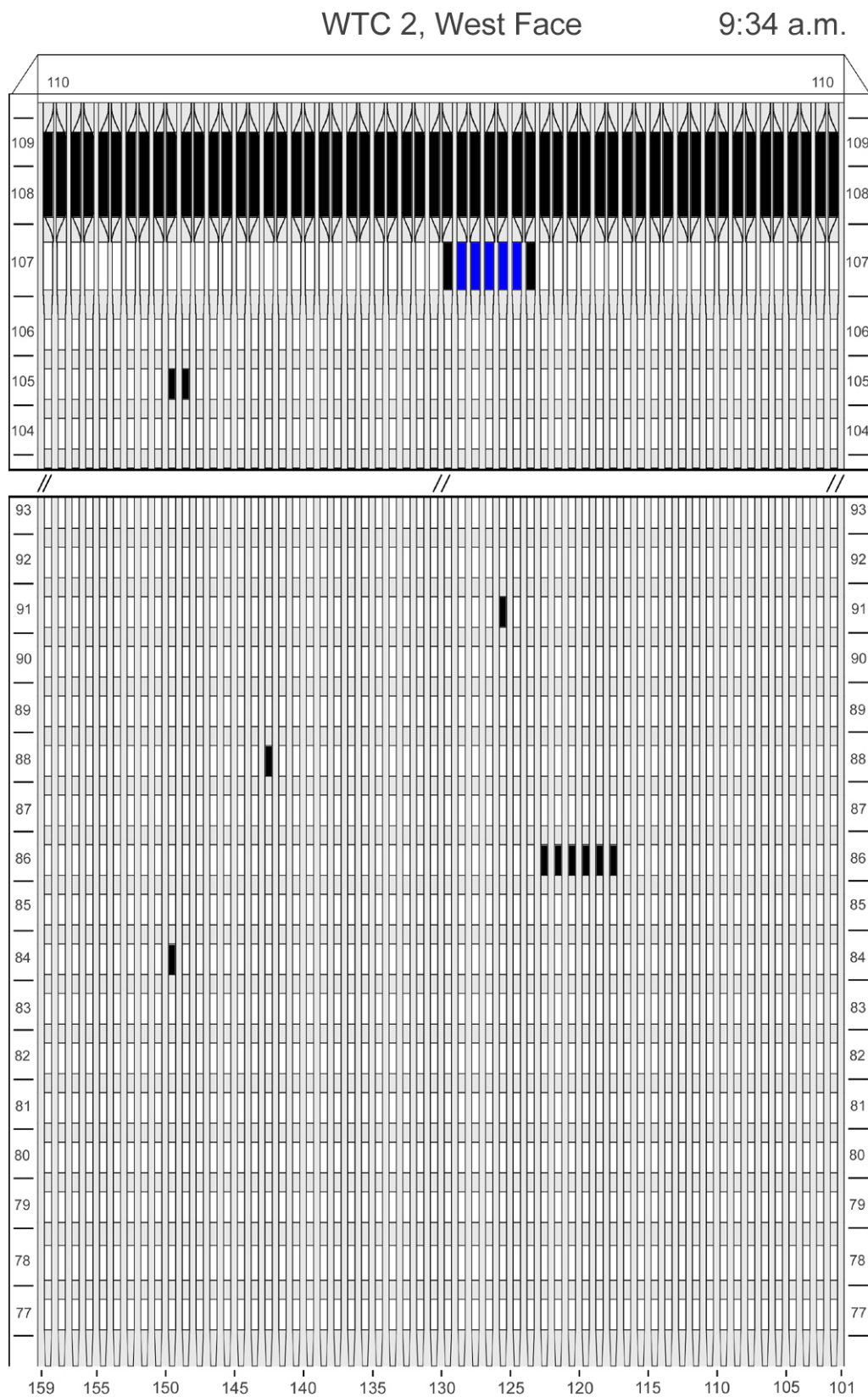


Figure J-33. Diagram of the west face of WTC 2 for floors 77 to 93 and floors 104 to 110 at 9:34 a.m. showing the condition of windows and locations of fires.

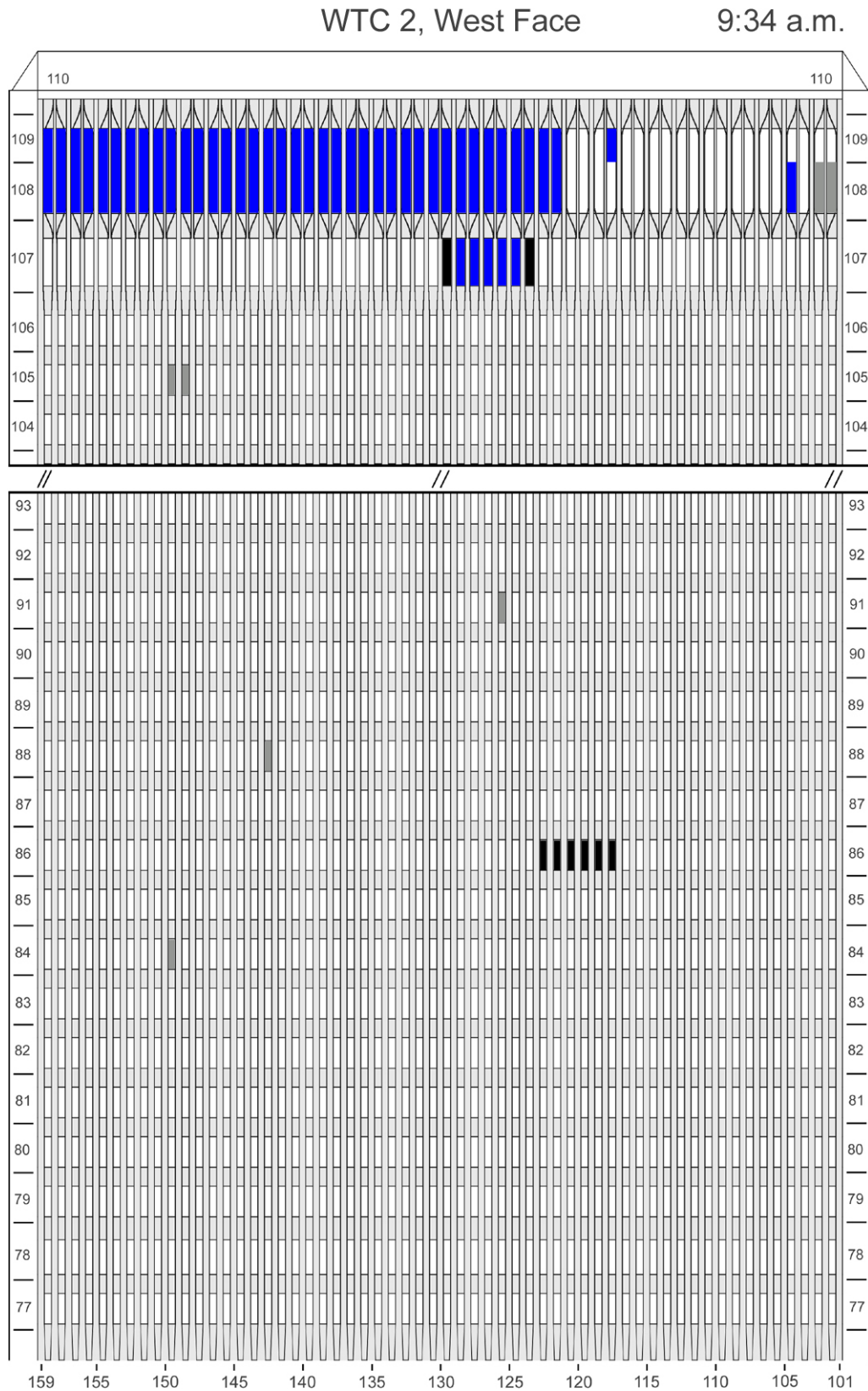


Figure J-34. Diagram of the west face of WTC 2 for floors 77 to 93 and floors 104 to 110 at 9:34 a.m. showing windows where smoke was observed and those hidden from view.

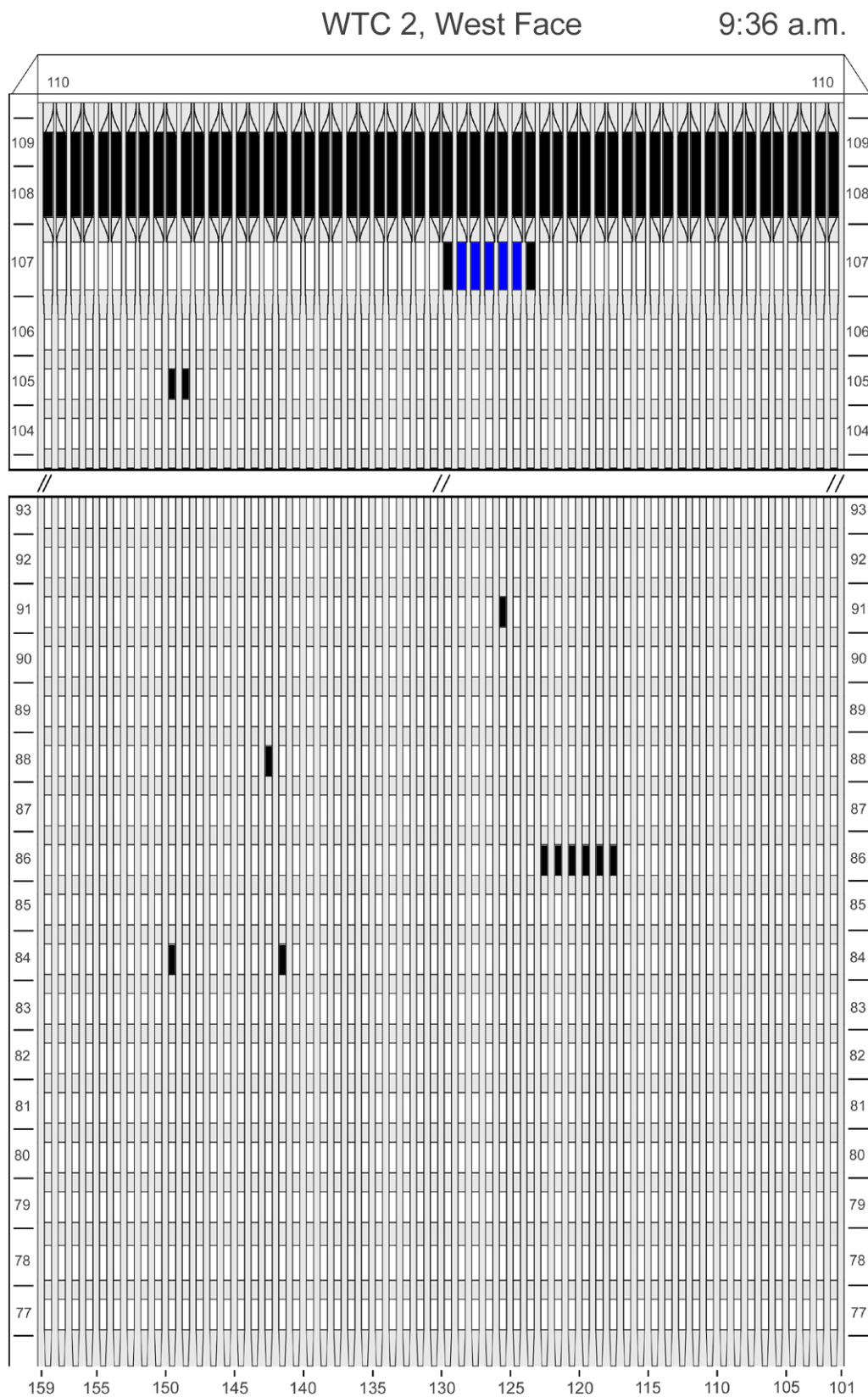


Figure J-35. Diagram of the west face of WTC 2 for floors 77 to 93 and floors 104 to 110 at 9:36 a.m. showing the condition of windows and locations of fires.

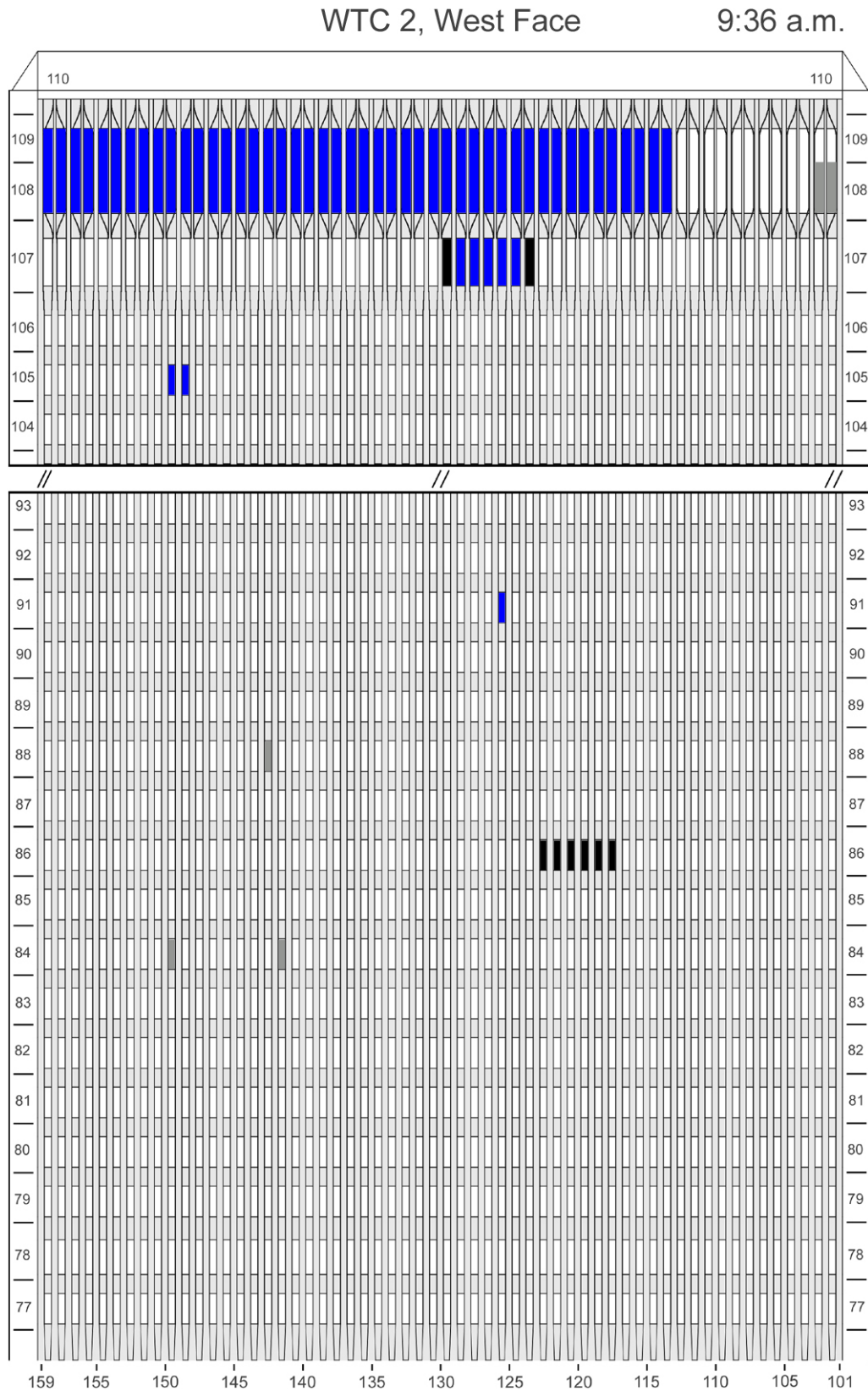
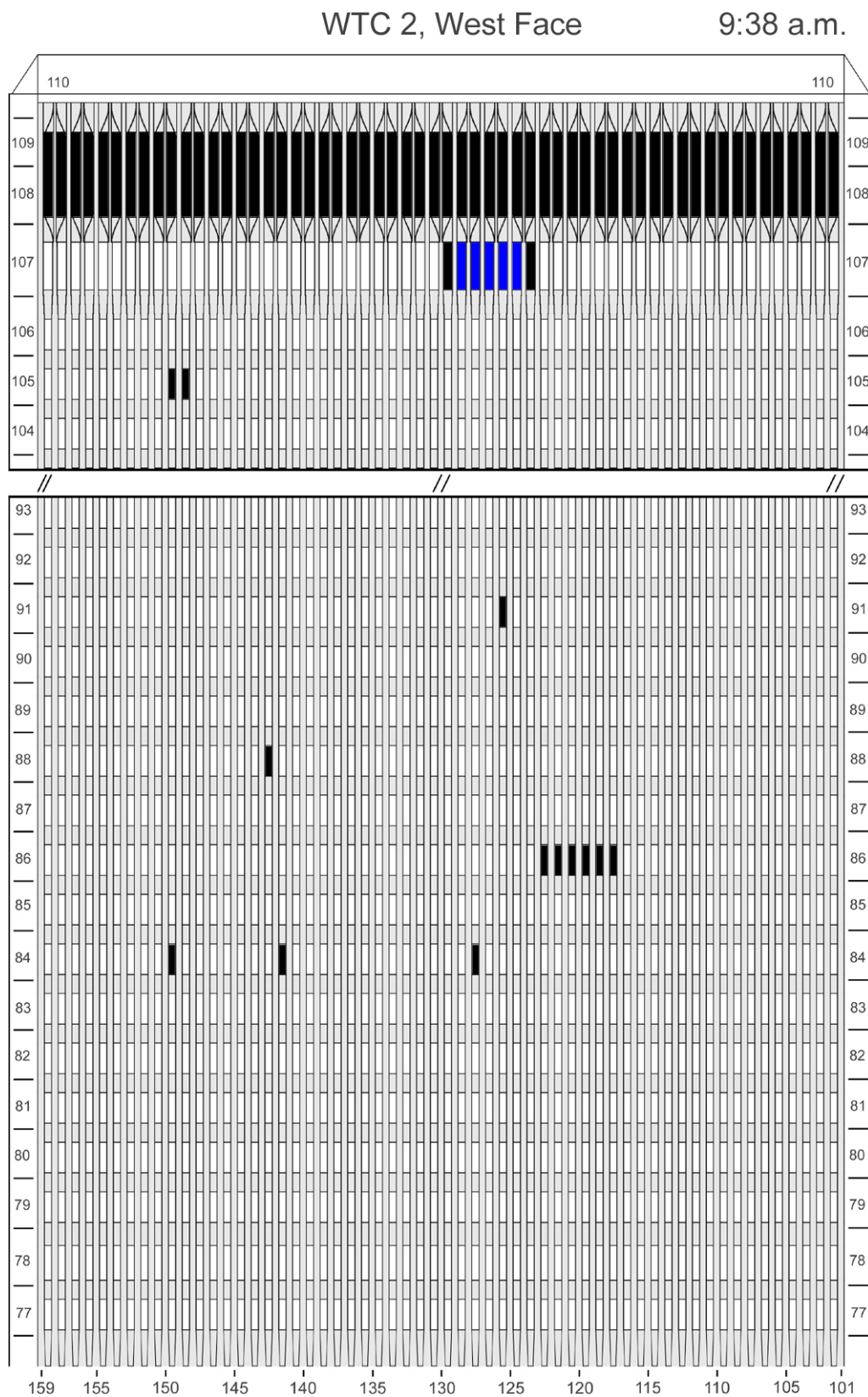


Figure J-36. Diagram of the west face of WTC 2 for floors 77 to 93 and floors 104 to 110 at 9:36 a.m. showing windows where smoke was observed and those hidden from view.



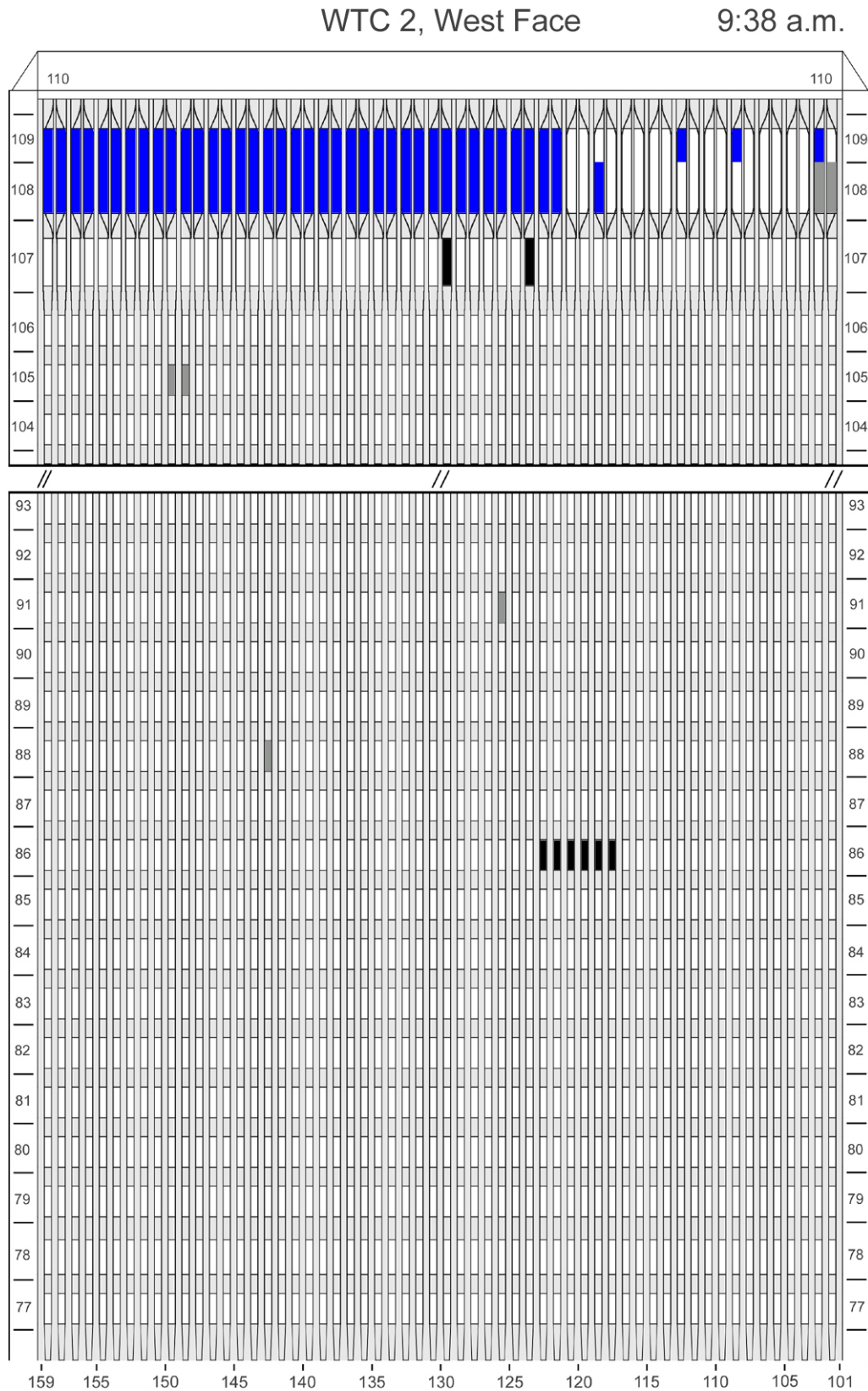


Figure J-38. Diagram of the west face of WTC 2 for floors 77 to 93 and floors 104 to 110 at 9:38 a.m. showing windows where smoke was observed and those hidden from view.

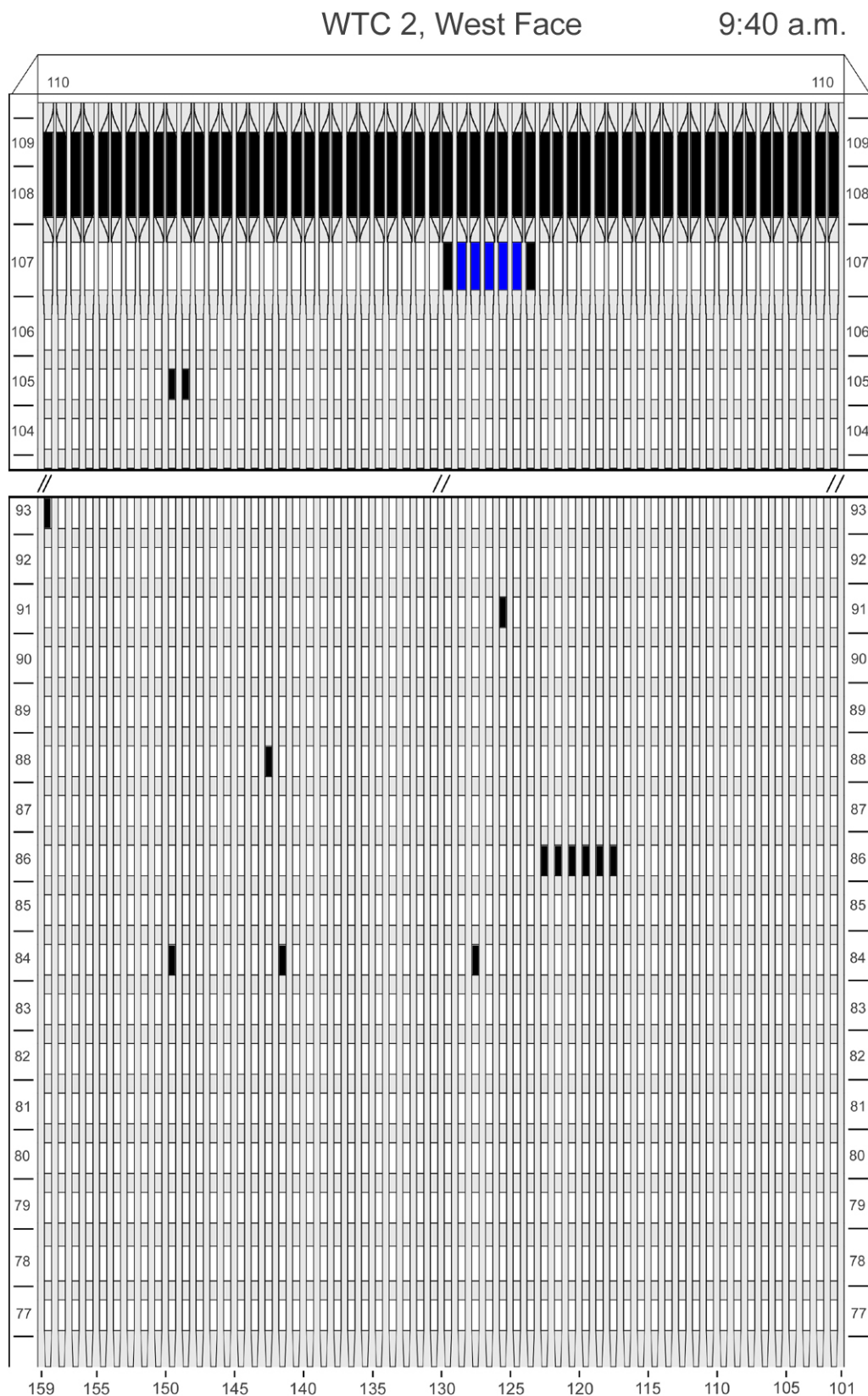


Figure J-39. Diagram of the west face of WTC 2 for floors 77 to 93 and floors 104 to 110 at 9:40 a.m. showing the condition of windows and locations of fires.





Figure J-41. Diagram of the west face of WTC 2 for floors 77 to 93 and floors 104 to 110 at 9:42 a.m. showing the condition of windows and locations of fires.

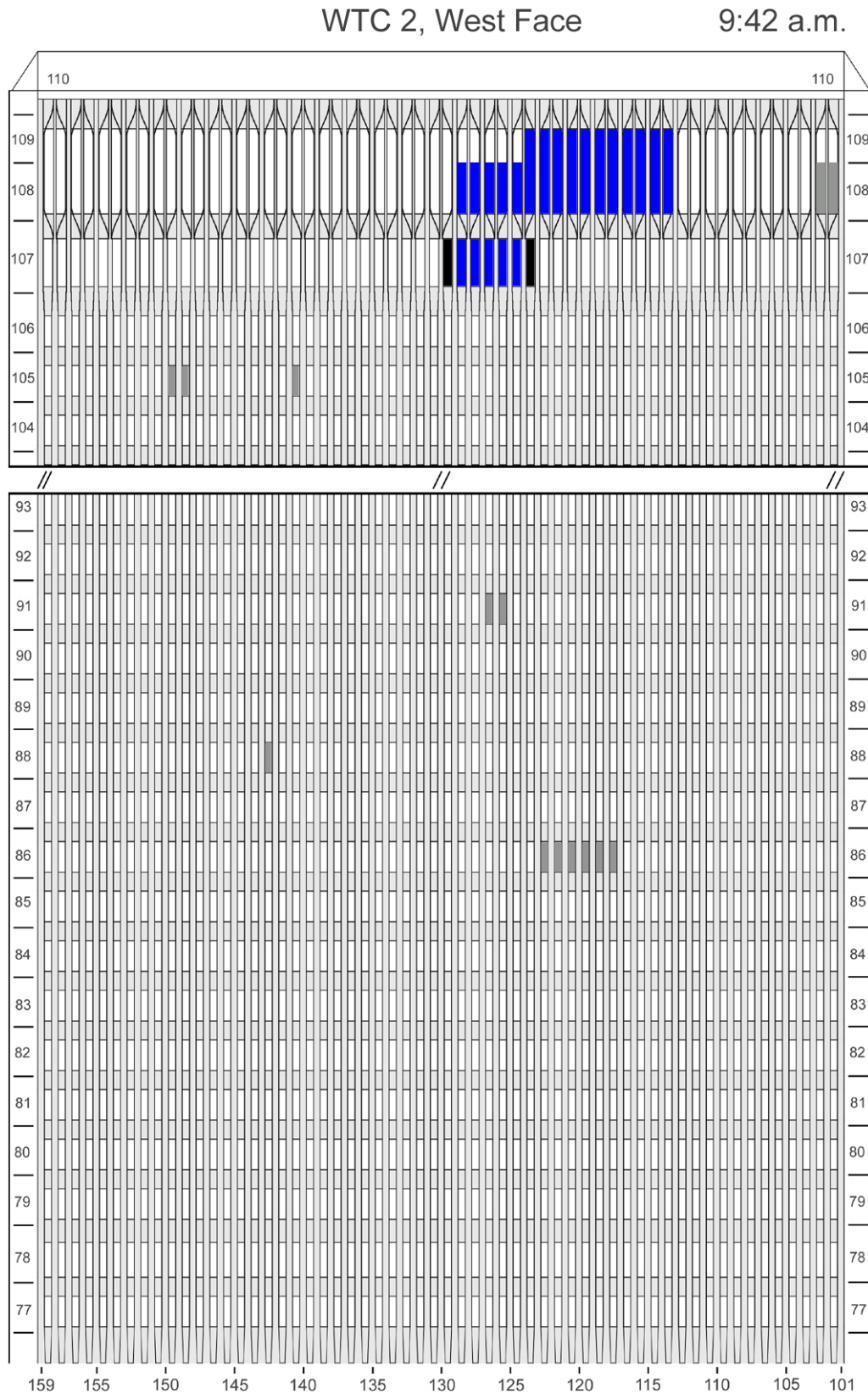


Figure J-42. Diagram of the west face of WTC 2 for floors 77 to 93 and floors 104 to 110 at 9:42 a.m. showing windows where smoke was observed and those hidden from view.

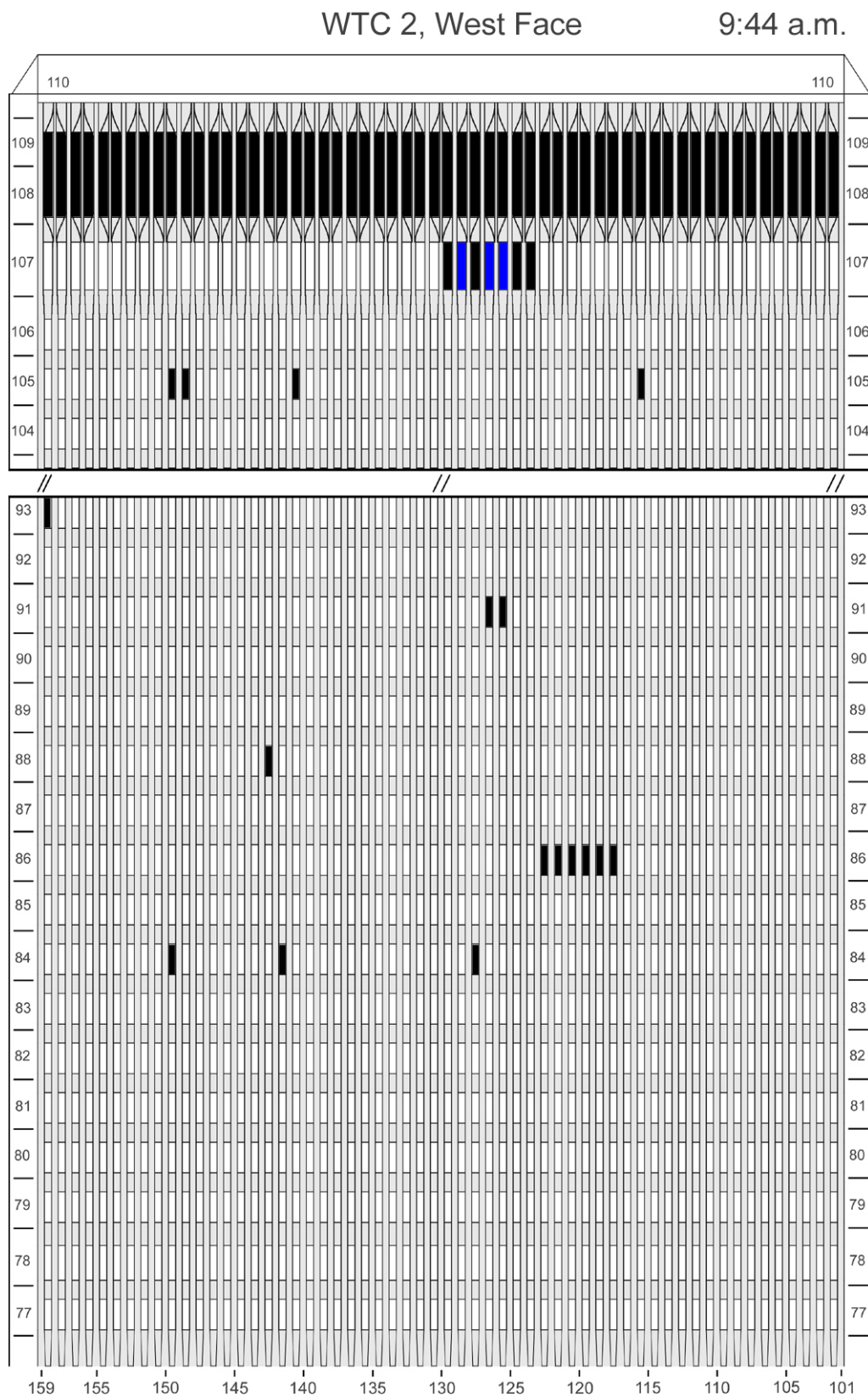


Figure J-43. Diagram of the west face of WTC 2 for floors 77 to 93 and floors 104 to 110 at 9:44 a.m. showing the condition of windows and locations of fires.

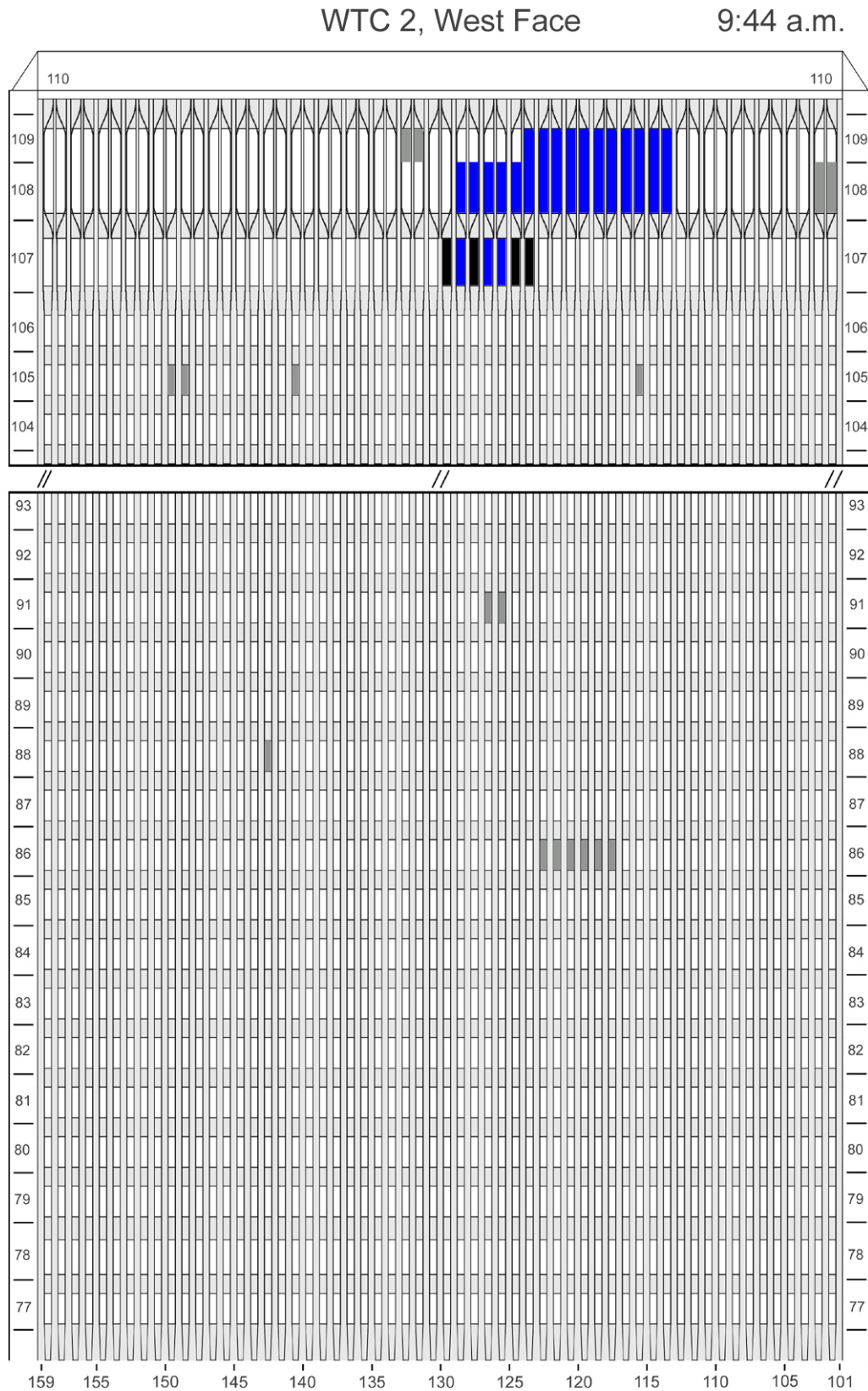


Figure J-44. Diagram of the west face of WTC 2 for floors 77 to 93 and floors 104 to 110 at 9:44 a.m. showing windows where smoke was observed and those hidden from view.

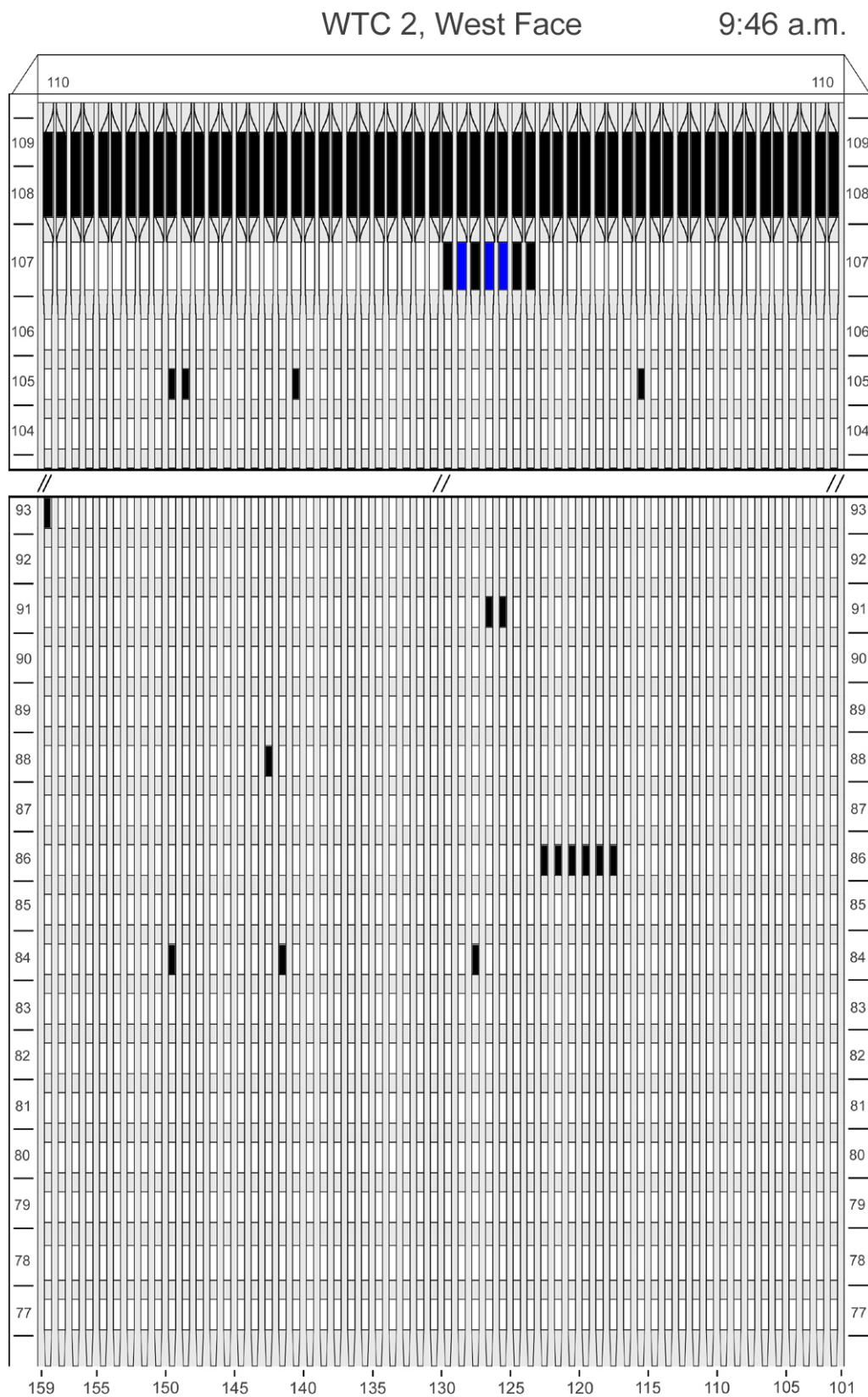


Figure J-45. Diagram of the west face of WTC 2 for floors 77 to 93 and floors 104 to 110 at 9:46 a.m. showing the condition of windows and locations of fires.

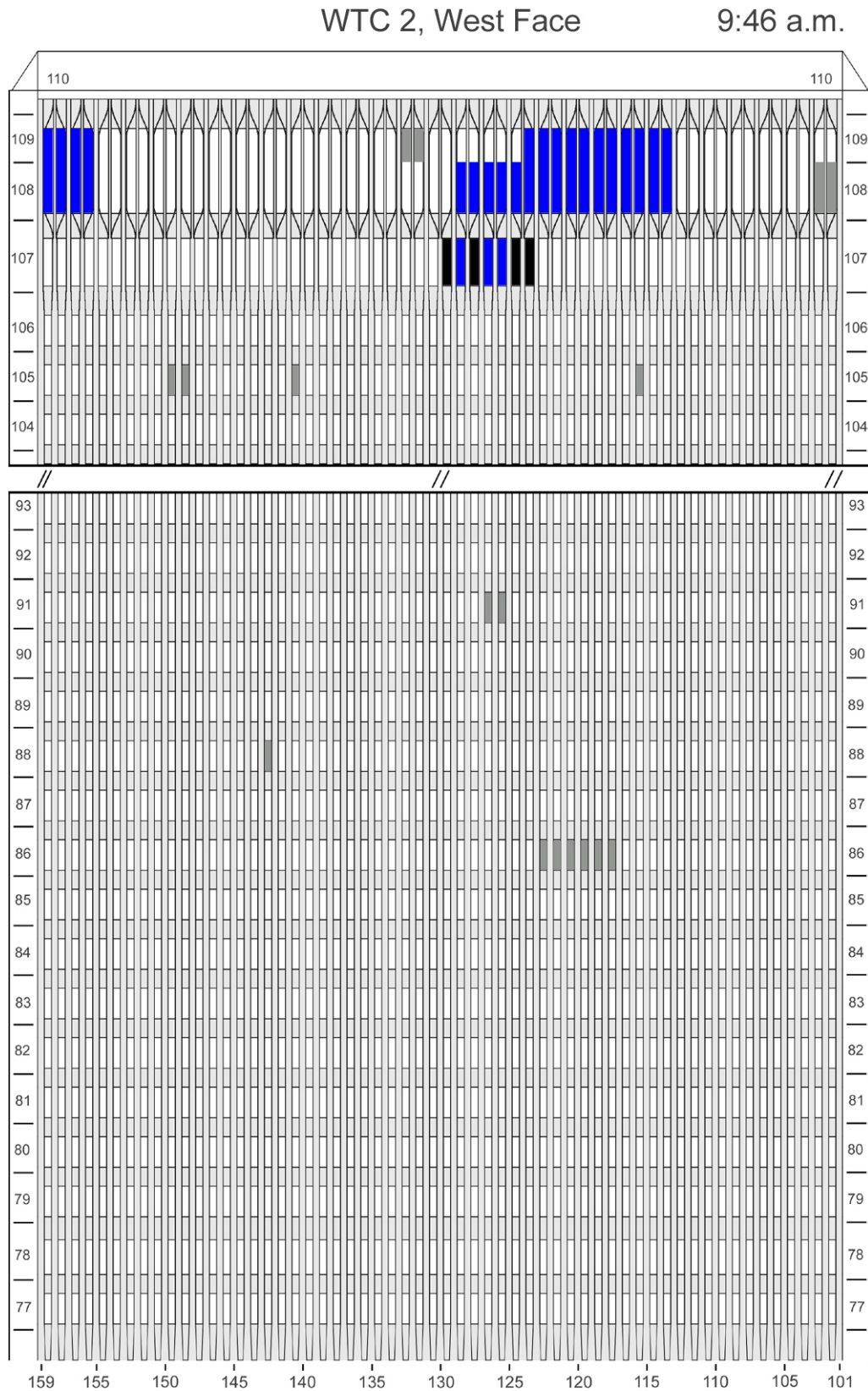


Figure J-46. Diagram of the west face of WTC 2 for floors 77 to 93 and floors 104 to 110 at 9:46 a.m. showing windows where smoke was observed and those hidden from view.

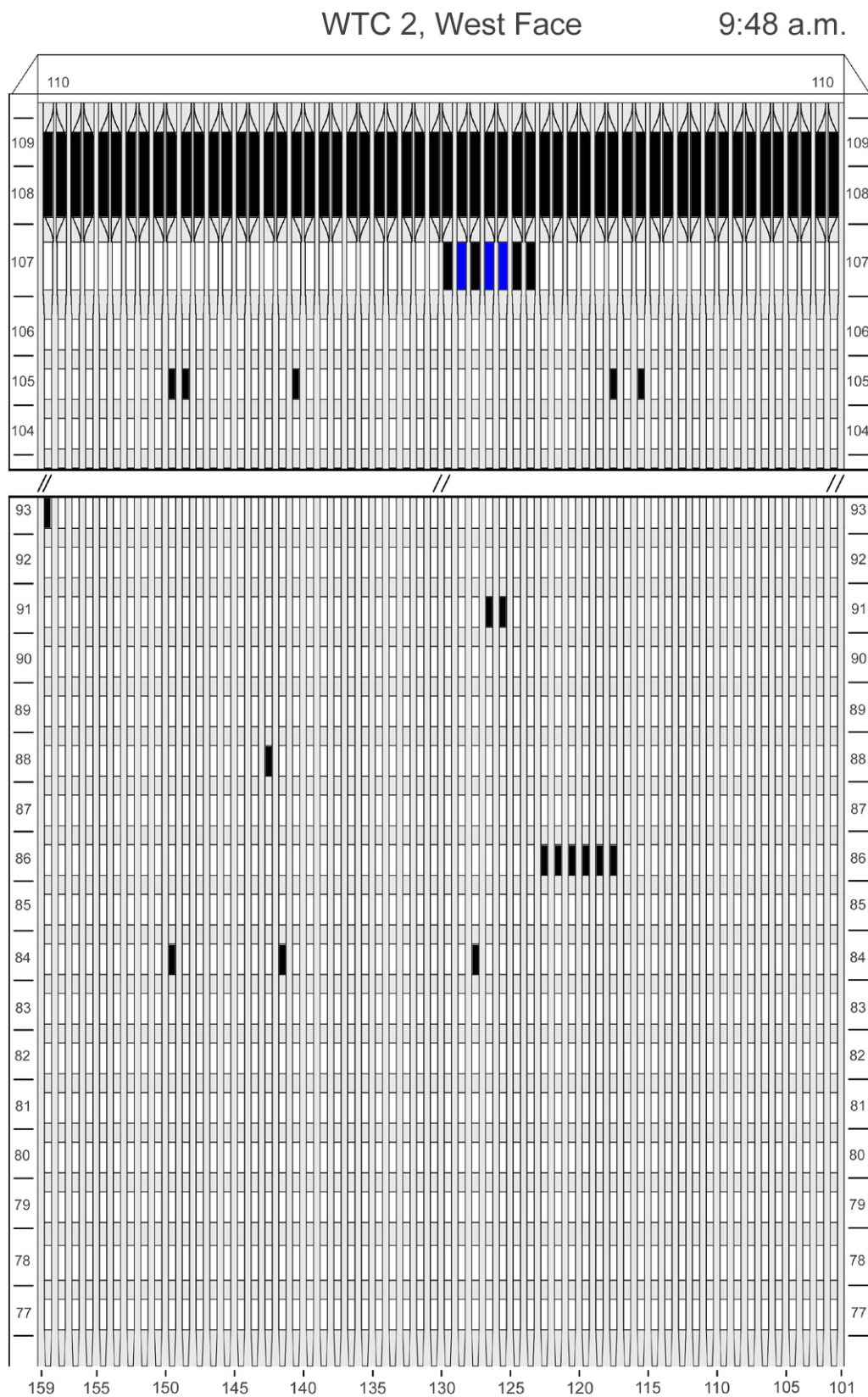


Figure J-47. Diagram of the west face of WTC 2 for floors 77 to 93 and floors 104 to 110 at 9:48 a.m. showing the condition of windows and locations of fires.

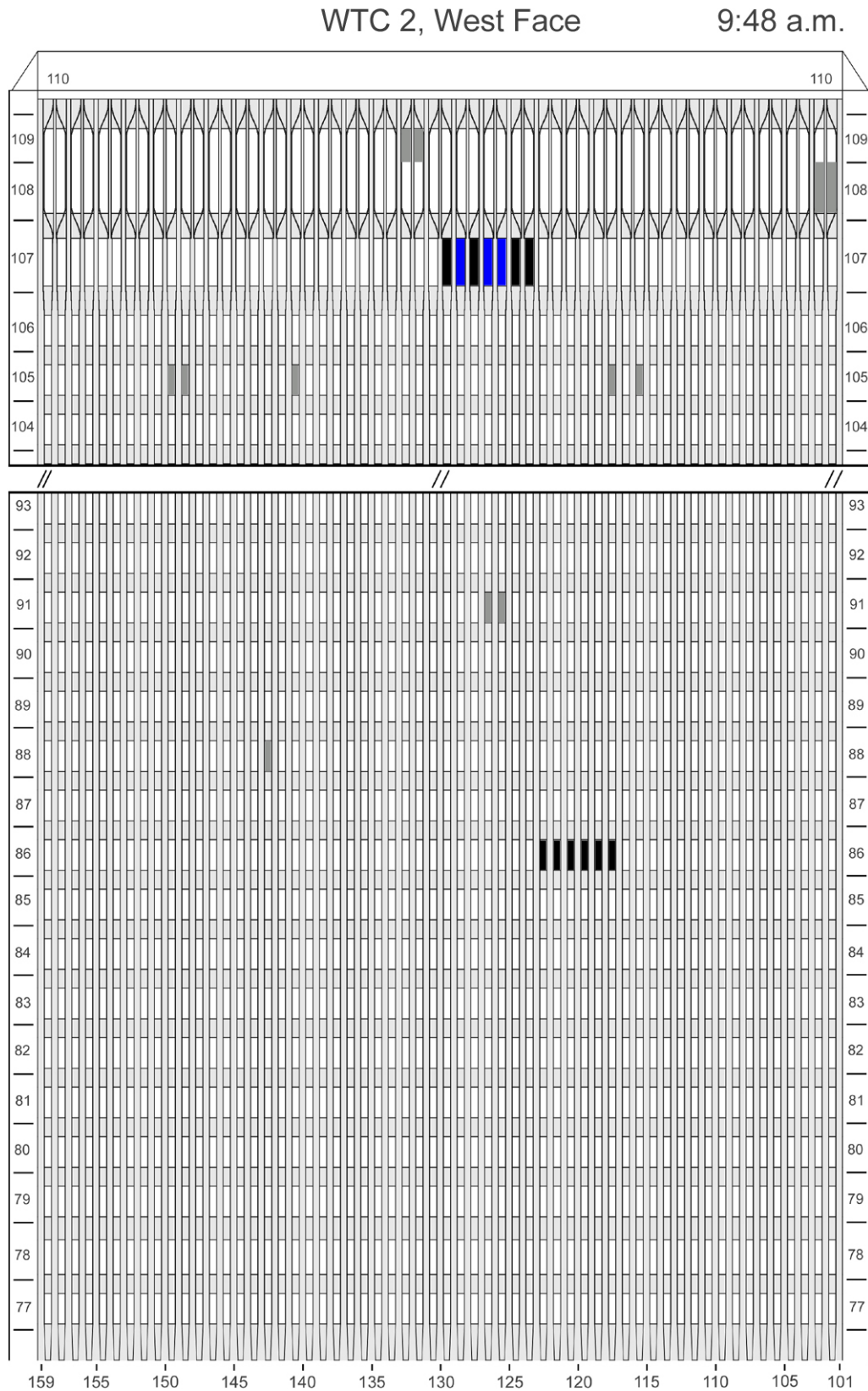


Figure J- 48. Diagram of the west face of WTC 2 for floors 77 to 93 and floors 104 to 110 at 9:48 a.m. showing windows where smoke was observed and those hidden from view.

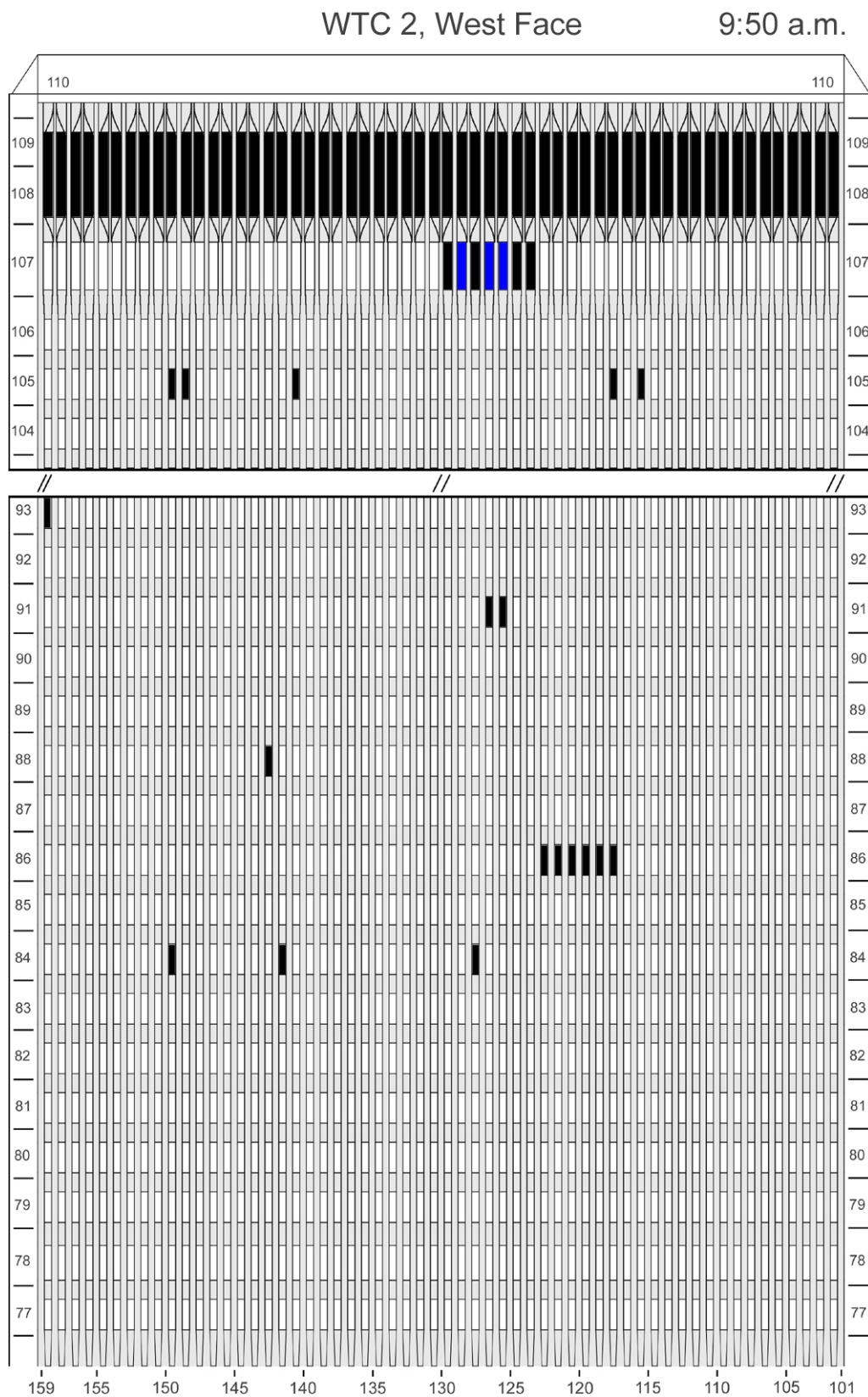


Figure J-49. Diagram of the west face of WTC 2 for floors 77 to 93 and floors 104 to 110 at 9:50 a.m. showing the condition of windows and locations of fires.

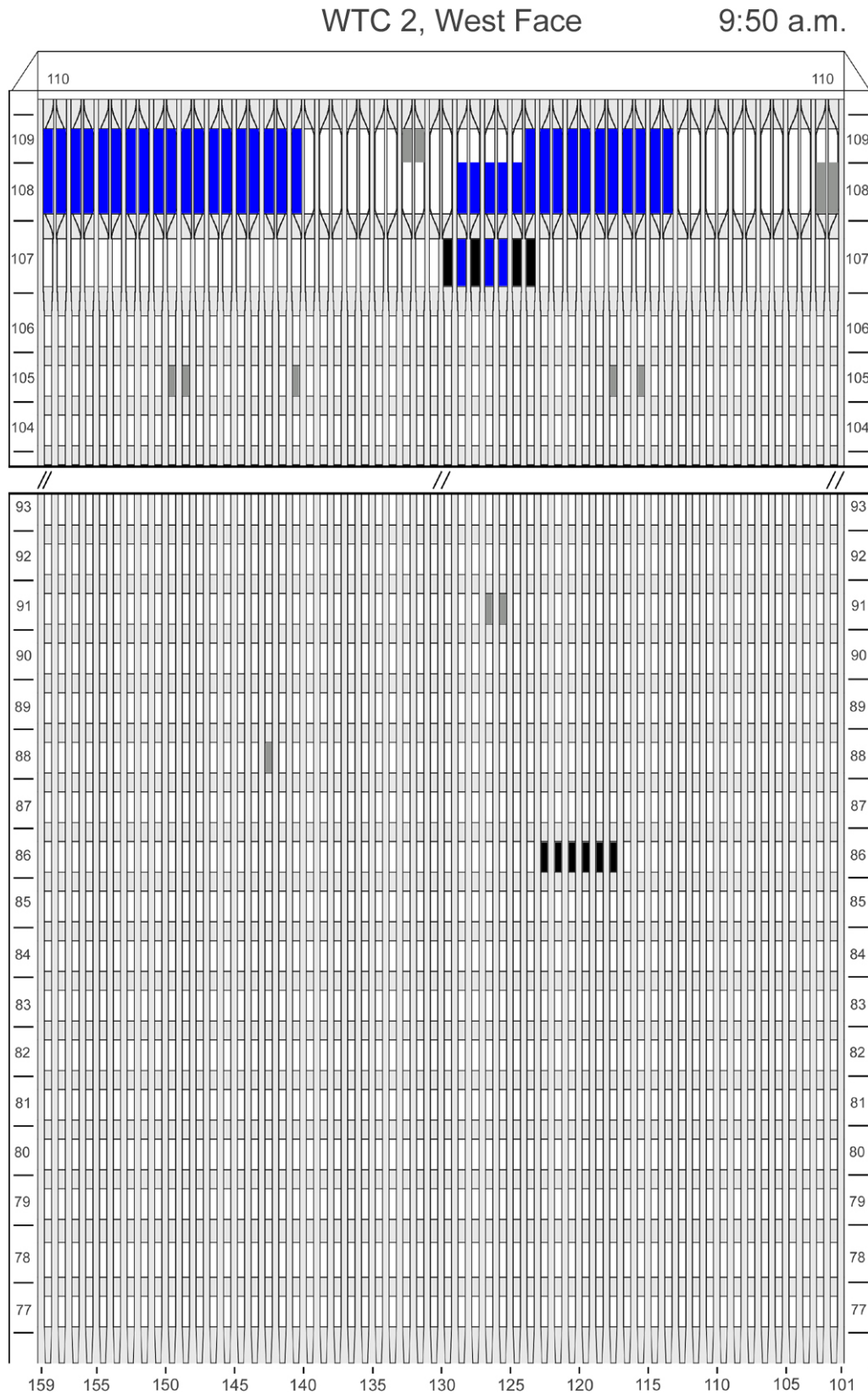


Figure J-50. Diagram of the west face of WTC 2 for floors 77 to 93 and floors 104 to 110 at 9:50 a.m. showing windows where smoke was observed and those hidden from view.

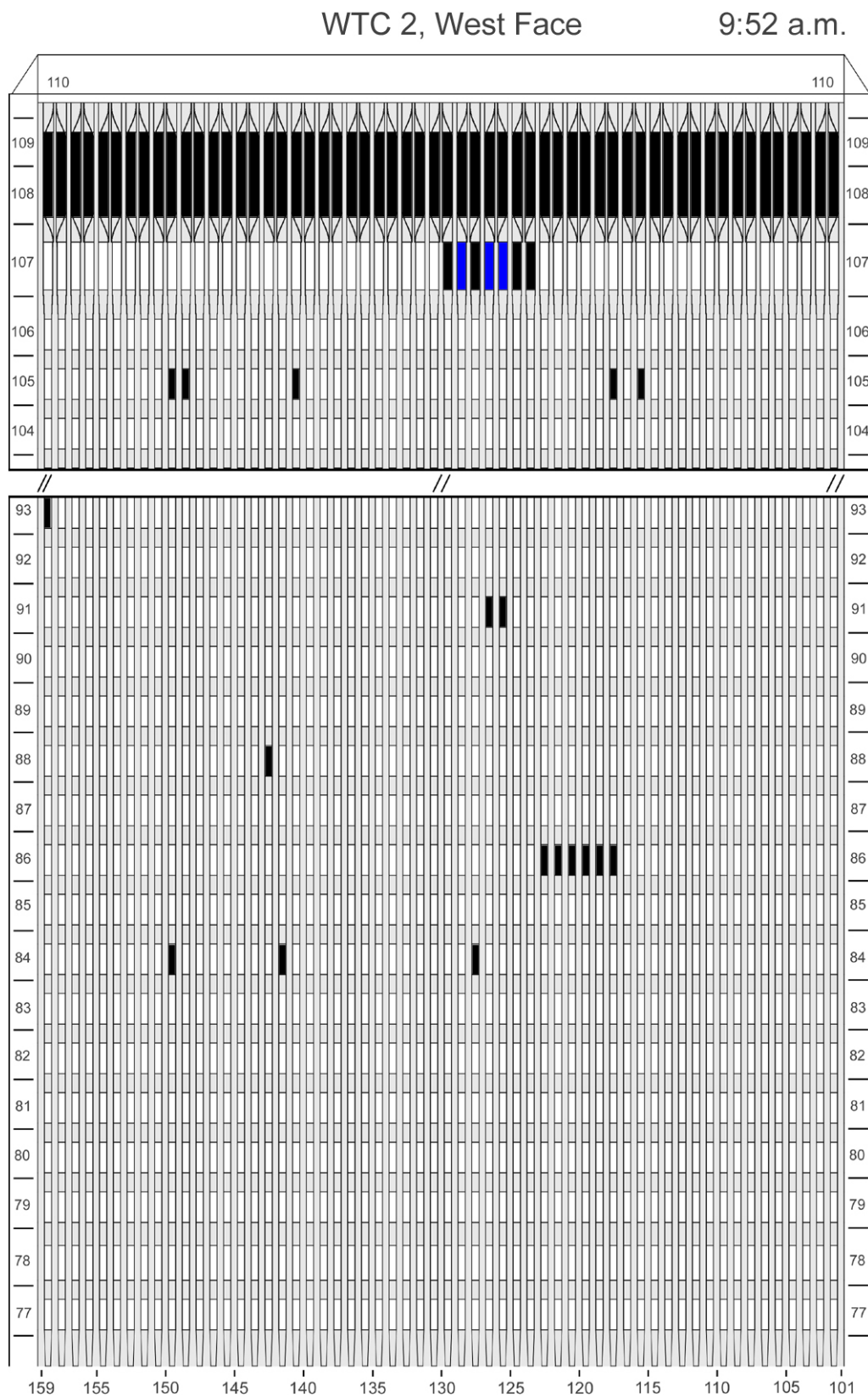


Figure J-51. Diagram of the west face of WTC 2 for floors 77 to 93 and floors 104 to 110 at 9:52 a.m. showing the condition of windows and locations of fires.

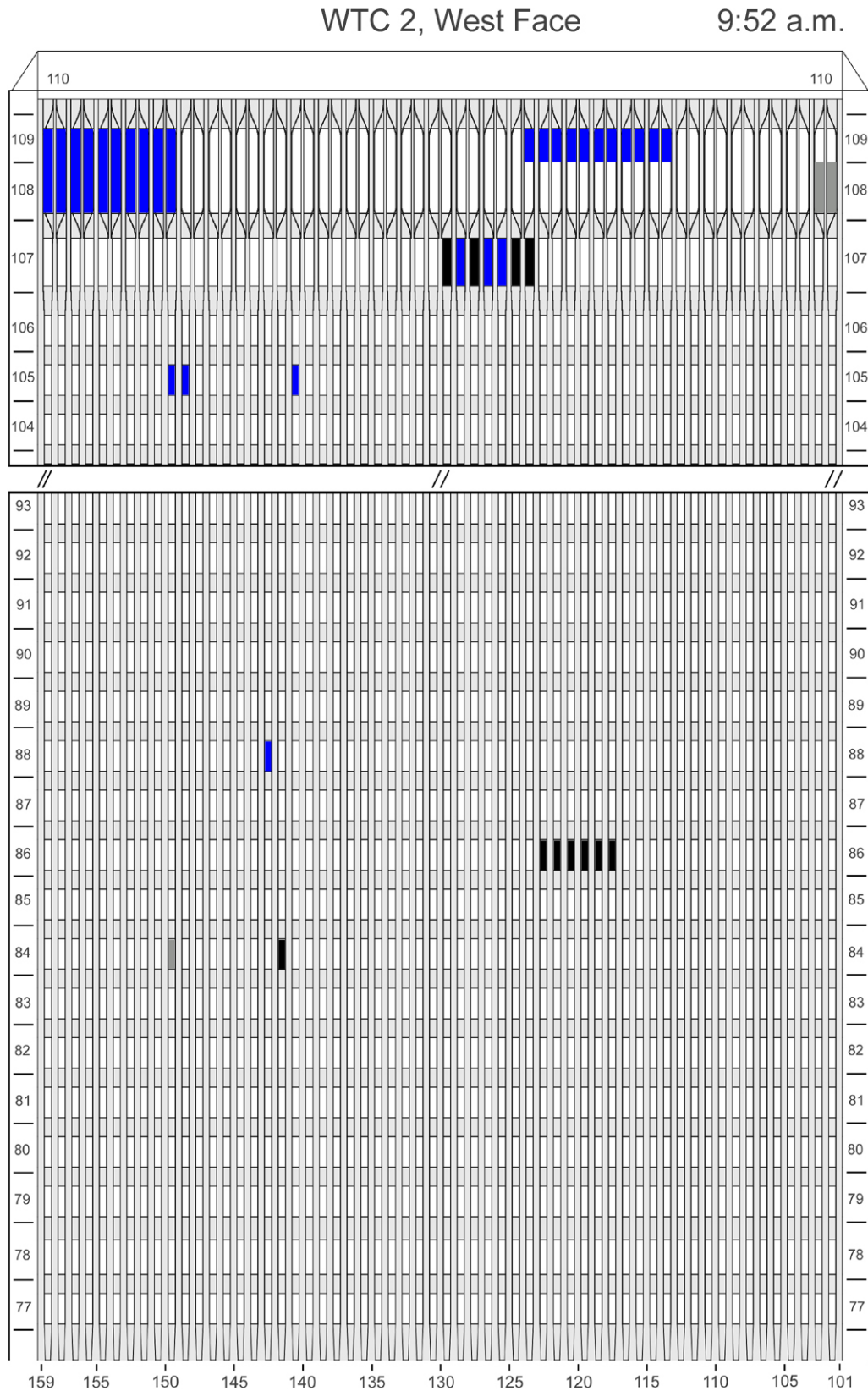


Figure J-52. Diagram of the west face of WTC 2 for floors 77 to 93 and floors 104 to 110 at 9:52 a.m. showing windows where smoke was observed and those hidden from view.

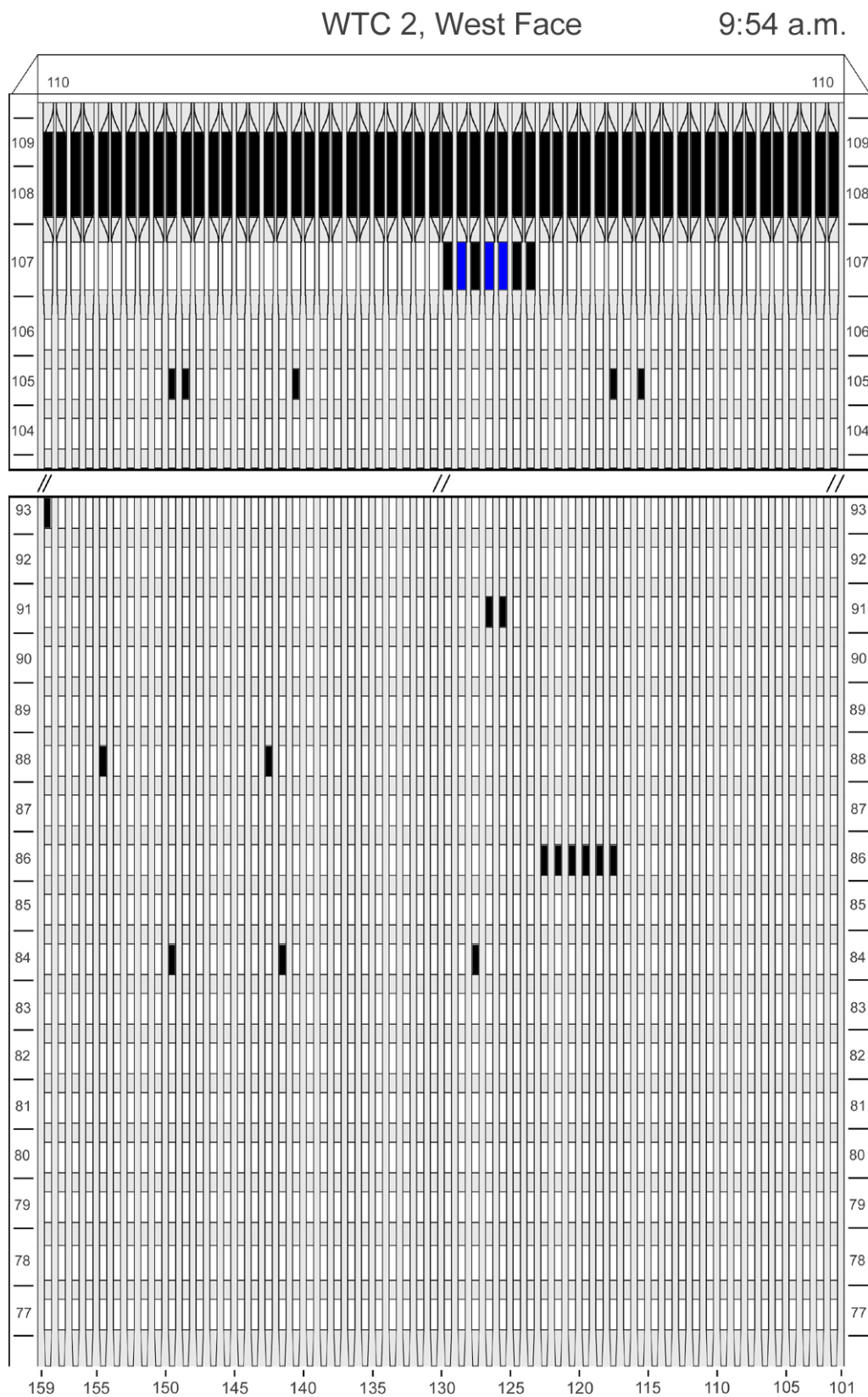


Figure J-53. Diagram of the west face of WTC 2 for floors 77 to 93 and floors 104 to 110 at 9:54 a.m. showing the condition of windows and locations of fires.

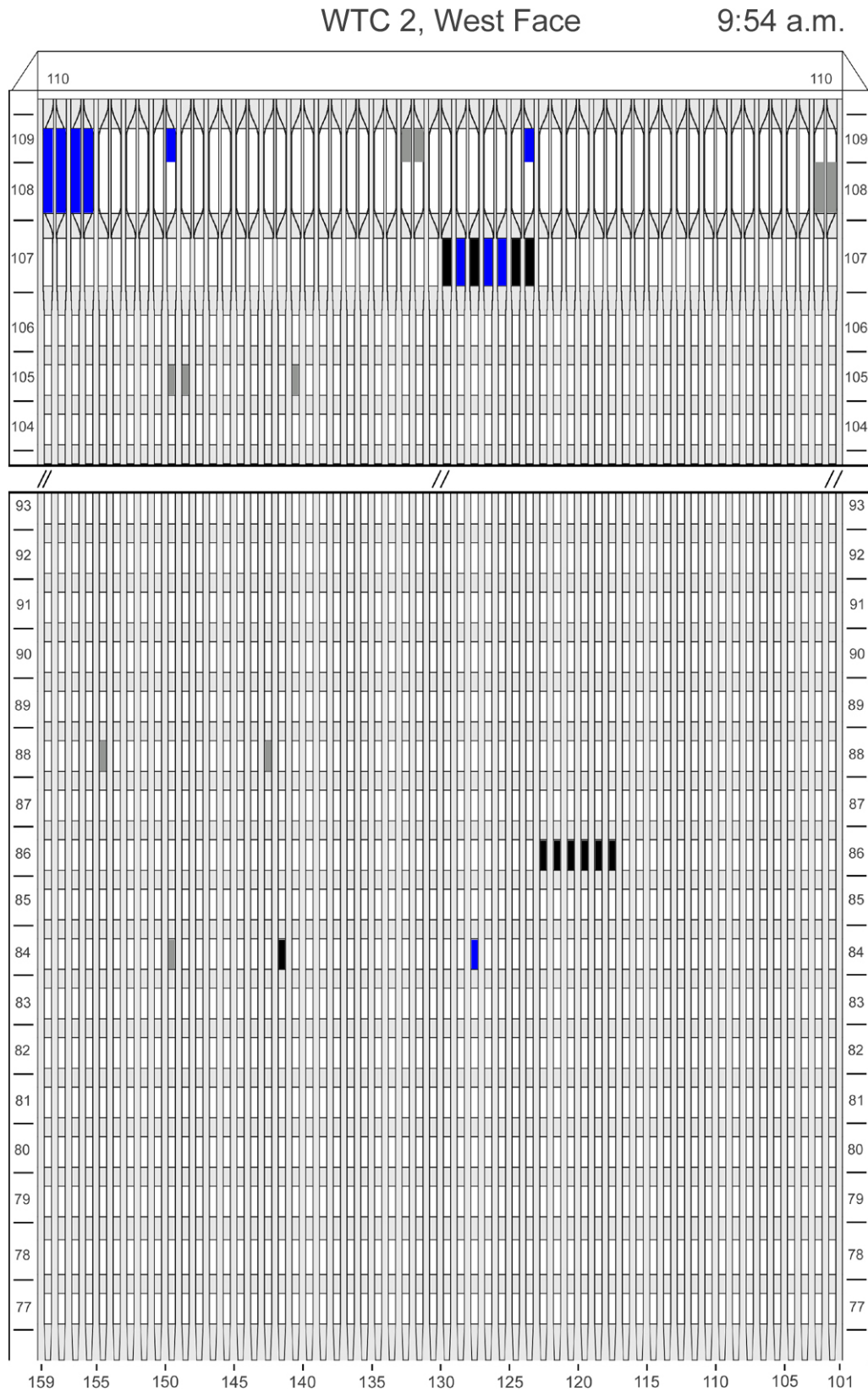


Figure J-54. Diagram of the west face of WTC 2 for floors 77 to 93 and floors 104 to 110 at 9:54 a.m. showing windows where smoke was observed and those hidden from view.

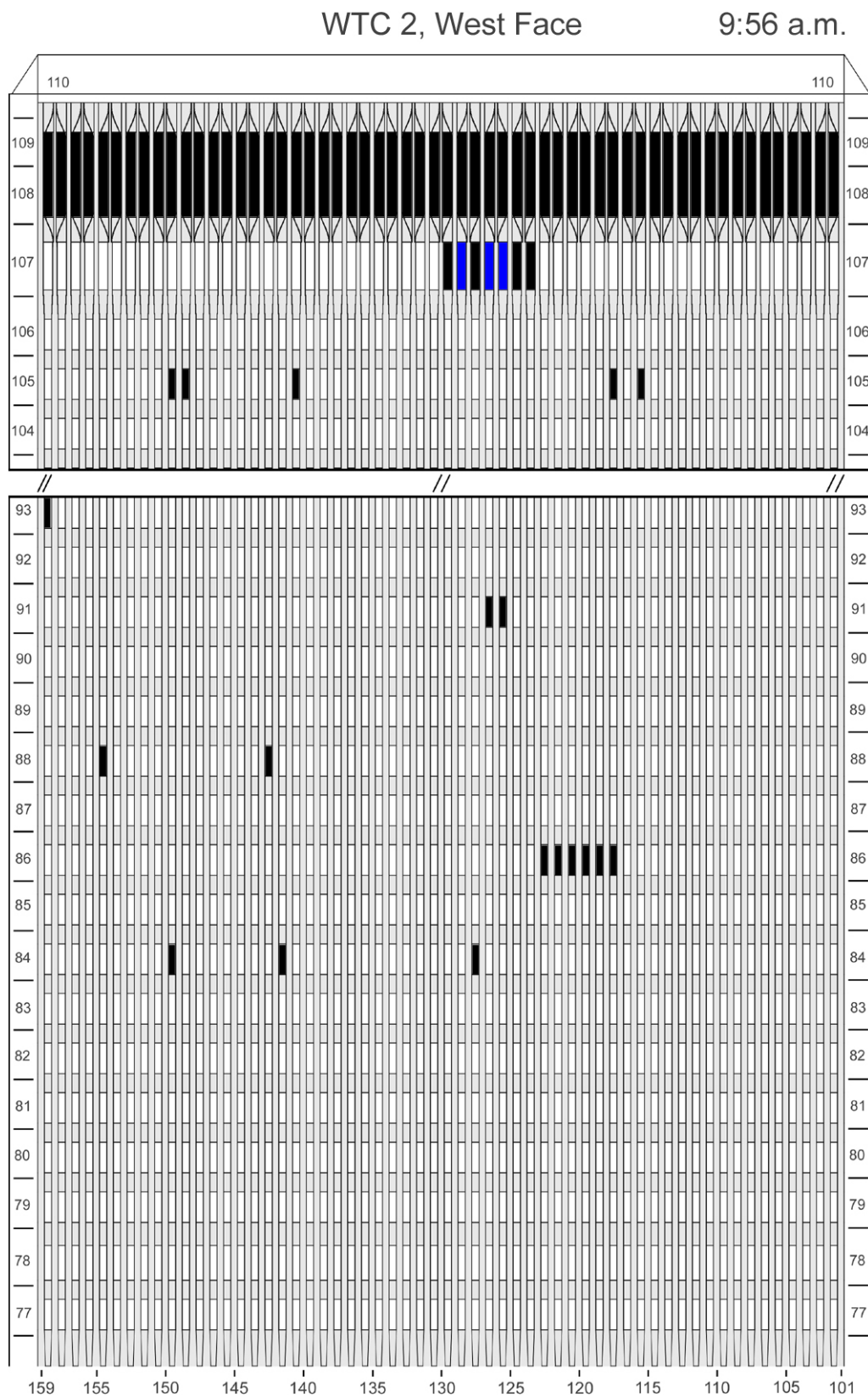


Figure J-55. Diagram of the west face of WTC 2 for floors 77 to 93 and floors 104 to 110 at 9:56 a.m. showing the condition of windows and locations of fires.

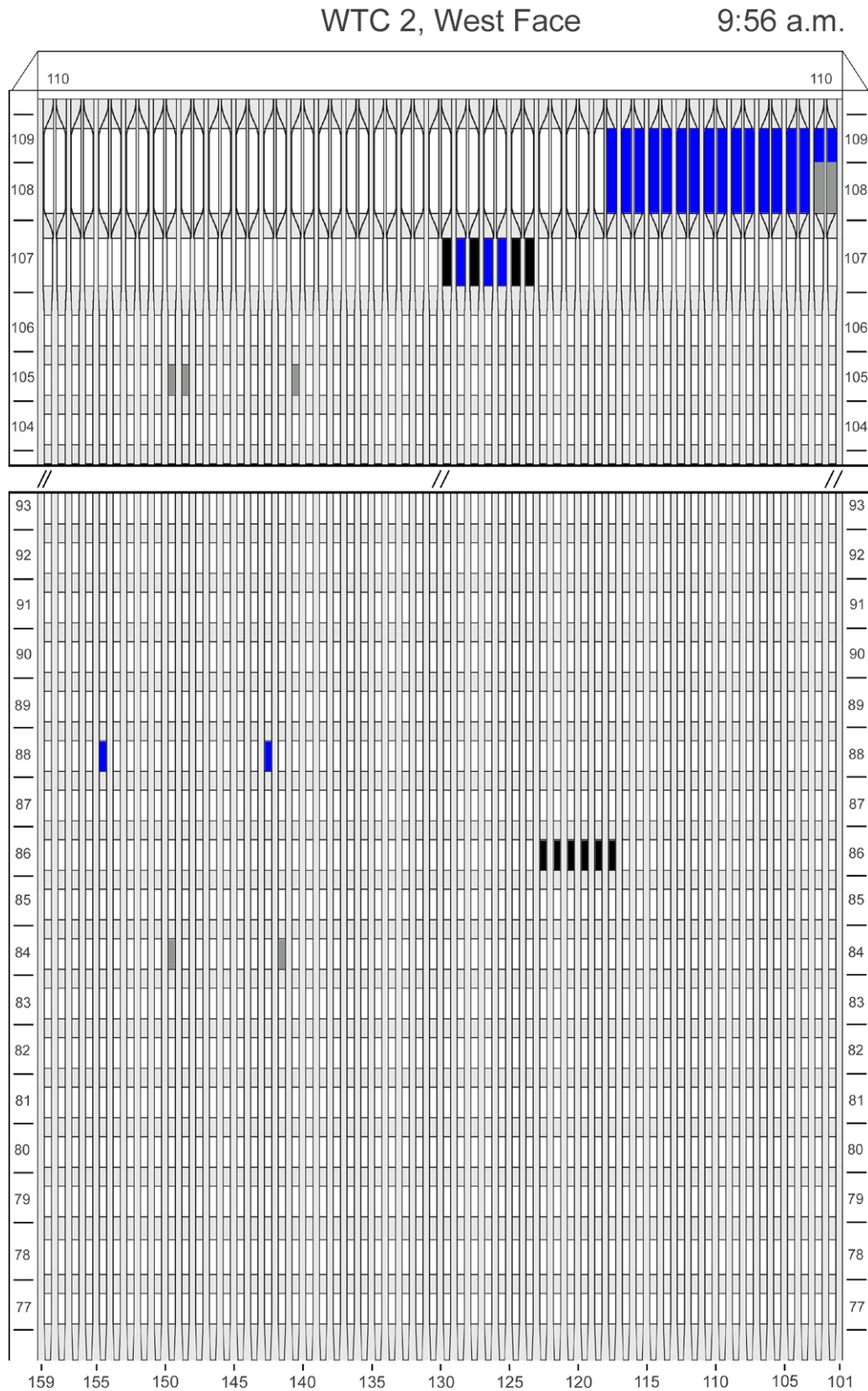


Figure J-56. Diagram of the west face of WTC 2 for floors 77 to 93 and floors 104 to 110 at 9:56 a.m. showing windows where smoke was observed and those hidden from view.

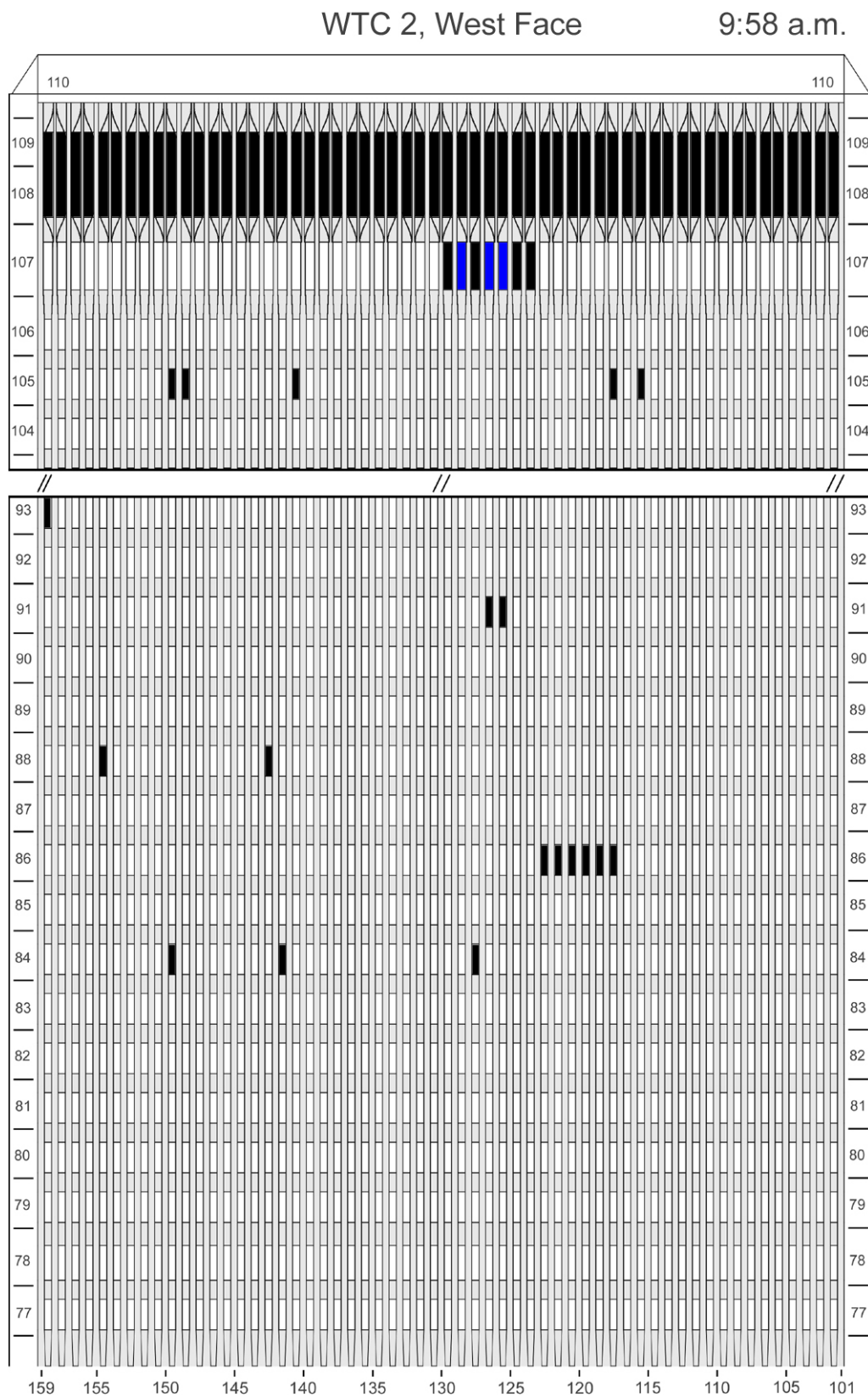


Figure J-57. Diagram of the west face of WTC 2 for floors 77 to 93 and floors 104 to 110 at 9:58 a.m. showing the condition of windows and locations of fires.

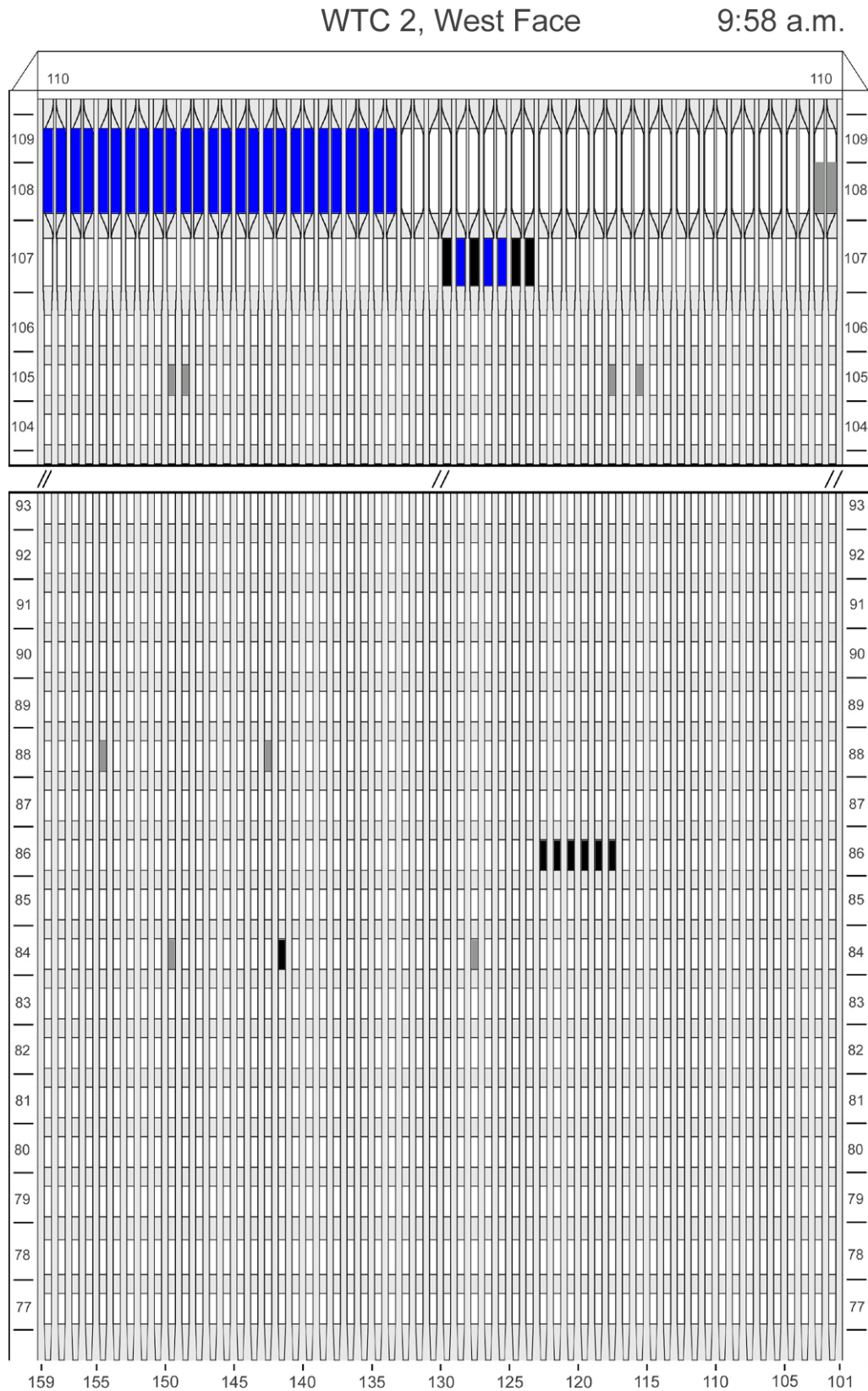


Figure J-58. Diagram of the west face of WTC 2 for floors 77 to 93 and floors 104 to 110 at 9:58 a.m. showing windows where smoke was observed and those hidden from view.

This page intentionally left blank.

Appendix K

MOIRE ANALYSIS OF PRIMARY FREQUENCIES AND TIME-DEPENDENT OSCILLATION AMPLITUDE FOLLOWING THE AIRCRAFT IMPACT FOR WTC 2

Detailed information about the motion of World Trade Center (WTC) 2, including the oscillation amplitude in the north-south and east-west directions and frequencies and magnitudes of planar and torsional modes, can be obtained through image analysis of the moiré patterns in two videos available in the National Institute of Standards and Technology (NIST) visual database: one taken from the east and the other from the north; these videos will be referred to as the East video and the North video, respectively.

The moiré effect occurs when two closely spaced gratings are superimposed, generating fringe patterns that attract the eye. It is commonly observed with fine textiles such as folds of lace. In this case, the two gratings are the lines of WTC 2 windows in perspective view superimposed on the vertical columns of pixels in the digital video images. As the building sways in response to the aircraft impact, the moiré pattern amplifies the motion, allowing it to be followed at a resolution considerably higher than that available in the direct image. Combining this information with the known building dimension of 40 inches from the center of one window to the center of the next enables the determination of the distance traveled by WTC 2 with an uncertainty on the order of plus or minus one inch. Since the natural oscillation frequency of a building reflects its structural properties, comparison of the frequency before and after the aircraft impact may provide insight into the nature of the damage suffered by WTC 2.

K.1 NORTH-SOUTH OSCILLATIONS

Figure K–1 shows a single frame taken from the East video. This particular frame is assigned the time $t = 0$ s and is within a frame or two of the actual aircraft impact. The video was filmed from a thirteenth floor balcony located approximately 1,000 ft to the east and slightly north of WTC 2—the camera viewpoint makes a horizontal angle of approximately 12 degrees with a line perpendicular to the east face of WTC 2 at its center. WTC 2 appears to the left of the frame and WTC 1 to the right. Overlapping both towers in front is 22 Cortlandt Street, a 34-story tall building. The damage to floors 79 and 80 of WTC 2 after the aircraft impact provide reference locations from which the lowest point on the frame can be identified as floor 70.

The video was recorded by a digital camcorder. During the recording process, each frame of the video is imaged onto an array of photosites that collect light and convert it into electrons, dividing the image into a set of tiny rectangles called pixels. The video frame is 720 pixels wide by 480 pixels high, a standard size for digital video media. Pixel width is 0.9 times pixel height to generate the standard video width-to-height ratio of 4:3. The frame rate is 29.97 frames per second.

Several aspects of this video make it highly useful for moiré analysis. In addition to the viewpoint from near right angles to the north-south axis of WTC 2, the magnification brings the structure close enough to distinguish architectural details, yet is far enough to encompass a large region of WTC 2 as well as nearby



Figure K-1. A single frame from the East video shot on September 11. This frame is defined as time $t = 0$ s for the moiré pattern analysis. The three rectangles denote regions discussed in the text.

buildings for reference. The architectural feature that enables the analysis is the vertical fenestration consisting of recesses running the full height of the building between the vertical columns, in which the windows are situated. This feature appears on the video frame as a set of dark lines, with small variations in intensity due to the spandrels in between the windows. (See Chapter 4 for further description of WTC 2 architecture.) These will be referred to as “window lines” in this appendix. From the camera’s perspective, the angles of window lines appear close to vertical on the video. As will be seen, this provides good amplification of the building motion. The camera is mounted on a tripod, keeping fluctuations to a minimum (though not zero, as will be shown later in this appendix). Most fortuitously, the video shows the motion of WTC 2 for an undisturbed eleven minutes after the aircraft impact, enough time to observe the entire building response until a time when the oscillations have faded to background noise.

K.1.1 Moiré Fringes

Figure K-2 demonstrates the basis for the moiré pattern observed on WTC 2 in this video. The window lines of WTC 2 can be represented as straight lines whose angle is determined by the camera perspective, as illustrated in Fig. K-2(a). The vertical columns of pixels in the digital medium form a grid as in

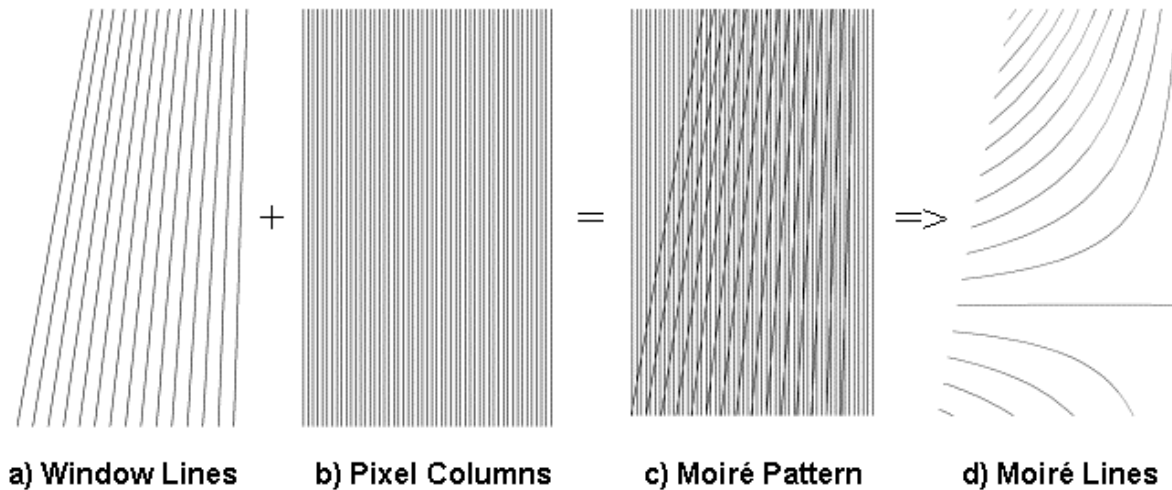


Figure K-2. Demonstration of moiré fringe pattern resulting from window lines in perspective view superimposed with vertical columns of pixels.

(b), which combines with the set of window lines to give the visual appearance of light curved lines in (c)—a moiré fringe pattern. A close look at (c) reveals that the points that the eye links to form the fringes are the intersection points between the lines of windows and pixel columns. The curvature is due to the fact that the window lines viewed in perspective are not parallel to each other. As the window lines become more vertical, the distance between intersection points increases. For a truly vertical window line, parallel to the pixel columns, the distance between intersection points would be infinite. Looking back at Fig. K-1, the curved fringes can be seen on the east face of WTC 2.

The superimposed grids and resulting fringes can be described mathematically.

For the set of window lines, a first order approximation assumes that the horizontal distance from one line to the next at the base is constant, and that there is a uniform increment in angle from one line to the next. The origin of the x-y coordinate system is the lower left corner of the video frame. Using the width of a single pixel as the basic unit of spatial measure, the window lines, as illustrated in Fig. K-2(a), are described by the equation

$$y = \frac{[x - (n - 1)p] - (d_1 + x_0)}{\tan[\theta_1 + (n - 1)\Delta\theta]} \quad (1)$$

where

y = vertical distance above the base of the video frame, pixel widths

x = horizontal distance from the origin, pixel widths

n = window line number (1 for the leftmost line to 58 for the rightmost)

p = apparent spacing between window lines at the base of the frame, pixel widths

x_0 = horizontal location of the leftmost (first) window line at the base of the video frame at a time just before the plane strike, pixel widths

d_1 = horizontal displacement of the lowest point of the leftmost window line from its initial position x_0 , pixel widths

θ_1 = angle made by the leftmost window line with the vertical, rad

$\Delta\theta$ = increment in angle from one window line to the next, rad

Equation (1) forms the basis for the moiré analysis. In response to the aircraft impact, the shaking of the building may cause changes in the positions and angles of the window lines, making d_1 , p , θ_1 , and $\Delta\theta$ the time-dependent variables in the problem. The basic linearity and relation of each line to the next are assumed throughout.

It should be noted that the numbering of window lines from left to right used throughout this appendix is in the opposite sense to the official numbering system. In building documents, the structural columns on the east face of WTC 2 are numbered from 301 for the column adjacent to the northeast corner to 359 adjacent to the southeast corner. Elsewhere in this report (Section 4.2.4) each window is assigned the number of the structural column to its right. To convert from the window line number n used in this analysis to its official number N , therefore, subtract n from 359.

The second grid that makes up the moiré pattern in the East video is the set of vertical lines generated by the columns of pixels, as illustrated in Fig. K-2(b). These lines are described by the equation

$$x = m \quad (2)$$

where m is the pixel column number, an integer value.

For common moiré patterns such as overlapping identical fabrics, the two superimposed grids have the same line spacing. In these simple cases, if the lines in the grids are indexed by m and n respectively, then the set of moiré fringes that appears to the eye is formed by the connection of the points of intersection, with indices given by $j = m - n$ (Kafri and Glatt 1990). An example is shown in Fig. K-3.

In the case of this video, however, the window lines are spaced slightly over three pixels apart at the base of the frame, and the simple indicial equation does not apply. The spacing can be seen in Figure K-4(a), which shows a closeup of the region enclosed by the small red rectangle in Fig. K-1. Eight window lines extend to the base of this portion of the video frame over a horizontal distance of 25 pixels. Although other moiré patterns exist in theory, the pattern that jumps out to the eye is defined by indices $j = m - 3n$. A set of equations that defines the moiré fringes can be obtained by recognizing that points in the fringes must satisfy both equations (1) and (2), which are linked through the common index j . To get an expression for the set of moiré fringes, therefore, substitute n in Eq. (1) with $n = (m - j) / 3 = (x - j) / 3$ to get

$$y = \frac{[x - (x - j - 1)p / 3] - (d_1 + x_0)}{\tan[\theta_1 + (x - j - 1)\Delta\theta / 3]} \quad (3)$$

This set of curves is plotted in Fig. K-2(d) for multiple values of j . The curvature of these lines is due to the appearance of x in the trigonometric term in the denominator, showing mathematically the result of the fact that the window lines are not parallel to each other from the camera's perspective.

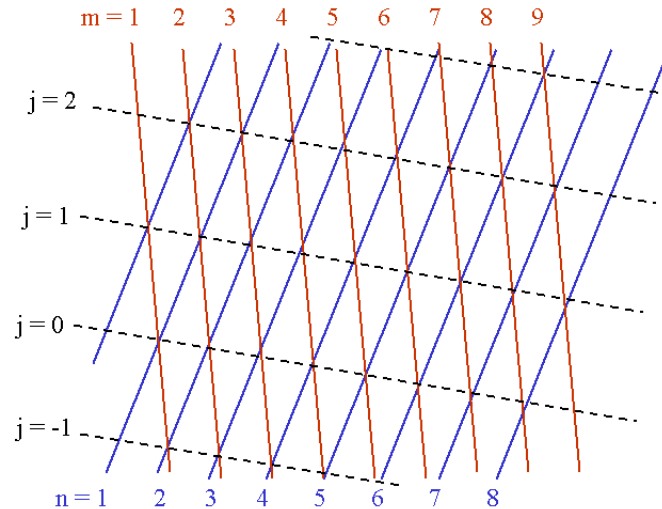


Figure K-3. Indexing of two superimposed grids (m and n) and the resulting moiré fringe ($j = m - n$).

The resolution of the north-south motion of the building that can be obtained from the moiré pattern is considerably higher than what is available from the direct image. In the video, as the window lines move from frame to frame with the sway of the building, the moiré pattern shifts. Figure K-4 shows closeups of the region at the base of the video where WTC 2 meets 22 Cortlandt Street at four times: the moment of the aircraft impact in Fig. K-4(a), the time of the maximum initial northward motion of WTC 2 at 1.80 s in Fig. K-4(d), and two intermediate times in (b) and (c). Portions of nine window lines tilting slightly clockwise from the vertical and of six moiré fringes sloping downwards from left to right can be seen in each frame. Note that the fringe lines connect the intersection points where a window line shifts from one pixel column to the next. At these points the pixel intensity, or darkness level, of the window line going up the first column matches that of the next. To see how the building motion is reflected in the moiré pattern, consider the upper intersection point in Fig. K-4(a) between the first (leftmost) and second pixel columns, indicated by an arrow. This intersection point is centered about $27\frac{1}{2}$ pixel heights above the base of the image. This point has moved down by about 2 pixels in Fig. K-4(b), about $5\frac{1}{2}$ pixels in (c), and about 6 pixels in (d), which corresponds to the maximum building motion after the impact. Comparing Fig. K-4(a) and (d) shows that the fringes are nearly in the same position, and the building has moved to the right (northward) by almost one full pixel. So building movement over one pixel width is amplified into moiré fringe movement over six pixel heights in this region of the video frame.

A rough estimate of maximum building sway can be performed at this point. Since the distance between windows is approximately $3\frac{1}{4}$ pixels at the base of the frame, and since the actual center-to-center window spacing is 40 in., the distance of the excursion is about $1 \times 40 / (3\frac{1}{4}) \approx 12$ in. at the 70th floor.

It should be noted that the windows positioned between the structural columns of WTC 2 are not in a continuous line, but separated by spandrels between floors. In a sharp closeup of the building façade,

such as in Fig. 4–8 elsewhere in this report, the spandrels appear lighter in color than the windows. Yet in the East video, the intensity of the window lines changes relatively smoothly from one pixel to the next. The reason for this lies in the smoothing properties of the digital video recording process, given the limits of the available pixel resolution. For the moiré analysis, the smoothing of some detail is actually beneficial and simplifies the automation of data collection. Although the presence of the spandrels may cause some variability in vertical intensity levels, the points defining the moiré pattern are determined by looking for equal intensities for adjacent pixels in the horizontal direction, thus reducing the potential error.

Initial assessment of the response of WTC 2 to the aircraft impact was obtained by the counting of pixels by eye. As can be seen in Fig. K–4, the vertical location of the intersection of a specific line of windows with adjacent pixel columns can be estimated to within half a pixel height. Adjacent pixels with roughly equal intensities, such as at the arrows in Figs. K–4(a) and (d), are at the halfway point between integer pixel locations (27-1/2 and 21-1/2 respectively), and checkerboard patterns such as in Fig. K–4(c) are on the integer (22 pixel heights). Since the maximum excursion is roughly 6 vertical pixels both up and down, the motion of the building can be readily distinguished for several oscillations. Figure K–5(a) shows the building motion obtained from measuring the location of a single intersection by eye at time intervals of about 5 frames, or 0.167 s. Although this data collection technique is approximate, resulting in an uncertainty of about ± 2 in., it distinguishes all the main features of the oscillatory motion in the north-south direction. The motion is not a pure sine wave. The displacement of the building appears to show plateaus at about 5 s, 10.5 s, and 16 s, when the building seems to stop moving back and forth for approximately one second. In the longer time sequence to the right of Fig. K–5, a period of about 70 s is superimposed on the primary oscillation. These features can be more finely delineated from computerized data collection, but their outlines are picked up by the simple counting technique.

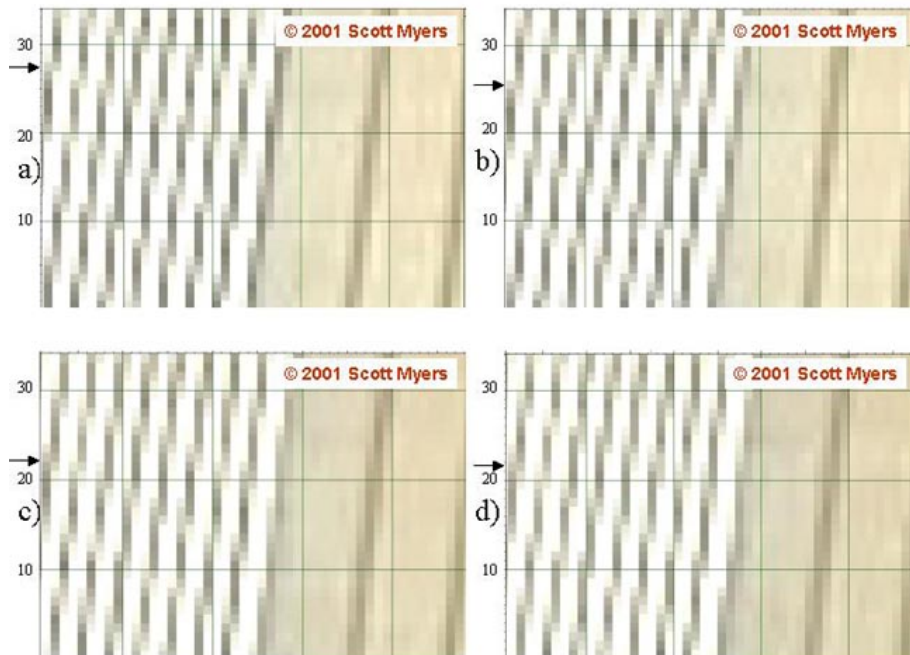


Figure K–4. Closeups of small rectangular region outlined in Fig. K–1 at times a) 0.00 s, b) 0.60 s, c) 1.20 s, and d) 1.80 s after impact. Horizontal and vertical lines crossing the images measure 10-pixel intervals.

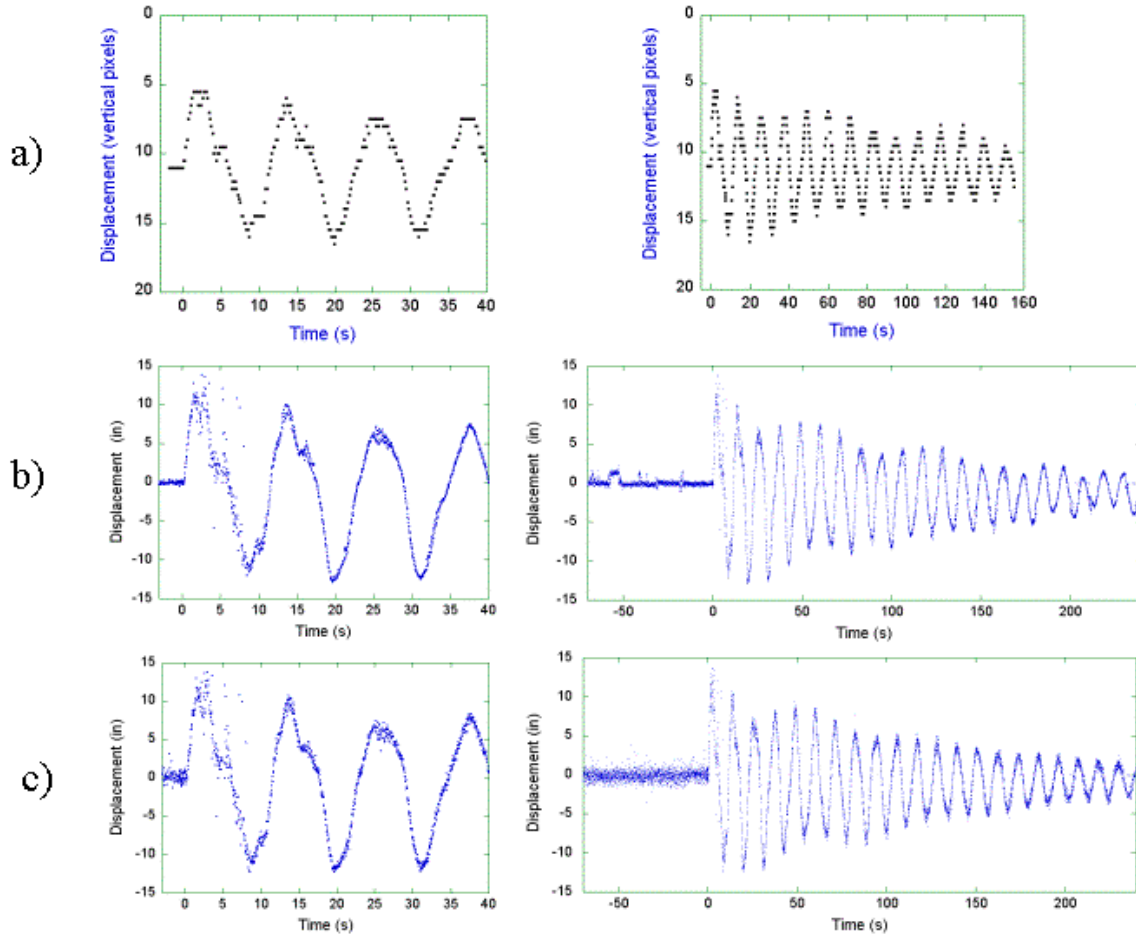


Figure K–5. Comparison of WTC 2 motion obtained from three approaches to moiré analysis: a) measurement of vertical pixel motion by eye, b) automated analysis of WTC 2 alone, and c) automated analysis corrected by subtracting out apparent motion of fixed building. Left hand plots show oscillations over first three cycles, and right hand plots show motion for four minutes after impact.

K.1.2 Automation of Moiré Pattern Analysis

The information about the period and amplitude of building motion obtained by eye in the previous section demonstrated the value of the moiré pattern approach. To fully analyze the motion, including determination of displacement d_l , window spacing p , angle of the first window line θ_l , and angle increment $\Delta\theta$, and to reduce the level of uncertainty, a large number of intersection points is needed for each video frame. This required the automation of the analysis procedure.

Figure K–6 illustrates the steps followed to determine analysis parameters for each frame. Following the figure, the numbered steps are as follows:

1. First, the region to be analyzed is cropped from the full 720 pixel \times 480 pixel video frame. Referring back to the video image in Fig. K–1, the analysis region is delineated by the dotted green rectangle. The selected region extends from pixel 75 to pixel 170 in the horizontal direction and from pixel 1 to pixel 94 in the vertical. This defines a region from the 70th to

the 79th floor that is relatively free of smoke through most of the duration of the video. It extends from just beyond the south edge of WTC 2 on the left to just beyond the edge of 22 Cortlandt Street on the right. There is some distortion in the images in Fig. K-6; the aspect ratio of the pixels is elongated so that the region appears wider than it is high. The original digital video was recorded in RGB color. To simplify the analysis, each frame is converted into Grayscale mode using Adobe Photoshop. Possible intensity values for each pixel range from 0 for black to 255 for white.

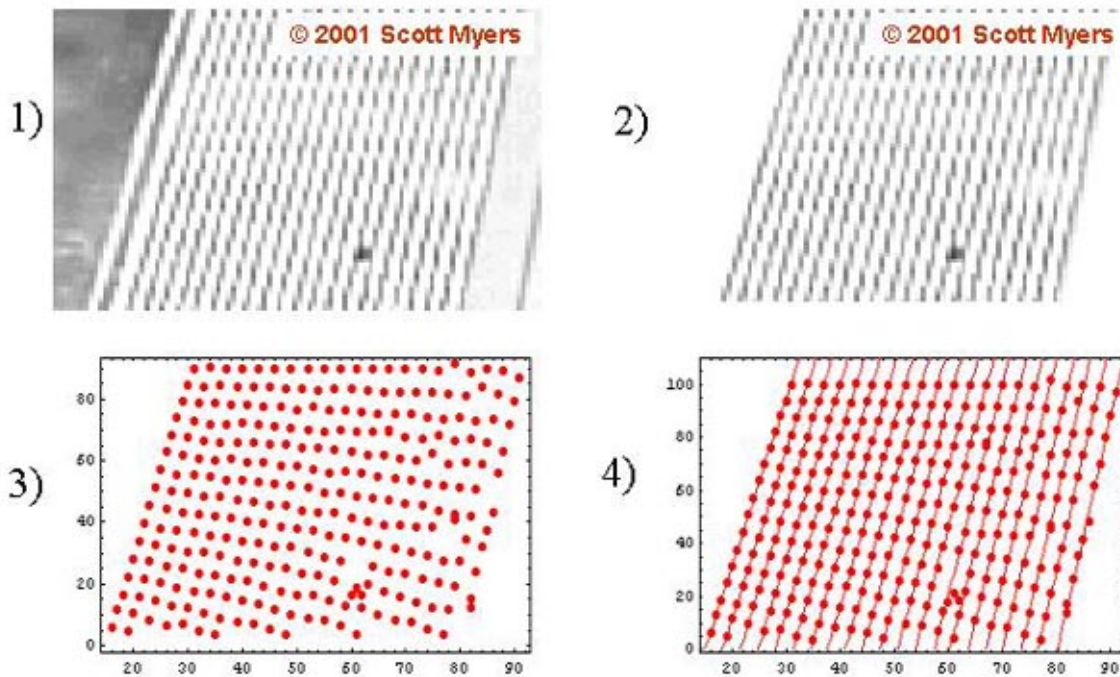


Figure K-6. Procedure for moiré analysis for WTC 2.

2. In the second step, pixels that lie outside of the set of window lines are deleted from consideration by setting first and last column numbers for each row. This is accomplished for the first row by studying the pixel intensities for this row. The windows are located at pixels of minimum values (darker intensity) spaced three or four pixels apart. A wider spacing identifies the space before the first window line, and a large number of higher (lighter) values identifies the space after the last window line. The rest of the rows are determined sequentially by starting with the same first and last column numbers as the previous row. The first column number is adjusted by shifting one to the right when lower intensities (darker pixels) are encountered. The algorithm is able to recognize regions of smoke and delete them from the analysis region.
3. Now the intersection points making up the moiré pattern can be calculated. Starting with the leftmost column remaining after step 2, sequences of intensity values are assembled column by column. For a single column from bottom to top, the intensity values decrease and increase as the column is crossed by successive lines of windows. Intersection points are found by assembling intensity sequences for adjacent columns where their row numbers overlap, smoothing the sequences near where intensities cross, and mathematically solving for the interpolated y value of the intersection point. Although the algorithm is tricked by the

dark piece of debris in this image and does not perfectly locate every point even in regions that are clear of debris, the large total number of points reduces the detrimental effect of this on the analysis.

4. In step 4, each intersection point is associated with a window line number n . The first window line is determined by collecting the highest row values y for each column x in the list of intersection points starting with the leftmost column and proceeding to the first column for which y is both above 81 pixels and exceeds the highest y for the next column. This identifies the points on window line one. After these points are deleted, a similar process determines the points on window line two. From the locations and angles of these two lines a sequence of lines is drawn to separate sets of intersection points belonging to individual window lines n . The vertical pixel height is corrected by the factor $1 / 0.9$ to convert to horizontal pixel units, changing the vertical scale on the plot.
5. Finally, the list of points (x, y, n) on the moire fringes is supplied to a least squares nonlinear fit to Eq. (1) to determine the values of the unknown parameters $(p, d_I, \theta_I, \Delta\theta)$ and their standard deviations. The uncertainty of each parameter with a confidence level of 95 percent is given by twice the standard deviation, or 2σ . Reference values for parameters are determined by averaging the values over (arbitrarily) 21 video frames just before the aircraft impact. The average location of the base of the first window line over these 21 video frames defines the fixed value of the initial location x_0 and the zero point of d_I . The average of the window spacings p provides a reference value of 3.241 pixels. The horizontal scale is set by the known 40 inch distance between windows. The conversion factor from pixel widths to inches for displacement and window spacing is therefore equal to 40 in. divided by the reference window spacing in pixel widths. This calculation assumes that WTC 2 is viewed at right angles to the east face and neglects viewing angle effects on window spacing. The angle of the line of sight with the center of the east face of WTC 2 is actually 12 degrees, or 2.09 rad. This assumption therefore causes a systematic error of +2 percent for length measurements. The viewing angle is shown to be important in extrapolating motion from the 70th floor to the top of WTC 2 later in this appendix.

The analysis procedure was implemented using Mathematica software. Displacement results from this analysis of WTC 2 are plotted in Fig. K-5(b) for the first three oscillation cycles on the left and for the last 70 seconds before the aircraft impact and first four minutes afterwards on the right. Results for all four parameters are plotted over a longer timescale in Fig. K-7.

The uncertainties in parameter values reflect imperfections in the collected data. The large amounts of debris falling from WTC 2 immediately after the aircraft impact cause problems for the automated analysis and result in a large amount of scatter during the first oscillation cycle. The automation is also challenged by dark and light regions that appear on long sequences of video frames, perhaps indicating debris or smudges on the camera lens. An example is the small lighter region about halfway up and to the right of the image shown in Fig. K-6. The algorithm also mistakenly drops the leftmost window line or two on some frames, resulting in errors in θ_I that appear in Fig. K-7(b). Out of the 22,591 frames analyzed, the procedure was unable to correctly analyze 883 frames. After elimination of these frames, the average uncertainty ($2\sigma_d$) for displacement d_I of the first window line is ± 1.7 in. over the first oscillation and ± 0.8 in. for the remaining 11 minutes of the video. The average uncertainties for the other parameters are $2\sigma_p = \pm 0.06$ in. for window spacing p , $2\sigma_\theta = \pm 0.001$ rad for angle θ_I of the first window line, and $2\sigma_\Delta = \pm 0.0001$ rad for angle increment $\Delta\theta$.

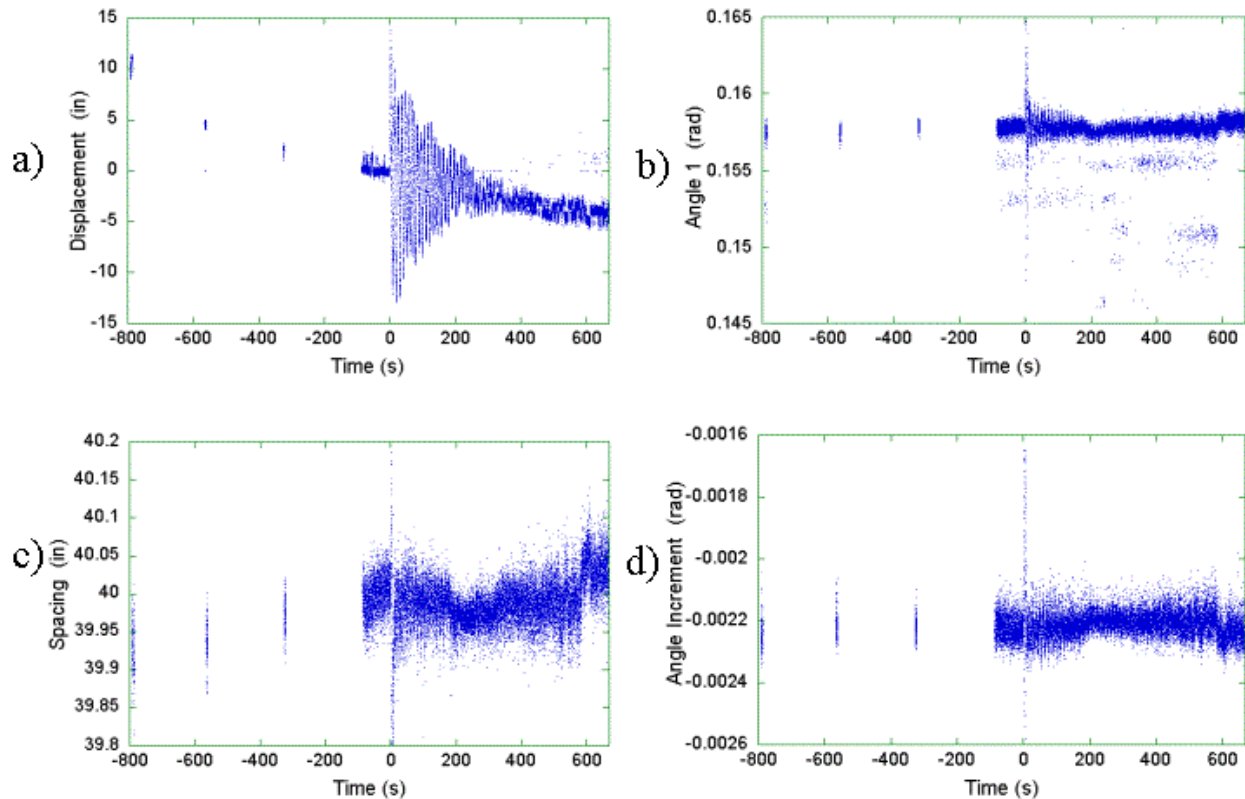


Figure K-7. Plots of WTC 2 analysis results over the entire duration of the uninterrupted video for a) displacement of the first window line d_1 , b) angle of the first line θ_1 , c) window spacing p , and d) angle increment $\Delta\theta$.

K.1.3 Correction Using Moiré Analysis of Fixed Building

Careful observation of the displacement data in Fig K-5(b), especially during the time before the aircraft impact, made clear that further analysis was needed. Short-lived jumps in the data by over an inch appear even before the impact. Frame-to-frame vibrations that last a few seconds at a time show disturbances on the order of an inch in magnitude periodically throughout the video, giving the appearance of double-valued peaks and anomalous tails in the plots. Moreover, analysis of five-second long samples of the video hundreds of seconds before the aircraft impact show a large change in apparent displacement of the building with time, as shown in Fig. K-7(a). Figures K-7(b), (c), and (d) show that spacing gradually increases over the nearly 25 min full duration of the video, although angles are relatively stable throughout. In the video itself, the displacement of all objects is indeed apparent to the eye when comparing frames from early and late times. Clearly the tripod-mounted camera was moving in time during filming. Displacement and spacing results from the analysis of WTC 2 alone are therefore questionable.

Fortunately, the composition of this video includes 22 Cortlandt Street in the foreground (Fig. K-1). This 34-story building across Church Street from the WTC complex provides a fixed reference whose apparent motion in the video reveals the camera motion. The 31 vertical lines running up the east face of the building provide a set of lines that can be used for a similar analysis to that performed on WTC 2, with the purpose of subtracting out the apparent motion caused by disturbances to the camera.

The procedure for automating the analysis of the apparent motion of the fixed building is similar but not identical to the automation procedure for analyzing WTC 2. The steps illustrated in Fig. K–8 are as follows:

As in the WTC 2 analysis, the first step is to crop the region to be analyzed from the full 720 pixel \times 480 pixel video frame. The selected region, outlined in the dashed blue rectangle in Fig. K–1, extends from pixel 160 to pixel 500 in the horizontal and pixel 1 to pixel 98 in the vertical. In this region, the building lines seen in perspective extend from the top to the bottom of the frame. The image mode is again changed from RGB color to Grayscale.

1. The goal of the second step is to establish a mask that contains only the pixels in the building lines. This eliminates the dark smudge near the top left corner and other distractions, such as flying debris that occasionally crosses between the building and the camera. This is accomplished by considering the intensities for each row of pixels in turn. For most rows, the dark building lines are easily distinguished as low intensity values along the row. Intensities above a set cutoff point are set to 255 (white), and the spacing of the remaining non-white minimum values is determined. Due to changes in video brightness over time, the cutoff point may eliminate some desired minima; these are replaced by an algorithm that enforces even spacing (plus or minus one pixel) across the row. Extra minima caused by debris are absorbed to maintain even spacing. The final mask distinguishes all building lines, each of which is three or four pixels wide.
2. Superimposing the mask on the original data results in well-defined building lines with intensities of all other pixels set to 255. Calculation of the intersection points is accomplished using the same method as used for WTC 2: by comparing increasing and decreasing sequences of intensities whose rows overlap for adjacent columns. The intensity data are noisy, resulting in some column sequences that are not monotonically decreasing then increasing as the building line crosses the column. The example shown in Fig. K–8 demonstrates the nature of the resulting set of intersection points, for which imperfect moiré patterns can be seen on the left half of the building but are more difficult to make out on the right.
3. The mask for building lines from step 2 assists in associating each intersection point with a line number. The vertical pixel height is corrected by the factor $1 / 0.9$.
4. A nonlinear regression analysis based on Eq. (1) to determine fixed building displacement d_f , line spacing p_f , first line angle ϕ_1 , and angle increment $\Delta\phi$ from the entire list of points (x, y, n) gave poor results and high values for standard deviations. Several forms for a solution were considered; the final choice was to use the calculated x -intercepts and angles for the first and last (31st) building lines. The x -intercept is the distance in pixel widths from the left edge of the analysis region to the position where the line crosses the base of the video frame.

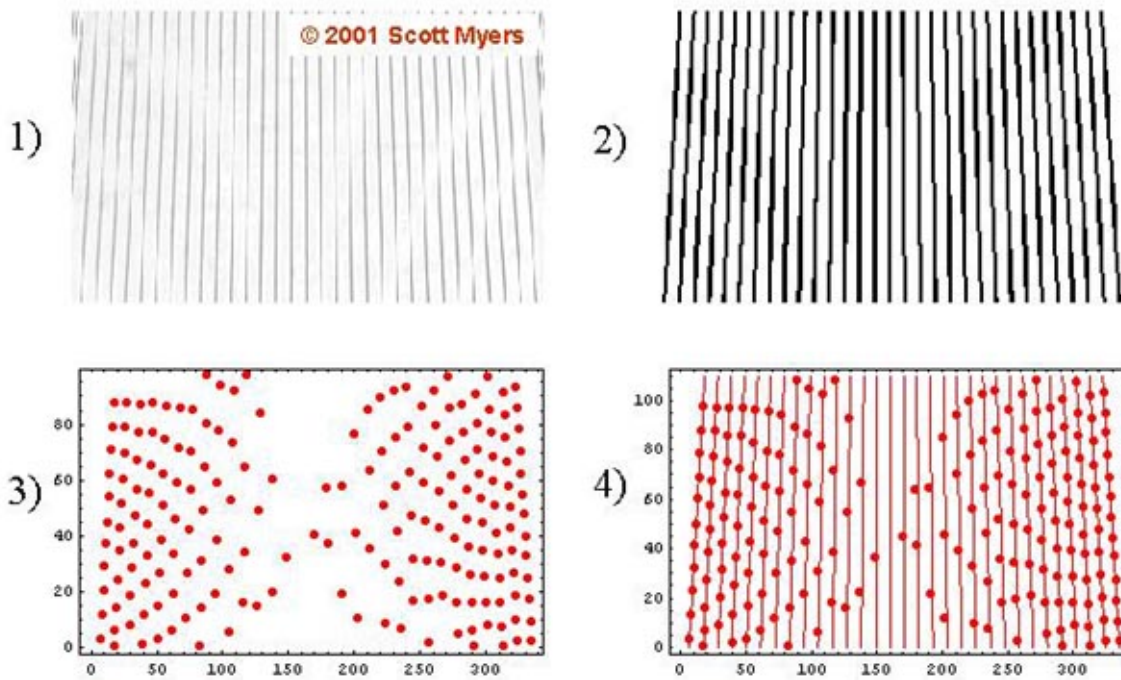


Figure K-8. Procedure for moiré analysis for fixed building in front of WTC 2.

Figure K-9 shows the results of the fixed building analysis over the full span of the uninterrupted video. In Fig. K-9(a)-(d) are the x -intercepts, s_1 and s_{31} , and angles, ϕ_1 and ϕ_{31} , from the 1st and 31st building lines as determined from a least squares fit of intersection points to the equation of a straight line. The spacing of building lines at the base of the frame, $\Delta s = (s_{31} - s_1) / 30$, is plotted in Fig. K-9(e), and the angle increment $\Delta\phi = (\phi_{31} - \phi_1) / 30$ is plotted in Fig. K-9(f). The x -intercepts clearly show the occasional jumps and frame-to-frame vibrations that appear in the WTC 2 displacement data, indicating rapid camera movements perhaps due to building vibrations or wind. They also indicate a long-term drift, best illustrated as a steady increase in spacing in Fig. K-9(e). This is consistent with a speculation that the camera mount slowly lowered with time, gradually including more of the buildings in the frame. This widens the buildings at the base, where calculations of displacement and spacing are made, from the perspective of the camera aiming up at the buildings. A careful comparison of early and late frames in the video supports this hypothesis; a top corner of One Liberty Plaza that appears in the upper left corner of the frame (see Fig. K-1) shifted upward by about 4 pixels over the 24.5 min video without moving significantly in the horizontal direction or changing size.

Angles for fixed building lines 1 and 31 show a long-time increase by about 0.0015 rad. The angle increment stays relatively steady, consistent with a slow counter-clockwise change in camera tilt looking at the camera from the rear.

Uncertainties for the fixed building analysis are about the same as those for the WTC 2 analysis. The linear regression analyses for 1st and 31st x -intercepts result in average uncertainties of ± 0.06 pixel widths and ± 0.07 pixel widths respectively over all analyzed frames. These can be compared with uncertainties for the WTC 2 analysis by dividing the average displacement uncertainty $2\sigma_d = \pm 0.8$ in. by the conversion factor of 40 in. / 3.241 pixels to get ± 0.06 pixel widths.

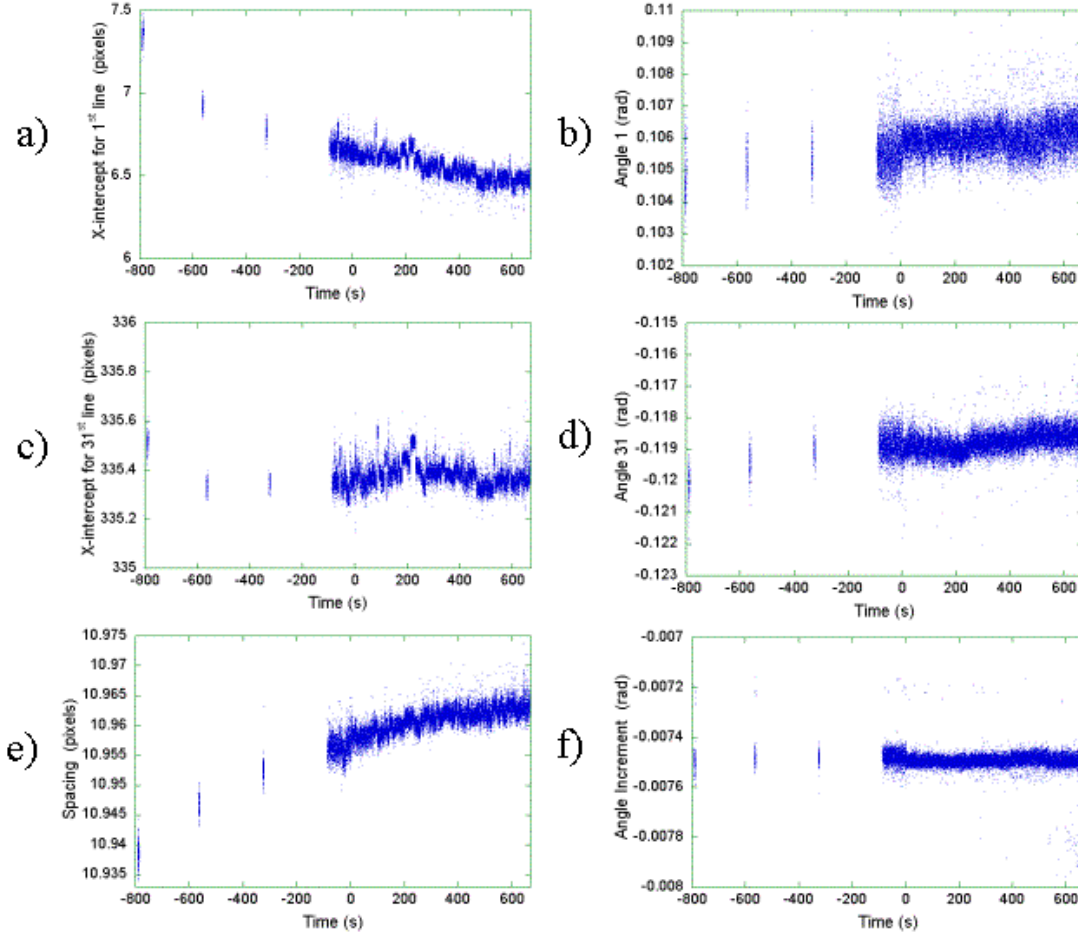


Figure K-9. Plots of fixed building analysis results over the entire duration of the unadjusted video for a) x-intercept of the first line s_1 in horizontal pixels, b) angle of the first line ϕ_1 , c) x-intercept of the 31st line s_{31} , d) angle of the 31st line ϕ_{31} , e) line spacing $\Delta s = (s_1 - s_{31}) / 30$, and f) angle increment $\Delta\phi = (\phi_1 - \phi_{31}) / 30$.

The next step was to use the results for the fixed building to determine the correct procedure to remove camera motion from the WTC 2 data. The fixed building analysis shows frame-to-frame and long-term variations in the first and last x- intercepts s_1 and s_{31} and in the spacing Δs between the lines on the building. The geometry chosen for the correction is shown in Fig. K-10. Neglecting angular variations, the simplest equation giving the base position of WTC 2 as the fixed building changes its position in the video frame is

$$d_k = s_{1,k} - (s_{1,0} - d_0) \left(\frac{s_{31,k} - s_{1,k}}{s_{31,0} - s_{1,0}} \right) \quad (4)$$

where

d_0 = initial location of x-intercept of the leftmost line of windows in WTC 2

$s_{1,0}$ = initial location of x-intercept of the first line on the fixed building

$s_{31,0}$ = initial location of x -intercept of the 31st line on the fixed building

d_k = location of x -intercept of the leftmost line of windows in WTC 2 at frame k

$s_{1,k}$ = location of x -intercept of the first line on the fixed building at frame k

$s_{31,k}$ = location of x -intercept of the 31st line on the fixed building at frame k

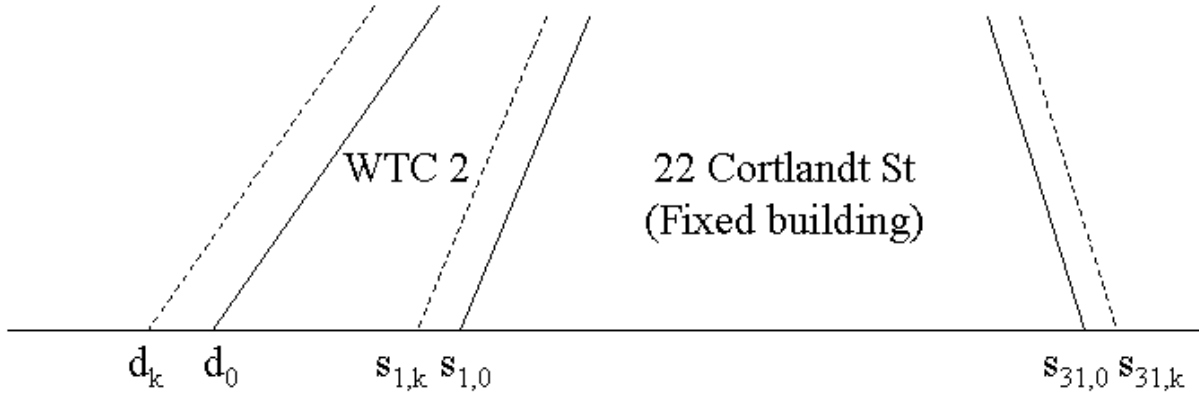


Figure K-10. Geometry for correction.

For this calculation, all locations are measured in pixel widths from the left edge of the video frame. The corrected displacement of WTC 2 in frame k in response to the aircraft impact is the difference $d_1 - (d_k - d_0)$ between the measured displacement d_1 and the displacement $(d_k - d_0)$ that would be expected in the absence of motion, converted back into inches. The window spacing p is corrected by subtracting the spacing p_k scaled by the relative dimensions of the fixed building in frame k :

$$p_k = p_0 \left(\frac{s_{31,k} - s_{1,k}}{s_{31,0} - s_{1,0}} \right) \quad (5)$$

The camera motion can now be subtracted from the WTC 2 data.

The resulting motion of WTC 2 with camera motion subtracted out is shown over the full duration of the video in Fig. K-11. A comparison of the plot of displacement with Fig. K-7(a) shows how well the fixed building analysis has corrected the displacement of WTC 2 to an average of zero inches over the entire period before the aircraft impact. Referring back to Fig. K-5, the plots in (c) show the corrected displacement over the first three cycles and the first four minutes after the aircraft impact for a direct comparison with the uncorrected WTC 2 analysis in (b) and with data collection by eye in (a). Note in the left-hand plot that the double-valued maximum of the third oscillation resulting from frame-to-frame vibration has been smeared (though not completely eliminated) by the camera correction. On the right-hand plot, the variations before the aircraft impact have been eliminated. The envelope containing the oscillations has been smoothed out, and the beating phenomenon with a period of approximately 70 s is clearer. The uncertainty of the corrected data $2\sigma_{corr}$ is calculated as a quadrature sum of the uncertainty $2\sigma_d$ of WTC 2 displacement plus the uncertainty $2\sigma_{fixed}$ of the fixed building displacement:

$$2\sigma_{corr} = \sqrt{4\sigma_d^2 + 4\sigma_{fixed}^2} \quad (6)$$

The average value of uncertainty for the corrected displacement is ± 1.2 in.

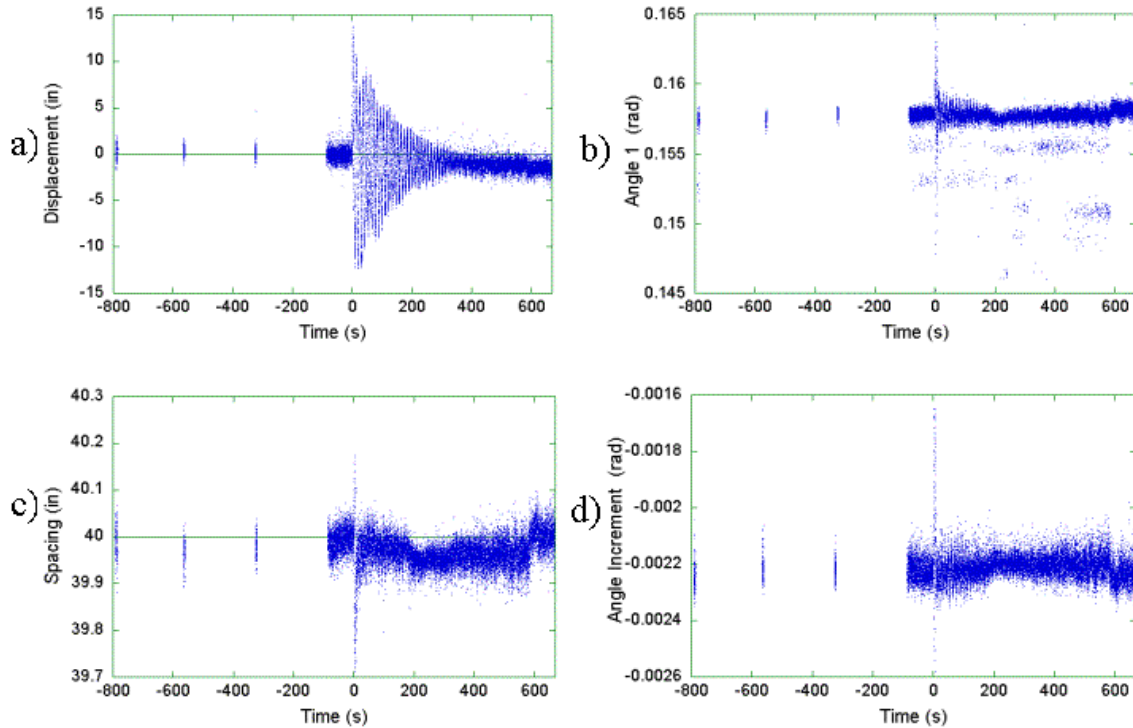


Figure K-11. Plots of corrected WTC 2 analysis results over the entire duration of the uninterrupted video for a) building displacement of the first window line at the 70th floor d_1 , b) angle of the first line θ_1 , c) window spacing p , and d) angle increment $\Delta\theta$.

The window spacing plotted in Fig. K-11(c) shows improvement in pre-impact data over the uncorrected values in Fig. K-7(c), although the correction is not as successful as for displacement. The angle data was not changed by this correction.

An interesting anomaly remains in the data after correction. In the absence of significant damage, a building responding to an impulse force would be expected to return to its original position. Once the oscillations caused by the aircraft impact have died down after 300 s, however, Fig. K-11(a) indicates a displacement toward the south at the 70th floor that increases with time, to a value of approximately -1.5 in. by eleven minutes after the aircraft impact. Unfortunately, the video content changes at this point, and it is not possible to track this motion farther in time or to determine definitively whether the building is tilting or deforming. Recall that the moiré pattern analysis is performed using data taken below the aircraft impact zone. A true offset of this magnitude at the 70th floor would require a much larger offset at the roof level, which is not in agreement with observations.¹

¹ Kausel, E. 2004. Professor of Civil Engineering, Massachusetts Institute of Technology, Cambridge, MA personal communication to T. McAllister, National Institute of Standards and Technology, Gaithersburg, MD. Observed dynamic response to collision.

The corrected data contains other abrupt changes that are not well explained. At around 200 s, the spacing in Fig. K–11(c) decreases suddenly, accompanied by a slight decrease in angle of the first window line in (b) and a slight increase in angle increment in (c). At around 600 s, the reverse conditions occur: a sudden increase in spacing accompanied by an increase in first line angle and decrease in angle increment. Visual evidence of WTC 2 shows no obvious events occurring at these times that might explain these phenomena.

K.1.4 Oscillation Modes

Figure K–12 shows the corrected data for WTC 2 motion over a ninety second time period that illustrates the oscillatory behavior of displacement, spacing, and angular data. Data for the first oscillation, from 0 s to about 11 s, are very noisy. As mentioned previously, this is because immediately after impact the automated analysis procedure finds it difficult to distinguish the underlying moiré pattern from the large amount of flying debris. Past the first oscillation, periodic behavior with a fundamental period of approximately 11 s is observed for displacement d_l , angle of the leftmost window line θ_l , and angle increment $\Delta\theta$. Interestingly, the fundamental period for window spacing p appears to be on the order of 5 s. This phenomena will be explored in a study of oscillation modes.

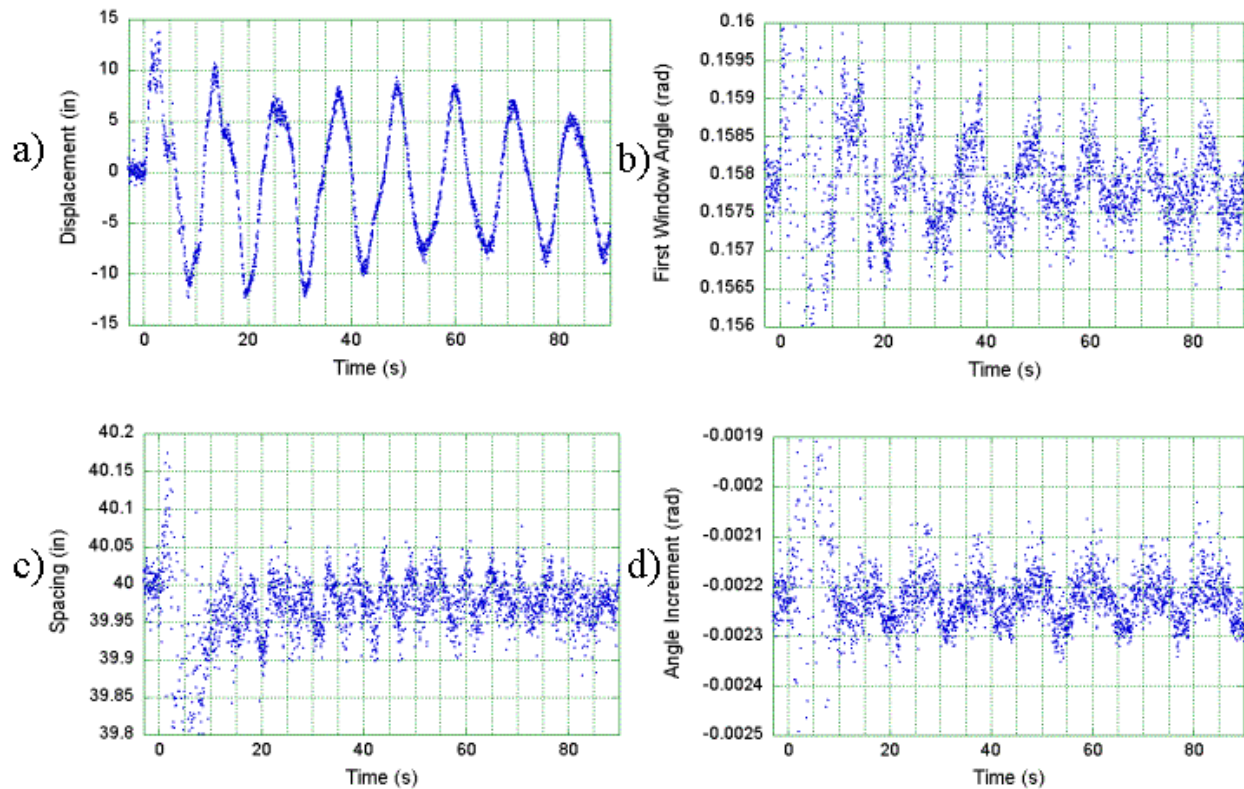


Figure K–12. Plots of WTC 2 analysis results corrected for camera motion over the first ninety seconds after impact for a) displacement of the first window line d_l , b) angle of the first line θ_l , c) window spacing p , and d) angle increment $\Delta\theta$.

The natural vibration frequencies and mode shapes of a building are properties of its design. Vibration modes for rectangular buildings are categorized into translational modes, for which the building sways

back and forth, and torsional modes, for which the building twists. The building is fixed at the ground for all modes. The fundamental mode, with the longest period of oscillation, is a simple swaying motion in either the north-south or the east-west plane. For the second translational mode, floors below a fixed level move in one direction while floors above move in the other direction in the same plane. For the first torsional mode, the building twists at an angle that increases with height, alternately rotating in clockwise and counterclockwise directions. For the second torsional mode, floors below a fixed level twist clockwise while floors above twist counterclockwise, then the directions reverse.

Table K–1 lists the periods for the lowest natural modes of WTC 2, calculated from a detailed structural model (NIST NCSTAR 1-2A, Chap. 2)². Periods are not the same in the north-south (N-S) and the east-west (E-W) directions because of the orientation of the rectangular central core. The stiffness of the building, and therefore its vibration period, is modified by additional overturning moments that become significant for large amplitude motions. This second-order behavior, known as the P-Delta effect, tends to increase the period for large amplitudes as shown in Table K–1.

Table K–1. Periods of modes for WTC 2 (NIST NCSTAR 1-2A).

WTC 2	N-S	E-W
Fundamental mode: no P-Delta effects	10.7 s	11.4 s
with P-Delta	11.2 s	12.1 s
Second translational mode	3.8 s	4.2 s
First torsional mode	5.2 s	
Second torsional mode	2.4 s	

Source: NIST NCSTAR 1-2A.

The modes activated by the aircraft impact may be understood as follows. The aircraft impacted the south face of WTC 2 at a location off-center towards the east while travelling in a northeast direction relative to the tower. The primary forward momentum was imparted along the north-south axis of the building. The angle of impact imparted an angular momentum as well, twisting the building in a counter-clockwise direction. Since the impact occurred at a height well below the roof, higher order modes were also excited. The excitation of east-west modes is expected to be small.

The dominant modes of vibration explain the evident periods for the four variables plotted in Fig. K–12.

As the building sways back and forth in the north-south direction with the translational modes, the displacement and angle of each window line follow this motion, but in such a way that the apparent spacing between each window line as viewed from the east does not change significantly. Thus it is not surprising that the dominant periodicity for d_l and θ_l agrees with the fundamental mode at approximately 11 s. The same periodicity is found in the plot of angle increment $\Delta\theta$, although this will be shown to result from the camera viewpoint more than from the building motion.

As the building twists with a torsional mode, the east face becomes alternately more and less perpendicular to the line of sight from the camera. This results in a change of apparent window spacing,

² This reference is to one of the companion documents from this Investigation. A list of these documents appears in the Preface to this report.

and to a lesser extent changes in displacement and angles. The dominant periodicity for p in Fig. K-12 agrees with the approximately 5 s period of the first torsional mode, as would be expected. The 5 s period of the dominant motion for p also provides evidence that little momentum was imparted in the east-west direction. If significant east-west vibrations had indeed occurred, the sway of the building toward and away from the camera would have caused vibrations with a period of about 11 s in apparent window spacing.

Determining the modal content of the data from the moiré analysis will provide specific information about the response of WTC 2 to the aircraft impact, including the period, amplitude, and decay rate of building oscillations as a function of time. The first set of data to be studied is the displacement d_l of the leftmost line of windows, plotted in Fig. K-11(a) and Fig. K-12(a). The damped harmonic nature of the signal is apparent in Fig. K-11(a), which also indicates the possibility of a roughly linear change in the zero point of the displacement with time. A mathematical model that describes this time-dependent motion is

$$d_l = [A + B(t - t_0)] + Ce^{-D(t-t_0)} \sin[2\pi(t - t_0)/E + F] \quad (7)$$

where

d_l = model approximation to the displacement, in.

t = time, s

t_0 = initial time of the building response, s

A = baseline offset, in.

B = linear slope of the baseline, in./s

C = initial amplitude at time t_0 , in.

D = decay rate, (s)⁻¹

E = oscillatory period, s

F = phase, rad

The values to be determined are A , B , C , D , E , and F . The frequency is equal to the reciprocal of the period, $(E)^{-1}$. To accurately fit this model to the data, a good approximation is needed for each of the six variables to be determined. These approximations are used as starting points for a nonlinear least squares fit of Eq. (7).

The first analysis is performed on the initial three minutes of displacement data. The excursion in displacement values begins in the 11th video frame after the frame shown in Fig. K-1, after a short lag in building response due to the finite time required to transfer momentum from the aircraft to the building. The initial time is therefore set to the frame before motion begins, at time $t_0 = (10 \text{ frames}) / (29.97 \text{ frames/s}) = 0.3337 \text{ s}$. The final frame is at $t = 181.849 \text{ s}$. If all frames had been included in this data sequence, the number of frames in the analysis would be 5103. Because of frames that were dropped

from the data set due to problems with the video frame analysis, the actual number of frames in the sequence is 5021.

To find the important modes in the displacement data, a sequential residual analysis is performed. Figure K–13 shows plots of successive residuals in the course of this analysis. The original data are plotted in Fig. K–13(a). The evident period of 11.4 s and an initial amplitude of 10 in. are used as initial guesses for E and C respectively. Initial guesses for A , B , D , and F are set to zero, and the nonlinear least squares fit is performed. The resulting parameter values for this first mode are given in the first line of Table K–2. Subtraction of this damped harmonic function from the original data results in the residual data shown in Fig. K–13(b). Inspection of this residual reveals periodic behavior with a period of about 5 s and an amplitude of about 3 in.. Using these as the initial guesses for E and C results in the parameter values given in the second line of Table K–2. Subtracting this second mode from the first residual results in the second residual shown in Fig. K–13(c). This residual shows oscillatory behavior with a period around 4 s and amplitude around 1 in.. This is used for the next nonlinear fit, with results on the third line of Table K–1. Finally the third residual, in Fig. K–13(d), displays a period around 2 s close to the start of the oscillations. The results of the final nonlinear fit are shown in the last line of Table K–2. The total standard deviation from the final fit, the square root of the estimated variance, is 0.48 in.. The uncertainty, with a confidence level of 95 percent, is twice the standard deviation, or ± 0.96 in..

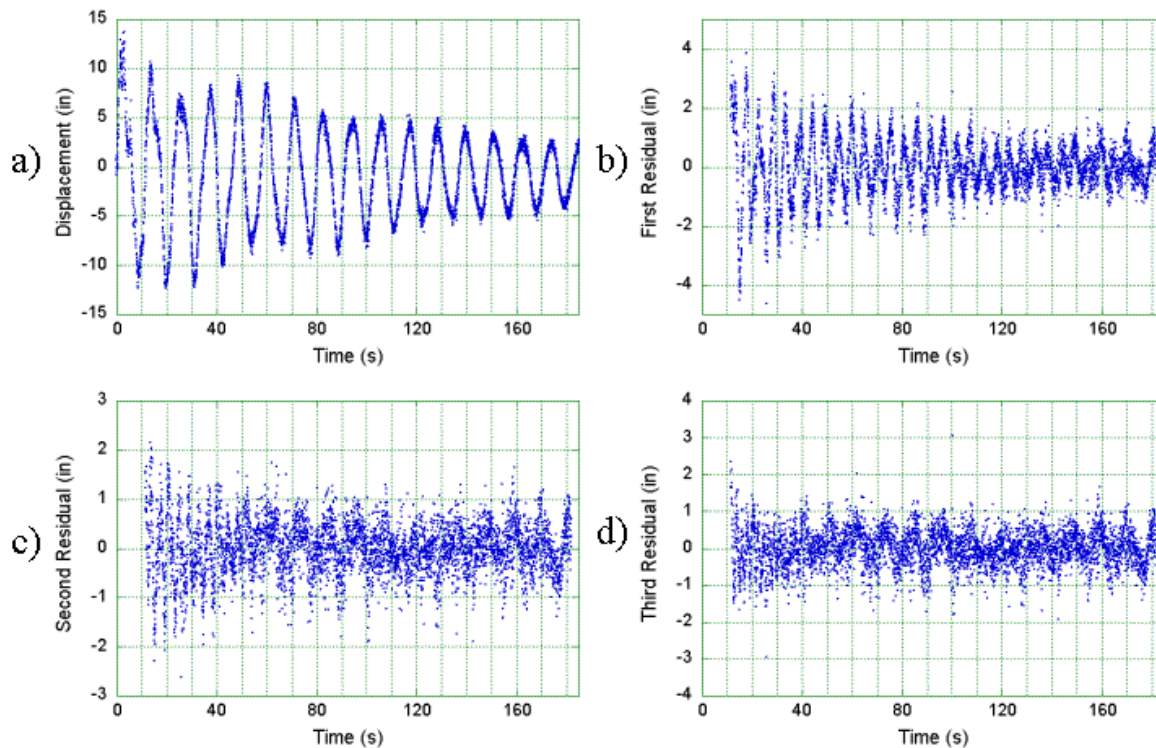


Figure K–13. Sequential residual plots: a) initial displacement data, b) first residual, c) second residual, d) third residual.

An improvement in the modal parameter values can be obtained by performing a nonlinear least squares fit on an 18-parameter model consisting of the baseline offset and slope terms plus all four damped modes, using the values listed in Table K-1 as initial guesses. The results of this analysis are given in Table K-2. Total standard deviation from this model is 0.47 in., giving an uncertainty of ± 0.95 in..

Table K-2. Modes from sequential nonlinear least squares analyses of residuals. Uncertainties are twice the standard deviation (95th percentile).

E Period (s)	C – Initial Amplitude (in.)	D Decay Rate (s ⁻¹)	F Phase (rad)	A Offset (in.)	B Slope (in./s)
11.396 \pm 0.003	10.7 \pm 0.1	0.0065 \pm 0.0001	-0.13 \pm 0.01	-0.91 \pm 0.06	0.0006 \pm 0.0006
5.259 \pm 0.003	2.78 \pm 0.09	0.0130 \pm 0.0006	-0.92 \pm 0.03	-0.04 \pm 0.03	0.0003 \pm 0.0003
3.892 \pm 0.007	1.1 \pm 0.1	0.022 \pm 0.003	-1.3 \pm 0.1	0 \pm 0.03	0 \pm 0.0003
2.151 \pm 0.008	2.4 \pm 0.5	0.07 \pm 0.01	4.7 \pm 0.2	0 \pm 0.03	0 \pm 0.0003

The periods of these four modes may be compared to the periods of natural vibrations of WTC 2 in Table K-1. At 11.4 s the period of the first mode found in the displacement data is longer than the basic value for the fundamental mode of WTC 2 in the north-south direction. However, it is much closer to the P-Delta value, which includes increased stiffness due to large amplitude distortions. It is also possible that the natural period has been lengthened by damage to the structure. Given the range of periods measured by monitoring instruments mounted on WTC 1 over multiple days (NIST NCSTAR 1-2A, Chap. 2), the difference in WTC 2 periods between data and calculation may not be significant. Note that the orientation of the WTC 1 core is at right angles to that for WTC 2, so north-south vibrations for WTC 2 correspond to east-west vibrations for WTC 1. The 5.3 s period of the second mode from Table K-3 is consistent with that expected for the torsional mode, and the periods of the third and fourth modes are comparable to those of the second translational mode and second torsional mode respectively.

Table K-3. Modes from nonlinear least squares analysis of original data with 18 parameters. Uncertainties are twice the standard deviation.

E Period (s)	C – Initial Amplitude (in.)	D Decay Rate (s ⁻¹)	F Phase (rad)	A Offset (in.)	B Slope (in./s)
11.392 \pm 0.001	10.70 \pm 0.06	0.00652 \pm 0.00007	0.027 \pm 0.006	-0.96 \pm 0.03	0.0010 \pm 0.0003
5.258 \pm 0.002	2.66 \pm 0.08	0.0125 \pm 0.0005	-0.54 \pm 0.03	—	—
3.897 \pm 0.007	1.3 \pm 0.1	0.026 \pm 0.003	-0.6 \pm 0.1	—	—
2.149 \pm 0.008	2.7 \pm 0.6	0.07 \pm 0.01	-0.7 \pm 0.2	—	—

The four decaying modes discovered by sequential analysis of displacement data residuals are plotted individually in Fig. K-14. As the period decreases, the decay rate increases. Although it decays the fastest, the initial amplitude of the fourth mode, with the highest frequency, is larger than that of the third mode.

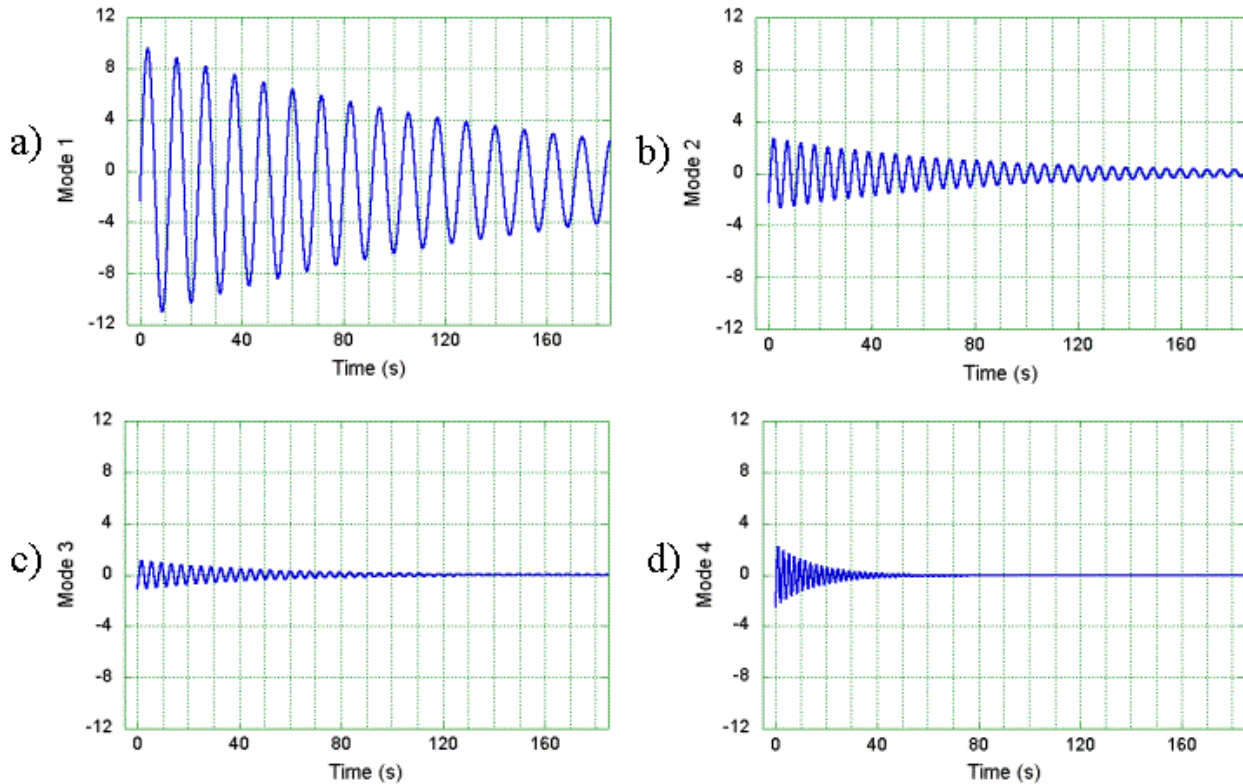


Figure K-14. Modes from analysis of displacement data, with periods of a) 11.39 s, b) 5.26 s, c) 3.90 s, and d) 2.15 s.

The sum of these four modes is displayed in Fig. K-15(a). Figures K-15(b), (c), and (d) compare this sum with the displacement data on various timescales. The sum of modes shows excellent agreement with the data over the initial four minutes of impact response. Fig. K-15(b) shows that the jerks in north-south building motion observed over the first couple of oscillations are captured by the modal analysis. Summation of only two modes at a time reveals that the cause is the high frequency fourth mode. The 70-second envelope appearing in Figs. K-15(c) and (d) is reproduced by the combination of the fundamental plus the torsional mode. In Fig. K-15(d) the sum of modes determined over the first 3 minutes is extrapolated over the full duration of the data and shows phenomena that are not well captured by this analysis. After the first four minutes, the fundamental mode begins to fall out of sync with the data, whose period appears to be decreasing with time. The increasing southward displacement with time shown in the data is also not found in the extrapolation, indicating that this unexplained anomaly in the data does not begin in the first few minutes after impact.

It is possible that changes in the vibration period with time could indicate structural changes that take place during the first 11 min after impact. To investigate changes in the fundamental mode with time, the displacement data was divided into 1000-point (33.37 s) segments for analysis. Linear interpolation was used to fill in any missing data points. The data sets are displayed on a common scale in Fig. K-16 and on a scale that spans each individual set of data in Fig. K-17. The increase in the amount of relative noise in the data as the initial motion damps out is apparent in the latter figure, indicating the increasing difficulty with time of separating signal from noise. This is reflected in the level of uncertainty for each segment upon analysis. Two segments from before the aircraft impact were also analyzed.

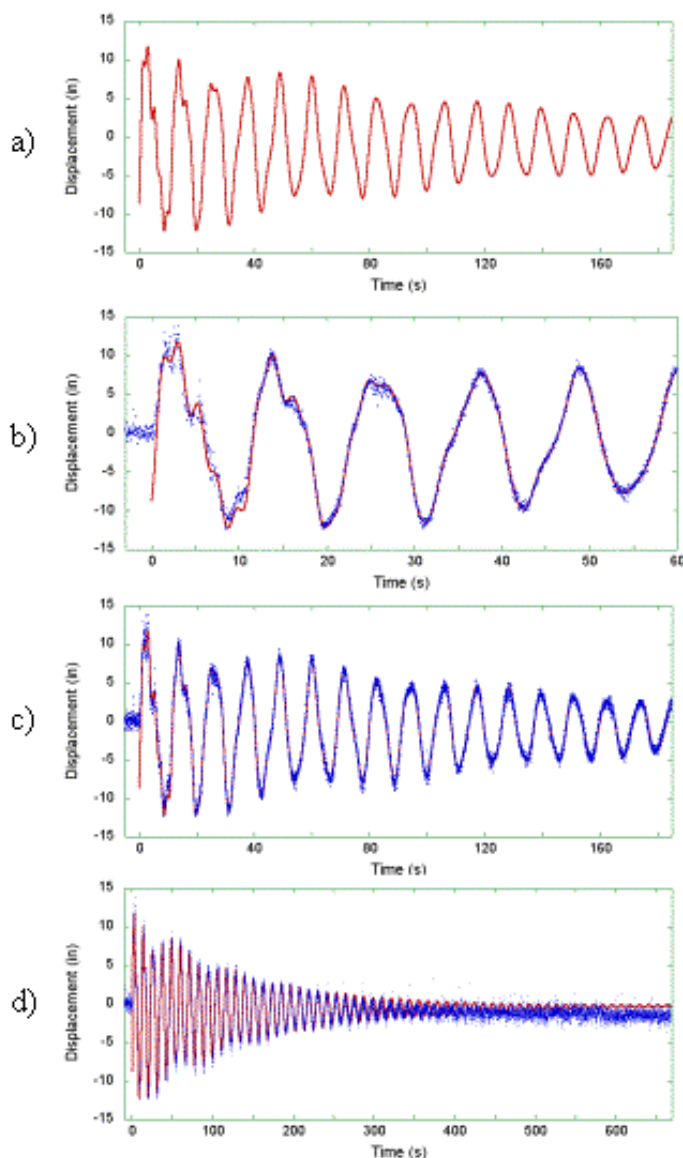


Figure K-15. Sum of four modes and a comparison with displacement data.

The analysis procedure for each data set is illustrated in Fig. K-18. Starting with the raw data in Fig. K-18(a), a good initial value for frequency is determined from the spectral plot in (b). The spectral plot is obtained from the Fourier transform of the autocorrelation plot, which smooths the raw data [NIST/SEMATECH *e-Handbook of Statistical Methods* (spectrum.htm), 2003]. This captures the frequency content of the raw data better than a Fourier transform of the raw data directly. A good approximation for amplitude is obtained from the complex demodulation amplitude plot in (c), [NIST/SEMATECH *e-Handbook of Statistical Methods* (compdeam.htm), 2003] and for phase from the complex demodulation phase plot in (d) [NIST/SEMATECH *e-Handbook of Statistical Methods* (compdeph.htm), 2003]. Fig. K-18(e) plots the damped harmonic mode estimated by this process superimposed on the raw data. The phase is improved in (f), which plots the raw data along with the initial guess to be submitted to the nonlinear least squares regression analysis. Plot (g) shows the results of the nonlinear fit to equation (7), and plot (h) shows the residual after subtracting this solution from the data.

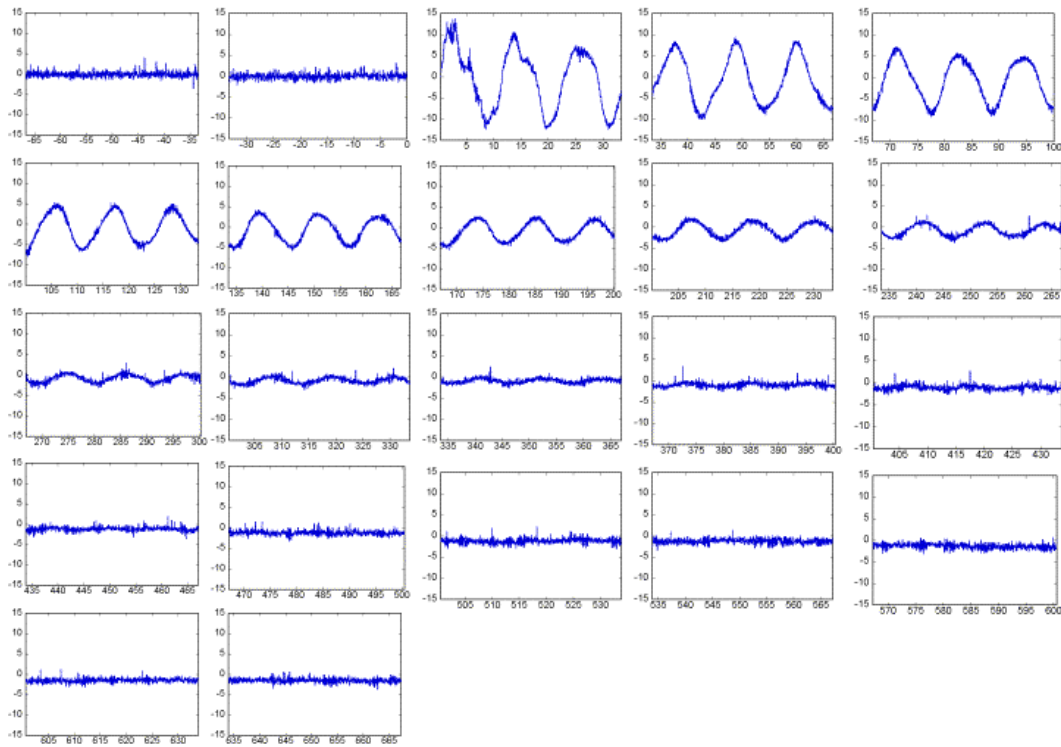


Figure K-16. Division of displacement data into subsets of 1000 points (33.37 s). Data displayed using a common displacement scale.

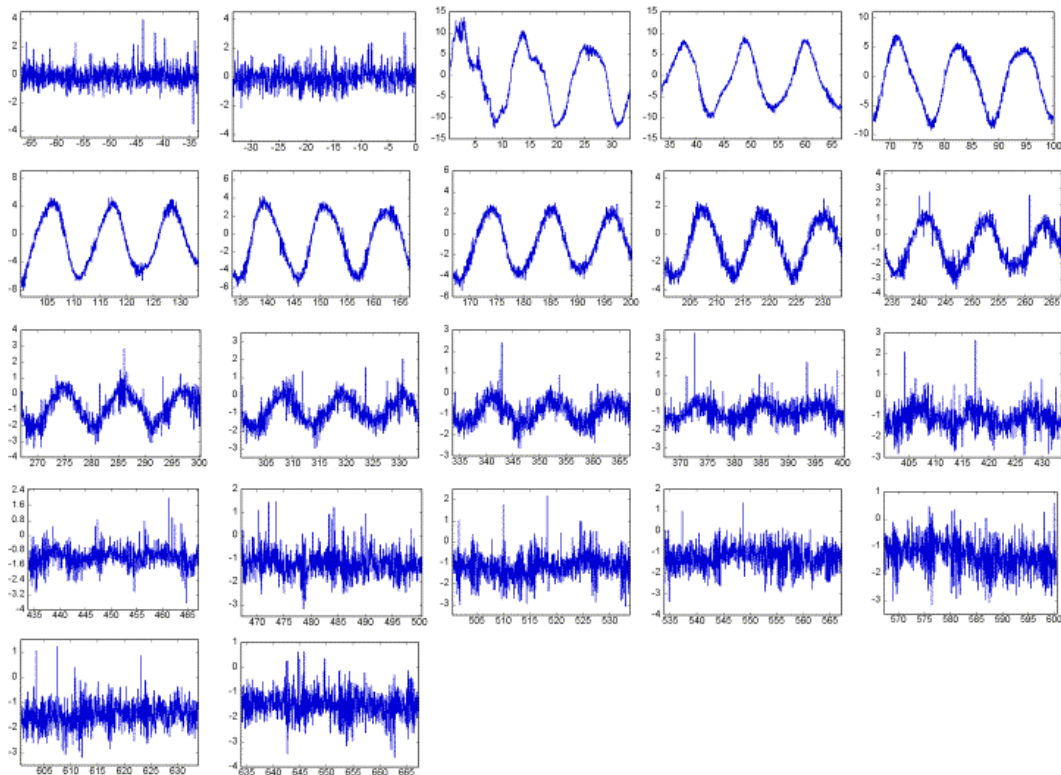


Figure K-17. Same as Fig. K-16 with 1000-point subsets of displacement data each displayed using a displacement scale that spans the data over the subset.

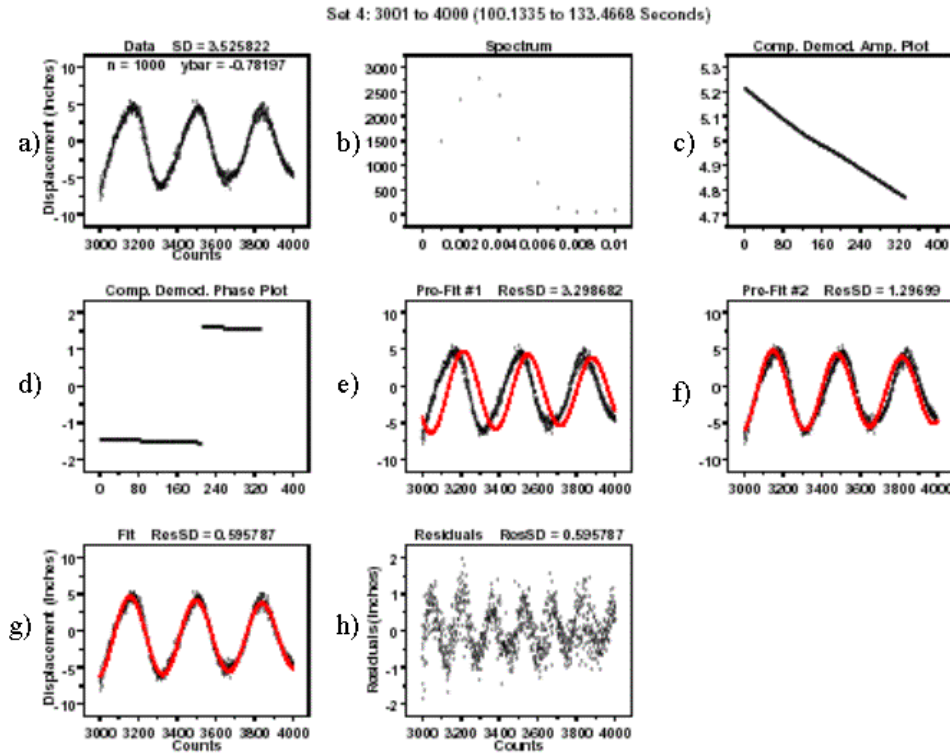


Figure K-18. Procedure for analysis of segments of displacement data.

The results of this analysis are shown in Fig. K-19. The period in Fig. K-19(a) decreases slowly from 11.5 s immediately after the aircraft impact to 11.1 s six minutes afterwards. Reflecting the decreasing signal-to-noise ratio, the uncertainties, indicated by the red bars at each point, increase sharply past a time of 500 seconds. A vibration period that decreases with time is the opposite of the trend that would be expected in the presence of increasing structural damage. A possible alternative explanation is that the initial large amplitude of the oscillation motion, which effectively stiffens the structure, gradually decreases to small amplitudes. A longer vibration period for larger amplitude motion is reflected in the P-Delta value in Table K-1. Supporting this interpretation is the tendency toward longer periods for higher wind speeds noted in the discussion of measured natural frequencies for WTC 1 in NIST NCSTAR 1-2A, Chap. 2.

Fig. K-19(b) plots the initial amplitude of each data set along with a nonlinear least squares fit to the equation for simple exponential decay,

$$y = Ae^{-Bt} \quad (8)$$

where A is amplitude and B is decay rate. The values determined by this nonlinear least square fit are $A = 10.4 \text{ in.} \pm 0.5 \text{ in.}$ and $B = 0.0068 \text{ s}^{-1} \pm 0.0005 \text{ s}^{-1}$, for an overall uncertainty of $\pm 0.6 \text{ in.}$ Both amplitude and decay rate are within five percent of the values for the first mode included in Table K-1. The decay rates over time for the individual samples are much smaller, on the order of 0.0003 s^{-1} as shown in Fig. K-19(d). Figure K-19(c) shows that the offset is more or less steady with a value of approximately -0.8 in. until a roughly linear decline begins around time $t = 300 \text{ s.}$

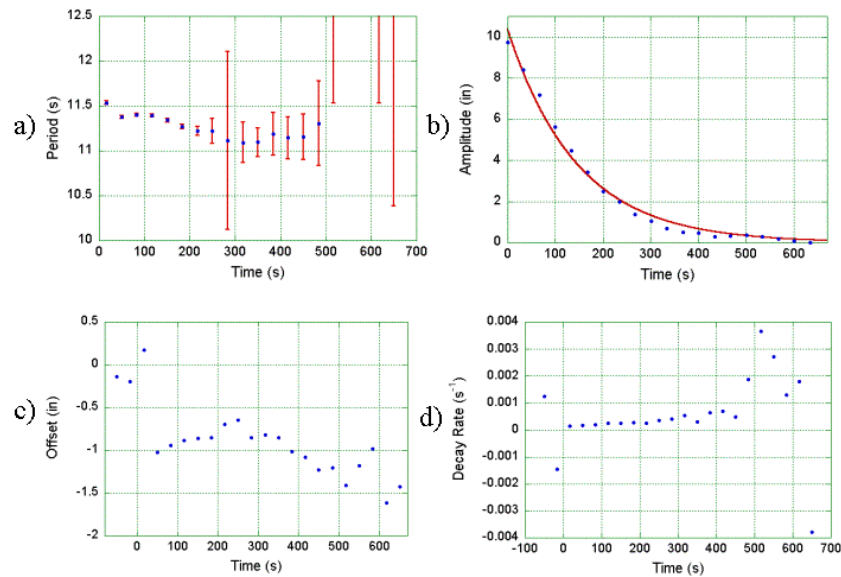


Figure K-19. Results of modal analysis as a function of time: a) fundamental period, b) amplitude, c) zero point offset, and d) decay rate.

In addition to the modal analysis of deflection data, modal analyses were also performed on the apparent window spacing p and angular data θ_i and $\Delta\theta$, whose data over the first ninety seconds are displayed in Fig. K-12. The modes investigated were the four modes identified in the displacement data. Initial guesses of modal periods for the nonlinear least squares analyses of the original data and its residuals were thus set sequentially to the values in Table K-3. Tables K-4 through K-6 list the period, amplitude, decay rate, and phase for these four modes as found in the spacing p , first window angle θ_i , and angle increment $\Delta\theta$ data respectively. Also listed are the offset, or initial value of the baseline, and the slope of the baseline with time. Figures K-20 through K-22 present plots of the sum of modes in (a), the sum superimposed on the data in (b), and the final residual in (c).

For window spacing, shown in Table K-4 and Fig. K-20, the second mode, with a period of 5.3 s, dominates. The third mode is second in importance initially, but the first mode extracted from this analysis has a negative decay rate and grows in time. Because of the physically unrealistic growth of the fundamental mode, this set of modes is useful only over the time period chosen for the analysis and may not be extrapolated beyond that time. The dominance of the second mode for the spacing data is consistent with the hypothesis that this is the torsional mode, since a twisting motion will change the apparent distance between objects in a plane as seen from a fixed location. The uncertainty of the nonlinear fit is given by twice the square root of the variance, or ± 0.048 in..

For the angle of the first window line θ_i , the first and third modes dominate, as seen in Table K-5 and Fig. K-21. This is consistent with these modes representing vibrations in the north-south plane roughly perpendicular to the line of sight. The uncertainty for θ_i is ± 0.00064 rad. The angle increment $\Delta\theta$, in Table K-6 and Fig. K-22, is dominated by the first mode, with a strong contribution from the second. The uncertainty is ± 0.000074 rad.

Table K–4. Spacing modes from nonlinear least squares analysis of original data with 18 parameters. Initial guesses were obtained from sequential analyses of residuals. Uncertainties are twice the standard deviation.

E Period (s)	C Initial Amplitude (in.)	D Decay Rate (s ⁻¹)	F Phase (rad)	A Offset (in.)	B Slope (in./s)
11.29 ± 0.06	0.004 ± 0.001	-0.006 ± 0.003	2.3 ± 0.4	39.975 ± 0.001	-0.00001 ± 0.00001
5.256 ± 0.008	0.031 ± 0.004	0.010 ± 0.002	-0.5 ± 0.1	—	—
3.83 ± 0.01	0.018 ± 0.004	0.014 ± 0.004	-2.4 ± 0.2	—	—
2.391 ± 0.008	0.002 ± 0.002	0 ± 0.008	1.1 ± 0.9	—	—

Table K–5. Angle modes from nonlinear least squares analysis of original data with 18 parameters.

E Period (s)	C Initial Amplitude (10 ⁻³ rad)	D Decay Rate (s ⁻¹)	F Phase (rad)	A Offset (rad)	B Slope (rad/s)
11.44 ± 0.02	1.03 ± 0.06	0.015 ± 0.001	0.22 ± 0.06	0.15790 ± 0.00002	-7×10 ⁻⁷ ± 2×10 ⁻⁷
5.27 ± 0.03	0.13 ± 0.05	0.011 ± 0.006	-0.2 ± 0.4	—	—
3.88 ± 0.01	0.7 ± 0.1	0.032 ± 0.006	2.3 ± 0.2	—	—
2.36 ± 0.01	0.06 ± 0.05	0.01 ± 0.01	-1.3 ± 0.8	—	—

Table K–6. Angle increment modes from nonlinear least squares analysis of original data with 18 parameters.

E Period (s)	C Initial Amplitude (10 ⁻³ rad)	D Decay Rate (s ⁻¹)	F Phase (rad)	A Offset (10 ⁻³ rad)	B Slope (rad/s)
11.32 ± 0.02	0.046 ± 0.005	0.006 ± 0.001	-0.3 ± 0.1	-2.234 ± 0.002	1.2×10 ⁻⁷ ± 0.2×10 ⁻⁷
5.33 ± 0.03	0.016 ± 0.006	0.014 ± 0.007	0.3 ± 0.4	—	—
3.80 ± 0.01	0.003 ± 0.002	-0.006 ± 0.006	-2.9 ± 0.8	—	—
2.390 ± 0.008	0.006 ± 0.005	0.01 ± 0.01	-2.0 ± 0.8	—	—

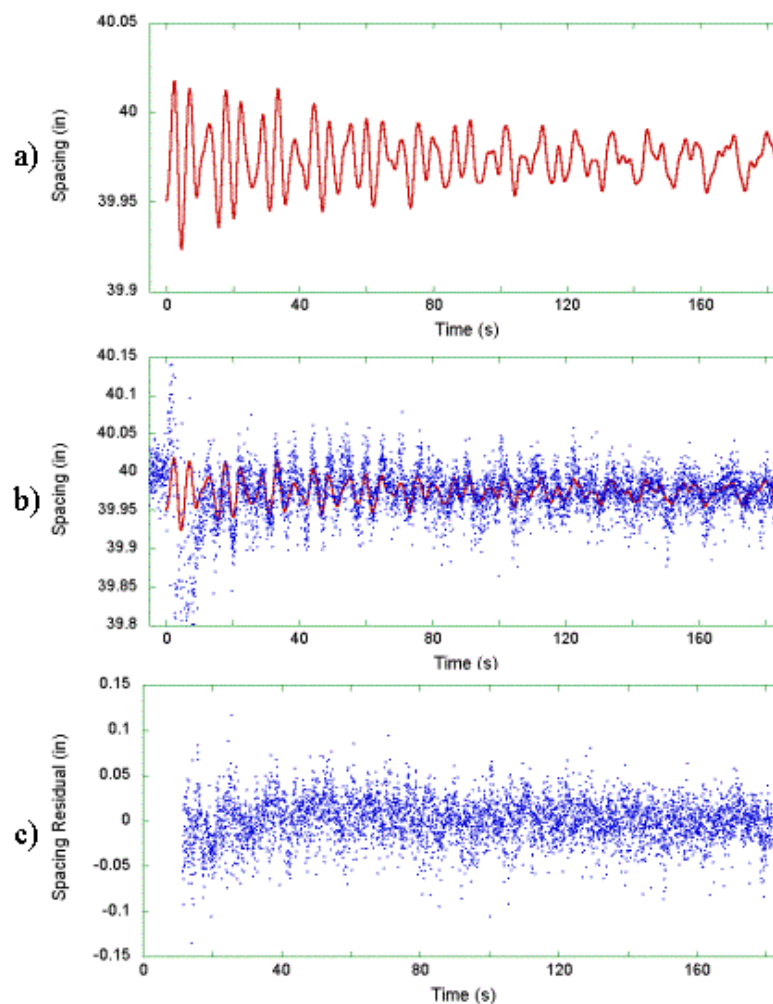


Figure K-20. Spacing modes: a) sum of four modes, b) comparison to data, c) residual after subtraction of sum of modes from data.

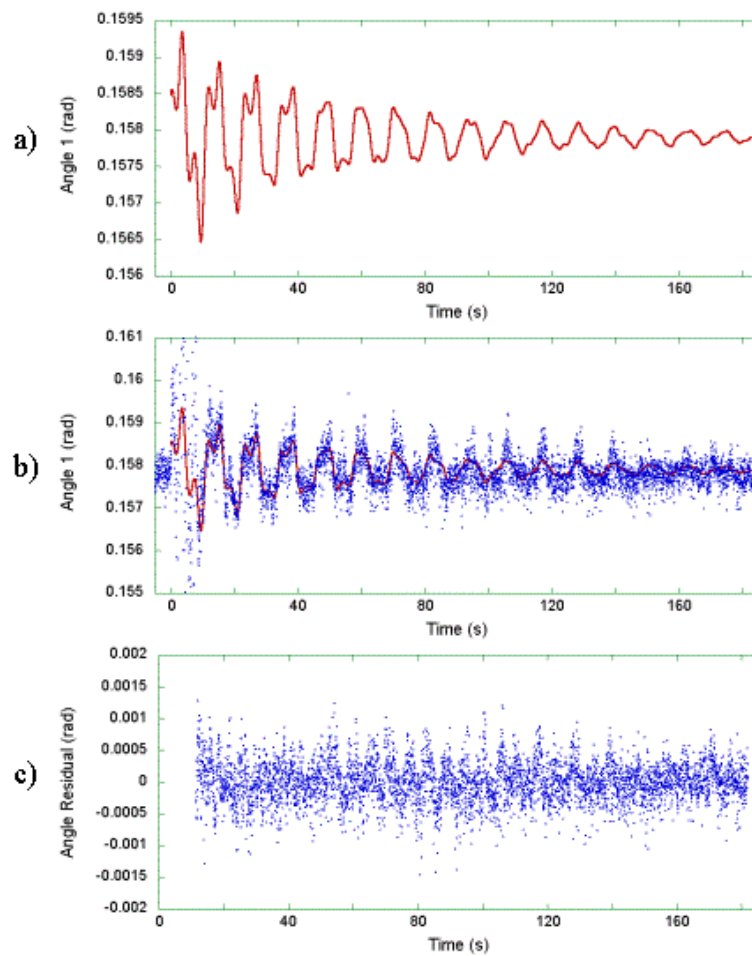


Figure K-21. Angle modes: a) sum of four modes, b) comparison to data, c) residual after subtraction of sum of modes from data.

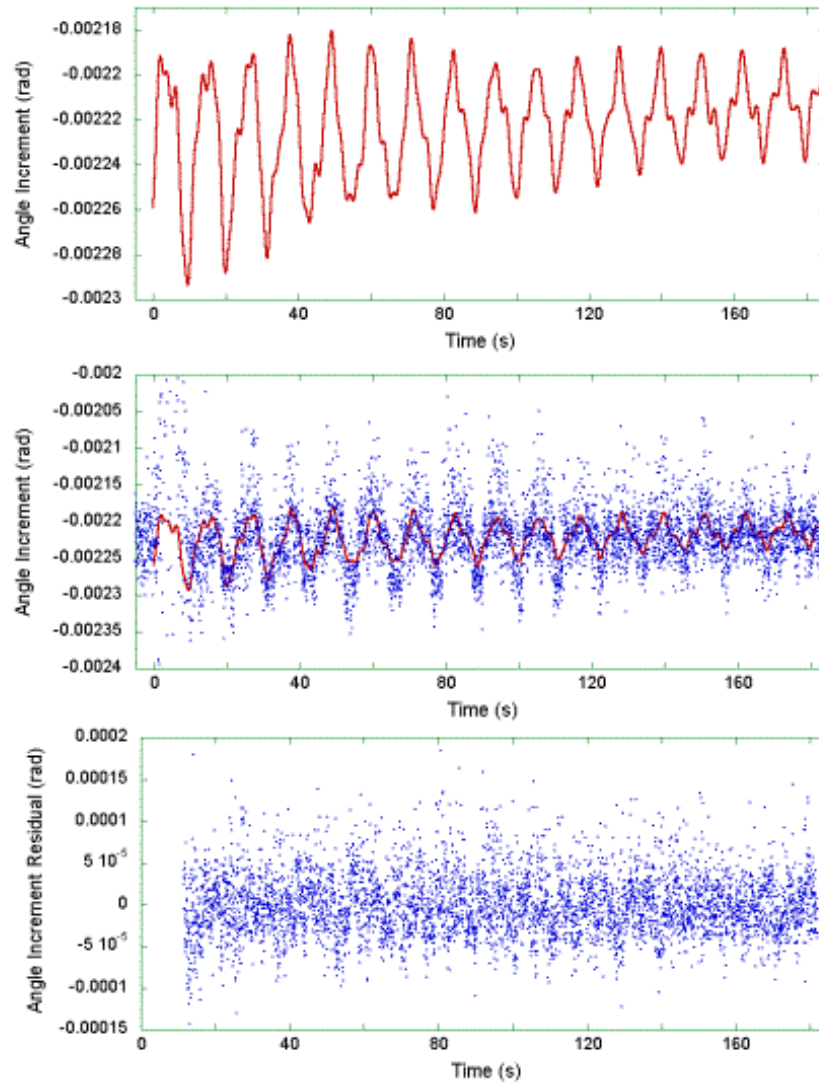


Figure K-22. Angle increment modes: a) sum of four modes, b) comparison to data, c) residual after subtraction of sum of modes from data.

The agreement among values found for the four identified modes varies among the four sets of data. Periods for the four modes agree well over all data. Values are within ± 2 percent for the first three modes and within ± 6 percent for the fourth mode. It is safe to say that the period is 11.4 s for the fundamental mode, 5.3 s for the first torsional mode, 3.9 s for the third measured mode, and 2.3 s for the fourth mode, with uncertainties less than ± 0.1 s for each. Decay rates for the four modes are expected to be consistent. However, this is the case only for the second mode, which ranges from 0.010 s^{-1} to 0.014 s^{-1} . The decay rate for the fundamental is near 0.006 s^{-1} for d_l and $\Delta\theta$, but is 0.015 s^{-1} for θ_l and (unrealistically) negative for p . Decay rates for the third mode range from 0.014 s^{-1} to 0.032 s^{-1} , except for the $\Delta\theta$ data set, for which this mode is lost in the noise. The amplitude of the fourth mode is not significant except for the displacement data set.

K.1.5 Sway at Roof of WTC 2

A final issue that can be addressed with this analysis is the motion at the roof of WTC 2. This requires extrapolation of the parameter values that have been determined at the 70th floor. Known quantities are the displacement d_l of the first window line and the window spacing p at the 70th floor, the angle θ_l of the first window line, and the angle increment $\Delta\theta$ from one line to the next. In the East video, the roof of WTC 2 is 310 vertical pixel counts above the base, or 344 pixel widths after dividing by the conversion factor 0.9. This is the height h . The locations in the horizontal direction and the angles of the first and last window lines are needed for the extrapolation. Straight window lines are assumed, although this assumption is not strictly true for the translational vibration modes. Since there are 58 lines, the time-dependent locations of the corners of the problem with respect to the zero point of d_l are:

$$x_{L \text{ bot}} = d_1 \quad (9)$$

$$x_{R \text{ bot}} = d_1 + 57p \quad (10)$$

$$x_{L \text{ top}} = d_1 + h \tan \theta_1 \quad (11)$$

$$x_{R \text{ top}} = (d_1 + 57p) + h \tan(\theta_1 + 57\Delta\theta) \quad (12)$$

where subscripts *bot* and *top* refer to the 70th floor and the roof of the building respectively and subscripts *L* and *R* refer to the leftmost (1st) and rightmost (58th) window lines. The time-dependent location at the center of the east face along the 70th floor is

$$x_{C \text{ bot}} = \frac{(x_{L \text{ bot}} + x_{R \text{ bot}})}{2} = \left(d_1 + \frac{57p}{2} \right) \quad (13)$$

and at the center of the WTC 2 roof is

$$x_{C \text{ top}} = \frac{(x_{L \text{ top}} + x_{R \text{ top}})}{2} = \left(d_1 + \frac{57p}{2} \right) + h \frac{[\tan \theta_1 + \tan(\theta_1 + 57\Delta\theta)]}{2} \quad (14)$$

The modal solutions for d_I , p , θ_I , and $\Delta\theta$ from Tables K-3 through K-6 are used to carry out these calculations. To determine displacements, the location of each point before the aircraft impact is subtracted from its time-dependent location. All distances are converted into horizontal pixel units for the calculation, then converted back into inches. The true distance between the 1st and 58th window lines is $57 \times 40 \text{ in.} = 2280 \text{ in.}$, so the multiplicative factor for converting pixels to inches at the top of the building is $2280 / (x_{R \text{ top0}} - x_{L \text{ top0}})$. Uncertainties for the displacement values at each of the six locations are calculated as twice the standard deviation determined by a quadrature sum of the standard deviations for each term. Since angles θ_I and $\Delta\theta$ are small, the tangents of these angles may be replaced in the calculation by the angles themselves. For example, the standard deviation of the displacement at the top center of WTC 2 is

$$\sigma_{C \text{ top}} = \sqrt{\left[(\sigma_d)^2 + \frac{57}{2} (\sigma_p)^2 + (h\sigma_\theta)^2 + \frac{57}{2} (h\sigma_{\Delta\theta})^2 \right]} \quad (15)$$

as derived from equation (14).

Table K-7 shows the maximum deflections of WTC2 as it swayed first to the north in response to the impact on its south face and then to the south. The extrapolated values at each of the six locations on the east face are listed under the columns marked Simple Projection. If equations (9), (10), and (13) accurately calculate displacements on the 70th floor, then values at the left, right, and central locations should match each other. Similarly, if equations (11), (12), and (14) accurately project displacements to the top of the building, then these three values should also match. It is clear from Table K-7 that this is not the case. Displacements extrapolated to the top of WTC 2 are in particularly poor agreement, falling outside of even the large limits of uncertainty for these values.

Table K-7. Maximum sway of WTC 2 after aircraft impact.

Location	Maximum deflection of first extremum—toward north (in.)			Maximum deflection of second extremum—toward south (in.)		
	Simple Projection	Corrected for Viewing Angle	Corrected plus Fixed $\Delta\theta$	Simple Projection	Corrected for Viewing Angle	Corrected plus Fixed $\Delta\theta$
70th floor: 1st window	11.7 ± 0.9	12.3 ± 1.0	12.3 ± 1.0	-12.2 ± 0.9	-13.9 ± 1.0	-13.9 ± 1.0
Center	11.9 ± 1.0	12.3 ± 1.0	12.3 ± 1.0	-13.5 ± 1.0	-14.0 ± 1.0	-14.0 ± 1.0
58th window	12.1 ± 1.0	12.3 ± 1.1	12.3 ± 1.1	-14.7 ± 1.0	-14.0 ± 1.1	-14.0 ± 1.1
Top: 1st window	22 ± 4	27 ± 4	22 ± 4	-22 ± 4	-34 ± 4	-26 ± 4
Center	26 ± 4	27 ± 4	22 ± 4	-34 ± 4	-36 ± 4	-27 ± 4
58th window	30 ± 5	27 ± 5	22 ± 5	-46 ± 5	-38 ± 5	-27 ± 5

The cause of this discrepancy was determined to be the neglect of the viewing angle of the east face of WTC 2 from the camera. Figures K-23 and K-24 demonstrate why this angle, although small, must be taken into account in order to accurately calculate north-south displacement along the east face.

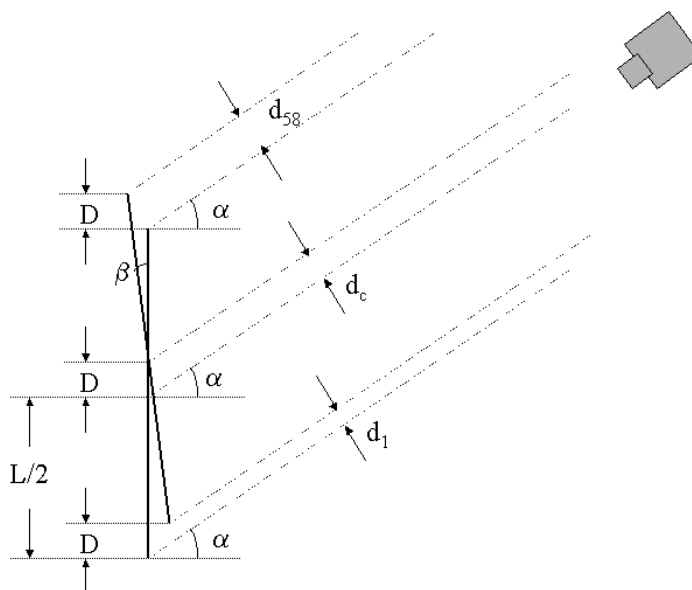


Figure K-23. Viewing angle geometry at first extremum of sway, with building displacement to north and counter-clockwise rotation.

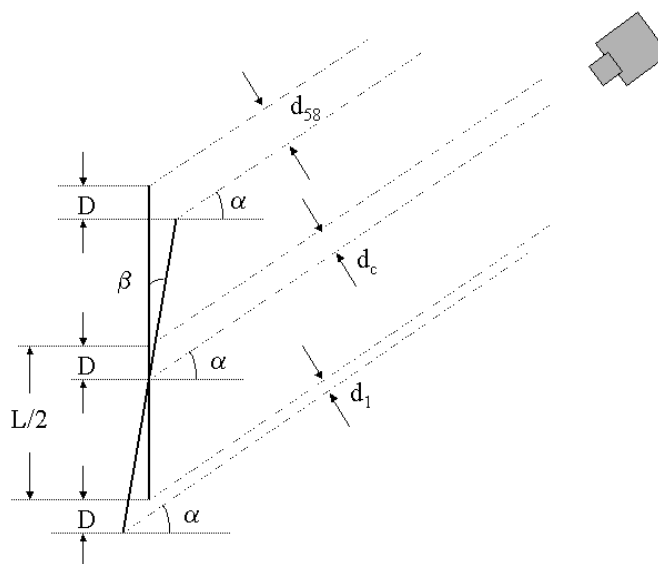


Figure K-24. Viewing angle geometry at second extremum of sway, with building displacement to south and clockwise rotation. Values of D and β are negative in this configuration.

As mentioned previously, the camera that recorded this footage was located to the east of WTC 2 and slightly north. The east face is not quite at right angles to the viewing direction. If the plane of the east face of WTC 2 is extended northward and a perpendicular line drawn to this plane from the camera location, then a second line drawn from the camera to the center of WTC 2 would make an angle of 12.3 degrees, or 0.2147 rad, with this line. The angle was measured within ± 0.2 degrees from a map from the FEMA study (FEMA 2002), although the accuracy of this map is uncertain. The angle of the perpendicular line with lines drawn from the camera to points along the east face of WTC 2 ranges from 7.3 degrees to 17.1 degrees. To simplify the problem, a constant angle of 15.3 degrees, or 0.2670 rad, corresponding to a line from the camera to the center of the zone used for the moiré analysis was chosen for the calculations. This is the angle α that appears in Figs. K-23 and K-24.

Figure K-23 shows the geometry of the east face of WTC 2 at the first extremum after the aircraft impact. The original position of the building is shown in the drawing by the vertical line. The aircraft strikes the building from the south at a northeast angle, forcing the building to swing north by deflection D and causing it to rotate by an angle β in the counter-clockwise direction as seen from above. The values of D and β are taken as positive in the northward and counter-clockwise directions respectively, and their magnitudes are a function of height. From a viewing angle α , the distances between a point in its original location and the same point on the deflected building increase from one end of the building to the other, so that the apparent distance d_l for the first window line is less than d_c for the center and d_{58} for the 58th window line. It can be shown that the three displacements D can be calculated as

$$D = \frac{d_l}{\cos \alpha} + \frac{L}{2} [\sin \beta \tan \alpha - (1 - \cos \beta)] \quad (16)$$

$$D = \frac{d_c}{\cos \alpha} \quad (17)$$

$$D = \frac{d_{58}}{\cos \alpha} - \frac{L}{2} [\sin \beta \tan \alpha - (1 - \cos \beta)] \quad (18)$$

The rotational angle β can be obtained from the spacing data. As the building rotates according to the torsional mode, the east face becomes alternately more and less perpendicular to the camera's point of view. When the face is closer to perpendicular, the spacing appears larger, and when it turns away the spacing appears smaller. The fractional variation of spacing allows the measurement of the rotational angle β , measured counter-clockwise, as

$$\beta = \alpha - \cos^{-1} \left[\frac{W_\beta}{W_0} \cos \alpha \right] \quad (19)$$

where W_β is the time- and height-dependent apparent width of the building as measured in the video frame and W_0 is the width in the absence of motion (before the aircraft impact).

Figure K-24 shows the geometry for the second extremum, when the building overshoots in its deflection by D to the south and rotates by angle β in a clockwise direction. (Note that these are not the same magnitudes as D and β in Fig. K-23 and are negative values.) Differences in the apparent displacement values for the 1st window line, center, and 58th window line are in the same sense as for Fig. K-23.

The displacement values obtained by taking viewing angle into account are listed in the second and fifth data columns of Table K-7. This correction has taken care of the discrepancies along the east face at both the 70th floor and the roof of WTC 2, so that the three displacements calculated at each height agree.

Unfortunately, this correction does not answer all discrepancies in the extrapolation of 70th floor data to the roof. Because the rotational angle β results from torsional motion, its oscillation period should match the torsional period of the building, or 5.3 s. This is obviously the case at the 70th floor, since β at this level depends directly on the measured apparent spacing p , whose dominant period is that of the torsional mode. However, when the data is extrapolated to the roof, it is found that β follows the fundamental mode period of 11.4 s rather than the expected torsional mode. The reason for this is the large contribution to the calculation of the apparent building width at the roof from the angle increment $\Delta\theta$. Recall from Table K-6 that the dominant mode for this variable is the fundamental mode. The oscillations in $\Delta\theta$ are likely due in large part to the camera perspective rather than the building motion. A final calculation of the projected motion at the roof is therefore made with the value of $\Delta\theta$ fixed and its oscillations removed.

The results of eliminating oscillations in the angle increment variable in addition to correcting for camera viewpoint are shown in the third and sixth data columns of Table K-7 and in Figure K-25. This figure shows the modal data measured at the 70th floor and extrapolated to the roof of WTC 2 for the first three minutes after impact. It demonstrates graphically the reduction in displacement discrepancies from the south end of the east face to the north resulting from correcting for camera viewpoint. Figure K-25(a) displays the application of equations (9) through (14) to the sum of the modal solutions for d_i , p , and θ_i and a fixed value of $\Delta\theta$ from Tables K-3 through K-6. In Fig. K-25(b), equations (16) through (19) are applied at the 70th floor and at roof level to correct for the viewing angle.

With the correction for camera viewpoint from both accounting for the average angle and removing variations in $\Delta\theta$, the deflections at the roof given those at the 70th floor are in reasonable agreement with the mode shape of the fundamental natural mode as determined by the structural model described in NIST NCSTAR 1-2A, Chap. 2.³

The final conclusion is that WTC 2 reacts to the aircraft impact with an initial sway to the north of 12 in. \pm 1 in. at the 70th floor and 22 in. \pm 5 in. at the roof. A better accounting of the effects of camera perspective on the data collected by the moiré analysis would give more accurate results.

³ Sadek, F. 2005. NIST personal communication.

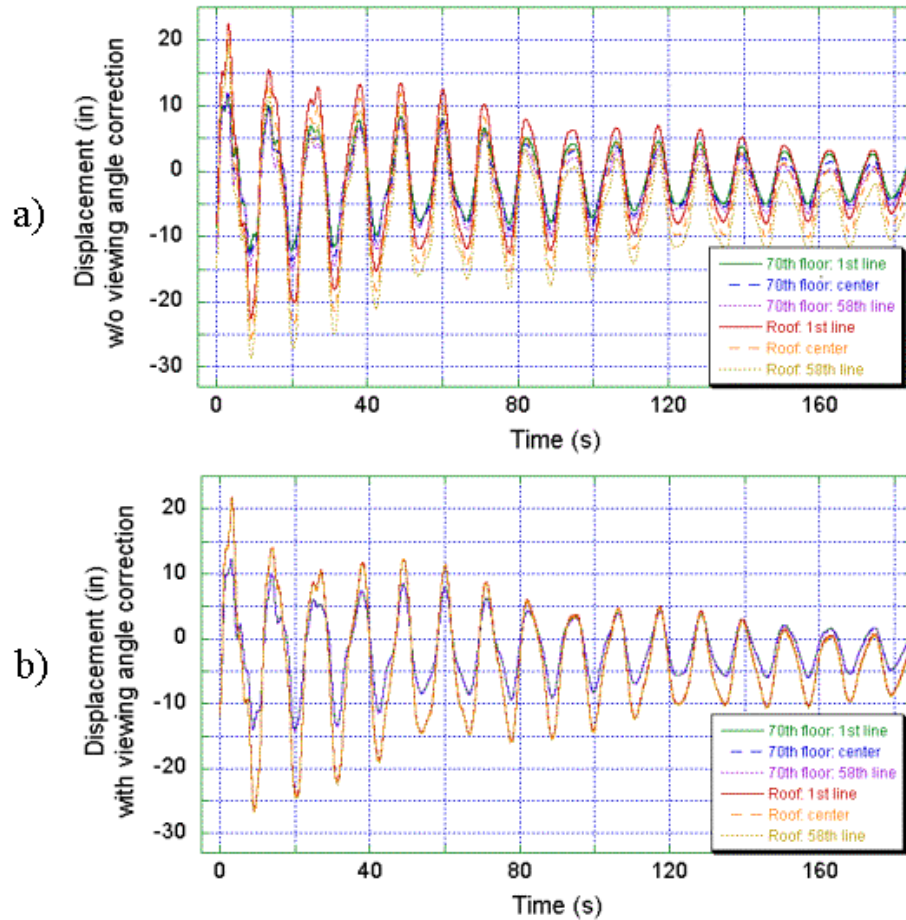


Figure K–25. WTC 2 displacement at 70th floor and extrapolation to displacement at roof (a) before and (b) after correction for camera viewing angle. Oscillations in the angle increment variable $\Delta\theta$ have been removed.

K.2 EAST-WEST OSCILLATIONS

An amateur video filmed from the north with the camera mounted on a tripod provides the opportunity to determine the east-west motion of WTC 2 for a brief time after the aircraft impact. The four frames in Fig. K–26 illustrate the appearance of the video around this time. In Fig. K–26(a), a frame taken just before impact shows the composition, with the tops of WTC 1 and WTC 2 filling much of the frame. The base of the video corresponds to the 94th floor of WTC 2. WTC 2 can be seen to move slightly (less than a pixel width) for a few seconds, first to the west then east, until the fireball covers the visible surface of WTC 2 in Fig. K–26(b). Figure K–26(c) shows that the smoke gradually clears from the west (right) side of the north face. Unfortunately, the video pulls back from the view a few seconds later in Fig. K–26(d), and the detail necessary to observe the building motion is lost.

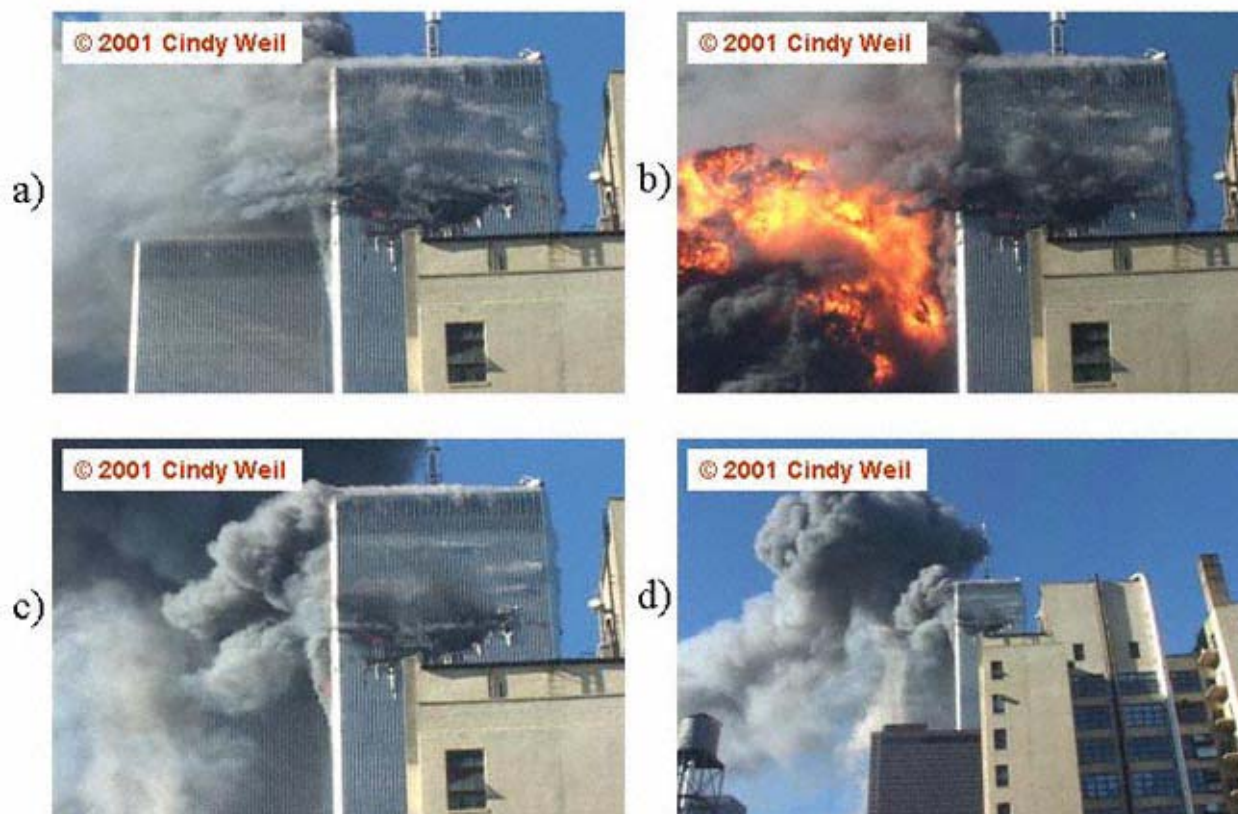


Figure K-26. North video of WTC 2 aircraft impact.

K.2.1 Moiré Fringes

The technique used to collect data from this video is illustrated in Fig. K-27. Figure K-27(a) shows the region with WTC 2 on the left and WTC 1 on the right at twice normal magnification with a superimposed grid. Consider the fifth window line from the right for WTC 2. In successively higher magnifications from (b) to (d) it can be observed that this window line is not quite vertical but at a small angle relative to the vertical pixel columns. Because of this angle, the window line must move from one column to the adjacent one as it moves from top to bottom. This is seen most clearly in Fig. K-27(c), where at the top of the figure the fifth window line is two columns wide next to the grid line, at the middle it becomes a single column, and at the bottom it is again two columns wide, but now separated from the grid line by one column. The marker point whose location over time reveals the building motion is the vertical pixel in the single column for which pixels on either side are the same intensity. The arrows in Fig. K-27(d) indicate the pixel judged to satisfy this requirement. Note that at the top of this figure the column to the left of the fifth window line is slightly darker than that on the right, and at the bottom the opposite is true. The uncertainty of the identification of the marker location is judged to be about plus or minus seven pixels.

The fifth window line from the right was selected for data collection because it is obscured by smoke for the least amount of time. The selected marker point is visible throughout this period.

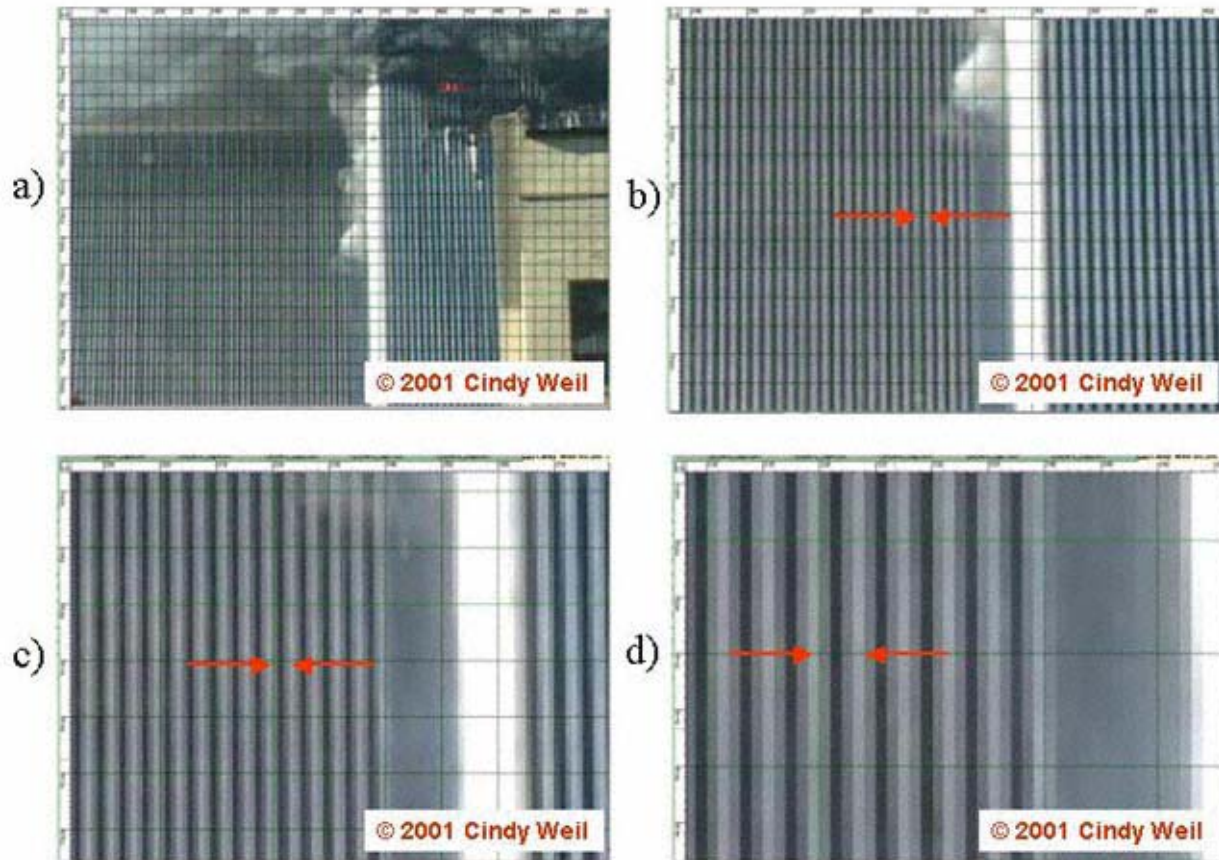


Figure K–27. Closeups of video frame showing the procedure for obtaining data on east-west motion of WTC 2 after impact. Magnification is a) 200 %, b) 400 %, c) 800 %, and d) 1600 %. Arrows indicate the vertical location on the fifth line of windows from the right at which the intensity appears to be equal on both sides of the dark column.

Figure K–28 shows the data obtained by estimating the vertical location of the marker point at 5-frame (0.167-s) intervals during time periods at which the marker location can be determined. (Automation of this procedure was not attempted due to time limitations.) East-west oscillatory motion is revealed, although it is only visible for slightly less than one period initially and about one period after the fireball. The period of this motion can be estimated by doubling the time difference between minimum and maximum points. These are located at 1.3 s and 4.7 s and later at 15.3 s and 17.8 s, giving periods of 6.8 s and 5.0 s respectively. The period can also be calculated by assuming a peak between the two maxima and dividing the time difference between them by two, for a third value of $(15.3 - 4.7) / 2 = 5.3$ s. The period and motion in the east-west direction are consistent with the torsional mode of WTC 2.

Note that the motion for the two observable oscillations is significantly offset from the null location at pixel 360. The reason for this is unknown.

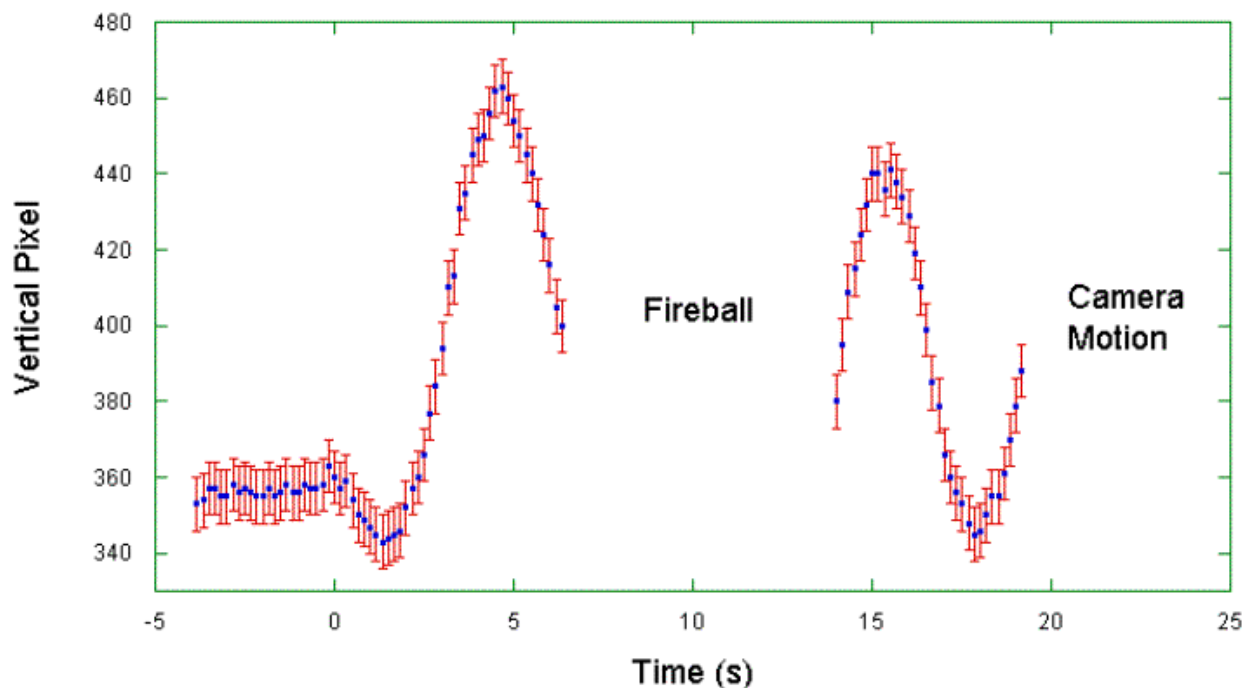


Figure K–28. Vertical displacement of index point measuring east-west motion of WTC 2 just before and after aircraft impact. Higher values indicate motion to the east. Red error bars indicate uncertainty.

The magnitude of the east-west oscillations can be estimated by determining the number of vertical pixels between the studied marker point and the next point on the fifth window line at which pixel values are equal on each side. The horizontal distance between these two points is exactly one pixel. Assuming that the north face of WTC 2 is truly perpendicular to the camera view, the thickness of a horizontal pixel in inches is given by the 40 inch window spacing divided by the number of pixels between windows. As can be seen in Fig. K–26(d), the distance between windows near the base of the frame is almost exactly 4 pixels. So a single pixel is 10 inches wide. Since the vertical distance corresponding to one horizontal pixel is $105 \text{ vertical pixels} \pm 15$, the maximum eastern motion of WTC 2 at the 94th floor is $(463 - 360) / (105 \pm 15) \times 10 \text{ in.} = 9.8 \pm 1.5 \text{ in.}$ The maximum western motion captured by this video is much less, at $(360 - 343) / (105 \pm 15) \times 10 \text{ in.} = 1.6 \pm 0.2 \text{ in.}$ For total uncertainty, the measurement uncertainty of ± 7 pixels, equivalent to $\pm 0.67 \text{ in.}$, is included through a quadrature sum such as that in Eq. (6). Extremes of motion are therefore $1.6 \pm 0.7 \text{ in.}$ westward at $t = 1.3 \text{ s}$ and $9.8 \pm 1.6 \text{ in.}$ eastward at $t = 4.7 \text{ s}$. The initial motion westward is consistent with excitation of the torsional mode by impact on the south face angled toward the east.

K.2.2 Oscillation Modes

Despite the small amount of data, a nonlinear least squares fit to Eq. (7) can be performed to obtain a more accurate estimate of the period. The resulting parameters are listed in Table K–8 and plotted against the data in Fig. K–29. The first analysis includes all data points from $t = 0 \text{ s}$ on. This fit is not very accurate, as seen from the uncertainties on the first line of the table and the dashed curve in Fig. K–29. A second and more successful fit, reported on the second line and plotted as a solid curve, neglects the first

two seconds of data. The improvement of this fit may reflect the fact that the impulse to the building caused by the aircraft impact was not instantaneous. The value of 5.3 s for the period of the oscillatory motion is in good agreement with the torsional mode found in the moiré analysis of north-south motion.

Table K-8. Modes from nonlinear least squares analysis for east-west displacement data starting at a) 0 s and b) 2 s. Uncertainties are twice the standard deviation.

Starting Time (s)	Period (s)	Amplitude (in.)	Decay Rate (s^{-1})	Phase (rad)	Offset (in.)	Slope (in./s)	Total Uncertainty 2σ (in.)
0	5.53 ± 0.08	6 ± 1	0.02 ± 0.02	2.7 ± 0.2	3.8 ± 0.7	-0.03 ± 0.06	3.1
2	5.32 ± 0.03	5.4 ± 0.4	0.015 ± 0.006	2.11 ± 0.08	5.6 ± 0.3	-0.16 ± 0.02	1.0

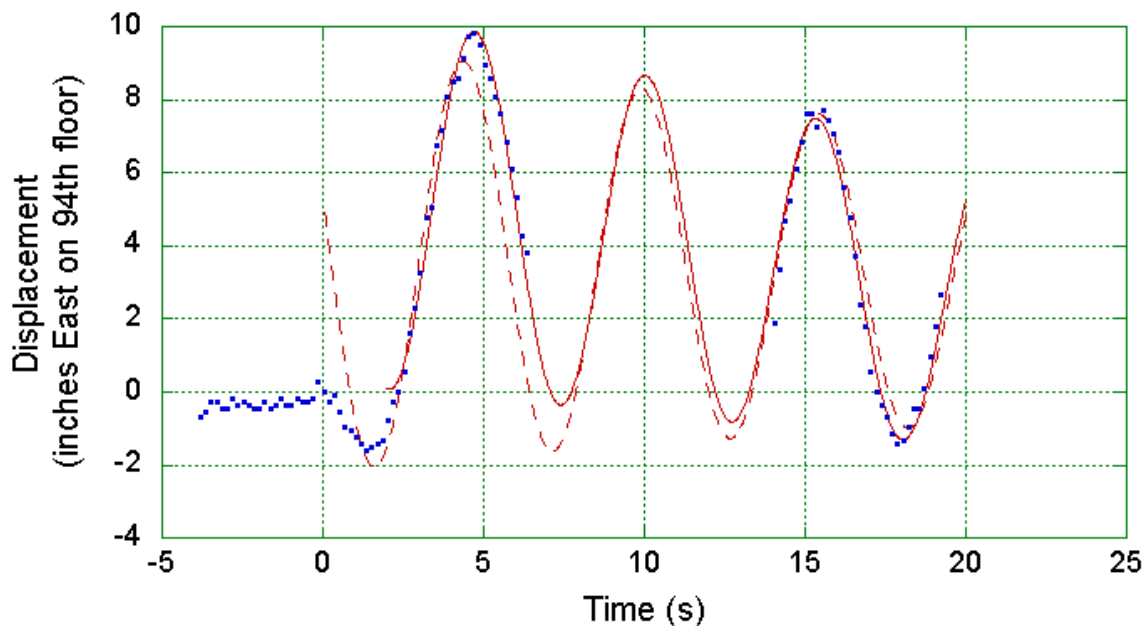


Figure K-29. Comparison of data (blue dots) to modes from nonlinear analyses of data starting at 0 s (dashed red line) and 2 s (solid red line).

K.3 CONCLUSIONS

Details of the oscillation of WTC 2 in response to the aircraft impact have been obtained through analyses of the moiré patterns caused by superposition of architectural features with the vertical columns of pixels in the digital video images. The East video, taken from a tripod-mounted camera to the east, shows motion in the north-south direction for 11 minutes after the aircraft impact. The North video, taken from the north, shows east-west motion for twenty seconds minus seven seconds interruption by the fireball. Modal analyses of the north-south displacement reveal the fundamental north-south mode with a period of 11.4 s, a torsional mode with a period of 5.3 s, and two higher modes with periods of 3.9 s and 2.1 s, all with uncertainties of less than ± 0.1 s. The torsional mode is confirmed in a modal analysis of the east-west motion. From the East video, the initial sway of WTC 2 toward the north is 12 ± 1 in. at the 70th floor and 22 ± 5 in. at the top. From the North video, the estimated total east-west sway at the 94th floor is 12 ± 2 in.

K.4 REFERENCES

- Kafri, O., and I. Glatt. 1990. *The Physics of Moire Metrology*. John Wiley & Sons. New York.
- FEMA (Federal Emergency Management Agency). May 2002. World Trade Center Building Performance Study: Data Collection, Preliminary Observations, and Recommendations. FEMA 403. New York.
- NIST/SEMATECH e-Handbook of Statistical Methods*,
<http://www.itl.nist.gov/div898/handbook/eda/section3/spectrum.htm>, 2003.
- NIST/SEMATECH e-Handbook of Statistical Methods*,
<http://www.itl.nist.gov/div898/handbook/eda/section3/compdeam.htm>, 2003.
- NIST/SEMATECH e-Handbook of Statistical Methods*,
<http://www.itl.nist.gov/div898/handbook/eda/section3/compdeph.htm>, 2003.

Appendix L

OBSERVATIONS OF STREAMERS FOR WORLD TRADE CENTER 1

The information in the following table was derived from review of photographs and videos assembled in the National Institute of Standards and Technology World Trade Center (WTC) Visual Database. Times when streamers were observed, along with the face of WTC 1 on which the observation was made, are provided. Additional location information and other details are provided when available.

Time	North	East	South	West
8:50:17 a.m.	Falls from near 94-115			
8:54:52 a.m.	Falls from 97-145			
8:55:04 a.m.	Falls from near 97-145			
8:55:19 a.m.	Falls from 97-146			
8:55:33 a.m.	Falls from 97-148			
8:55:41 a.m.	Falls from near 97-147			
8:55:45 a.m.	Falls from 97-151			
8:56:21 a.m.	Falls from near 96-150			
8:56:41 a.m.	Falls from near 97-150			
8:56:47 a.m.	Falls from near 97-151			
8:56:54 a.m.	Falls from 97-142			
8:57:23 a.m.	Falls from near 96-150			
8:57:26 a.m.				Two falling on face
8:57:30 a.m.	Falls from near 96-153			
8:57:54 a.m.				Falls from 97 th floor near center of face
8:58:18 a.m.				Two falling on face
8:58:23 a.m.	Falls from 97-440			
8:58:23 a.m.	Falls from near 97-154			
8:58:25 a.m.	Falls from 96-148			
8:58:35 a.m.		Falls along face		
8:58:37 a.m.	Falls along face			
8:58:52 a.m.		Falls along face		
8:58:55 a.m.	Falls from 97-147			
8:59:11 a.m.				Two falling on face
8:59:22 a.m.		Falls along face		
8:59:41 a.m.				Falls along face
8:59:55 a.m.			Falls near center of face	
9:00:01 a.m.		Falls along face		
9:00:10 a.m.				Falls along face
9:00:53 a.m.		Falls along face		

Time	North	East	South	West
9:01:15 a.m.		From near 95-227		
9:01:25 a.m.				Falls along face
9:01:37 a.m.			Falls from near 96-350	
9:01:57 a.m.		Two fall from 94-226		
9:01:58 a.m.	From near 96-151			
9:02:14 a.m.	From near 96-152			
9:02:15 a.m.				Falls along face
9:02:18 a.m.		Falls along face		
9:02:21 a.m.		Falls along face		
9:02:37 a.m.		Falls along face		
9:02:52 a.m.		Falls along face		
9:03:11 a.m.		Two fall along face		
9:03:20 a.m.	From near 97-104			
9:04:26 a.m.		From near 96-231		
9:04:41 a.m.				Falling along column 114
9:04:33 a.m.		Falls along face		
9:05:13 a.m.	From 97-103			
9:07:41 a.m.	From 97-106			
9:08:37 a.m.		Falling along face		
9:08:55 a.m.		From near 97-107		
9:16:07 a.m.			Falls along face	
9:16:42 a.m.				Falls along face
9:17:23 a.m.				Falls along face
9:18:36 a.m.	Near east side			
9:18:43 a.m.	Falls along face			
9:18:48 a.m.		Falling along face		
9:19:19 a.m.	From near 96-153			
9:19:29 a.m.	From near 96-153			
9:19:36 a.m.	From 96 th floor near east edge			
9:19:42 a.m.	From 94-111			

Time	North	East	South	West
9:19:52 a.m.		Falls along face		
9:20:07 a.m.	Falls along east side			
9:20:16 a.m.	Falls along east side			
9:20:54 a.m.	Falls along column 122			
9:20:56 a.m.	Falls along face			
9:21:03 a.m.	Falls from near east edge			
9:21:04 a.m.		Falls along face		
9:21:07 a.m.		Falls from 96-202		
9:21:09 a.m.		Falls along face		
9:21:28 a.m.		Falls along north side		
9:22:35 a.m.		Falls along north side		
9:24:34 a.m.	Two fall from near east edge			
9:25:47 a.m.	Falls from near east edge			
9:30:32 a.m.		Falls along face		
9:30:46 a.m.	From near 98-122			
9:34:44 a.m.		Falls along face		
9:35:46 a.m.		Falls along face		
9:35:57 a.m.		Falls near column 216		
9:36:20 a.m.	From near 98-153			
9:36:54 a.m.		Falls along face		
9:37:31 a.m.		Falls along face		
9:38:11 a.m.	From near 98-136			
9:38:22 a.m.	From near 98-142			
9:38:32 a.m.	Falls along face			
9:38:39 a.m.	From near 98-138			
9:39:13 a.m.	From near 98-128	Falls along face		
9:39:23 a.m.				Falls along face
9:39:38 a.m.	From near 98-142			
9:40:02 a.m.		Falls along face		
9:40:04 a.m.	Near east edge			

Time	North	East	South	West
9:40:18 a.m.			Three fall along face	
9:40:38 a.m.	From near 98-125			
9:40:41 a.m.			Falls along face	
9:40:58 a.m.	From near 98-434			
9:41:00 a.m.			Observed near ground	
9:41:06 a.m.	From near 98-125			
9:41:08 a.m.				Falls along south side
9:41:10 a.m.	From near 98-151			
9:41:27 a.m.	From 94-145			
9:41:44 a.m.	Falls near east edge			
9:41:45 a.m.	From near 98-135			
9:41:55 a.m.	From near 98-128			
9:42:26 a.m.	From 94-102			Falls along south side
9:42:33 a.m.				
9:42:46 a.m.	Two from 98-153			
9:42:53 a.m.	From 98-153			
9:42:55 a.m.		Falls along face		
9:43:08 a.m.	From near 98-155			
9:43:09 a.m.	From near 98-156			
9:43:21 a.m.				From near 98-404
9:43:31 a.m.	From 98-140			
9:43:51 a.m.	From 94-101			
9:44:09 a.m.	From near 98-151			
9:44:05 a.m.				From 98-418
9:44:15 a.m.	From 98-147			
9:49:18 a.m.	Falls along west side			
9:52:03 a.m.		Falls along south side		
9:55:55 a.m.	Falls from west side			
9:58:21 a.m.	Falls along west side			
10:13:34 a.m.				From 94-448
10:13:36 a.m.				From 94-447

This page intentionally left blank.

Appendix M

OBSERVATIONS OF FALLING HUMAN BEINGS FOR WTC 1

The information in the following table was derived from review of photographs and videos assembled in the National Institute of Standards and Technology World Trade Center (WTC) Visual Database. Times when falling people were observed, along with the face of WTC 1 on which the observation was made, are provided. Additional location information is provided when available.

Time	North	East	South	West
8:51:01 a.m.	From 93-149			
8:58:04 a.m.		From 93-215		
8:58:05 a.m.		From 92-215, climbed to here from above		
8:58:14 a.m.		From 93-215		
8:58:19 a.m.		From 93-227		
8:58:21 a.m.		From 93-215		
8:58:23 a.m.		From 92-223		
9:00:09 a.m.		From 92-210		
9:00:14 a.m.		From near 92-219		
9:20:27 a.m.		From 92-220		
9:00:30 a.m.		From 92-220		
9:01:01 a.m.		From 92-220		
9:01:11 a.m.		From 105-255		
9:01:46 a.m.		From 92-210		
9:01:46 a.m.			From 98-301	
9:02:08 a.m.		From 92-209		
9:02:36 a.m.		From near 105-207		
9:03:02 a.m.		From 100-238		
9:03:08 a.m.				From high on face
9:03:08 a.m.				From high on face
9:04:05 a.m.		From above 95 th floor on south edge		
9:06:17 a.m.				South side of face
9:09:30 a.m.				South side of face
9:10:02 a.m.				South side of face
9:10:44 a.m.		Southeast corner		
9:14:26 a.m.		From near 104-257		
9:14:57 a.m.			From high on face	
9:15:47 a.m.	From near 100-147			Along column 412
9:15:52 a.m.				

Time	North	East	South	West
9:16:41 a.m.		From near 105-246		
9:17:51 a.m.				Near southwest corner
9:18:15 a.m.			Location unknown	
9:18:26 a.m.	From near 104-123			
9:18:35 a.m.			Location unknown	
9:19:08 a.m.	From 104-123			
9:21:58 a.m.			Location unknown	
9:22:55 a.m.		Along column 255		
9:29:10 a.m.				From 103-457
9:30:01 a.m.				From high on north side
Approximately 9:34 am.				Along column 425
9:37:33 a.m.		Near column 239		
9:38:37 a.m.				From near center of 94 th floor
9:38:45 a.m.	Near northeast corner			
9:39:18 a.m.				From near center of 94 th floor
9:39:31 a.m.				From 94-435
9:39:40 a.m.				From 94-437
9:40:02 a.m.				From 94-435
9:40:10 a.m.				From near center of 94 th floor
9:40:14 a.m.				From near 94-435
9:40:29 a.m.	From 105-121			
9:40:51 a.m.				Along column 415
9:41:27 a.m.				From above 98 th floor
9:41:34 a.m.				Climbed from 94-433
9:42:38 a.m.				Along column 417
9:43:13 a.m.				Near column 416
9:46:26 a.m.	From 106-105			

Time	North	East	South	West
9:47:01 a.m.				From high near column 445
9:47:19 a.m.	From 106-105			
9:47:42 a.m.				South side of face
9:48:32 a.m.	From 104-118			
9:49:12 a.m.	From 104-120			
9:49:31 a.m.	From 105-115			
9:53:22 a.m.		Near column 247		
9:58:02 a.m.		From high near column 245		
9:59:06 a.m.		Along column 248		
9:59:20 a.m.	From 106-105			
10:06:11 a.m.				From near center of 95 th floor
10:06:11 a.m.				From near center of 95 th floor
10:06:57 a.m.				From 95-428
10:06:58 a.m.				From 95-427
10:06:59 a.m.				From 95-426
10:06:59 a.m.				From 95-426
10:06:59 a.m.				From 95-425
10:07:00 a.m.				From 95-426
10:07:00 a.m.				From 95-425
10:07:01 a.m.				From 95-425
10:07:03 a.m.				From 95-424
10:07:44 a.m.				From 95 th floor
10:07:48 a.m.				Location unknown
10:07:51 a.m.				Location unknown
10:07:55 a.m.				From 95 th floor
10:08:08 a.m.				Location unknown
10:08:18 a.m.				From near 97 th on north

Time	North	East	South	West
				side
10:08:47 a.m.				High from unknown location
10:11:34 a.m.	Along column 103 from above 103 rd floor			
10:13:00 a.m.	Along column 117			
10:13:01 a.m.	Along column 110			
10:13:20 a.m.	Near column 118			
10:18:35 a.m.	From 103-115			
10:19:07 a.m.	From near 105-157			
10:19:08 a.m.	Along column 114			
10:19:45 a.m.	Along column 112			
10:19:50 a.m.	Along column 112			
10:19:54 a.m.	Along column 114			
10:20:16 a.m.	Near column 118			
10:20:21 a.m.	From high near center			
10:23:49 a.m.	From near 106-116			
10:24:06 a.m.				From high on south side
10:25:36 a.m.	Near column 110			
10:26:20 a.m.	Near column 130			
10:28:09 a.m.				From near 106-455

This page intentionally left blank.